INFORMATION TO USERS

This manuscript has been reproduced from the microfilm master. UMI films the text directly from the original or copy submitted. Thus, some thesis and dissertation copies are in typewriter face, while others may be from any type of computer printer.

The quality of this reproduction is dependent upon the quality of the copy submitted. Broken or indistinct print, colored or poor quality illustrations and photographs, print bleedthrough, substandard margins, and improper alignment can adversely affect reproduction.

In the unlikely event that the author did not send UMI a complete manuscript and there are missing pages, these will be noted. Also, if unauthorized copyright material had to be removed, a note will indicate the deletion.

Oversize materials (e.g., maps, drawings, charts) are reproduced by sectioning the original, beginning at the upper left-hand corner and continuing from left to right in equal sections with small overlaps. Each original is also photographed in one exposure and is included in reduced form at the back of the book.

Photographs included in the original manuscript have been reproduced xerographically in this copy. Higher quality 6" x 9" black and white photographic prints are available for any photographs or illustrations appearing in this copy for an additional charge. Contact UMI directly to order.

U·M·I

University Microfilms International
A Bell & Howell Information Company
300 North Zeeb Road Ann Arbor MI 48106-1346 USA
313 761-4700 800 521-0600

Order Number 9218280

Spin-tagged electron-hydrogen scattering: Ionization in the near threshold region

Tang, Fu-Ching Frank, Ph.D.

City University of New York, 1989

Copyright ©1989 by Tang, Fu-Ching Frank. All rights reserved.

U·M·I
300 N. Zeeb Rd.
Ann Arbor, MI 48106

SPIN-TAGGED ELECTRON-HYDROGEN SCATTERING: IONIZATION IN THE NEAR THRESHOLD REGION

by

FU-CHING TANG

A dissertation submitted to the Graduate Faculty in Physics in partial fulfillment of the requirements for the degree of Doctor of Philosophy, The City University of New York.

1989

© 1989
FU-CHING TANG

All Rights Reserved

This Manuscript has been read and accepted for the Graduate Faculty in Physics in satisfaction of the dissertation requirement for the degree of Doctor of Philosophy.

Sept 28, 1988
Date

Chair of Examining Committee
Prof. Michael S. Lubell

Sept 29, 1988
Date

Executive Officer

Prof. Kurt Becker

Prof. Alvin Halpern

Prof. Marvin H. Mittleman

Prof. Leonard O. Roellig

The City University of New York

Abstract

SPIN-TAGGED ELECTRON-HYDROGEN SCATTERING: IONIZATION IN THE NEAR THRESHOLD REGION

by

Fu-Ching Tang

Adviser: Michael S. Lubell

Electron-hydrogen atom scattering continues to remain an interesting subject for study, first because of the relative simplicity that characterizes the three-body problem, and second because of the complexity introduced by the long-range nature of the electromagnetic interaction. As the precursor to many-body physics, in which closed-form analytical solutions do not exist, it is apparent that a detailed understanding of the electron-hydrogen problem is extremely desirable. In order to provide improved sensitivity for testing theoretical approximations methods, I carried out an experiment in which spin served to tag the electrons, thereby reducing the ambiguities introduced by the identical nature of the projectile and target electrons. Stated somewhat differently, the use of polarized particles helped to distinguish the direct and exchange scattering channels, in the absence of which, tests of the predictive capabilities of theoretical approximation are often blurred.

I performed the experiment using a high-intensity beam of polarized electrons originating from a GaAs photoemission source and a highly-dissociated beam of polarized hydrogen atoms produced by an rf discharge and a magnetic hexapole selector. For incident electron energies ranging

from 13.6 eV to 15.0 eV, I investigated total impact ionization using electrons with a characteristic energy spread of approximately 100 meV. The quantity I determined was the cross-section asymmetry A_I, defined by

$$A_I = [\sigma(\uparrow\downarrow) - \sigma(\uparrow\uparrow)]/[\sigma(\uparrow\downarrow) + \sigma(\uparrow\uparrow)],$$

where $\sigma(\uparrow\downarrow)$ and $\sigma(\uparrow\uparrow)$ correspond respectively to the total cross sections for incident and target spins antiparallel and parallel. The source of polarized electrons provided typically several tens of nA of electrons in the interaction region with a polarization of 35%. The atomic hydrogen beam was characterized in the interaction region by a density of 1-2 x 10^{10} atoms/cm^3 and polarization of 0.515. Frequent reversal of the electron polarization direction allowed the determination of the asymmetry.

The value of A_I was found to be of the order of 0.4 for the energy range investigated, in agreement with previous measurements. As function of energy, A_I was not inconsistent with the Wannier picture, although additional data are needed to justify this conclusion completely.

ACKNOWLEDGEMENTS

First and foremost, I would like to express my appreciation to my thesis adviser, Professor Michael S. Lubell. I have benefited much from his knowledge, guidence and friendship, not only in experimental physics, but also in a diversified fields.

Special thanks go to my co-conspirations on the experiment: Drs. A. Vasilakis and F.J. Mulligan; Professors M. Eminyan, K. Rubin and J. Slevin; and Messrs D.C. Crowe and N. Chan. Together Dr. Vasilakis and I spent several years with many frustrating attempts to make the machine work from scratch. Without the various resources and assistance from these people and a number of others, this thesis would have impossible.

I thank the staff of the CCNY machine shop, in particular, S. Forst and G. Cannella, for the excellent job they have done. I also acknowledge the help of Ms. Rhina Herrera in typing this thesis, and the efforts of Professor Lubell in providing the necessary corrections. I greatly appreciate the contributions of Mr. Crowe who performed much of the data analysis and Mr. Chan who carried out the Monte Carlo simulations of the polarized hydrogen beam.

This long-time study would not have been possible without the love, consideration and understanding of my parents, Quen-Yuan and Eau-Eler, my wife Ei-Shine and my children, Jonathan and Karen. Their tolerance and appreciation permitted me to complete this work and continue in physics research. Finally, I acknowledge the encouragement from all my friends and from my wife's family.

TABLE OF CONTENTS

LIST OF TABLES

LIST OF ILLUSTRATIONS

I. INTRODUCTION

A. HISTORICAL SURVEY OF ELECTRON-HYDROGEN ATOM COLLISIONS

The theory of atomic collisions finds its major interest not in the study of the nature of fundamental interactions, as is the case of elementary particle theory, but rather in the development of approximation methods to handle the many-body problem involving long-range forces. With potential applications to atmospheric and astrophysical phenomena, laser development, and plasma dynamics, as well as surface physics and material processing, tests of the approximation methods have an impact on our understanding of a vast array of physical phenomena. As a testing ground for the various approximation methods, electron-hydrogen atom scattering is the ideal candidate from theoretical perspective, since the wave functions of the hydrogen atom are known to high accuracy. It is for this reason that more than one hundred theoretical papers have been published within the last twenty years on the subject of electron-hydrogen atom scattering.

The agreement between measurements and calculations has been extremely good over a wide range of energies and scattering angles for several scattering channels [1.1-1.6], provided averages are taken over spin and angular momentum. Significant experimental studies include those by Fite and his coworkers, and Williams and his coworkers, and Teubner and his coworkers.

Within the last few years new experimental methods involving polarized beams and coincidence techniques [1.8] have been developed which provide the opportunity for probing scattering in far more detail. The results of several experiments utilizing these techniques [1.9-1.16] have been published thus far, and they have, in fact, revealed substantial

discrepancies between theoretical predictions and experimental measurement for elastic scattering, inelastic scattering and impact ionization. As convincing as those studies may be, they still suffer from limitations on electron energy resolution, statistical uncertainty, or kinematic range. This dissertation describes experimental studies that employed high intensity polarized beams of hydrogen atoms and electrons, the latter characterized by an energy resolution of less than 100 meV. Under these experimental conditions, the results of the studies already completed place much stricter constraints on the predictive capabilities of theoretical approaches to the electron-hydrogen scattering problem.

The apparatus used was designed to permit a variety of reaction channels to be investigated over a range of projectile energies and a range of scattering angles, with emphasis on the ionization threshold region, the n=2 elastic resonance region, intermediate energy region (10-50 eV) for the elastic scattering, the high-energy region (> 200 eV) for ionization, and a wide region for n=2 excitation. For 1S-2P excitation studies, in particular, the experimental design provides for the incorporation of polarized beams techniques with those of electron-photon coincidence.

This thesis emphasizes asymmetry measurements for ionization near threshold, and additionally contains descriptions of the experimental design applicable to many of the studies referred to previously.

B. POLARIZED ELECTRONS

1. The Background of Electron Spin

Spin, an intrinsic property of particles that has no real analog in classical physics, has played a central role in physics research since its discovery in 1921 [1.17]. Much effort has been devoted to the understanding of effects associated with particle spin whether they be in the field of atomic [1.18-1.21], nuclear, elementary particle, or solid state physics. Recently, with the development of polarized beams and targets, spin has been used as a probe of fundamental interactions. For a description of the applications of polarized electron beams to various areas of physics, the reader is referred to a number of excellent review articles [1.22-1.29] and the references contained in them.

The history of spin begins in 1921, when Stern and Gerlach [1.17,1.30,1.31] confirmed Sommerfeld's space quantization by detecting the separation of a silver atomic beam into two discrete components following passage through an inhomogenous magnetic field. While the separation was expected, the two-component nature of the separation was not. In 1925 [1.32], Goudsmit and Uhlenbeck introduced the concept of electron spin to explain the anomalous nature of this fine structure splitting. Three years later, Dirac [1.33] showed that the electron spin and its associated magnetic moment followed from a linearizing of the relativistic generalization of the Schrodinger equation. Spin-dependence in atomic scattering first received serious attention in 1930 when Mott [1.20] examined the role of spin-orbit effects in electron scattering from heavy atoms. Although the successful demonstration of Mott scattering did not occur until 1943 [1.5], the principle has since been widely applied in the development of electron polarimetry [1.34].

Since 1948, when Kusch and Foley [1.35] measured the magnetic moment of the electron bound in an atom to high precision and found that the g-factor differed from 2, in constrast to the prediction of the Dirac theory, the electron spin has continually served as a probe of fundamental theoretical principles. Quantum electrodynamics [1.36], weak interactions [1.37], electroweak unification [1.38] and quark models [1.39] of the strong interaction have all been investigated with the use of the electron spin.

2. Definition of Polarization

The observable "spin" is represented by the operator $\vec{S}$ which satisfies the commutation relations characteristic of angular momenta,

$$[S_x, S_y] = i\hbar S_z \tag{1.1}$$

and the two additional equations obtained by cyclic permutation. From the above commutation relation and the additional condition that the Pauli spin matrix σ_z is diagonal, one obtains the Pauli matrix representation

$$\sigma_x = \begin{bmatrix} 0 & 1 \\ 1 & 0 \end{bmatrix} \quad \sigma_y = \begin{bmatrix} 0 & -i \\ i & 0 \end{bmatrix} \quad \text{and} \quad \sigma_z = \begin{bmatrix} 1 & 0 \\ 0 & -1 \end{bmatrix}$$

where now

$$\vec{S} = \hbar/2\ \vec{\sigma}.$$

A pure state of spin 1/2 particles can be described by a matrix, $\begin{pmatrix} a_1 \\ a_2 \end{pmatrix}$ called a spinor, where a_1 and a_2 in general are complex numbers. The polarization is then defined as the expectation value of the spin operator ($\vec{P} = \langle \vec{\sigma} \rangle$), in the

rest frame of the particles, and its magnitude is unity for a pure state.

In the case of a partially polarized beam, which is a statistical mixture of spin states, the polarization of the total system is the average of the polarization vector $\vec{P}^{(n)}$ of the individual subsystems which are in the pure spin states $\chi^{(n)}$. Thus $\vec{P}$ is given by

$$\vec{P} = \sum_n W^{(n)}\vec{P}^{(n)} = \sum_n W^{(n)} \langle \chi^{(n)} | \vec{\sigma} | \chi^{(n)} \rangle,$$

$$W^{(n)} = N^{(n)} / \sum_{(n)} W^{(n)} , \tag{1.2}$$

where the weighting factor takes into account the relative proportion of the state $\chi^{(n)}$, and $N^{(n)}$, the occupation number, is the number of particles in the state $\chi^{(n)}$. The partially polarized system can be also described by density matrix ρ given by

$$\rho = \sum_n W^{(n)} | \chi^{(n)} \rangle \langle \chi^{(n)} | . \tag{1.3}$$

Using Eqs. (1.2) and (1.3) it can be shown that $\vec{P}$ and ρ are related by the equation

$$\vec{P} = \mathrm{Tr}\ (\rho \vec{\sigma}), \tag{1.4}$$

or equivalently

$$\rho = \frac{1}{2} (1 + \vec{P} \cdot \vec{\sigma}), \tag{1.5}$$

where it is tacitly assumed that $\mathrm{Tr}(\rho) = 1$.

Since $|a_1^{(n)}|^2$ is the probability that the eigenvalue $\frac{\hbar}{2}$ will be obtained from a spin measurement in the z direction on the nth subsystem, the probability that $\frac{\hbar}{2}$ will be obtained for the total system is $\sum_n W^{(n)}|a_1^{(n)}|^2$. This probability can also be expressed as $N\uparrow/(N\uparrow + N\downarrow)$, where $N\uparrow$ is the number of measurements that yield the value $\hbar/2$ and $N\uparrow + N\downarrow$ is the total number of measurements. Thus one can write

$$N\uparrow/(N\uparrow + N\downarrow) = \sum_n W^{(n)}|a_1^{(n)}|^2 = 1/2\ (1 + P), \tag{1.6}$$

as consequence of which one obtains for the polarization P the usual expression

$$P = (N\uparrow - N\downarrow)/(N\uparrow + N\downarrow) \tag{1.7}$$

3. The Development of Polarized Electron Sources

The proposal for building a source of polarized electrons dates back to the work of Fues and Hellman [1.39] in 1930, but the first success was achieved only much later [1.40-1.42]. The performance characteristics and the status of polarized electron sources have been reviewed a number of times in the last few years [1.41-1.43,1.53]. Generally speaking, polarized electron sources fall into two categories: those based on atomic physics principles and those based on solid state physics principles. Among the atomic techniques, those which have been developed into operating sources are low-energy Mott scattering [1.44], photoionization of unpolarized alkali atoms by polarized light [1.45] (Fano effect), photoionization of state-selected alkali atoms by unpolarized light [1.46], and optical pumping of a helium gas discharge [1.47].

Among the solid state techniques, field emission from magnetized EuS coated tungsten [1.48], photoemission from magnetized materials [1.49], photoemission from non-magnetic materials such as alkali metals [1.50], tungsten [1.51], platinum [1.52] and GaAs [1.53], and low-energy electron diffraction [1.54] (LEED) from tungsten, have all received considerable attention. Of these, photoemission from single crystal GaAs has achieved the greatest prominence for reasons that will become clear shortly.

In general, a number of parameters characterize a source of spin polarized electrons, and each application has its own requirements. The quantity P^2I, where P is the polarization and I is the beam current, is often used as a figure of merit in discussing polarized electron source. This figure of merit applies when counting statistics are the chief source of experimental uncertainty. However, because of systematic errors, some minimum P is often required to make the measurements possible at all. Moreover, in any experimental configuration, the beam current, I, ultimately will be limited by space charge effects. The current may also be limited by other constraints, such as heating of beam line components for high-energy beams or radiation damage of targets. Thus it is not always possible to trade off a decrease in P for an increase in I. Nonetheless, with appropriate caution, P^2I can serve as a useful source charaterization. In addition to the magnitudes of P and I, the time structure of source may be important. For example, many experiments require that the polarization of the incident beam be reversible. The possibility of modulating the polarization at a desired frequency or with arbitrary time structure can be a significant advantage. In this context the effect of polarization reversal on the position, angle, intensity or energy of the beam becomes important. Sources in which a magnetic field must be reversed in order to reverse the polarization are less desirable because often

the field can not be switched rapidly, and more importantly it cannot be switched without disturbing the beam.

The electron optical characteristics of the polarized electron beam determine how much of the beam can be accepted by other devices such as an energy analyzer or monochromator. In the paraxial beam approximation, the product, $EA\Omega$, of the beam is conserved; that is, $E_1A_1\Omega_1 = E_2A_2\Omega_2$ for any two cross sections 1 and 2 along the beam path, where E is the electron kinetic energy, A is the cross-sectional area, and Ω is the solid angle subtended by the electron beam envelope. When a magnetic field is present, such as when the beam originates at a magnetic photocathode, the situation is more complicated and requires the use of a generalized phase space, as has been discussed in detail elsewhere [1.55]. If the acceptance phase space product of an electron optical device $(EA\Omega)_d$ is smaller than that of the incident beam $(EA\Omega)_i$, the beam current is reduced by the ratio $(EA\Omega)_d/(EA\Omega)_i$. A high current beam with a large $EA\Omega$ may not be as useful as a lower current beam with much smaller $EA\Omega$. Thus, $EA\Omega$ may be regarded as an electron optical figure of merit for polarized electron sources.

The emittance of a beam is defined as $\varepsilon = R\alpha$ where R is the radius of the electron beam at the source or an image of the source, and α is the cone half-angle of the electron beam envelope at that point. The invariant emittance, ε_{inv}, is defined as $R\alpha\sqrt{E}$, and is equivalent to $EA\Omega$ in its role, since $EA\Omega = \pi^2 \varepsilon_{inv}$. Also, one often finds reference made to electron optical brightness which is defined as $\beta = dI/dAd\Omega$, where dI is the differential current through a differential area dA, and $d\Omega$ is the differential solid angle subtended by the beam at dA. Since $EA\Omega$ is conserved, β/E is also a conserved quantity. Finally, the energy spread ΔE, the stability of the polarization and current

from the source are important and must be considered when one wants to specify requirements of the source.

For the crossed-beams electron-atom scattering asymmetry measurements reported in this thesis, the figure of merit, the invariant emittance, the energy spread, the stability of both polarization and intensity, and the method of polarization reversal are all of major importance. The facts are these: for high resolution experiments, the parameter ΔE is obviously important; the crossed-beams differential scattering experiment in which the electron beam is restricted to a small diameter and a small divergence, the spatial stability of the beam and the parameter ε_{inv} are important; for asymmetry measurements in which the electron polarization is to be reversed, the frequency of reversal and the spatial stability under reversal are important. Of course, both the stability of polarization and intensity are important, particularly if counting rates are low and continuous long-term operation is required. For a precise measurement of asymmetry, where counting statistics plays a significant role, in the experimental uncertainty, then a high value of P^2I is desirable. Finally, the requirement that magnetic fields be small and well controlled in the scattered region is extremely important.

From the operating experience of many research groups using GaAs (100) photoemission in a dc mode, typical source characteristic are as follows: polarization, 0.25 - 0.40; quantum yield, 1%-10%; emittance (at 1ev), < 7.0 mrad cm; lifetime, > 10 hours. Moreover, the direction of electron polarization can be modulated by modulation of the circular polarization of the incident laser light, a process that minimally affects other characteristics of the electron beam. Based upon the requirements of the asymmetry measurements and the characteristics of a GaAs source, its choice for use in the study of electron-hydrogen scattering was obvious. Although

this kind of source is limited in its polarization, its high current and high brightness compensate for many of its drawbacks. While attempts by many groups to enhance the polarization have failed, the ease and reliability of operation of GaAs source have increased steadily.

II. THEORY OF ELECTRON-HYDROGEN ATOM SCATTERING

A. PRELIMINARIES

The scattering process in non-relativistic quantum mechanics is described by the Schrodinger equation with the particle wavefunction satisfying well defined asymptotic conditions. Different mathematical methods and approximations can be applied to this problem. In order to make this chapter self-contained and simple, the concepts of cross section of quantum particle scattering are introduced and a simple mathematical method partial wave analysis is discussed based on central potential scattering. The extension of this simple case to the scattering problem of electrons from atomic hydrogen requires a more complicated mathematical formulation.

The integral formulation and the variational technique are two general mathematical methods that have been applied to the electron-atom scattering problem. In this chapter the application of these approximation methods the case of electron-hydrogen scattering will be discussed. Some of their specific dynamic features and their limitations in kinematic range will be pointed out.

The presence of exchange effects, inherent in a problem treating identical particles, such as electron-hydrogen scattering, is reflected in cross section differences for singlet and triplet states. Thus the use of spin polarized beams provides the potential for probing the effects of exchange, thereby increasing the sensitivity with which theoretical methods can be tested. In this chapter, I will discuss these points as they bear particularly on the case of ionization near threshold, referring to the models of Wannier and Temkin.

B. GENERAL FORMULATION

Scattering deals with the interaction between a projectile and a target with the interaction conveniently described by a potential energy $V(\vec{r})$. In the center of mass (c.m.) system, then, the problem reduces to the solution of the time dependent equation

$$H\Phi(\vec{r},t) = i\hbar\frac{\partial\Phi(\vec{r},t)}{\partial t}, \tag{2.1a}$$

where H is the Hamiltonian defined by the operator

$$H = -\frac{\hbar^2}{2\mu}\nabla^2 + V(\vec{r}). \tag{2.1b}$$

Under the simplifying assumptions that the incident beam is described a plane wave and that $V(\vec{r})$ is time independent, $\Phi(\vec{r},t)$ can be separated into a space part and time part:

$$\Phi(\vec{r},t) = \Psi_E(\vec{r})\, e^{-iEt/\hbar}. \tag{2.2}$$

Substitution of Eq. (2.2) into (2.1) results in the time independent Schrodinger equation

$$[\nabla^2 - U(\vec{r}) + k^2]\,\Psi_k(\vec{r}) = 0, \tag{2.3}$$

where $U(\vec{r}) = 2mV(\vec{r})/\hbar^2$, $\vec{k} = \vec{p}/\hbar$, and $k^2 = 2mE/\hbar^2$.

At large distances from the scattering center, the asymptotic form for $\Psi_k(\vec{r})$ can be invoked in which $\Psi_k(\vec{r})$ is expressed in terms of an

incident plane wave and outgoing spherical wave:

$$\Psi_k(\vec{r}) \xrightarrow[r\to\infty]{} e^{i\vec{k}\cdot\vec{r}} + \frac{e^{ikr}}{r} f(\theta, \phi), \tag{2.4}$$

where $f(\theta, \phi)$ is called the scattering amplitude. The differential cross section $d\sigma(\theta,\phi)/d\Omega$ and the total cross section σ_T both directly measurable quantities, are then given by the expressions $d\sigma/d\Omega = |f(\theta, \phi)|^2$, and

$$\sigma = \int |f(\theta, \phi)|^2 \, d\Omega.$$

Stated succinctly, the fundamental goal of scattering theory is to find the scattering amplitude $f(\theta, \phi)$. Many mathematical methods have been developed to achieve this goal. Prime among them is partial wave analysis, the fundamental approach to the simple case of static central potential field systems. Variational methods derived from integral formulas and, in the case of high energy scattering, Born techniques are powerful theoretical tools for the more complex nature of actual electron-atom collision systems. For high-energy collisions, semi-classical aproximations are also sometimes used.

C. PARTIAL WAVE ANALYSIS

Mathematically, partial wave analysis reduces a partial differential equation in three variables to a system of second order differential equations in which the wave function is expressed as a sum over angular momentum states. The procedure is generally valid only if the potential $V(\vec{r})$ is central and the expansion converges. In other words, in practical applications, the approach is accurate only if the potential is of relatively short range and the energy is weak.

It can be shown that the asymptotic form of a wave function in a central field is [2.2]

$$\psi(\vec{r}) \underset{r\to\infty}{\longrightarrow} \sum_{\ell=0}^{\infty} \frac{2\ell+1}{2ikr} C_\ell \left[e^{i(kr+\eta_\ell)} - (-1)^\ell e^{-i(kr+\eta_\ell)}\right] P_\ell(\cos\theta), \quad (2.5)$$

where the scattering amplitude in turn can be written in the form

$$f(\theta) = \frac{1}{2ik} \sum_{\ell=0}^{\infty} (2\ell+1)\,(e^{2i\eta_\ell} - 1)\, P_\ell\,(\cos\theta), \quad (2.6)$$

and the differential and total cross sections are expressed respectively as

$$d\sigma/d\Omega = |f(\theta)|^2 \quad (2.6a)$$

and

$$\sigma_T = \frac{4\pi}{k^2} \sum_{\ell=0}^{\infty} (2\ell+1)\,\sin^2\eta_\ell. \quad (2.6b)$$

The argument η_ℓ is the called phase shift and is the indicator of the presence of a scattering potential. The scattering problem is thus reduced to finding the set of phase shifts η_ℓ. Many mathematical techniques can be used to calculate the phase shift η_ℓ resulting in solutions that are particularly applicable when the scattering potential is spherically symmetric and only a few terms of angular momentum state are important.

D. ELECTRON-HYDROGEN ATOM COLLISIONS

Thus far we have been considering only the simple case of a pure central force problem. Given even the most fundamental atomic scattering problem, on the other hand, involves several complications. The atomic electrons require that the problem be formulated as a many-body problem which cannot be solved in closed form. Furthermore, if the projectile particles are electrons, the additional requirements of Fermi-Dirac statistics must be satisfied; namely, the total wavefunction must be antisymmetric upon interchanging the incident electron with an atomic electron. Also, we must consider the possibility of inelastic scattering.

In the theoretical formulation of the scattering of electrons by hydrogen atoms (and other light atoms) relativistic effects such as the spin-orbit interaction are generally neglected. If the Hamiltonian describing the incident and atomic electrons treats the nucleus as infinitely heavy and further contains only kinetic and electrostatic terms, the nonrelativistic wave equation in atomic units takes the form (in atomic unit)

$$\left[\frac{1}{2}\nabla_1^2 - \frac{1}{2}\nabla_2^2 - \frac{1}{r_1} - \frac{1}{r_2} + \frac{1}{|\vec{r}_1-\vec{r}_2|} - E\right]\Psi(\vec{r}_1 s_1, \vec{r}_2, s_2) = 0, \qquad (2.7)$$

where $(\vec{r}_1, s_1)$ and $(\vec{r}_2, \vec{s}_2)$ are the corresponding spatial and spin coordinates of the incident and atomic electrons, respectively, and ∇_1^2 and ∇_2^2 are the respective kinetic energy operators. Since the Hamiltonian does not depend explicitly on the spin coordinates, the two-electron wave function can be written as a product of spatial and spin functions:

$$\Psi(\vec{r}_1 s_1, \vec{r}_2 s_2) = \Psi(\vec{r}_1, \vec{r}_2)\chi(s_1, s_2). \qquad (2.8)$$

The requirement of exchange antisymmetry on the total wave function imposed by Fermi-Dirac statistics then reduces to a combination of a symmetric spatial wave function with an antisymmetric (singlet) spinor or alternatively an antisymmetric spatial wave function with a symmetric (triplet) spinor. Since two appropriately symmetrized spatial wave functions can be formed, it should be expected that in the asymptotic limit, scattering amplitudes for the symmetric spatial wave function, corresponding to singlet scattering, and the antisymmetric spatial wave function, corresponding to triplet scattering, will be different.

The singlet and triplet amplitudes can also be expressed in terms of the direct and exchange amplitudes, with the help of equation (2.9) - (2.11) below. In each of these equations the atom is assigned an ambitrary spin detection and the scattering of electrons is considered with spins either parallel or antiparallel to the atomic spin.

Process	Cross Section	
$e(\uparrow) + A(\uparrow) \rightarrow e(\uparrow) + A(\uparrow)$	$\lvert f\rvert^2$	(2.9)
$e(\uparrow) + A(\uparrow) \rightarrow e(\uparrow) + A(\downarrow)$	$\lvert g\rvert^2$	(2.10)
$e(\uparrow) + A(\uparrow) \rightarrow e(\uparrow) + A(\uparrow)$	$\lvert f-g\rvert^2$.	(2.11)

In Eq. (2.9) the process illustrated is direct scattering, denoted by the amplitude f; in Eq. (2.10) the interchange of the incident and atomic electrons leads to the exchange amplitude g; in the last process, the indistinguishability of electrons results in the triplet amplitude f-g, the minus sign arising from the requirements of Fermi-Dirac statistics.

Generally, theoretical approximations provide values of the singlet and triplet, or equivalently, the direct and exchange amplitudes.

Theoretical models for solving the Schrodinger equation for electron-hydrogen collisions, vary from low energy approximations, where the scattering wavefunction is usually expanded in terms of a limited set of the eigenstates of the target, to the simple, if primitive, first Born approximation, which is expected to have reasonable validity at some sufficiently high energy. For the case of low energies, two main approaches exist for the solution of Eq. (2.7) -- perturbative and variational. In the perturbative approach, a solution is formed in terms of exact eigenfunctions of an approximate Hamiltonian. In the variational approach, a solution is sought in terms of approximate eigenfunctions of an exact Hamiltonian.

E. SPIN ASYMMETRY IN ELECTRON-HYDROGEN ATOM COLLISIONS

As noted earlier, spin-dependent effects in electron-atom collisions arise from the mechanisms of spin-orbit coupling and exchange. The spin-orbit interaction can polarize initially unpolarized beams or produce a left-right asymmetry when polarized beams are used. In pure exchange collisions unpolarized beams cannot be polarized by the collision, and if electrons and atoms are initially polarized no left-right asymmetry can be produced. However, for the case of two polarized beams, another asymmetry can be defined in terms of spin-parallel and antiparallel combinations, and because it depends on an interference between direct and exchange processes, the measurement of this asymmetry is a particularly sensitive test of the various theoretical methods used to calculate the scattering amplitudes. In this section I will demonstrate the role of exchange

asymmetry.

Collisions involving unpolarized beams results in the determination of a cross section $d\bar{\sigma}/d\Omega$ that is averaged over initial spin state and summed over final spin states. For the hydrogen atom, $d\bar{\sigma}/d\Omega$ is just the weighted average of the singlet and triplet state cross sections:

$$\frac{d\bar{\sigma}}{d\Omega} = \frac{1}{4} |f+g|^2 + \frac{3}{4} |f-g|^2 \tag{2.12}$$

or alternatively

$$\frac{d\bar{\sigma}}{d\Omega} = |f|^2 + |g|^2 - |f| |g| \cos\theta, \tag{2.13}$$

where f and g are respectively the direct and exchange amplitudes, as used in Eqs. (2.9) - (2.10) of Section II.C, and θ is the relative phase between f and g. The combination $s = (f+g)$ is the singlet amplitude, while the combination $t = (f-g)$ is the triplet amplitude.

In the experiment we performed with polarized beams, in which the spins of the incident free electron and target valence electron are either antiparallel ($\uparrow\downarrow$) or parallel ($\uparrow\uparrow$), a cross-section asymmetry A, can be determined that is defined by

$$A = \left[\frac{d\sigma}{d\Omega} (\uparrow\downarrow) - \frac{d\sigma}{d\Omega} (\uparrow\uparrow)\right] / \left[\frac{d\sigma}{d\Omega} (\uparrow\downarrow) + \frac{d\sigma}{d\Omega} (\uparrow\uparrow)\right]. \tag{2.14}$$

It can be shown that A can also be expressed as

$$A = \mathrm{Re}\,(f^{*}g)/\left(\frac{d\bar{\sigma}}{d\Omega}\right) = |f||g|\cos\theta/\left(\frac{d\bar{\sigma}}{d\Omega}\right) = \frac{1-r}{1+3r}, \qquad (2.15)$$

where $r = |t|^2/|s|^2$. From the form of Eq. (2.15) it is clear that the measurement of A indeed results in the determination of the interference between the direct and exchange amplitude, provided $d\bar{\sigma}/d\Omega$ is already known, as was suggested previously.

For the case of angle integrated impact ionization, the corresponding asymmetry A_I is defined by

$$A_I = [\sigma_I(\uparrow\downarrow) - \sigma_I(\uparrow\uparrow)]/[\sigma_I(\uparrow\downarrow) + \sigma_I(\uparrow\uparrow)] = (1 - r_I/(1 + 3r_I), \qquad (2.16)$$

where $\sigma_I(\uparrow\downarrow)$ and $\sigma_I(\uparrow\uparrow)$ now are the total ionization cross sections for the antiparallel and parallel spin-orientation respectively, and r_I is the ratio of triplet to singlet total ionization cross sections. Note that A_I can be expressed as

$$A_I = \sigma_I^{\mathrm{int}}/\bar{\sigma}_I, \qquad (2.17)$$

where

$$\sigma_I^{\mathrm{int}} = \frac{1}{2}\int_0^E dE'_1 \int\int \frac{k'_1 k'_2}{k_1}\,\mathrm{Re}\,[f^{*}(\vec{k}'_1,\vec{k}'_2)\; g\;(\vec{k}'_1,\vec{k}'_2)]\; d\hat{k}'_1\, d\hat{k}'_2 \qquad (2.18)$$

and

$$\bar{\sigma}_I = \frac{1}{2}\int_0^E dE'_1\, \frac{k'_1 k'_2}{k_1}\left(\frac{1}{4}\,|f+g|^2 + \frac{3}{4}\,|f-g|^2\right) d\hat{k}'_1 d\hat{k}'_2. \qquad (2.19)$$

Here $\vec{k}'_1, \vec{k}'_1$, and $\vec{k}'_2$ are respectively the momenta of the incident,

scattered, and ejected electrons; E'_1 is the energy of the scattered electron; and $E + \frac{1}{2}$ is the energy of the incident electron, all quantities being given in atomic units. The interference cross section σ_I^{int} can also be written as

$$\sigma_I^{int} = \sigma_I - \bar{\sigma}_I,$$

where σ_I is the total ionization cross section calculated in the absence of exchange.

F. INTEGRAL EQUATION FOR SCATTERING

The solution of the Schrodinger equation for scattering requires the imposition of the correct physical asymptotic condition on the wave function. By transforming the problem into an integral equation, the asymptotic conditions may be incorporated from the outset. Starting from the time-independent Schrodinger equation

$$[H_0(\vec{r}_1) + H_a(\vec{r}_2) + V(\vec{r}_1,\vec{r}_2) - E]\ \psi(\vec{r}_1,\vec{r}_2) = 0, \qquad (2.20)$$

with

$$H_0(\vec{r}_1) = -\frac{\hbar^2}{2m}\vec{\nabla}_1^2,$$

$$H_a(\vec{r}_2) = -\frac{\hbar^2}{2m}\vec{\nabla}_2^2 - \frac{e^2}{r_2},$$

and

$$V(\vec{r}_1,\vec{r}_2) = -\frac{e^2}{r_1} + \frac{e^2}{|\vec{r}_1-\vec{r}_2|},$$

where $\vec{r}_1$ and $\vec{r}_2$ are the coordinates of the incident and target electrons,

respectively. We recast Eq. (2.20) in the inhomogenous form

$$[E - H_0(\vec{r}_1) - H_a(\vec{r}_2)]\ \Phi = V(\vec{r}_1,\vec{r}_2)\ \Phi. \tag{2.21}$$

The problem can now be formally solved by applying the Green's function operator $[E - H_0(\vec{r}_1) - H_a(\vec{r}_2)]^{-1}$ to obtain a particular solution that satisfies the boundary conditions. To this is added the solution of the homgeneous equation, which represents the incident wave and the initial state of the target atom, to yield the complete solution

$$\psi(\vec{r}_1,\vec{r}_2) = e^{i\vec{k}\cdot\vec{r}_1}\ \psi_0(\vec{r}_2) + [E - H_0(\vec{r}_1) - H_a(\vec{r}_2)]^{-1}\ V(\vec{r}_1,\vec{r}_2)\ \psi(\vec{r}_1,\vec{r}_2). \tag{2.22}$$

Here, $[E - H_0(\vec{r}_1) - H_a(\vec{r}_2)]^{-1}$ is the two-particle separable Green's function integral operator [2.2]

$$2m/\hbar^2 \int\int d\vec{r}_1\ d\vec{r}'_2\ G_{0a}^{+}\ (\vec{r}_1\vec{r}_2;\ \vec{r}_1,\vec{r}_2).$$

The outgoing asymptotic condition applies only to the part of the Greens's function containing the incident particle, presently chosen to be $\vec{r}_1$, and the total Green's function satisfies [2.2] the relation

$$\left(\frac{2m}{\hbar^2}\right)[E - H_0(\vec{r}_1) - H_a(\vec{r}_2)]\ G_{0a}^{+} = \delta(\vec{r}_1-\vec{r}'_1)\ \delta(\vec{r}_2-\vec{r}'_2). \tag{2.23}$$

With the closure relations

$$\delta(\vec{r}_1-\vec{r}'_1) = \frac{1}{2\pi}\int d\vec{k}\ e^{i\vec{k}\cdot(\vec{r}_1-\vec{r}_2)},$$

and

$$\delta(\vec{r}_2-\vec{r}'_2) = \sum_{\gamma} \psi_\gamma(\vec{r}_2)\ \psi_\gamma{}^*(\vec{r}'_2)$$

or

$$\int d\vec{r}_2\ \psi_\gamma(\vec{r}_2)\ \psi^*{}_{\gamma'}(\vec{r}_2) = \delta_{\gamma\gamma'},$$

where $\psi_\gamma(\vec{r})$ satisfies $H_a\psi_\gamma = E_\gamma\psi_\gamma$, the Green's function takes the form [2.2]

$$G_{oa}{}^{+}\ (\vec{r}_1,\vec{r}_2 - \vec{r}'_1,\vec{r}'_2) = -\frac{1}{4\pi} \sum_{\gamma} \frac{e^{ik_\gamma\left|\vec{r}_1-\vec{r}_1\right|}}{\left|\vec{r}_1-\vec{r}'_1\right|}\ \psi_\gamma(\vec{r}_2)\psi_\gamma{}^*(\vec{r}'_2). \quad (2.24)$$

When Eq. (2.24) is inserted into Eq. (2.22), the integral equation becomes

$$\psi(\vec{r}_1,\vec{r}_2) = e^{i\vec{k}_o\cdot\vec{r}_1}\ \psi\gamma(\vec{r}_2) - \frac{1}{4\pi} \sum_{\gamma} \psi_\gamma(\vec{r}_2)\ x$$

$$\frac{2m}{\hbar^2} \int\int d\vec{r}'_1\ d\vec{r}'_2\ \frac{e^{ik_r\left|\vec{r}_1-\vec{r}'_1\right|}}{\left|\vec{r}_1-\vec{r}'_1\right|}\ \psi_\gamma{}^*\ (\vec{r}'_2)\ V(\vec{r}'_1,\vec{r}'_2)\ \psi(\vec{r}'_1,\vec{r}'_2), \quad (2.25)$$

and the scattering amplitude $f_{or}\ (\hat{k}_o,\hat{k}_r)$ is given by

$$f_{or}\ (\hat{k}_o,\hat{k}_\gamma) = -\frac{1}{4\pi}\int\int d\vec{r}'_1 d\vec{r}'_2\ e^{-i\vec{k}_\gamma\cdot\vec{r}_1'}\ \psi_\gamma(\vec{r}'_2)\ \frac{\hbar^2}{2m}\ V(\vec{r}'_1,\vec{r}'_2)\psi(\vec{r}'_1,\vec{r}'_2). \quad (2.26)$$

The iterative solution of Eq. (2.26) may indeed be complicated and requires an assumption for $\psi(\vec{r}'_1,\vec{r}'_2)$. Perhaps the simplist solution arises when $\psi(\vec{r}'_1,\vec{r}'_2) = e^{i\vec{k}_o\cdot\vec{r}'_1}\ \psi_o(\vec{r}'_2)$ in Eq. (2.26). The result is the first Born

approximation [2.13]. The second Born approximation is then obtained by inserting the wave function of first order for $\psi(\vec{r}'_1, \vec{r}'_2)$ into Eq. (2.26), with higher order solutions proceding in like manner. Physically, the Born approximation starts with the substitution of a plane wave near the interaction for the actual wave function, a procedure which is valid when the kinetic energy of the incident particle is very large relative to the interaction potential. The effects of the interaction potential are then included by expanding the scattered wave function in a series, which represents succesively higher order correction to the plane wave function.

Distorted wave [2.14], Born-Oppenheimer, Born exhange [2.15-2.16], and Glauber approximations [2.17-2.18] are extensions of the simple Born approximation. The Distorted Wave Born Approximation (DWBA) is a refinement of the Born approximation which allows the incident plane wave to be distorted by the scattering potential. The Born-Oppenheimer approximation (BO) is an attempt to include exchange in the Born approximation by letting the wave function be

$$\psi_{\gamma\pm}(\vec{r}_1,\vec{r}_2) = e^{i\vec{k}\cdot\vec{r}_1}\,\psi_\gamma(\vec{r}_2) \pm e^{i\vec{k}\cdot\vec{r}_2}\,\psi_\gamma(\vec{r}_1). \qquad (2.27)$$

The Born Exchange (BE) approximation is a further refinement of the Born approximation that handles the question of electron exchange in a simpler way than the BO approximation. The BE approximation has been, to date, the method most frequently used by theorists in the calculation of electron impact ionization in atomic hydrogen. In this method, the indistinguishability between the two electrons is assumed at the outset of the formulation, and the property of symmetry is invoked in a simplistic fashion at the end. Specifically, the amplitude f is first calculated for

direct scattering using the Born approximation with an expression for g resulting from the application of exchange symmetry. The need for distinguishing between higher and lower energy outgoing particles is removed since the BE approximation explicitly assumes that they are indistinguishable. The major difficulty with the BE approximation is that it does not determine the phase between f and g.

The Glauber approximation for the solution of collision problem in high energy and nuclear physics can be adapted to atomic physics problem. In high energy scattering, the interaction between the target and projectile can be considered to be limited to a small volume surounding the target, and the scattering amplitude can be determined from knowledge of the wave function within the region of interaction. The approximate wave whose function is taken to be a plane wave whose phase is altered by the presence of the potential, V. The scattering amplitude is then obtained by substituting this trial function into the time independent Schrodinger equation.

G. VARIATIONAL TECHNIQUES

Consider the trial integral [2.2]

$$I_t = \int_0^\infty d^3x \; \psi_t \left(- \frac{d^2}{dr^2} + U - k^2\right)\psi_t, \tag{2.28}$$

with the boundary conditions

$$\psi_t(0) = 0, \tag{2.29a}$$

and

$$\psi_t \underset{r\to\infty}{\longrightarrow} \sin kr + \tan \eta_t \cos kr, \tag{2.29b}$$

in which $U = 2mV/\hbar^2$ and $k^2 = 2mE_k/\hbar^2$. It can be shown that, in the asymptotic limit, variation of Eq. (2.28) results in the expression $\delta I = k\delta\lambda = k(\lambda_t - \lambda)$, where $\lambda = \tan \eta$. Thus a first order change in λ from its correct value is equal to $1/k$ times the first order integral I. The procedure for solving scattering problem is to choose an n-term trial wave function with variables C_i and overall phase shift λ_t. Two standard prescriptions for the choice of the parameters are those of Hulthen [2.19] and Kohn [2.20], in which the n + 1 equation are

$$\frac{\partial I_t}{\partial C_i} = 0 \qquad i = 1,2, \ldots, n$$

(Hulthen) (2.30)

$$I_t = 0,$$

and

$$\frac{\partial I_t}{\partial C_i} = 0 \qquad i = 1,2,\ldots,n$$

(Kohn) (2.31)

$$\frac{\partial I_t}{\partial \lambda_t} - k = 0.$$

The accuracy of the variational method depends upon the trial function that was picked, and it will, in general, be better at energies below the highest state in the trial wave function. The variational method has become increasingly practical with the aid of large and fast computers to perform the in gration of Eq. (2.28). The approximation methods which

follow differ from one another in the specific trial functions that are chosen. For the electron-hydrogen system, the trial functions are most often constructed from the eigenfunctions of the unperturbed hydrogen atom. The static exchange, strong-coupling exchange, close-coupling, polarized orbital, and correlation methods are of examples of variational approaches to the electron-hydrogen system.

The simplest basis that can be chosen is just the 1S state of the target atom. This approximation is called the static exchange (SE) approximation [2.21]. The major limitation of the SE approximation is that it does not account for any distortion of the target atom. The next simplest basis that can be chosen for variational treatment consists of the 1S and 2S states of the hydrogen atom, this approximation being referred to as the strong coupling exchange (SCE) approximation [2.21]. The SCE approximation is somewhat of an improvement over the SE approximation in that distortion of the target hydrogen atom is allowed, but only S states are included in the basis, as a consequence of which no allowance is made for atomic polarizability of the target.

The close coupling (CC) approximation [2.22-2.24] is an extension of the SE and SCE approximation in that it employs additional hydrogen atom wave functions in the basis. The name is derived from the assumption that the incident electron wave function is closely coupled to the target atom wave functions included in the basis, and that coupling between the incident electrons and other states of the atom can be neglected. The CC approximation is the most widely used variational method for calculating low energy elastic collision processes.

The simplest CC basis contains just the 1S, 2S, and 2P states of the hydrogen atom. Much of the work in using the CC approximation lies in

determining the trial wave basis, and several methods have been developed to account for the omission of the higher atomic wave functions. Burke [2.6] argues that since an infinite number of real states have been omitted from the trial function, the missing states can be in part made up for by introducing into the trial function several nonphysical states, called "pseudo states". Of all the variational approximations, the close coupling approximation generally give the best results at low energies. The physical implication is that slow incident electrons, which have small values of angular momentum, couple strongly to atomic states of similar angular momentum.

The method of polarized orbitals (PO)[2.25-2.27], introduced by Temkin in 1957, is an attempt to account explicitly for both the long range reaction of the target atom to the presence of the incident electron and for the exchange effects between target and projectile electron. The trial function explicitly contains provision for the polarizability of the atom as well as for exchange symmetry or antisymmetry. The correlation method [2.28] (CM) is an attempt to include in the trial function terms which allow for electron correlation. The trial function consists of a small number of target atom wave function, plus additional states that represent electron-electron interaction.

H. APPROXIMATION METHODS OF IONIZATION NEAR THRESHOLD

One aspect of the general three-body problem that is of interest in many areas of physics is the behavior of the system at energies in the vicinity of which a new scattering channel opens. The resulting analysis produces a so-called threshold law. Atomic physics systems, in which all three outgoing partners are charged, has particular subtleties because of

the presence of long-range forces. When two electrons escape from a positive ion with a small energy excess E above the threshold for this process, one can expect strong correlation to be developed between the escaping particles, given the competing long-range forces and the large time of interaction over which correlation can develop. Accounting theoretically for detailed observations of reactions or transmutations in this process is very difficult unless some simplifying assumptions are made either classically or quantum mechanically.

Two approaches to the ionization threshold law (ion yield as a function of energy) are that of Wannier [2.29] and that of Temkin [2.30]. The physical model are different but the results for the behavior of the cross section and the cross-section asymmetry predicted by these two approaches come close and not easy to distinguish at the present time in the experiment. In the following sections I will discuss some of the important features of these approaches.

1. Wannier's Ionization Threshold Law

In 1953 Wannier extended to the three-body system the concepts Wigner had earlier developed for a two-body reaction system using quasi-ergodic assumptions. In this manner Wannier derived a threshold law from detailed arguments involving classical equations of motion and phase space. The detailed description is not shown here; rather only important arguments and results are given.

Using phase space arguments, Wannier showed by careful inspection of the equation of motion that the only subspace relevant for double escape is one in which both electrons are approximately the same distance away from the ionic cone and traveling in opposite directions. The potential

surface describing the double escape process in fact shows a saddle point for this configuration. This is easily seen by introducing hyperspherical coordinates R, α, and θ given by $R = \sqrt{r_1^2+r_2^2}$, $\alpha = \tan^{-1}(r_1/r_2)$, and $\theta = \cos^{-1}(r_1,r_2)$, respectively, where $\vec{r}_1$ and $\vec{r}_2$ are the coordinates of the incident and target electrons with respect to the nucleus as illustrated in Fig. 2.1. The saddle point has the coordinates $\alpha = \pi/4$ and $\theta_{12} = \pi$. The potential in the case of the hydrogen atom near this point has the form

$$U = \sqrt{2}\, R^{-1} \left[-3/2 - 11/4\, (\alpha-\pi/4)^2 + \frac{1}{16}\, (\theta-\pi)^2+\ldots\right]. \qquad (2.32)$$

Inspection of Eq. (2.32) shows a motion stable in θ but unstable in α at constant R. Double ionization results from an increase of the R coordinate accompanied by limited deviation of θ from π and of α from $\pi/4$. These deviations remain limited because U is stationary in α and θ at constant R. The instability of this configuration with respect to deviation in α has the limited effect of decreasing the cross section near threshold.

Following these arguments and using a detailed mathematical derivation, the threshold law for ionization follows:

$$\sigma(E) \propto E^m, \qquad (2.33)$$

where σ is the cross section and E is the total kinetic energy of two outgoing electrons. For a neutral atom m has the value of 1.127. Wannier's law was also derived quantum mechanically by Rau [2.31] (1971) and Peterkop [2.32] (1971) for a ^1S_e state using the WKB approximation, and was extended to P states by Roth [2.35] (1971). The Wannier law was

verified for hydrogen in 1968 by McGowan and Clark [2.33], and for helium [2.34] in 1974 by Cvejanovic and Read. In 1976, Klar and Schlecht [2.36] concluded that at threshold singlet scattering follows the Wannier law, whereas all triplets are considerably suppressed at threshold with a $E^{3.881}$. Such a conclusion would lead to an ionization asymmetry $A_I = 1$ at threshold in seeming disagreement with the experimental observation of Alguard et al. [2.37] (1977) and Baum et al. (1981). Subsequently, Greene and Rau [2.39] showed that, only the $^1S^e$ and $^1P^e$ states were suppressed, and moreover that the L=1 and L=2 states contribute significantly to the cross section at threshold, implying that the threshold value of A_I can differ from unity. The actual value of A_I reflects the details of the dynamics of the problem and provides insight into the strong correlations that exist during the double escape process.

2. Temkin's Modulated Quasilinear Law

More recently, Temkin using a Coulomb-dipole interaction for two escaping electron obtained a modulated linear threshold law [2.30], and predicted that A_I itself showed oscillations in direct contradiction to the predictions of Wannier. In Temkin's argument, the threshold law is dominated by the Coulomb-dipole region, that is, the region where the outgoing electrons have very different energies and where the slower electron sees the full charge of the residual ion whereas the faster electron sees the dipole potential formed by the residual ion and the slower electron. The Coulomb-dipole picture of the double escape process is illustrated in Fig. 2.2(a) and 2.2(b).

Developing these arguments mathematically, Temkin derived a threshold law given by

$$\sigma(E) \propto [E/(\ell nE)^2]\,[1+\sum_{\ell} C_\ell \sin(\alpha_\ell \ell nE + \mu_\ell)], \qquad (2.34)$$

where $\alpha_\ell = [R_\ell - \ell(\ell+1) - \frac{1}{4}]^{1/2}$, $C_\ell = [R_\ell]^{-1/2}$, R is the lower limit of the radial coordinate of the slower electron for which the analysis is valid, E is the total kinetic energy of two outgoing electrons, and the parameters C_ℓ, α_ℓ and μ_ℓ are quantities that are independent of energy but dependent on total orbital angular momentum. The threshold law is the same for each partial wave (ℓ), because any finite partial wave eventually will be dominated by an attractive dipole potential:

$$\lim_{r>R_\ell} Vd(r) = -\frac{[R_\ell - \ell(\ell+1)]}{r^2}. \qquad (2.35)$$

The asymmetry A_I displays oscillation as shown by the following relation:

$$A_I(E) = \beta + \frac{1+2\beta-3\beta^2}{4}\left[\frac{\sin(\alpha_s \ell nE+\mu_s)}{\alpha_s} - \frac{\sin(\alpha_t \ell nE+\mu_t)}{\alpha_t}\right]. \qquad (2.36)$$

Here α_s, μ_s and α_t, μ_t refer to singlet and triplet state parameters respectively, and $\beta = (C_s - C_t)/(C_s + C_t)$.

Although experiments carried out thus far, whether aimed at the measurement of σ_I or A_I, are all consistent with the Wannier model, they are also consistent with the Coulomb dipole model within statistical and systematic uncertainties. New insights can be gained only through high resolution (< 10 meV) electron measurements or through positron scattering

measurements in which the energy resolution perhaps is not so critical.

Since I use the detailed results of atomic scattering theory I refer the reader to textbook discussions by Mott and Massey [2.1], Geltman [2.2], Burke [2.3], Joachain [2.4], and Bransden [2.5] for further information. I also point out that various approximation methods have been reviewed recently in several excellent articles [2.6-2.10], and the specifics of spin asymmetry in electron-atom collisions have been discussed in several additional reviews [2.11-2.12].

Fig. 2.1: Final State Threshold Configurations (Wannier)

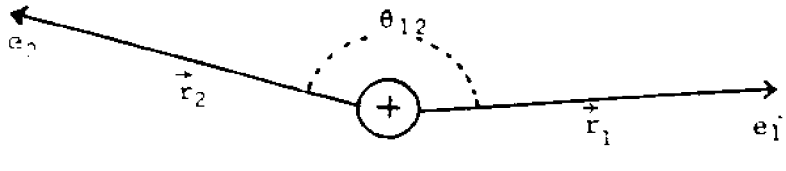

$\vec{r}_1 \simeq -\vec{r}_2$

Physics:

Electrons emerge on opposite side of nucleus with almost equal and opposite momenta: ridge (saddle) point of total potential energy)

→ $r_1 \simeq r_2$

$\theta_{12} \simeq \pi$

Fig. 2.2a: (Temkin)

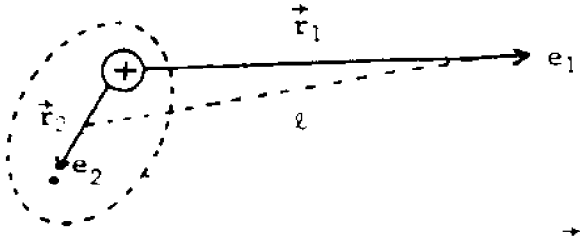

$r_1 > r_2, \theta_{12} > \pi/2$

→ $\ell \simeq r_1, b \simeq r_2$

Physics:

e_1 sees dipole formed by e_2 and ion potential

Fig. 2.2b: The Coulomb-Dipole Final State (Temkin)

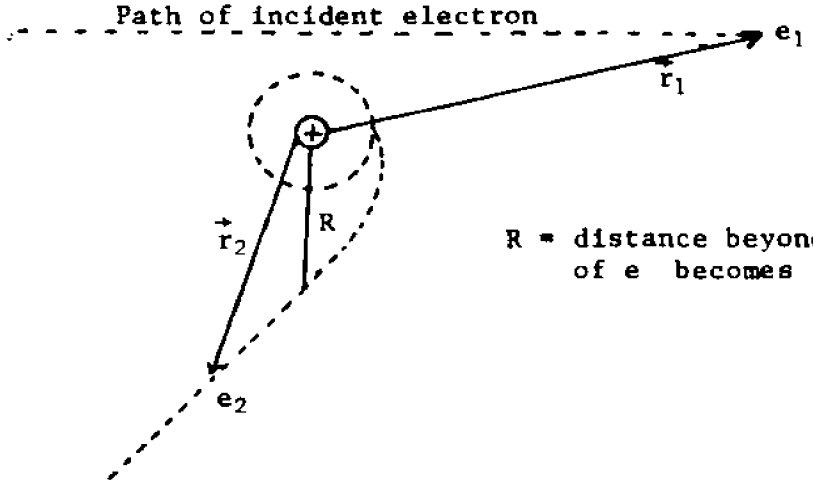

R = distance beyond which path of e becomes straight

III. EXPERIMENTAL APPARATUS

A. OVERVIEW

The experimental layout is shown schematically in Fig. 3.1. Longitudinally polarized electrons are produced from a negative electron affinity (NEA) GaAs photoemission source, and are bent through 90° by a quadrant of a spherical deflector traveling through about 500 mm of electron optics. They are again bent, this time through 180° by a hemispherical deflector that serves as a monochromator. After traversing the interaction region, the electrons are collected by a Faraday cup for current measurement and data normalization.

The hydrogen atom beam line consists of an RF discharge dissociation tube, two sections of high-field hexapole magnet for state selection, a mechanical beam chopper, an interaction region where the atoms and electrons collide, a Stern-Gerlach magnet for polarization measurements, and a quadrupole mass analyzer (QMA) for the measurement of H_1, H_2 content of the beam. The QMA is movable under vacuum and is used to scan the beam profile, an essential ingredient of the polarization measurement. Along the hydrogen beam line there are several magnetic guide fields that permit the spin of the hydrogen atom to be rotated adiabatically into the desired directions.

The orientation of the polarization vector of the electrons and atoms is indicated by arrows in Fig. 3.1. The direction of the electron polarization vector can be flipped by modulation of the direction of the ir laser light used in the photoemission process. The direction of the hydrogen polarization vector is controlled by the direction of the magnetic

field at the interaction region created by a pair of small solenoids, coaxial with the hydrogen beam (not shown in Fig. 3.1). A solenoid along the electron beam provides the capability of rotating the electron polarization vector through small angle in the plane of scattering.

The design details and the operating characteristics of both polarized beams are contained in Appendices A, B and D with some elements described briefly in Parts B and Part C of this chapter as well. The interaction region is described in Part D, while the control and data acquisition systems are reviewed in Appendix C. A diagram of the vacuum system is presented in Fig. 3.2 and typical operating pressures are given in Table 3.1.

B. POLARIZED ELECTRON SOURCE

As explained in detail in Appendix A, polarized electrons are produced by photoemission from a negative electron affinity (NEA) GaAs (100) crystal. The operating characteristics of the source are summarized in Table 3.2. The remainder of this section is devoted to the ir laser system which is not covered in Appendix A.

As illustrated in Fig. 3.3, a circularly polarized ir laser beam originating from a 3 mW GaAlAs diode laser, is formed with the use of a condensing lens. With its helicity determined by the orientation of sequential half-wave ($\lambda/2$) and quarter wave ($\lambda/4$) retardation plates, the beam is focussed onto the GaAs crystal through a hole, 2 mm in diameter, in the 90° electron deflector. A target inside the vacuum chamber permits the laser beam to be positioned from outside while the crystal is under vacuum, the elements of the optical train already having been aligned by standard auto-collimation techniques. As can be seen from the figure, a

linear polarizer with "escape windows" is employed to "clean up" the polarization of the GaAlAs solid state laser light, thereby raising the degree of circular polarization from 97% to 99.3%. The measurement of the degree circular polarization is performed in accordance with the following procedure. The light leaving the optical system in principle contains an unpolarized component as well as an elliptically polarized component. Therefore the light must be characterized by a total polarization $P_T \leq 1$. If P_C is the degree of circular polarization and P_L is the degree of linear polarization, then it follows from basic optical principles that $P_C = [P_T^2 - P_L^2]^{1/2}$.

The determination of P_C is thus accomplished by the separate measurement of P_L and P_T and requires the use of a single analyzer. Once the laser beam is collimated properly, the $\lambda/2$ plate is oriented such that its optical axis is parallel to the electric field of the linearly polarized light. Then a linear polarizer, employed as the analyzer, is set behind the lens F_2 shown in Fig. 3.1, followed immediately by a power meter (Newport, Model 815). The intensity modulation M produced by the rotation of the analyzer is measured for two cases: (i) setting of the $\lambda/4$ plate which produces minimum modulation and (ii) setting of the $\lambda/4$ plate which produces maximum modulation.

The intensity modulation M which is proportional to the degree of linear polarization P_A of the light incident upon the analyzer is given by

$$M = (I_{max} - I_{min})/(I_{max} + I_{min}),$$

where I_{max} and I_{min} denote respectively the maximum and minimum intensities of the light transmitted by the analyzer. This leads to the

relation $P_A = P_L$ for case (i) and $P_A = P_T$ for case (ii). For our system we found $P_T = 0.997 \pm 0.005$ and $P_L = 0.088 \pm 0.005$, as a consequence of which we obtained $P_e = 0.993 \pm 0.007$. During experimental operation, the $\lambda/4$ plate is first set for minimum modulation and is then rotated through intervals of 90^o with the use of a motorized drive under the command of a computer, as described in Section IV. The $\lambda/2$ plate, equipped with a similar rotational drive, is driven back and forth through 45^o at less frequent intervals. In this manner the helicity of the light, and therefore the electrons, are flipped by two independent operations.

C. POLARIZED HYDROGEN ATOM BEAM LINE

High purity hydrogen molecules from a gas handling system, shown in Fig. 3.4, are fed into an rf dissociation tube shown in Fig. 3.5. Hydrogen atoms, produced by dissociation in discharge, leave the tube through the nozzle and are formed into a beam by a skimmer aperture prior to entrance into a pair of hexapole high-field state selectors as illustrated by Fig. 3.2. As described in detail in Apendix B, the $m_s = + {}^1/_2$ atoms are preferentialy transmitted by the hexapole magnet pair and are focussed at the interaction point after passing through a 6 mm diameter aperture which defines the radial extent of the beam just upstream of the interaction point as shown in Fig. 3.6. Downstream, a Stern-Gerlach magnet and a quadrupole mass analyzer are used to measure the polarization of atoms and the fraction of components, H_1 and H_2. As shown in Fig. 3.1, several sets of solenoid coils and one helmholtz coil are employed in the hydrogen beam line to prevent Majorana (nonadiabatic) spin depolarization. One pair of solenoids located inside the scattering chamber, provide longitudinal magnetic field of - 100 mG which defines the direction of the hydrogen

polarization vector.

It should be noted that in principle the rf discharge can produce ions and electrons, as well as excited states of hydrogen and both Balmer and Lyman series photons. In order to test for the presence of these contaminants, the discharge tube was moved slightly upstream, and a pair of electrodes 2 cm long and 1 cm apart was temporarily installed between the nozzle and the skimmer. With 500 V applied across the plates, 2S atoms should be quenched, most Rydberg states should be ionized, and all charged particles should be swept out of the beam. In fact, regardless of the plate voltage status, the hydrogen related background signal on a channel electron multiplier (CEM) located downstream of the interaction point, as shown in Fig. 3.6 remained unchanged, having a typical value of 0.5 to 3 counts per second whenever the rf dissociator was on. Under the operating conditions of the source, such a background appears consistent with Lyman-α emission.

The characteristics of the polarized atom beam are listed in Table 3.2, and as already has been indicated, a detailed desription of the beam is presented in Appendix B. In addition to descriptions of the operation of rf discharge and the dissociation fraction, the polarization, and the atom density, Appendix B contains a description of a Monte Carlo analysis of the polarized hydrogen beam as well as analyses based upon an optical model of the state-selecting hexapoles and separately on phase space considerations.

D. INTERACTION CHAMBER

With the use of Mu metal shielding inside the interaction chamber, the residual magnetic field at the interaction region can be maintained at about 5 mG downstream and 20 mG laterly with respect to the hydrogen beam

direction. As shown in Fig. 3.1, an electron monochromator, a Faraday cup and an ion detector are incorporated around the scattering point, the first of these to be used in future elastic and inelastic scattering studies, and the second employed as an electron intensity monitor. Since thermal ions produced by low-energy electron impact at the interaction point are very sensitive to stray electric fields, the interaction region must be well shielded electrostatically from its surroundings. A detailed picture of the ion detector and its associated shield in Fig. 3.6.

The thermal ions produced at the scattering point travel along the direction of the hydrogen beam within a cone angle of 90°. The collection cone of the CEM is biased at -700 V, resulting in a detection efficiency of - 12%, the low bias value chosen to avoid field perturbations at the interaction region. In additon, two meshes, each having a 90% transparency intercept the thermal ions before they reach the entrance to the CEM, as shown in Fig. 3.6. The overall detection efficiency of ions created at the interaction point is therefore only 10%.

For electron energies above 10.2 eV, excitation of 2S and 2P states can occur. While the 2P state quickly decays to the ground state, the 2S state is metastable, and 2S atoms can easily travel the short distance between the interaction point and the entrance to the CEM, where they will be quenched in the field created by the cone bias. Thus, in the immediate vicinity of the ionization threshold, where the ionization cross section is very low, 2S excitation can create an unwanted background which must be treated with care for high precision measurements particular 100 meV near the threshold region.

TABLE 3.1 Vacuum Chambers and Typical Operating Pressure (beam on)

Chamber	Pressure (Torr)
H_2 Reservoir	0.4
RF Discharge Tube	0.2
H Source	2×10^{-7}
Hexapole Magnet	3×10^{-8}
Interaction Region	4×10^{-8}
e^- Source	1×10^{-8}
Stern-Gerlach	10^{-8}
QMA	$P_T = 1\times10^{-8}$
	$P_H = 10^{-10}$
	$P_{H_2} = 10^{-9}$

TABLE 3.2 Typical operating conditions at interaction region

Electron beam		
Intensity[a]	100	nA
Polarization, P_e	0.35	
Emittance	25	mrad cm $eV^{1/2}$
Energy resolution[b]	<100	meV (FWHM)
Hydrogen beam		
Density	2×10^{14}	atoms/cm^3
Electronic polarization, P_H	0.515	
Molecular fraction	0.02	
Residual gas pressure	4×10^{-8}	Torr

(a) The quantum yield of the GaAs crystal decays with an e-folding lifetime of 12-24 h.

(b) The electron monochromator was not operated at its ultimate design resolution of 30 meV full-width-at-half-maximum (FWHM), in order that high currents be maintained.

Figure 3.1 - Schematic Layout of Experiment

1. RF Hydrogen Source
2. Hexapole State-Selecting Magnets
3. Hydrogen Beam Chopper
4. Solenoidal Hydrogen Spin Rotator
5. Hydrogen Polarization Vector
6. Hemispherical Electron Monochromator
7. Channeltron Ion Detector (see Fig. 3.6 for details)
8. Rotatable (20^{o} - 105^{o}) Hemispherical Electron Spectrometer
9. Hydrogen Spin Guide Solenoid
10. Transverse Hydrogen Spin Rotator
11. Stern-Gerlach Polarimeter
12. Quadrupole Mass Analyzer
13. Circularly Polarized Laser Beam for Photoemission
    (GaAlAs 787 nm Diode Laser)
14. GaAs Crystal Mounted on Saphire Block
15. Electrostatic 90^{o} Spherical Bender
16. Solenoidal Electron Spin Processor
17. Electron Polarization Vector
18. Rotatable (20^{o} - 105^{o}) Lyman-Alpha Detector
19. Movable Faraday Cup
20. To Mott-Scattering Electron Polarimeter (not used in these studies)
21. GaAlAs Diode Laser
22. Lenses
23. Quarter Wave Plate
24. Half-Wave Plate
25. Laser Beam Flag
26. Vacuum Window

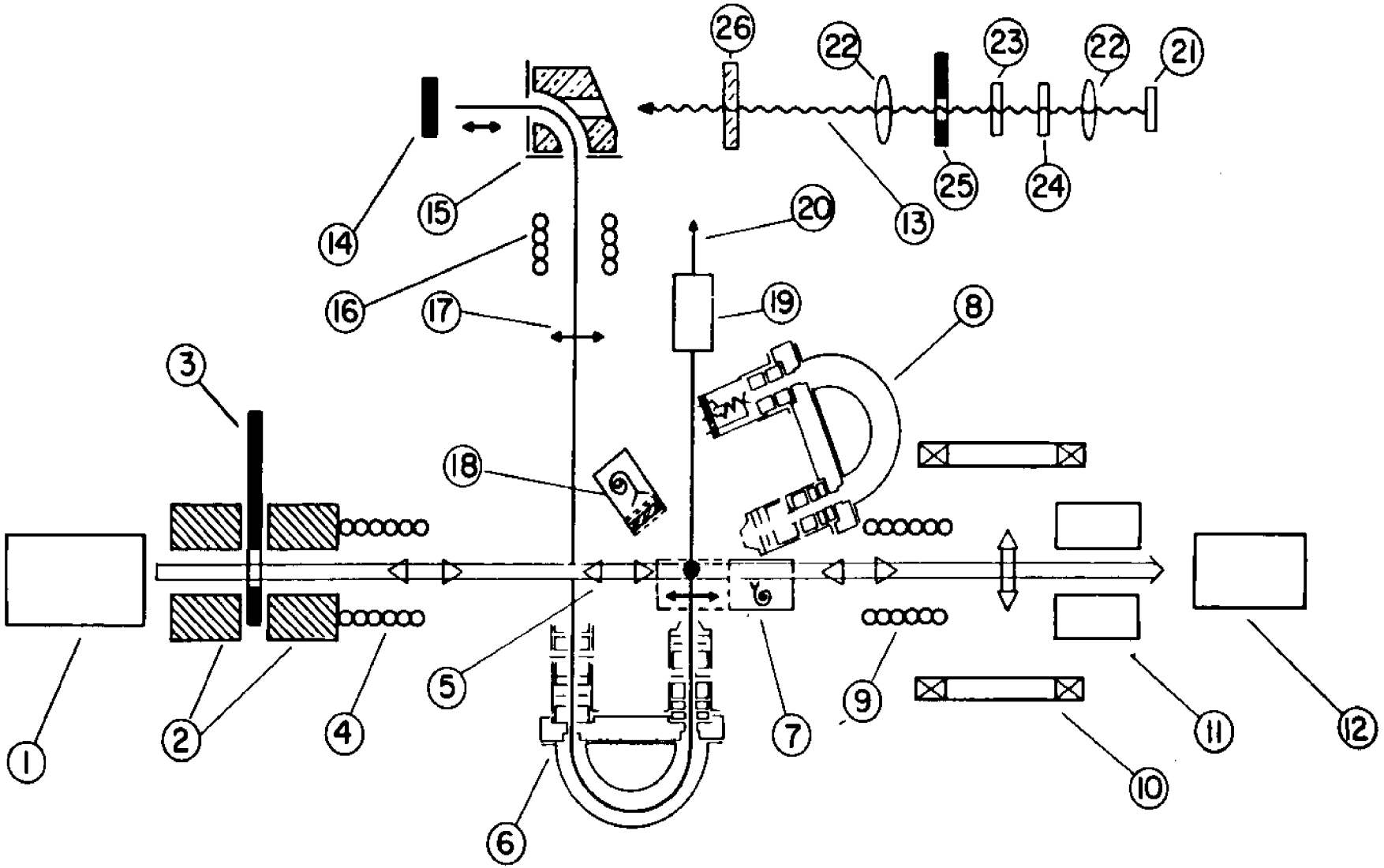

Fig. 3.1 Schematic Layout of Experiment

Figure 3.2 - Vacuum Systems

Vacuum chamber layout of beam line showing conductances between chambers for molecular hydrogen, typical pressures under operating conditions, and effective speeds of pumping modules for both hydrogen and air, the latter enclosed in parentheses. The numbered elements shown are:

1. Hydrogen Source Chamber
2. Diffusion Pump Port
3. Turbomolecular Pump Port
4. Hexapole Chamber
5. Hexapole Magnets
6. Beam Chopper
7. Beam-Line Gate Valve
8. Ion Pump Port
9. Interaction Chamber
10. Ion Pump Port
11. Stern-Gerlach Magnet
12. Cryopump Port
13. Quadrupole/Dump Chamber
14. Quadrupole Mass Analyzer

Not shown are bypass pumping lines and valves between the hexapole and hydrogen source chambers and between the quadrupole and interaction chambers. Note that conductances for air may be obtained by multiplying the hydrogen conductances by a factor of 0.27.

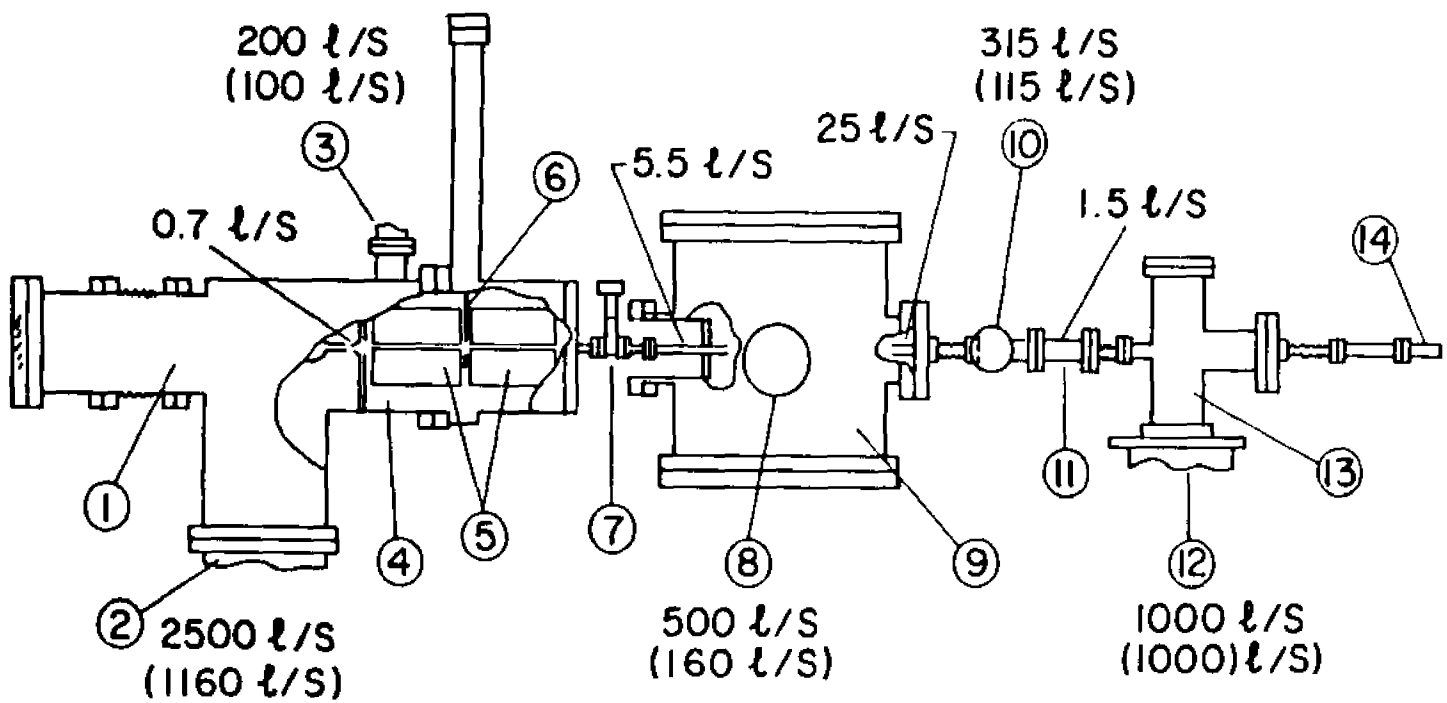

Fig. 3.2. Vacuum System

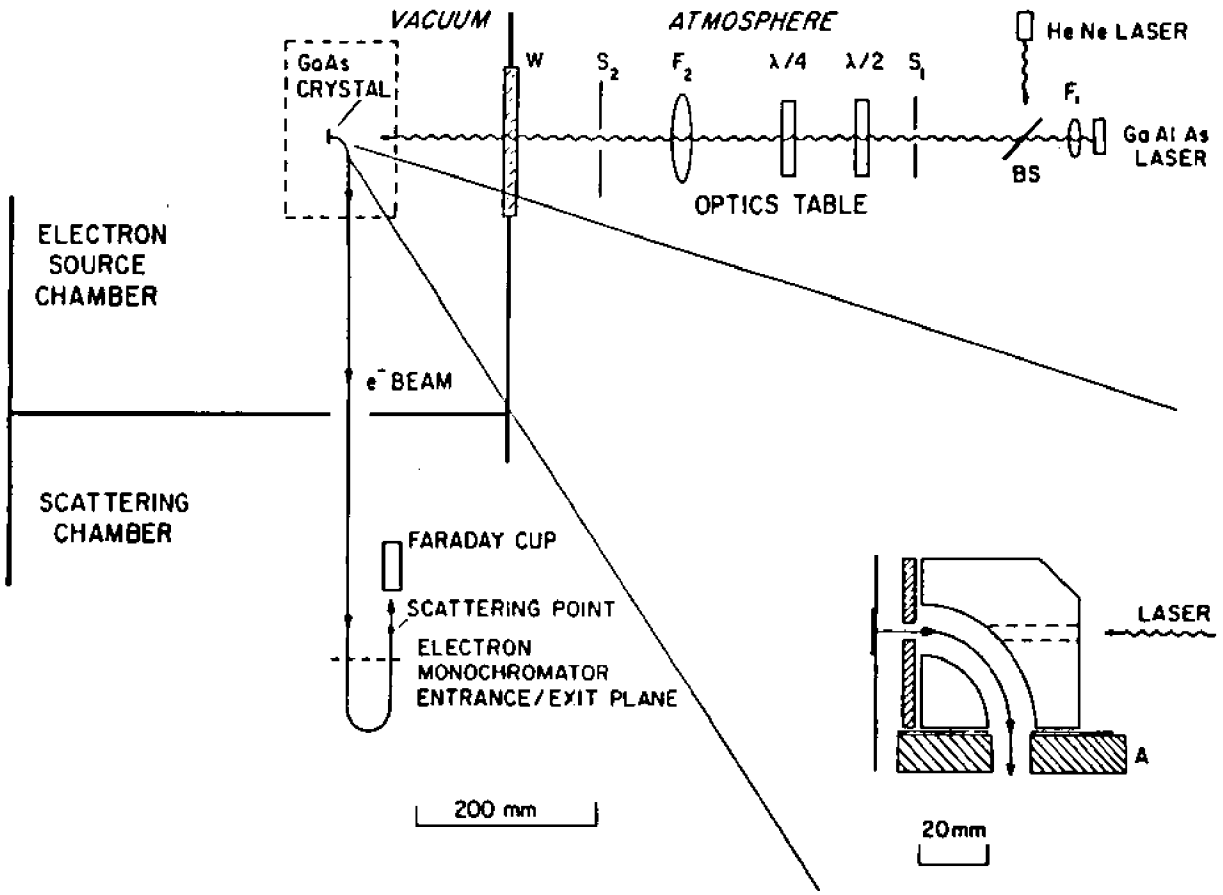

FIG. 3.3. Photoemission GaAℓs Laser System

Figure 3.4 - H_2 Gas Handling System and Reservoir

1. Palladium Leak Finger
2. Metal-Glass Joint Seal
3. Metal-Glass Joint Seal
4. Pumping Line Connecting to Hexapole Chamber
5. Thermocouple Pressure Gauge
6. Pumping Line Connecting to Hexapole Chamber
7. S.S. Mini-Gate Valve
8. Dry N_2 Line for Venting
9. Nupro S.S. Valve
10. Exhausting Line to Outside of Room
11. 2 liters H_2 S.S. Tank
12. Regulators
13. Research Grade H_2 Gas Tank
14. To Bellow Pump

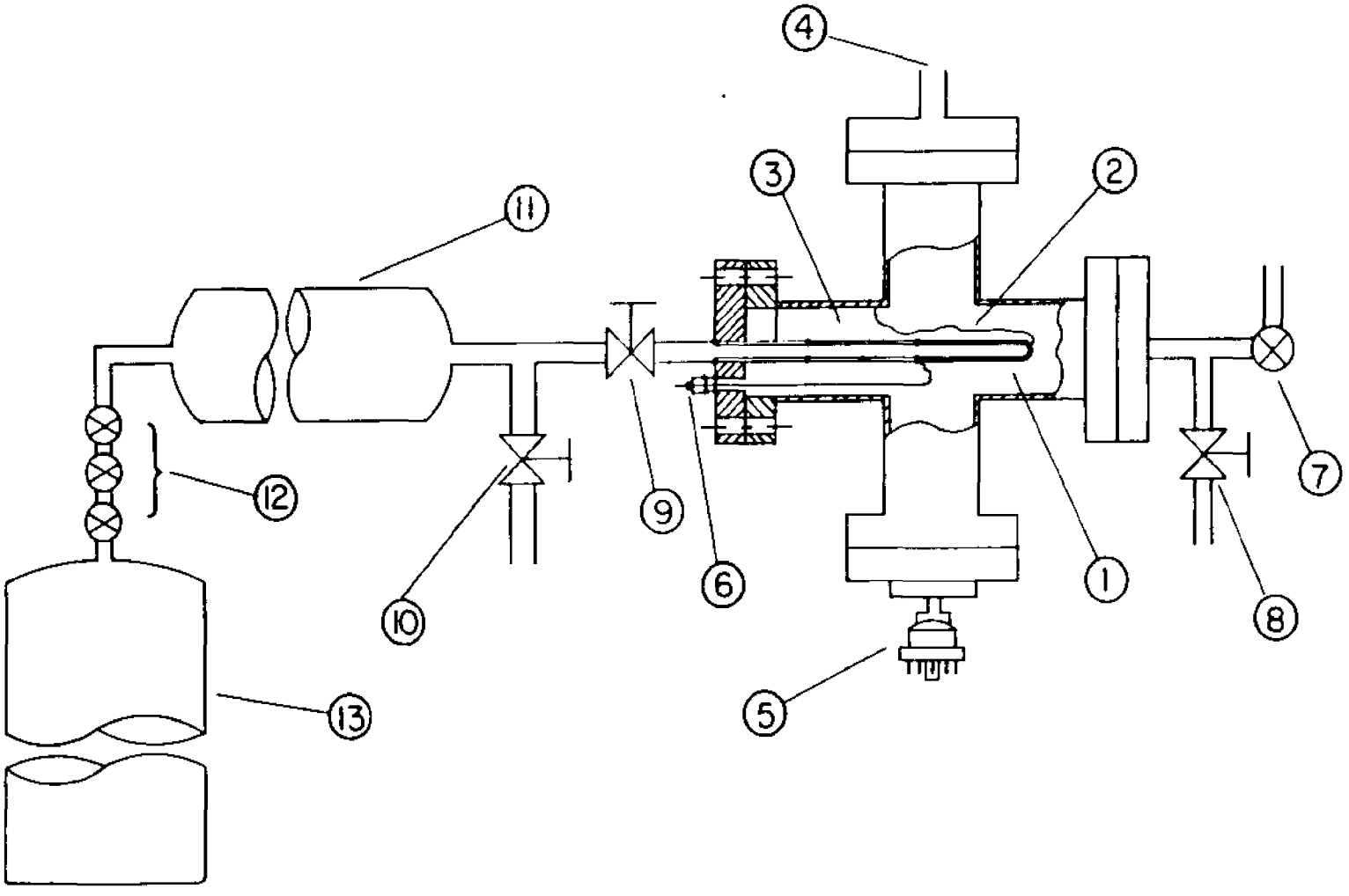

Fig. 3.4. H_2 Gas Handling System and Reservoir

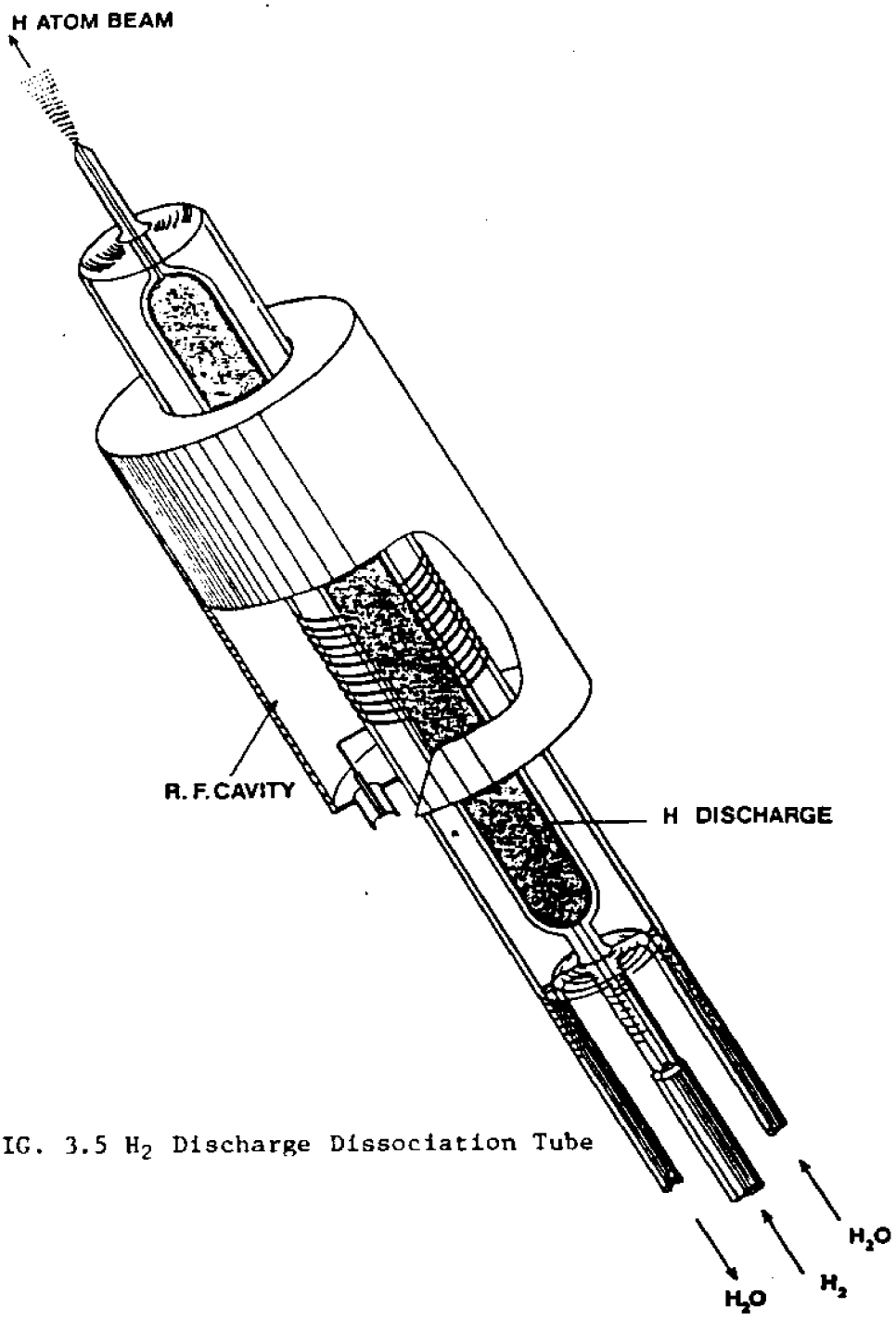

FIG. 3.5 H_2 Discharge Dissociation Tube

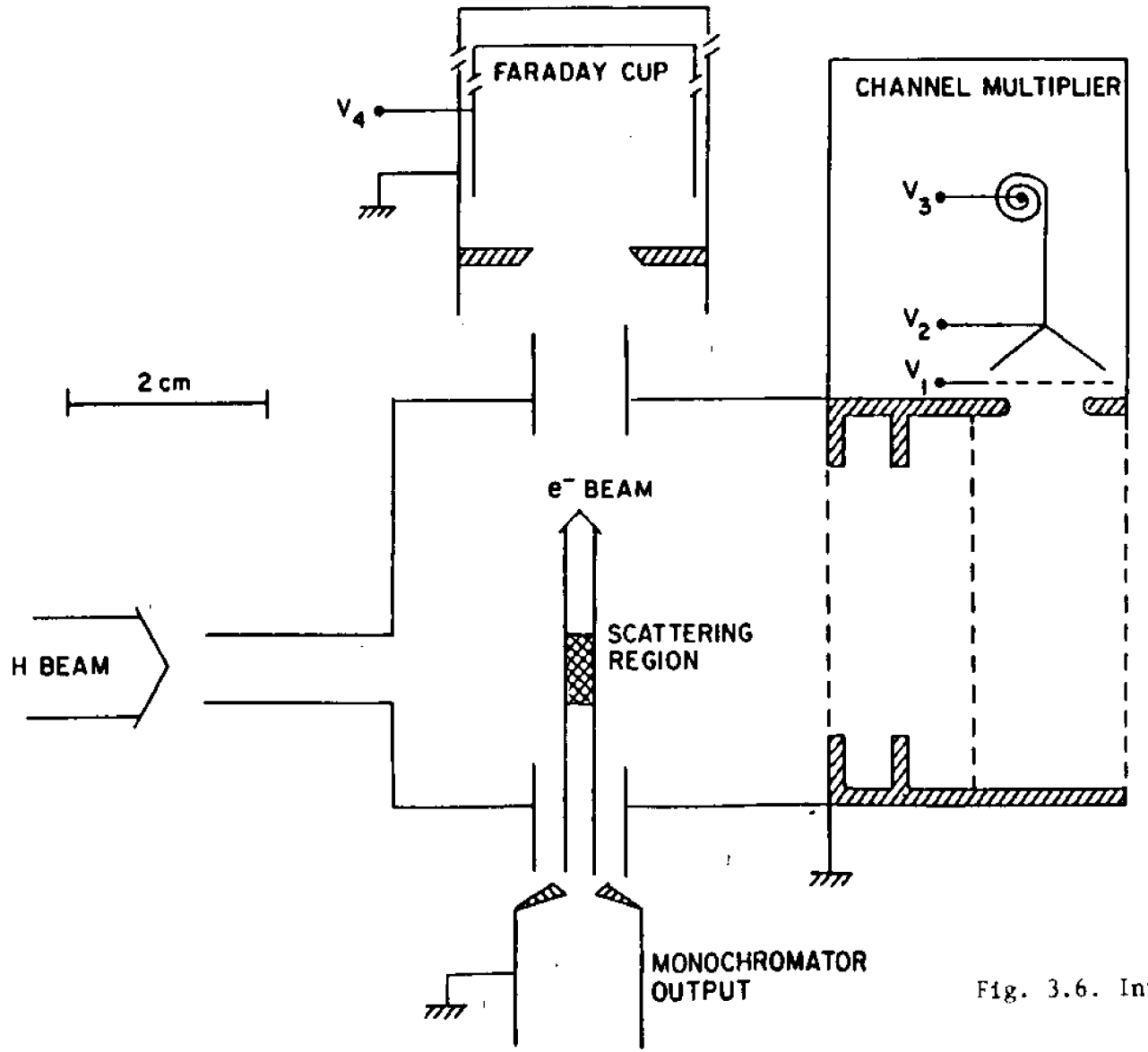

Fig. 3.6. Interaction Region

IV. EXPERIMENTAL PROCEDURE

A. GENERAL DESCRIPTION

In this chapter, a description of the data acquisition procedure is presented for the measurement of the total cross section asymmetry, A_I, for ionization in the near threshold region. The experimentally determined quantity Δ_I is related to A_I via an equation involving the degrees of polarization of both the electron and hydrogen beams, as well as the relative orientation of both polarization vectors. Specifically, in the data acquisition procedure a relative ionization rate asymmetry,

$$\Delta_I = [R(\uparrow\downarrow) - R(\uparrow\uparrow)]/[R(\uparrow\downarrow) + R(\uparrow\uparrow)], \tag{4.1}$$

is measured for incident and target electrons spin antiparallel ($\uparrow\downarrow$) and parallel ($\uparrow\uparrow$). In general Δ_I can be expressed as

$$\Delta_I = P_e P_H (1-F_2) |\cos\theta| A_I, \tag{4.2}$$

where $\vec{P}_e$ and $\vec{P}_H$ are the polarization vectors of the electron and hydrogen beams respetively, F_2 is the fraction of events attributable to hydrogen molecules, θ is the angle between the two polarization vectors. For the range of energies between 13.6 and 15.0 eV which spanned the measurements, F_2 can be taken to be effectively zero, since the ionization threshold for hydrogen molecules is 15.4 eV.

The counting rates, $R'(\uparrow\downarrow)$ and $R'(\uparrow\uparrow)$, actually measured, must be corrected for background and noise effects and further must be normalized to both incident beam fluxes in order to generate the rates $R(\uparrow\downarrow)$ and $R(\uparrow\uparrow)$

that appear in Eq. (4.2). Asymmetry effects not related to spin dependence are called systematic and can be probed through the examination of various false asymmetries as described in Chapter V. For the most part, systematic effects can be eliminated, at least at the precision of this experiment, by the frequent reversal of the direction of the electron polarization vector.

The quantities P_e, P_H, F_2, and $\cos\theta$, appearing in Eq. (4.2), can be measured independently as described in Section IV.B. Also described in Section IV.B is the calibration procedure for the incident electron energy. The determination of background effects such as detector dark current, residual gas scattering, ion-pump charged particle contamination, and Lyman-α contributions are described in Section IV.C. Also described in Section IV.C is the normalization of the event rates to the incident beam intensities.

B. DETERMINATION OF F_2, P_e, P_H, $|\cos\theta|$, AND E_e

For the purpose of the measurements described in this thesis, F_2 is taken as zero, as already indicated. The values of P_e and P_H are taken respectively as 0.35 ± 0.07 and 0.515 ± 0.005, based upon measurements that will be described shortly. It should be noted that P_e and P_H were measured several times and displayed little variation within the uncertainties of the measurement.

From Hall probe magnetometer measurements inside the interaction chamber, carried out before the asymmetry data-taking began, field values of 100 ± 5 mG along the direction of the hydrogen atom beam and 20 ± 5 mG transverse to the beam were obtained, leading to a value of 0.98 ± 0.01 for $|\cos\theta|$. However, from a comparison between the value of the asymmetry at

14.0 eV determined in this work and that determined by Fletcher et al., a value of 0.70 is obtained for $|\cos\theta|$. The discrepancy between these two values can be explained by stray magnetic fields associated with coupling between the magnetic shielding and the current leads for the internal solenoids. As a result of a wiring error, an accidental current loop was created around the shielding with the consequence that a large transverse field was produced following multiple reversals of the solenoidal fields.

Subsequent to the acquisition of the data presented in this thesis, the current loop was eliminated, and the fields were found to remain constant after many reversals. Since interest in the ionization threshold region centers around relative rather than absolute asymmetries, the reduced value of $|\cos\theta|$ is not too significant except for its effect on the ultimate precision with which the asymmetry is determined.

The absolute electron impact energy at the scattering point, E_e, is most easily determined from known features of either e-H or e-H_2 scattering. Although the crystal bias voltage is used to scan the electron kinetic energy at the scattering point (as described in Appendix D), the bias voltage reading is an undependable absolute measure of the beam energy. In general, the energy of the electron beam at the scattering point is different from that one would deduce from the applied potential at the source, such a difference resulting from contact potential differences, work function differencies, or even unanticipated stray electric fields.

In order to calibrate the beam energy we chose to measure the impact ionization rate for both hydrogen atoms and hydrogen molecules as functions of the source bias voltage. The differences between the bias voltage and the 13.595 eV threshold energy for atoms on one hand and the

15.4 eV threshold energy for molecules on the other hand provide two independent calibration points for the beam energy. The measured ionization rates as functions of the source bias voltage for atoms and molecules are shown in Figs. 4.1(a) and (b) respectively. Characterized in precision by the 100 meV full width at half maximum (FWHM) energy resolution of the hemispherical electron monochromator. The typical voltage offset as indicated in the figures was 2.60 eV: that is, the actual beam energy was lower than the bias voltage. We attribute this difference, principally, to the work function difference between stainless steel, which characterizes the environment of the interaction region, and activates GaAs which characterizes the source.

In the absence of Mott polarimetry measurements, the value of P_e was determined from a comparison of a measurement of A_I at 23.0 eV incident energy with the value of A_I measured by Fletcher et al. at the same energy. For this purpose P_H was taken as 0.515 ± 0.005, as already indicated, and $|\cos\theta|$ was taken as 0.99 ± 0.01, since the induced field problem was not present during this measurement. Following the methods outlined by Fletcher et al., F_2 was determined to be 5% at the 23.0 eV incident energy. The uncertainty of ± 0.07 in the value of 0.35 that we quote for P_e is heavily dominated by the uncertainty in the value of A_I quoted by Fletcher et al., as well as by the 3 eV FWHM energy resolution characteristic of the Fano type polarized electron beam that was employed by Fletcher et al.

C. DATA ACQUISITION: SIGNALS AND BACKGROUND

The asymmetry A_I defined by Eq. (4.1) assumes that the rates R(↑↓) and R(↑↑) are free from all backgrounds. In fact, the directly measured rates

$R'(\uparrow\downarrow)$ and $R'(\uparrow\uparrow)$ include effects due to detector dark current (about 0.05 counts/s); ion-pump charged particle contamination (about 0.3 counts/s); photon contributions, predominantly Lyman-α events (0.5 to 3.0 counts/s); and ions resulting from electron collisions with the residual gas in the interaction chamber (30 to 200 counts/s).

For purposes of real-time background substraction, the hydrogen beam is equipped with a mechanical chopper located between the two hexapole magnets and capable of operating at a frequency of 10 Hz. Since the characteristic e-folding pumping time for the interaction chamber is 0.3 s, a rate measurement made when the chopper as in the "closed" position of its cycle correctly accounts for residual gas effects that include beam loading of the interaction chamber pressure. In fact, the chopper "closed" rate measurement, B closed, on, with the electron beam "on" accounts for the sum of all backgrounds, except those related to the hydrogen beam itself and its accompanying contaminants, the latter potentially comprising of Rydberg atoms that might be field ionized near the ion detector, metastable atoms that might be quenched in the vicinity of the ion detector, H^+ ions that would mimic the real signal, and photons that might enter the channel detector after several reflections.

In order to search for the first three of these beam contaminants we installed a pair of electrostatic plates on either side of the beam at the exit of the nozzle of the hydrogen source. With an electric field of 250 V/cm applied across the beam over a length of 2 cm, we saw no change in the "chopper open" background rate obtained with the electron beam "off".

Based upon the beam geometry illustrated in Fig. 3.2, we therefore conclude that except for some low-lying Rydberg states, the hydrogen beam is mainly contaminated by photons. We confirmed this hypothesis by

temporarily shutting the gate value in front of the ion pump, turning off the electron beam, and applying a positive bias to the entrance cone of the ion detector. Under these conditions, we observed a "chopper open" count rate B_{photon} of 3 counts/s above the normal detector dark current. Note that B_{photon} can be expressed in terms of the chopper "closed", electron beam "off" signal, $B_{closed,off}$, and the chopper "open", electron beam "off" signal $B_{open,off}$ as

$$B_{photon} = B_{open,off} - B_{closed,off}. \tag{4.3}$$

It is tempting to define a total spin-independent background rate B_{total} as

$$B_{total} = B_{photon} + B_{closed,on}, \tag{4.4}$$

assuming the residual gas is unpolarized. However, Eq. (4.4) ignores the contributions of electron excitation of the hydrogen beam atoms to the observed ion signal. As in the case of source-related beam contamination, metastable atoms resulting from electron beam 2S excitation can be quenched in the presence of the electric field of the ion detector, thereby liberating a Lyman-α photon which can be detected, albeit with a reduced efficiency. Similarly Rydberg excitations can produce signals if the atoms undergo field ionization near the ion detector. Although both of these effects are small, they may effect the measured value of Δ_I at incident energies very close to the ionization threshold where the impact ionization is very small. We will return to this point in Chapter V.

In order to reduce the influence of systematic effects the direction of the electron polarization was reversed at frequent intervals (typically every 30 s). Two reversal devices were employed in the optical train -- a half-wave plate ($\lambda/2$) and a quarter-wave ($\lambda/4$) plate as illustrated in Fig. 3.3. With the use of a stepping motor, the $\lambda/4$ plate was rotated through 360^{o} in steps of 90^{o} while the $\lambda/2$ plate was rotated back and forth between two positions 45^{o} apart. In this way, eight combinations of $\lambda/4$ and $\lambda/2$ plate settings could be generated, with four corresponding to one sense of circular polarization (photon helicity) and four to the other.

For the determination of the "real" asymmetry, Δ_I, data were binned according to the helicity of the light incident on the GaAs crystal. Data were separately binned to generate a set of 18 false asymmetries, Δ_I^{Fi} (i = 1,2...,18), for combination of $\lambda/4$ and $\lambda/2$ settings that should yield asymmetries equal to zero in the absence of systematic effects. In all instances, the measured rates were corrected for background events and normalized to collision fluxes, as described in Chapter V.

The data acquisition was controlled by a PDP 11/23 computer with appropriate electronic interfacing and software as described in Appendix C. For a single acquisition cycle the control functions were applied in the following command sequence:

1. Set the initial position of the $\lambda/2$ and $\lambda/4$ plate.
2. Open the mechanical chopper (open time 500 ms).
3. With 5 ms time delay after chopper open completely, count ion events and monitor the Faraday cup for incident electron intensity as well as the QMA for H_1 H_2 and mass 6 intensities.
4. Close the mechanical chopper (close time 500 ms).

5. With 5 ms time delay after chopper close completely, count ion events and monitor the Faraday cup and the QMA for H_1, H_2 and mass 6.
6. Repeat step 2 through 5 three times.
7. Accumulate the total of time intervals, ion events, integrated electron intensity, and integrated H_1 and H_2 intensities separately for chopper open and closed. Display data in a digital format on the computer screen and write onto floppy disk.
8. Compare the integrated electron intensity to a preset value. If the intensity exceeds the preset value proceed to step 9; otherwise repeat steps 2 through 8.
9. Change the position of the $\lambda/4$ and $\lambda/2$ plates in conformity with a sequence which is programmed in a preselected combination of $\lambda/4$ and $\lambda/2$ positions (see Table 4.1) for each combination of the $\lambda/4$ and $\lambda/2$ plate, repeat step 2 throughs 8.
10. At conclusion of $\lambda/4$ and $\lambda/2$ random sequence, terminate run and clsoe data file.

Note that each data file comprises several hundred lines of data with a code number is assigned to each line. The code number indicates the experimental conditions: the setting positions of $\lambda/4$ and $\lambda/2$ plate, scattering point magnetic guide field orientation (parallel and antiparallel to beam direction) and QMA mass setting.

Data points contained a maximum of about 10^6 events for energies near 15.0 eV and a minimum of about 10^4 events for energies near 13.6 eV. Signal to background ratio varied from a maximum of 2.5 at an incident electron energy of 15.0 eV to a minimum of 0.2 at 13.6 eV. Maximum signal rates at these energies were 500 and 10 ions/s respectively. Data files

were ultimately transferred to magnetic tape and analyzed off-line on a Vax 11/780 computer. The data analysis is described in Chapter V which follows.

TABLE 4.1 Feeding Program of λ/2 and λ/4 Plate Setting Position

POL08.DAT		POL16.DAT		POL32.DAT	
λ/2	λ/4	λ/2	λ/4	λ/2	λ/4
2	2	2	2	1	3
1	3	2	2	1	3
2	1	2	3	2	3
1	4	2	3	2	3
1	1	1	3	2	4
2	4	1	3	2	4
1	2	1	2	1	1
2	3	1	2	1	1
		1	4	2	2
		1	4	2	2
		2	4	1	4
		2	4	1	4
		2	1	1	2
		2	2	1	2
		1	1	2	1
		1	1	2	1
				1	4
				1	4
				1	1
				1	1
				2	2
				2	2

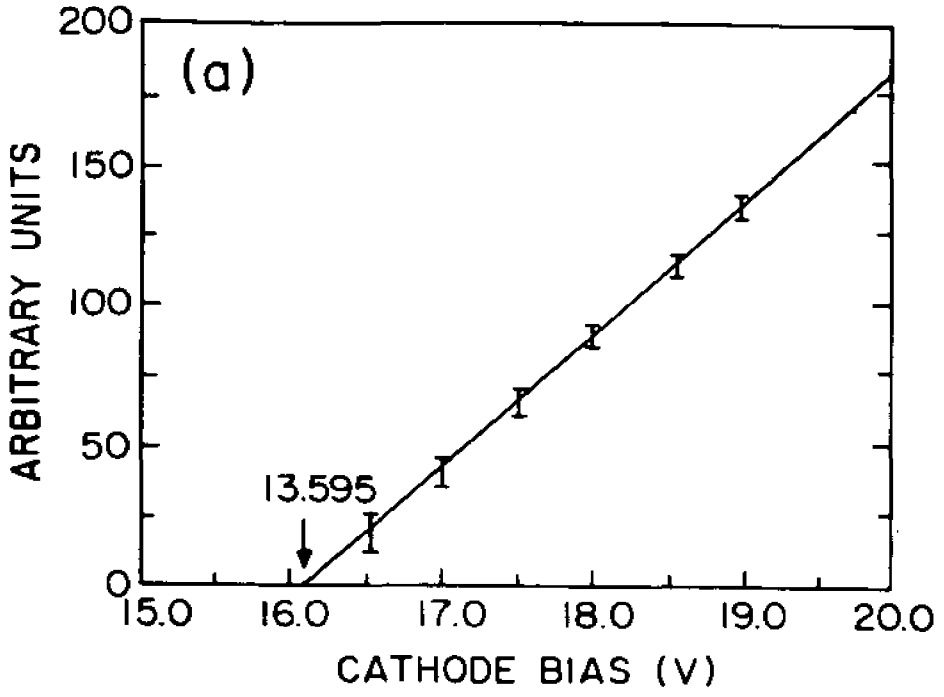

FIG. 4(a). H_1 Ionization for Energy Calibration

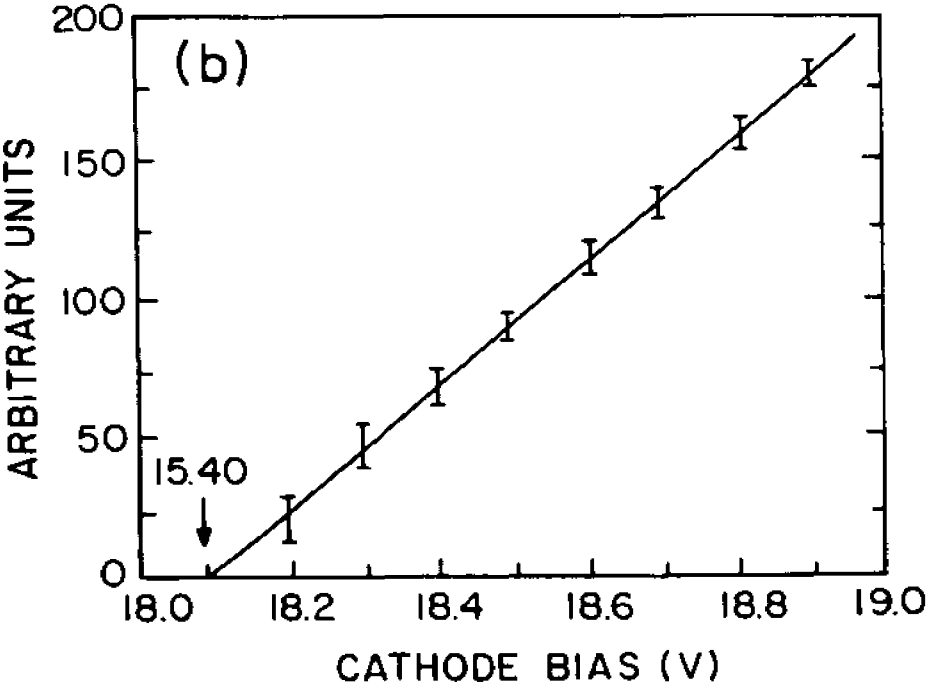

FIG. 4(b). H_2 Ionization for Energy Calibration

V. DATA ANALYSIS AND RESULTS

In accordance with the experimental procedure described in Chapter IV, once a computer run was completed, a data file was generated and stored on a floppy disk. The files were then transferred to magnetic tape, and analyzed off-line with a VAX 11/780 computer. For a given direction of hydrogen polarization, the data analysis was performed for each data file (one computer run) according to the following procedure.

1. Discriminate Data From Electronic Noise

Print hard copy of data and display histograms of the data on the computer screen. Review histograms for evidence of non-statistical behaviour, as evidenced by ion event rates or electron and atom monitoring rates that deviate from the respective norm by more than 4 standard deviation. These occurences, accounting for 0.5% of the data acquired and attributed to bursts of electronic noise, were rejected as spurious in accordance with Chauvenet's criterion [5.1].

2. Calculate the Net Signals (Real Signals)

Sum signal events over the same code number to generate for a given atomic polarization direction 16 lines of sum of data, 8 associated with H_1 monitor and 8 associated with H_2 monitor, with each of the eight sums corresponding to one unique combination of $\lambda/4$ and $\lambda/2$ plate settings. Calculate net ion signal R_{net} (assuming equal chopper open and closed times) according to the relation

$$R_{net} = R_{open,on} - B_{total},$$

where $R_{open,on}$ is the noise-free ion signal with chopper "open" and electron beam "on", and B_{total} is the background rate defined by Eqs. (4.3) and (4.4). Calculate net ("open" minus "closed") signals for mass 1 and 2 QMA monitoring, total time intervals, and Faraday cup current. Form data files for all net integrated signals according to code numbers.

3. Normalize Data

Apply two normalization techniques. First, normalize to integrated net incident electron intensity and integrated H_1 QMA monitoring signal. Second, normalize to integrated net incident electron intensity only. Compare both normalization approaches for non-statistical fluctuations.

4. Calculate Real Asymmetry Δ_I

Re-sort data from the eight combinations of $\lambda/4$ and $\lambda/2$ plate for each normalization procedure according to direction of electron spin. Sum data for each direction of electron spin to obtain R(↑↓) and R(↑↑) for each normalization method. Examine all results for non-statistical behaviour. Calculate Δ_I from Eq. (4.1):

$$\Delta_I = [R(\uparrow\downarrow) - R(\uparrow\uparrow)]/[R(\uparrow\downarrow) + R(\uparrow\uparrow)].$$

Also calculate the statistical uncertainty in Δ_I according to standard practices. For a given collision energy, calculate the real asymmetry and its associated uncertainty via statistical weighting procedures from all Δ_I values obtained at that energy.

5. Correct Data for 2S Contamination (Where Necessary)

For the data points corresponding to incident electron energies of 13.6 eV, apply corrections for the presence of 2S contamination as follows. Assign the notation A_{1S-2S} and σ_{1S-2S} respectively to the asymmetry and

total cross section associated with 2S excitation, and let ϵ be the overall detection efficiency for Lyman-α photons relative to ions (H^+). Express the measured asymmetry $A_{measured}$ as

$$A_{measured} = [\epsilon\ \bar{\sigma}_{1S-2S}\ A_{1S-2S} + \bar{\sigma}_I A_I]/[\epsilon\ \bar{\sigma}_{1S-2S} + \bar{\sigma}_I], \qquad (5.1)$$

thereby reflecting the statistical weight of both contributions. Recast Eq. (5.1) into the form

$$A_I = A_{measured}\ [1 + \kappa_1(1 - \frac{A_{1S-2S}}{A_{measured}})] = \kappa_2 A_{measured} \qquad (5.2)$$

where κ_1 is given by

$$\kappa_1 = \frac{\epsilon\ \bar{\sigma}_{1S-2S}}{\bar{\sigma}_I}, \qquad (5.3)$$

and κ_2, is given by

$$\kappa_2 = 1 + \kappa_1(1 - \frac{A_{1S-2S}}{A_{measured}}). \qquad (5.4)$$

From knowledge of the theoretical values of the differential asymmetry $A_{1S-2S}(\theta)$ [5.2] and the spin-averaged differential and total cross sections, $\bar{\sigma}_{1S-2S}(\theta)$ [5.3] and $\bar{\sigma}_{1S-2S}$ [5.4] respectively, calculate A_{1S-2S} according to the prescription

$$A_{1S-2S} = \int A_{1S-2S}(\theta) \frac{\bar{\sigma}_{1S-2S}(\theta)}{\bar{\sigma}_{1S-2S}} d\Omega. \qquad (5.5)$$

Assume absolute detector sensitivities of $s_\gamma = 0.05$ for Lyman-α photons and $s_I = 0.12$ for H^+ ions, in accordance with published data [5.5] for the Mullard channel electron multiplier (CEM), and thereby obtain a value of $\epsilon = (s_\gamma/s_I)(\Delta\Omega/4\pi) = 0.024$, where $\Delta\Omega = 0.72$ sr is the detector acceptance for assumed isotropic prompt Lyman-α emission induced by the spatially varying electric field associated with the cone of the CEM. In accordance with the form of Eq. (4.1), express $A_{measured}$ as

$$A_{measured} = (\Delta_{measured})/(P_e P_H |\cos\theta|), \qquad (5.6)$$

where F_2 is implicitly taken as zero, P_e is taken as 0.35, P_H as 0.515, and $|\cos\theta|$ as 0.70. Finally combine Eqs. (5.2) - (5.6) with the measured asymmetries (H_1 normalization excluded) obtained by the procedures already described to generate the results given in Table 5.1. Note that this procedure ignores corrections due to cascade from higher P-states, which might affect $(\kappa_2 - 1)$ at a level of about 10% of itself, thereby making the impact rather minor.

5. Calculate False Asymmetries

Define a quantity called a false asymmetry for combinations of $\lambda/4$ and $\lambda/2$ settings that produce the same sense of electron polarization and have a predicted zero asymmetry. For each data file corresponding to a given normalization procedure, generate 18 such false asymmetries $(\Delta_I^F)_1$.

For each energy and each normalization procedure obtain weighted averages of all 18 false asymmetries with corresponding statistical uncertainties.

Having carried out the procedure outlined above, we then display the asymmetries as generated. Table 5.1 as before summarizes the asymmetry results A_I without H_i normalization. Table 5.2 summarizes the asymmetry results with H_i normalization. Fig. 5.1 and 5.2 are graphical displays of the tabulated results. The vertical error bars are one standard deviation uncertainties (including all uncertainties), while the horizontal error bars indicate the energy spread of the beam. Table 5.3 is a summary of the false asymmetries $(\Delta_I^F)_i$ along with their chi-squares per degree of freedom $\chi^2(0)/d.f.$ and $\chi^2(arg)/d.f.$ respectively about zero and their corresponding average values, where the averages are taken over runs irrespective of energy. Such averaging is justified since the parent distribution distribution for $\chi^2(0)$ should be the same over the entire energy range if systematic effects are absent.

Table 5.1 Lyman-α 1S-2S Correction to Ionization Asymmetry (H_1 Normalization Excluded)

E(eV)	(a) $\sigma_{1S-2S}(\pi a_0^2)$	(b) $\sigma_I(\pi a_0^2)$	(c) A_{1S-2S}	$\Delta_{measured}$	$A_{measured}$	κ_1	(d) κ_2	(e) A_I
13.6	0.154	0.002	0.41	0.0403 (421)	0.322 (336)	1.85	1.044	0.336 (351)
13.7	0.152	0.005	0.41	0.0501 (218)	0.400 (124)	0.73	1.017	0.407 (175)
13.8	0.152	0.010	0.41	0.0520 (215)	0.416 (172)	0.36	1.008	0.419 (173)
13.9	0.151	0.015	0.41	0.0686 (187)	0.548 (149)	0.24	1.012	0.554 (151)
14.0	0.150	0.025	0.41	0.0521 (116)	0.617 (92)	0.14	1.007	0.420 (92)
14.1	0.149	0.033	0.41	0.0482 (99)	0.386 (79)	0.11	1.007	0.389 (79)
14.2	0.149	0.040	0.41	0.0538 (93)	0.430 (74)	0.09	1.001	0.430 (74)
14.3	0.148	0.048	0.41	0.0545 (58)	0.436 (46)	0.07	1.000	0.436 (46)
14.4	0.147	0.055	0.41	0.0515 (73)	0.412 (58)	0.06	1.000	0.412 (58)
14.5	0.147	0.063	0.41	0.0462 (42)	0.370 (33)	0.05	1.000	0.370 (33)
14.6	0.146	0.071	0.41	0.0466 (29)	0.373 (23)	0.05	1.000	0.373 (23)
14.7	0.146	0.078	0.41	0.0424 (29)	0.339 (23)	0.04	1.000	0.339 (23)
14.8	0.145	0.086	0.41	0.0470 (29)	0.376 (23)	0.04	1.000	0.376 (23)
14.9	0.145	0.094	0.41	0.0470 (28)	0.375 (23)	0.04	1.000	0.376 (23)
15.0	0.144	0.105	0.41	0.0497 (33)	0.398 (26)	0.03	1.000	0.398 (26)

(a) See Ref. [5.4]

(b) See Ref. [5.6]

(c) From Eq. (5.5) and the data of Refs [5.2] - [5.4] A_{1S-2S} remains almost constant between 13.6 and 15.0 eV.

(d) In Eq. (5.4), $A_{measured}$ is taken as a running 5-point average over adjacent data points in order to smooth out statistical fluctuations. For the cases of 13.6 and 13.7 eV, the average is asymmetric with respect to the nominal energy.

(e) The uncertainty in $A_{measured}$ dominates the uncertainty in κ_2.

Table 5.2 Lyman-α 1S-2S Correction to Ionization Asymmetry (H_1 Normalization Included)

E(eV)	(a) $\sigma_{1S-2S}(\pi a_0^2)$	(b) $\sigma_I(\pi a_0^2)$	(c) A_{1S-2S}	$\Delta_{measured}$	$A_{measured}$	κ_1	(d) κ_2	(e) A_I
13.6	0.154	0.002	0.41	0.0376 (421)	0.300 (336)	1.85	1.024	0.307 (344)
13.7	0.152	0.005	0.41	0.0489 (218)	0.391 (124)	0.73	1.009	0.393 (175)
13.8	0.152	0.010	0.41	0.0527 (215)	0.413 (172)	0.36	1.005	0.415 (173)
13.9	0.151	0.015	0.41	0.0680 (187)	0.543 (149)	0.24	1.009	0.548 (151)
14.0	0.150	0.025	0.41	0.0538 (117)	0.430 (92)	0.14	1.005	0.432 (92)
14.1	0.149	0.033	0.41	0.0458 (99)	0.366 (79)	0.11	1.001	0.370 (79)
14.2	0.149	0.040	0.41	0.0645 (93)	0.515 (74)	0.09	1.000	0.515 (74)
14.3	0.148	0.048	0.41	0.0579 (58)	0.463 (46)	0.07	1.000	0.463 (46)
14.4	0.147	0.055	0.41	0.0599 (74)	0.478 (58)	0.06	1.000	0.478 (58)
14.5	0.147	0.063	0.41	0.0408 (42)	0.342 (33)	0.05	1.000	0.342 (33)
14.6	0.146	0.071	0.41	0.0433 (30)	0.346 (23)	0.05	1.000	0.346 (23)
14.7	0.146	0.078	0.41	0.0426 (29)	0.340 (23)	0.04	1.000	0.340 (23)
14.8	0.145	0.086	0.41	0.0482 (29)	0.385 (23)	0.04	1.000	0.385 (23)
14.9	0.145	0.094	0.41	0.0462 (28)	0.369 (23)	0.04	1.000	0.369 (23)
15.0	0.144	0.105	0.41	0.0481 (33)	0.384 (26)	0.03	1.000	0.384 (26)

(a) See Ref. [5.4]

(b) See Ref. [5.6]

(c) From Eq. (5.5) and the data of Refs [5.2] - [5.4] A_{1S-2S} remains almost constant between 13.6 and 15.0 eV.

(d) In Eq. (5.4), $A_{measured}$ is taken as a running 5-point average over adjacent data points in order to smooth out statistical fluctuations. For the cases of 13.6 and 13.7 eV, the average is asymmetric with respect to the nominal energy.

(e) The uncertainty in $A_{measured}$ dominates the uncertainty in κ_2.

Table 5.3 False Asymmetries

n	$\bar{\chi}^2_{noq}(\bar{\Delta})$ **(a)**	$\bar{\chi}^2_{noq}(0)$ **(b)**	$\bar{\chi}^2_{q}(0)$ **(c)**	$\bar{\chi}^2_{q}(\bar{\Delta})$ **(d)**
1	1.3343	1.4464	1.4516	1.4161
2	1.5466	1.6060	1.6561	1.6802
3	1.1584	1.1930	1.3898	1.3823
4	1.4541	1.5733	.2484	1.2143
5	1.4480	1.4445	1.6972	1.7268
6	1.1445	1.1736	1.2210	1.2071
7	1.4923	1.6319	1.6306	1.5158
8	1.5856	1.6696	2.2276	2.2255
9	1.8141	1.8208	1.7532	1.7818
10	1.1997	1.3570	1.5163	1.4049
11	1.8111	1.7916	1.7599	1.7764
12	1.3837	1.3933	1.6736	1.6997
13	1.0156	1.0314	1.6166	1.6381
14	1.4090	1.3961	3.0327	2.0590
15	1.7228	1.8678	1.5366	1.4463
16	1.2686	1.2844	1.9157	1.9444
17	1.9657	2.0418	2.1430	2.1492
18	1.8494	1.9816	1.8890	1.7973

(a) chi-square calculation with respect to average $\bar{\Delta}$ (H_1 normalization excluded)

(b) chi-square calculation with respect to zero (H_1 normalization excluded)

(c) With respect to zero (H_1 normalization included)

(d) With respect to average (H_1 normalization included)

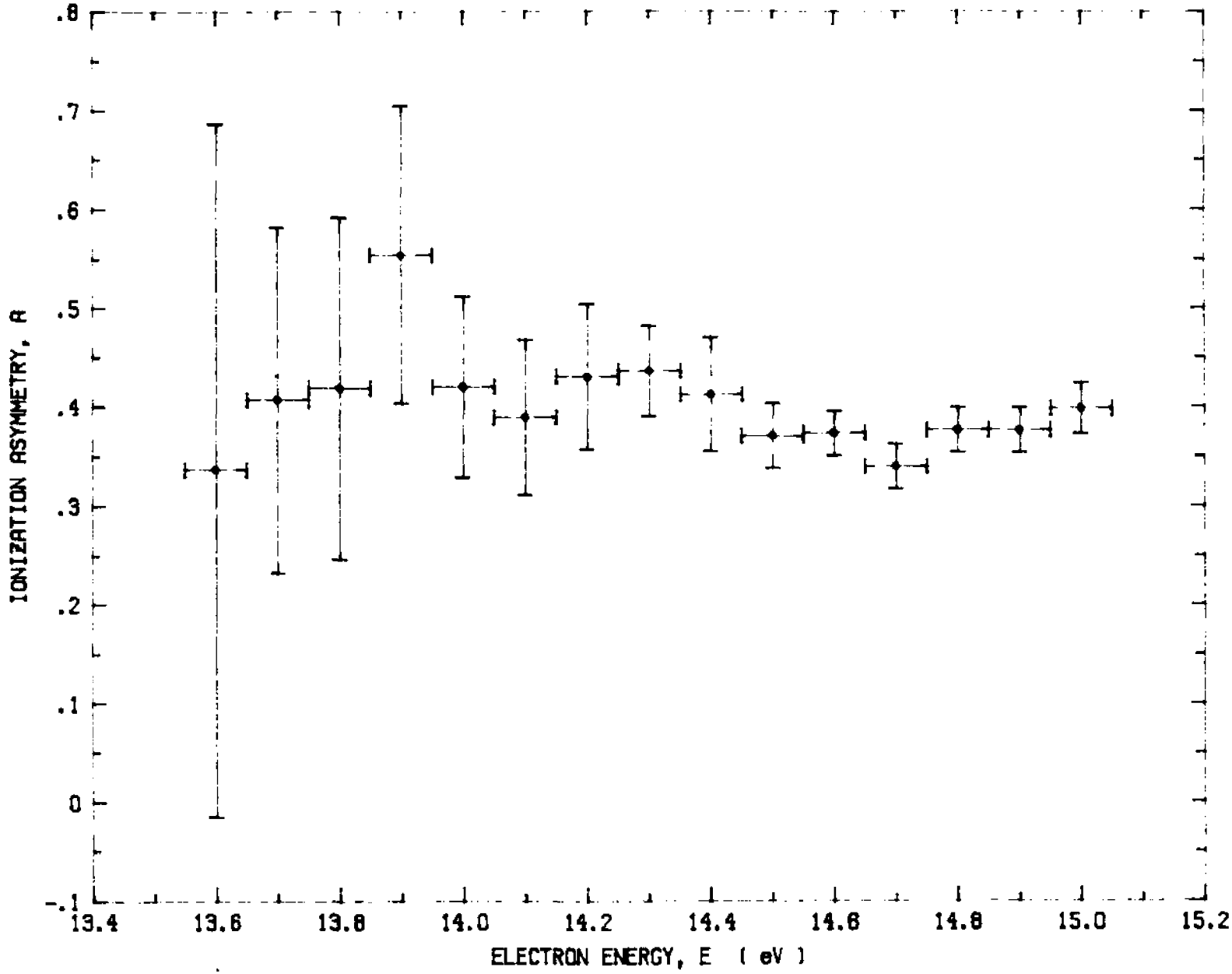

Fig. 5.1. Ionization Asymmetry (H_2 normalization Excluded)

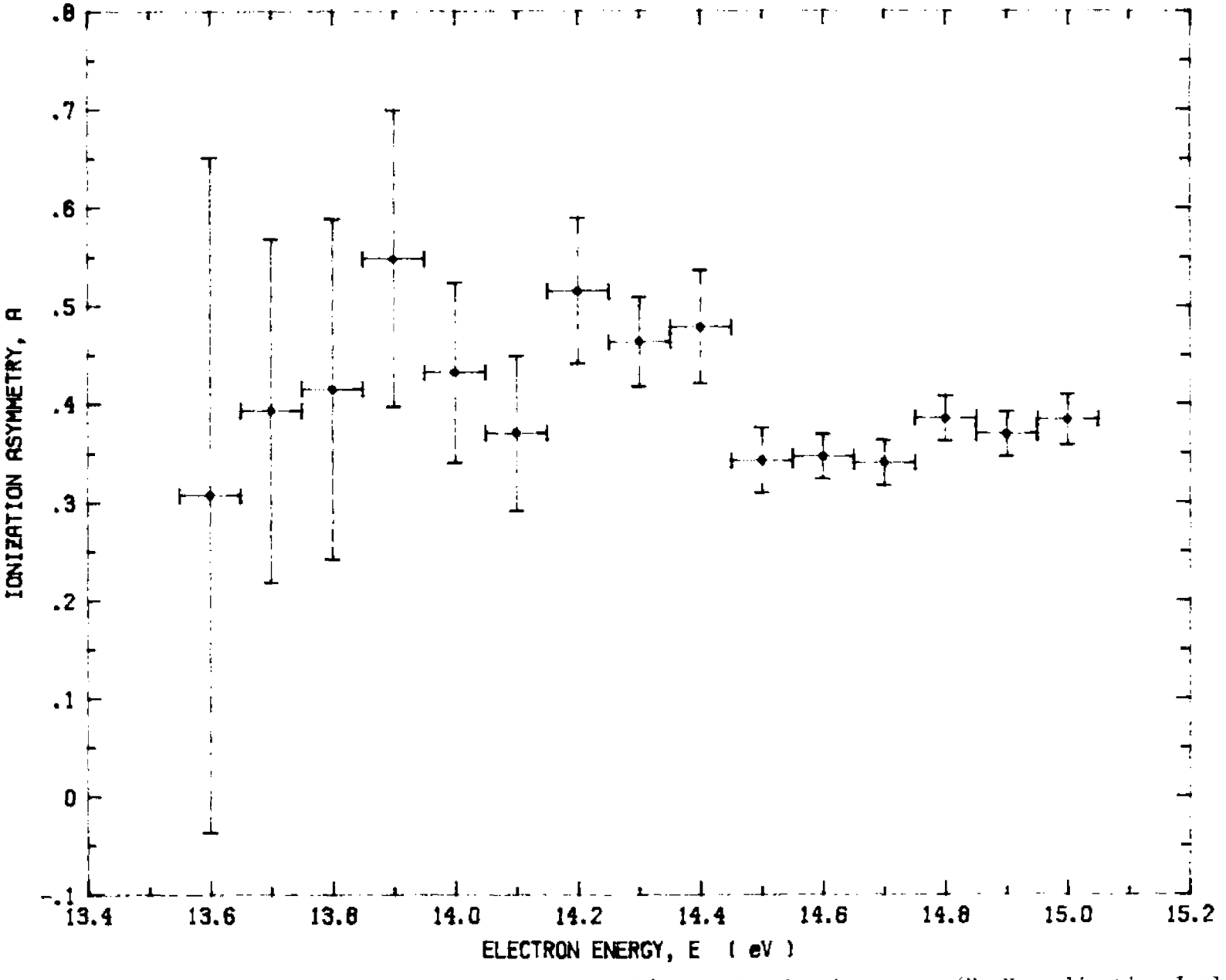

Fig. 5.2. Ionization Asymmetry (H_1 Normalization Included)

VI. CONCLUSIONS AND IMPLICATIONS FOR THE FUTURE

From the false asymmetries shown in Table 5.3, we find that the case with H_1 normalization excluded produces a set of $(\Delta_I^F)_1$ values that are generally more consistent with zero than the corresponding set generated with H_1 normalization included. Moreover the reduced chi-square, $\chi^2(o)/d.f.$, is also smaller for the case of with H_1 normalization excluded, thus implying that the QMA beam monitor suffered from instabilities or electronic noise that was visibly greater than the instabilities in the hydrogen beam itself. Detailed studies of the QMA performance, carried out after data taking had been completed, revealed thermal instabilities in the QMA that were related to ambient temperature. Fluctuations in the laboratory, thus confirming this conclusion.

For the purpose of the data presented in this thesis, the results obtained with the H_1 normalization excluded are deemed more accurate. It should be noted that although the reduced chi-square for this case still reveals substantial non-statistical behavior (as might be expected for an atomic beam treated as unmonitored), the values of the various false asymmetries are consistent with zero at a level that is 5 to 10 times smaller than the measured values of Δ_I. For the statistical uncertainties of the data presented, the quality of the false asymmetries may be regarded as quite adequate. For future, more precise measurements however, it is clear that the H_1 normalization must be included, and that the stability of the QMA signals must be improved. Such an improvement has in fact already been achieved with the removal of the Stern-Gerlach magnet and its small aperture defining slits. The removal made possible by the completion of the detailed hydrogen polarization studies described

in Appendix C.

Our initial asymmetry measurements are in the near ionization threshold region. Within the accuracies of the measurement, the results show no evidence of the modulation predicated by the Coulomb-dipole model [6.1]. We therefore conclude that either the model is incorrect or its narrow feature appear so close to threshold that they are not visible under our present operating conditions. The relative high energy resolution require to observe such narrow features and the low cross section characteristics of threshold region combine to produce low counting rates, thereby making such measurements extremely difficult. The problem is compounded by the presence of contaminants such as 2S states or excited state cascades. Furthermore, the Coulomb dipole model contains several unknown parameters, which theoretically may have values that cause the oscillation frequency to be high, its amplitude small, and its region of applicability so close to threshold that experimental probes are all but ruled out on technological grounds. It would appear that future work might be best directed elsewhere.

Our crossed polarized beams machine can in fact be used to perform a variety of "second generation" [6.2] asymmetry measurements, in which the interference of the direct and exchange channels play a prominent role. With the apparatus it is possible to examine different reaction channels in electron-hydrogen atom scattering. In view of the existing theoretical data base, it would appear that the experimental emphasis should be placed on the elastic resonance region, the elastic intermediate energy (10-50 eV) region, 1S-2S excitation, and 1S-2P excitation, the last incorporating coincidence techniques.

It should be noted that the asymmetry measurement for the 1S-2S excitation channel will complement the measurement of the exchange amplitude $|g|^2$ which was measured some years ago [6.3]. The combined knowledge of A, $|g|^2$ and $\bar{\sigma}$ will then complete a "perfect" [6.4] experiment. It should be noted further, however, that an ambiguity in the sign of θ still remains if only two polarization devices are employed as in "second generation" experiments. An additional experiment is required in which these polarization devices are employed such an experiment might be called "third-generation" experiment.

In the case of e-H scattering, where the spin orbit interaction can be neglected, such a "third generation" experiment can be viewed as follows. Consider the situation of a longitudinally polarized electron beam incident along the x-axis and a longitudinally polarized hydrogen beam incident along the y axis with an electron polarimeter employed to determine the z component of the scattered electron. The polarization component $(P'_e)z$ of the scattered electron is then related to the incident electron polarization, $\vec{P}_e = (P_e)_x \hat{x}$, and the incident atom polarization, $\vec{P}_H = (P_H)_y \hat{y}$, according to the expression

$$(P'_e)_z = P_e P_H \, I_m(f^* g) \, (\frac{d\bar{\sigma}}{d\Omega})^{-1} \tag{6.1}$$

or alternatively

$$(P'_e)_z = P_e P_H \, |f| \, |g| \, \sin\theta \, (\frac{d\bar{\sigma}}{d\Omega}). \tag{6.2}$$

Thus the determination of $\sin\theta$ from such a measurement together with the previous determination of $\cos\theta$ serves to specify θ completely. A compact and high efficiency of spin polarimeter [6.5] will make "third generation" experiments possible in the future.

The improvement in polarized beam and polarimeter technologies, which has taken place over the last twenty years has made possible access to the details of the scattering process. Further advances in such technologies hold great promise for the future. For the present, the results of this thesis work should provide greater insight into the dynamics of the double escape process in the simplest of all atomic configurations.

APPENDIX A

Operating Experience With a GaAs Photoemission Electron Source

F.C. Tang, M.S. Lubell, K. Rubin, and A. Vasilakis
Department of Physics, The City College of the
City University of New York, NY 10031

M. Eminyan
Unites d'Enseignement et de Recherche de Physique, Universite Paris VII,
F-75221 Paris, France

and

J. Slevin[a]
Department of Physics, University of Stirling, Stirling FK9 4LA, Scotland

ABSTRACT

We report on the development of several operating procedures that promise to make GaAs photoemission electron sources easier to construct, more reliable to operate, and more amenable to use in dynamic vacuum systems. We describe in particular a method for "ohmically" heating a <100> crystal of GaAs under vacuum to approximately 600 ^{o}C. We also discuss our observations of the role of oxygen in the activation of the crystal surface, the use of continuous cesiation, and of the performance of the crystal under varying vacuum conditions.

(To be submitted for publication)

I. INTRODUCTION

In 1975, succeeding by one year the suggestion of Garwin, Pierce, and Siegmann,[1] Pierce Meier, and Zürcher reported[2,3] the development of an intense source of polarized electrons based upon photoemission from a p-type crystal of GaAs that was activated to negative electron affinity (NEA) by coadsorption of cesium and oxygen.[4,5] With the electron currents I_e polarization P_e combined to form the customary figure of merit[6,7] $P_e\sqrt{I_e}$, the GaAs source represented a substantial improvement over a variety of other sources.[8-14] The widespread use of the GaAs source during the last ten years, encompasssing many areas of research,[15-23] bears ample testimony to its advantageous performance characteristics that include high-brightness and narrow energy spread as well as a very favorable figure of merit.

Nonetheless, the source is not without drawbacks: its polarization faces a fundamental restriction of ≤ 0.5 due to crystal symmetry considerations; its intensity degrades with time as a result of surface contamination; and its construction involves certain complexities, due in part to the need for heat-cleaning and activation of the crystal. In recent years, much effort has been devoted by various research groups to eliminating these drawbacks and to generally facilitating the use of the GaAs source.[14,16,24-29] (An excellent summary of the field can be found in the review article by C.K. Sinclair.[30]) While some progress has been made, much more remains to be realized. In this paper we present information which we believe simplifies the construction of the source, diminishes its sensitivity to contaminants, and extends its applicability to vacuum conditions ordinarily thought to be incompatible with effective operation. Our conclusions are based upon experience gained during

approximately one year of operation of our source, in the course of which we have worked with more than ten crystal samples. Although our tests are not yet complete and certainly are not as detailed as they eventually will be, we have chosen to publish our findings at this time because we believe that they may be of help to other researchers.

While only incidental to the information presented in the paper, we point out that we developed our source specifically for the study of spin-tagged electron-hydrogen scattering,[21] the motivation of which is discussed at length in a recent paper treating a series of first-generation experiments in this field.[31] As a consequence, some of the design characteristics, particularly those associated with the extraction electron optics, were dictated by the needs of the hydrogen scattering experiment and, in fact, may not be entirely appropriate to optimal source performance.

The principles that govern the operation of GaAs polarized electron sources have been described in a number of papers, with the greatest detail appearing in the reports of Pierce and his coworkers[14,24,32] and Lampel and his coworkers.[25] Electron polarization is achieved through the pumping of the conduction band by circularly polarized near ir laser light, while photoemission is enhanced through the activation of a negative affinity surface[33] by the application of cesium in conjunction with O_2. (More recently NF_3 has been employed in place of O_2.[34,35]) For the GaAs polarized electron sources currently in use, most of which now employ <100> crystals, typical values of photoemission polarization range from a low of 0.35 to a high of 0.45, with liquid nitrogen cooling of the crystal required for the latter case.[25,30,36] While quantum yields as high as 20% have been observed[34] more typical values lie in the 1-10% range.

The lifetime of an activated crystal is limited by a degradation in the quantum yield that results from alterations in the surface conditions. Such alterations, in turn, may result from surface deposition of contaminants present in the residual atmosphere of the vacuum system, from cesium migration off the crystal surface, or from bombardment by backstreaming ions produced when the photoelectrons collide with residual gas molecules or nearby surfaces. As a consequence, great pains are usually taken to maintain a vacuum of $\leq 10^{-10}$ Torr[29] and to extract the photoelectrons with a minimum of aperture scraping. The latter is particularly important for extracted beam energies that exceed several keV.

During the course of our work we have developed techniques that appear to minimize the degradation of the crystal surface, thereby extending the lifetime substantially. We have achieved this improvement under vacuum conditions in which the base pressure has been as high as 3×10^{-9} Torr and under circumstances where the operating pressure has risen to 10^{-6} Torr. In the following section we present the design details of our source and describe the operating procedures we customarily employ.

II. EXPERIMENTAL DESIGN

The CCNY source is contained in a commercially available six-way stainless steel cross,[30] shown schematically in Fig. 1. Pumped by a 150 ℓ/s conventional diode-type ion pump with assistance from a mini Ti-ball[31] sublimator, the vacuum system typically achieves a base pressure of 10^{-10} Torr after a 4-day bakeout at 250°C. Pressures are measured by a nude ionization gauge[32] that is separated from the various components in the vacuum system by a fine grounded stainless steel mesh. The ionization gauge is equipped with

dual thoria-coated iridium filaments instead of a tungsten filaments as a precaution against the formation of CO, a contaminent known to be harmful to the surface of the GaAs cathode.

All components contained in the source chamber are fabricated from materials that are ultra-high-vacuum compatible and free from potentially damaging contaminants. With the use of low-conductance apertures (< 1 $\ell\ s^{-1}$), the gas load (dominantly molecular hydrogen) from the experimental chamber adjacent to the source is maintained below 2×10^{-8} Torr $\ell\ s^{-1}$. In the adjacent experimental chamber, the same stringent materials standards are applied as in the case of the source. In view of the low conductance between the source and experimental chambers and the nature of the conducted gas, we believe that the influence of the experimental chamber on the operation of the source is almost nil.

In all of our work we used <100> p-type crystals that are Zn-doped to provide a carrier concentration of ~ 10^{19} cm^{-3}. The wafers, purchased from Laser Diode Laboratories (Metuchen, NJ) with a thickness of 0.325 mm, are cleaved outside the vacuum system to provide rectangular samples, each measuring 0.7 cm x 1.0 cm. The quoted etch pit density (EPD) characterizing the wafers ranged from 6,000 - 10,000 in our earlier measurements to less than 5,000 in our later studies.

Inside the vacuum system the GaAs sample is attached to a sapphire holder by means of two tantalum clamps, 75 um thick, as shown in Fig. 2. The sapphire, in turn, is fastened to a molybdenum bar that couples the holder to a linear motion feedthrough,[50] used to move the crystal between its activation position in front of a cesium dispenser[51] and its operating position in front of the beam-forming extraction optics, as shown in Fig. 1.

The choice of an electrically insulating sapphire mount permits the GaAs crystal to be heated "ohmically" by passage of an electrical current through the sample itself. To this end, electrical contacts are made through the tantalum clamps, a mechanism that produces extremely even heating of the crystal as observed visually from the uniformity of the color temperature. "Ohmic-heating" of the crystal avoids the complexity of electron-bombardment, as well as the temperature non-uniformity across the crystal surface that often accompanies such a heating process. As constrasted with radiative heating, "ohmic-heating" ensures that the crystal remain the hottest object in the vacuum system, thereby minimizing the deposition of contaminants on the crystal surface during the heat-cleaning process. While the crystal is undergoing "ohmic-heating", its temperature is monitored continuously by a chromel-alumel thermocouple[52] that makes contact with the crystal from the rear through a hole in the sapphire.

The geometry of the tantalum clamps is critical to the reliable operation of the heating method. The hairpin spring shape, shown in Fig. 2, provides excellent uniform electrical contact with the crystal without creating undue mechanical stress, and represents the most successful of a number of designs tried. The low profile of the clamps also produces a minimum amount of electric-field distortion in the diode extraction configuration. While not specifically related to the crystal holder itself, it should be noted that when the position of the linear motion feedthrough is adjusted for activation, the crystal faces a molybdenum pin 4 cm away that serves as an electron collector.

As a final point, it can be seen that the sapphire mount shown in Fig. 2 contains a groove around its perimeter. In the future, small diameter stainless steel tubing will be inserted in this groove to provide the

possibility for cooling the GaAs crystal with liquid nitrogen, at the temperature of which sapphire is a relatively good thermal conductor. Presently, the source is operated at room temperature with cool-down from the ~ 600°C heat cleaning temperature facilitated by the use of an OFHC copper strap connecting the molybdenum transition bar to the vacuum chamber flange.

During activation, cesium is supplied from a commercial dispenser[41] that is mounted approximately 5 cm away from the crystal surface, as shown in Fig. 1. Ordinarily used for commercial gettering, the dispenser produces cesium vapor (almost totally free of contaminents) when it is resistively heated by the passage of current through it. As contrasted with the combination of a glass ampoule and a valved, externally-heated cesium vapor line (an approach used in several other laboratories[15,17,36]), the dispenser provides a simple method of cesiation in which the evolution of cesium can be precisely controlled as well as rapidly terminated.

Oxygen used during activation is provided by a conventional gas handling system employing the research grade (99.99% pure) oxygen. The leak rate into the polarized source chamber is accurately controlled by a Granville-Phillips variable leak valve,[43] bakeable to 450°C. It should be noted that for maximum protection against leaks to the atmosphere, all joints on the oxygen system are either welded or closed by means of stainless steel Conflat flanges.

The optical system employed in the studies comprises a 1-mW GaAlAs infrared diode laser[44] operating at 787 nm and a 1.6-mW HeNe laser used for alignment and activation, as well as standard circular polarizing elements, mirrors, lenses, and alignment apertures. With all of the optical elements in place, the attenuation losses result in approximate maximum powers of 0.34 mW and 0.45 mW incident on the crystal from the GaAlAs and HeNe lasers respectively. At 0.34 mW incident power, the GaAlAs 787 nm light is just

visible to the naked eye provided the room is darkened.

III. EXPERIMENTAL PROCEDURE

In order to prepare a crystal sample, a p-type <100> GaAs wafer, 0.325 mm thick, purchased from Laser Diode Laboratories in a 25 cm^2 format, is cleaved to form pieces, each measuring 0.7 cm x 1.0 cm. The piece to be used is then chemically etched to remove all carbon traces from its surfaces. Contained in a Pyrex beaker, the etching solution consists of a mixture of H_2SO_4 (98%), H_2O_2 (30%), and distilled water in an 8:1:1 ratio by volume.

The crystal sample is supported in the beaker by a glass holder and is exposed to ultrasound for approximately 10 minutes, at the end of which time the acid is flushed off the crystal with distilled water in a sequence of 5 ultrasound rinsing baths, each lasting 8 minutes. At no time during the etching and rising process is the sample exposed to air. At the conclusion of the final rinse, the sample is removed from its holder with a pair of clean stainless tweezers and quickly inserted into the mount shown in Fig. 2. The flange to which the crystal assembly is attached is bolted into place, resulting in the configuration shown in Fig. 1. Typically, the crystal is under vacuum at a pressure of $< 5 \times 10^{-6}$ Torr within 40 minutes of its removal from the beaker.

Following a preliminary helium leak check, the source chamber is wrapped with heater tapes and insulation, and a bakeout of the system is begun. The bakeout is maintained at 250°C for 2 to 4 days, depending upon how long the vacuum chamber was exposed to air prior to the installation of the crystal. Upon completion of the bakeout, the source chamber is pumped for an additional day at room temperature before crystal studies are begun.

Once the vacuum falls below 10^{-9} Torr, crystal heat-cleaning can be started. First, however, the cesium dispenser is outgassed by resistive heating at currents of 3.0 A and 4.5 A for periods of 10 minutes and 3 minutes respectively. According to the manufacturer,[45] at these levels CO evolution, which is very harmful to the crystal, is below 0.1 Torr ℓ s^{-1}.

Crystal heat-cleaning is accomplished by passage of a current directly through the crystal. Although either ac or dc may be used, there is some evidence that the former may provide a slightly more uniform temperature across the crystal surface and thereby yield better performance characteristics if a large area is used for photoemission. During the cleaning process, the chamber pressure and the crystal temperature (measured by the chromel-alumel thermocouple) are monitored continuously on a strip-chart recorder. The heater current is ramped up slowly to ensure that the chamber pressure never rises above 7×10^{-9} Torr. Typically, the current is increased in steps of 0.25 A every 3 or 4 minutes until the crystal reaches a temperature of ~ 630°C. At this temperature the equilibrium current is between 2.5 and 3.0 A, and the crystal sample, now dark red in appearance, is characterized by a resistance of approximately 3 Ω.

The crystal is maintained at full heating current for at least 20 minutes during which time the surface is frequently inspected for signs of roughness, an indication that arsenic evaporation might have begun.[46] Arsenic depletion, which severely degrades the photoemission properties, is also accompanied by a jump in the chamber pressure and can be observed on the strip chart recording. If any sign of incipient local evaporation is detected, the heating current is immediately reduced.

The heat treatment is completed by a slow reduction of the heating current to zero. Cooldown to 50°C, the highest temperature at which cesium

has been successfully applied during activation, typically, requires about 15 minutes. Crystals that have the best ultimate performance characteristics are those that achieve the greatest uniformity in color temperature and reach at least 630°C.

Once the crystal heat cleaning is completed and a crystal temperature of < 50°C, achieved, the activation process is started as illustrated graphically in Fig. 3. The source chamber pressure at this point is usually < 2×10^{-10} Torr. At the outset of activation, a current of 4.5 A is passed through the cesium dispenser, and the photocurrent is monitored[47] while the crystal is illuminated by white light from a projection-lamp operated at 35 W.[48] Typically, within 10 minutes a rapidly rising photocurrent is observed at the nanoampere level.[49] As can be seen from Fig. 3, the current reaches several hundred nanoamperes by the time 15 more minutes have elapsed. At this point, a HeNe laser is substituted for the white light source, bringing the wavelength of the incident light closer to that of the near ir required for producing polarized electrons, while still providing an easily visible illumination spot on the crystal surface. The former allows reasonable optimization of the ir quantum yield during the balance of the activation procedure, and the latter allows different regions of the crystal surfae to be probed with ease.

Cesiation is continued in the presence of HeNe illumination until a peak in the photocurrent is reached, typically at ~ 1 μA for ~ 0.4 mW of incident light, as shown in Fig. 3. The photocurrent is allowed to pass its peak and drop by 10 - 20%, at which point the cesiator current is turned off and oxygen is allowed to enter the system. Ordinarily, the oxygen leak rate is adjusted until the chamber pressure reaches ~ 2×10^{-9} Torr, although some activations have been carried out at oxygen partial pressures as high as 1×10^{-8} Torr without appreciable differences in ultimate performance. Under the application

of oxygen, the photocurrent begins to rise and reaches a second peak that is higher than the first cesium peak. As in the case of cesiation, the photocurrent is allowed to pass its peak and drop by 10 - 20% before the oxygen supply is turned off. Despite the fact that the oxygen is admitted to the source chamber at a port some distance away from the crystal and is not directed toward the crystal surface, the response time of the photocurrent and chamber pressure to the removal of oxygen is still very rapid (of the order of seconds), reflecting the good oxygen pumping qualities of ion pumps.

The alternation between cesiation and oxygenation is continued for a number of cycles, as illustrated in Fig. 3, until the differences between successive photocurrent peaks become small. At this point the activation process is terminated, and the GaAlAs circularly polarized ir laser light is substituted for that of the HeNe laser in order to produce polarized electron photoemission. (The peak to valley appearance of the photocurrent shown in Fig. 3 leads to the use of the terminology "yo-yo method" to describe the activation process in which the cesium and oxygen are applied sequentially.) It should be noted that in most of our work, oxygen was used to provide the final surface layer, rather than cesium, as is the practice in other laboratories.

IV. OPERATING CHARACTERISTICS

With the use of the operating procedures described in the previous section, the CCNY source has produced quantum yields, as high as 11% for HeNe (623.8 nm) illumination and 6% for GaAlAs (787 nm) illumination. The ratio of these yields appears to be consistent with observations made elsewhere.[30,32] In the absence of any additional cesium deposition following the termination of the activation procedure, the typical e-folding lifetime for the crystal is 12 h, although for several samples lifetimes as short as 4 h were observed. The dramatic difference in lifetime appears to be related variations in the quality of the crystal samples, since handling and operating procedures were the same in all cases. All lifetime studies were carried out for constant dc emission at typical photoelectron intensities of ~ 10 μA.

Under the influence of low level continuous cesiation, the crystal lifetime changes considerably, as indicated by the study illustrated in Fig. 4. In this study, the cesium dispenser is turned on and operated at a low heating current of 3.2 A after the final oxygen layer has been applied in the activation process. The photoemission current, I_e, grows essentially monotomically for approximately 80 h, at the end of which time it peaks and begins to fall. The rapid rise of I_e at a clock time of 93 h, coincident with the cessation of cesiation, indicates that the earlier fall is symptomatic of over cesiation. Indeed, this conclusion is borne out by the decrease in I_e at a clock time of 96 h, initiated by the resumption of cesiation. The rise and fall of I_e, coincident respectively with elimination and resumption of cesiation is again evident in the time period 115-118 h. At 140 h, when the cesium is turned off permanently, I_e increases rapidly and then finally falls monotonically, indicating in this last stage the absence of sufficient cesium.

When cesiation is adjusted properly, however, the lifetime of the crystal appears to be essentially without limit.

The role played by cesium in the constant cesiation mode is somewhat uncertain. It may be needed to replenish cesium that migrates off the crystal surface, or it may be needed to balance the deposition of additional oxygen that slowly outgasses from the chamber walls. It may also simply act as a getter for contaminants, such as CO, that also out outgas from the chamber walls. However, this last hypothesis is at variance with the observation that the beneficial effects of the low-level cesiation are largely mitigated when the crystal is not within line-of-sight of the dispenser.

Conventional wisdom holds that GaAs electron sources must operate under vacuum conditions in which pressures are maintained on the 10^{-10} Torr scale. For the activation and photocurrent studies shown in Figs. 3 and 4, these conditions indeed were met, as indicated by the respective pressure curves plotted in the figures. Whether these stringent vacuum requirements still need to be met under the condition of constant cesiation, however, demands exploration. Fig. 5 illustrates the response of the crystal when the ion pump in the source chamber is turned off and the ambient pressure is allowed to rise to > 10^{-7} Torr. As can be seen, the photocurrent remains essentially constant for pressures as high as 5×10^{-7} Torr. As might be expected, the behavior of the photocurrent is critically dependent on the level of cesiation.

Further pressure studies are shown in Fig. 6, in which instabilities in the photocurrent become apparent only after the chamber pressure rises above 5×10^{-6} Torr. The curves in Fig. 6 indicate the need for an increasing amount of cesium as the pressure increases, a result that is consistent with the oxygen-balance hypothesis mentioned earlier. From a comparison of the HeNe curve and the isolated GaAlAs crosses in Fig. 6, it can also be seen that the

photocurrent behavior for HeNe illumination is mimicked by that for GaAlAs illumination: the ratio of the quantum yields for each illumination remains essentially constant over the wide range of pressures displayed. (It should be noted that for the data shown in Fig. 6, the GaAlAs incident power is not known absolutely; however, it is substantially below the maximum 1 mW available.)

The pressure studies discussed thus far for operation under constant cesiation were all carried out with the pressure of the source initially at $\sim 2\times10^{-10}$ following bakeout. Since the effects of higher base pressures are clearly important for determining the ultimate utility of the constant cesiation method, additional investigations were made in which the source chamber was pumped down from atmosphere to a base pressure of only $\sim 2.5\times10^{-9}$ Torr. The activation and long-term performance of the crystal under these less than favorable conditions are illustrated in Fig. 7. As can be seen, the behavior of the photocurrent is not inconsistent with that found for the more traditional, low base-pressure conditions.

During the source studies a quadrupole mass analyzer[50] was used to monitor the constituent gases in the system at various times during the source studies. Although the analyzer was approximately one meter away from the source and connected to it through a vacuum pipe 3.5 cm in diameter, thereby making absolute partial pressure readings unreliable, the relative partial pressures measured for the residual gas still have some validity. Mass analyzer measurements taken for a baked system invariably showed that mass 2 (H_2) and mass 28 (CO and N_2) overwhelmingly dominated the system, with the former approximately 2 times the latter. These results are consistent with standard observations made for a clean, baked stainless steel system, for which it is known that H_2 and CO dominate the outgassing.

Recently, in conjunction with our electron-hydrogen collision work, we have been able to make preliminary measurements of the electron polarization for the CCNY GaAs source. By referencing ionization asymmetry measurements to values obtained in earlier studies,[31] and from our knowledge of the polarization of the hydrogen beam used in our present studies, we obtained a polarization of 0.35 for the GaAs photoelectron beam. We wish to stress that this value is preliminary and that we will carry out more complete measurements in the future.

V. CONCLUSIONS

Based upon our operating methods and our measurements we arrive at the following primary conclusions for GaAs photoemission sources:

1. Direct heating of the crystal using the clamping arrangement shown in Fig. 2 provides a simple method for heat cleaning in which uniform temperatures are achieved across the crystal surface and in which the crystal is the hottest object in the vacuum system.
2. The yo-yo activation method provides an easy, reproducible means of preparing negative electron affinity surfaces with high quantum yields.
3. Although requiring more time than the simultaneously cesium-oxygen activation method and producing slightly lower initial quantum yields, the yo-yo approach, using oxygen as the final layer with subsequent low-level continuous cesiation, results in extremely stable crystal performance with virtually infinite lifetime and final quantum yields comparable to those obtained with the simultaneous activation method.
4. With the use of the operating procedures described in Section III, GaAs photoemission can be achieved under vacuum conditions often considered

to be incomparable with stable, high-yield source performance.

In the course of our studies we have also made the following observations:

1. In the absence of continuous cesiation, where the quantum yield steadily decreases with time, the photocurrent, I_e, can be restored to its original value solely by the application of cesium, provided the system pressure is $\leq 10^{-9}$ Torr. This procedure can be used many times, but ultimately heat cleaning becomes necessary to fully recapture the initial value of I_e.
2. In the absence of continuous cesiation, the e-folding lifetime for GaAlAs illumination is approximately 20% shorter than that for HeNe illumination.
3. Should the vacuum system require backfilling to atmospheric pressure, the use of dry nitrogen in combination with prior cesium deposition on the crystal surface preserves the crystal for future use.
4. If the crystal is activated at ~ 4×10^{-8} Torr in an unbaked system, the quantum yield is reduced by about a factor of 10 and continuous cesiation is required for any useful performance.

As we stated at the outset of this paper, our studies are by no means complete. For example, we have not yet studied the polarization of the photoelectrons in much detail, nor have we determined the energy spread of the extracted beam. We will investigate both of these properties in the near future, the former with the use of a spherical mini-Mott polarimeter[51] and the latter with a hemispherical energy analyzer.[52] We will also investigate the operation of the source with the crystal cooled to liquid nitrogen temperature as well as with the surface prepared for positive electron affinity. In spite of the incomplete nature of our work, however, we hope that the information

reported in this paper will be of significant assistance to users of GaAs sources.

ACKNOWLEDGMENTS

We wish to express our appreciation to Mr. Gerard Cannella and Mr. Sol Forst as well as other members of the CCNY Machine Shop, who ably assisted in fabricating and modifying components of the apparatus often with very short notice. We also wish to thank Mr. Gordon Cates and Prof. Reiner Schaefer of Yale, Dr. Robert Celotta and Dr. Daniel Pierce of NBS, and Dr. Charles Sinclair of SLAC for many useful discussions. Finally we wish to acknowledge the financial support of the U.S. National Science Foundation (Grant No. PHY83-02868), the City University of New York (PSC-CUNY Award No. RF665279), the U.K. SERC, the French CNRS, and the NATO Division of Scientific Affairs.

REFERENCES

(a) Present address: Department of Physics, St. Patricks College, Maynooth, Co. Kildare, Ireland.

1. E. Garwin, D.T. Pierce, and H.C. Siegmann, Helv. Phys. Acta 47, 393 (1974). [A similar proposal was also made independently by G. Lampel and C. Weisbuch, in Solid State Commun. 16, 877 (1975).]
2. D.T. Pierce, F. Meier, and P. Zürcher, Phys. Lett. 51A, 465 (1975).
3. D.T. Pierce, F. Meier, and P. Zürcher, Appl. Lett. 26, 670 (1975).
4. J.J. Scheer and J. Van Laar, Solid State Commun. 3, 189 (1965).
5. R.L. Bell and W.E. Spicer, Proc. IEEE 58, 1788 (1970).
6. J. Kessler, Polarized Electrons (Springer Verlag, Berlin, 1976).
7. M.S. Lubell, in Atomic Physics 5, edited by R. Marrus, M. Prior, and H. Shugart (Plenumm, New York, 1977).
8. R.J. Celotta and D.T. Pierce, Adv. At. Mol. Phys. 16, 102 (1980).
9. P.F. Wainwright, M.J. Alguard, G. Baum, and M.S. Lubell, Rev. Sci. Instrum. 49, 571 (1978).
10. M.J. Alguard, J.E. Clendenin, R.D. Ehrlich, V.W. Hughes, J.S. Ladish, M.S. Lubell, K.P. Schüler, G. Baum, W. Raith, and R.H. Miller, Nucl. Instrum. Meth. 163, 29 (1979).
11. L.A. Hodge, F.B. Dunning, and G.K. Walters, Rev. Sci. Instrum. 50, 1 (1979).
12. E. Kisker, G. Baum, A.H. Mahan, W. Raith, and B. Reihl, Phys. Rev. B 18, 2256 (1978).
13. E. Garwin, F. Meier, D.T. Pierce, K. Sattler, and H.C. Siegmann, Nucl. Instrum. Meth. 120, 483 (1974).

14. D.T. Pierce, R.J. Celotta, G.-C. Wang, W.N. Unertl, A. Galejs, C.E. Kuyatt, and S.R. Mielczarek, Rev. Sci. Instrum. 51, 478 (1980).

15. P. Souder et al., in High-Energy Spin Physics - 1982 (Brookhaven National Laboratory), Proceedings of the Fifth International High Energy Spin Symposium, edited by G.M. Bunce (AIP, New York, 1983), p. 574.

16. E. Reichert, ibid, p. 580. (We include the source described in this reference under the generic heading of GaAs, although it actually uses GaAsP.)

17. A.B. McDonald, E.D. Earle, and E.T.H. Clifford, ibid, p. 586.

18. C.Y. Prescott et al., Phys. Lett. 77B, 347 (1978); 84B, 524 (1979).

19. G. Baum, M. Moede, W. Raith, and W. Schroder, J. Phys. B 18, 531 (1985).

20. K. Bartschat, G.F. Hanne, and A. Wolcke, Z. Phys. A 304, 89 (1982).

21. A. Vasilakis, M.S. Lubell, K. Rubin, F.C. Tang, J. Slevin, and M. Eminyan, Fourteenth International Conference on the Physics of Electronic and Atomic Collisions, Palo Alto, 1985), Abstracts of Contributed Papers, edited by M.J. Coggiola, D.L. Huestis and R.P. Saxon (ICPEAC XIV, SRI International, Palo Alto, 1985), p. 180.

22. J.M. McClelland, M.H. Kelley, and R.J. Celotta, Phys. Rev. Lett. 55, 689 (1985); M.H. Kelley, W.T. Rogers, R.J. Celotta, and S.R. Mielczarek, Phys. Rev. Lett. 51, 2191 (1983).

23. D.T. Pierce and R.J. Celotta, Adv. Electron.Electron Phys. 56, 219 (1981) and references therein; J. Vac. Sci. Techol. A 1, 1119 (1983) and references therein.

24. C.S. Feigerle, D.T. Pierce, A. Seiler, and R.J. Celotta, Appl. Phys. Lett. 44, 866 (1984).

25. H.-J. Drouhin, C. Hermann, and G. Lampel, Phys. Rev. B 31, 3859 (1985); 3872 (1985).

26. E.L. Garwin, R.E. Kirby, C.K. Sinclair, and A. Roder, Vacuum 31, 553 (1981).

27. P. Zorabedian, SLAC-Report 248 (Stanford Linear Accelerator Center, Stanford, California, 1982).

28. S.F. Alvarado, F. Ciccacci, S. Valeri, M. Campagna, R. Feder, and H. Pleyer, Z. Phys. B 44, 259 (1981).

29. C.K. Sinclair and R.H. Miller, IEEE Trans. Nucl. Sci. NS-28, 2649 (1981).

30. C.K. Sinclair, J. Phys. (Paris) 46, C2-669 (1985).

31. G.D. Fletcher, M.J. Alguard, T.J. Gay, V.W. Hughes, P.F. Wainwright, M.S. Lubell, and W. Raith, Phys. Rev. A 31, 2854 (1985).

32. D.T. Pierce and F. Meier, Phys. Rev. B 13, 5484 (1976).

33. W.E. Spicer, Phys. Rev. 112, 114 (1958).

34. C.K. Sinclair of SLAC in private communications has reported substantially improved performance with the use of NF_3.

35. One of us (MSL), in collaboration with researchers from MIT, Syracuse University, and Yale University, has experimented with the use of NF, on the polarized electron source at the Bates Linear Accelerator Center. For the Bates installation, at least, the difference in crystal performance with the use of NF_3 and O_2 is somewhat ambiguous.

36. C.K. Sinclair, E.L. Garwin, R.H. Miller, and C.Y. Prescott, in High-Energy Spin Physics - 1982 (Brookhaven National Laboratory), Proceedings of the Fifth International Spin Symposium, edited by G. Bunce (AIP, New York, 1983), p. 424.

37. V/G model XX F150.

38. Varian model 916-0009.

39. Granville - Phillips model 271 controller with model 274-023 gauge head.

40. The feedthrough, VG model LMD 100, was modified to reduce the runout and

to eliminate all magnetic materials.

41. SAES Getters (Colorado Springs, CO) CS/NF/3.9/12 T14 + 14.

42. Potentially, the thermocouple can give a spuriously low temperature reading for the crystal as a whole, since thermal conductivity along the wire leads can reduce the temperature at the point where the thermocouple comes into contact with the crystal. In order to minimize this effect, small diameter (0.125 mm) bare leads were used. From a comparison with readings made with an infrared thermometer (Ircon series G), we believe that the thermocouple provides a reading accurate to within 20 °C.

43. Granville-Phillips model 203-022.

44. Mitsubishi model 4102, rated for 3 mW maximum power.

45. P. Della Porta, C. Emili, and S.J. Hellier, SAES Getters Technical Report TR 18. All specifications provided by the manufacturer assume that dispensers are not exposed to water or any cleaning solvents prior to use. In our case dispensers are stored in dessicators and are handled only with gloves and clean instruments free of hydrocarbons.

46. Note that for <100> GaAs, the maximum congruent evaporation temperature of Ga and As is 663°C, according to B. Goldstein, J. Szostak, and V.S. Ban, Surface Sci. 57, 733 (1976).

47. The photocurrent is monitored continuously by a molybdenum collector pin connected to an electrometer. Care is taken to ensure that the collector bias is high enough (from perveance considerations) on one hand, to capture all of the current, and low enough, on the other, to prevent crystal damage due to ion backstreaming. For currents up to 20 μA and for the geometry shown in Fig. 1, a collector-cathode bias voltage of 60 V suffices for 100% collection, provided the crystal

cathode is maintained at -30 V with respect to ground. If the crystal is grounded, however, a bias of - 500 V is required for complete collection. In either case the crystal performance characteristics (quantum yield and lifetime) are the same, implying that ion backstreaming does not pose a problem within these bias limits.

48. Sylvania/GTE 300 W model ELH.

49. For the geometry used, backgrounds due to the ion pump and ionization gauge are negligible at least the level of 0.1 nA. At the subnanoampere level, however, a background associated with high-current (> 4.5 A) operation of the cesium dispenser is visible. This background is believed to be produced by a stripping reaction that affects a small fraction of the cesium atoms as they emerge from the hot slit of the cesium dispenser. It can be observed as either a positive current at the crystal cathode or a negative current at the collector pin, thus suggesting that both electrons and Cs^+ ions emerge from the dispenser under normal operating conditions.

50. VG Supavac Quadrupole Residual Gas Analyzer.

51. L.G. Gray, M.W. Hart, F.B. Dunning, and G.K. Walters, Rev. Sci. Instrum. 55, 88 (1984).

52. C.E. Kuyatt and J.A. Simpson, Rev. Sci. Instrum. 38, 103 (1967).

FIGURE CAPTIONS

Fig. 1 Scale drawing of the source showing (1) GaAs crystal, (2) sapphire mounting block, (3) titanium sublimation pump port, (4) solenoidal electron spin-precessor, (5) beam pipe to interaction chamber, (6) electron beam, with horizontal arrows indicating transverse polarization, (7) electron transport optics, (8) 90° spherical bender, (9) in situ GaAlAs laser beam, (10) vacuum window, (11) activation HeNe laser beam, (12) cesium dispenser, (13) electron collector, (14) electrical feedthrough, (16) sublimation pump baffle (17) roughing line port, and (18) oxygen line port. Not shown is 150 ℓ/s conventional ion pump.

Fig. 2 (a) Top and side views of sapphire mounting block for GaAs crystal showing (1) milled slot for crystal, (2) channel for platinum thermometer (not used), and (3) machined step and hole for mechanical support. (b) Top and side views of clamp assembly showing (4) GaAs crystal and (5) tantalum clamps.

Fig. 3 "Yo-yo" crystal activation process showing the photoemission current I_e as a function of time and status of incident light, cesiator current I_{Cs}, and oxygen flow. Also shown as a function of time is the chamber pressure P. The dip in the photocurrent occuring at 35 min and its subsequent rise are related to changes in laser alignment.

Fig. 4 Photoemission current I_e and chamber pressure P of an activated crystal as functions of time and cesiation current I_{Cs}, during a 150-hour test. Note that during this "continuous" cesiation test, I_{Cs} was set at 3 A, as contrasted with a value of 4.5 A, typical of the crystal activation process illustrated in Fig. 6.

Fig. 5 Photoemission current I_e as a function of increasing ambient chamber pressure resulting from shut-down of chamber pumps. Note that the crystal was activated at a base pressure of $2x10^{-10}$ Torr. The correlation between I_e and the cesiator current I_{Cs} is clearly visible for the time period 20-45 h.

Fig. 6 Dependence of photoemission current I_e on cesiation current I_{Cs} and chamber pressure P spanning six orders of magnitude in P. The solid curve for I_e corresponds to HeNe illumination, while the crosses correspond to GaAlAs illumination, the latter used periodically as a check on proper operation. Note that the chamber base pressure was $< 5x10^{-10}$ at the start of activation.

Fig. 7 Photoemission current I_e as a function of time for activation at a base pressure of $\sim 2x10^{-9}$ Torr.

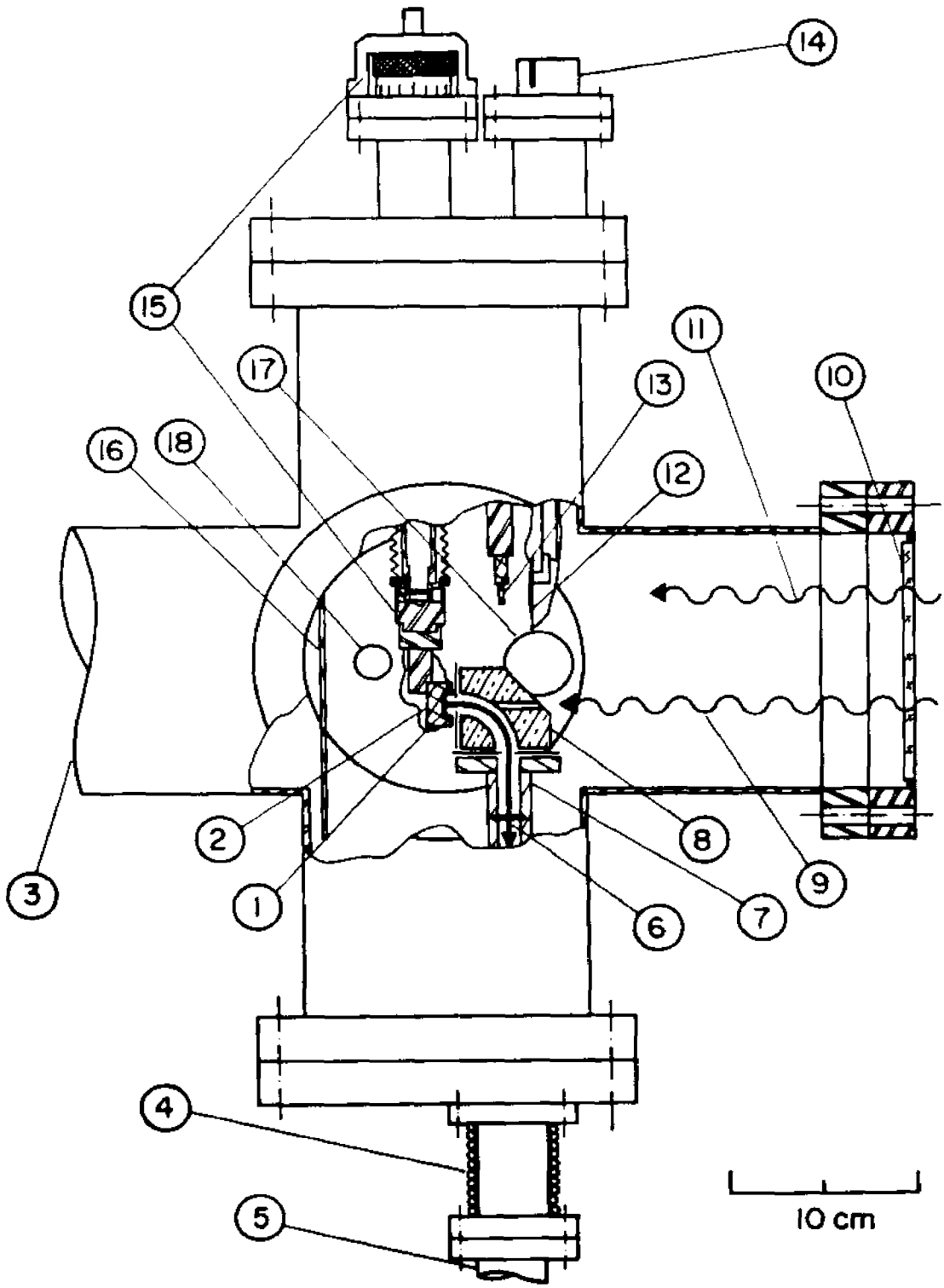

FIG. 1

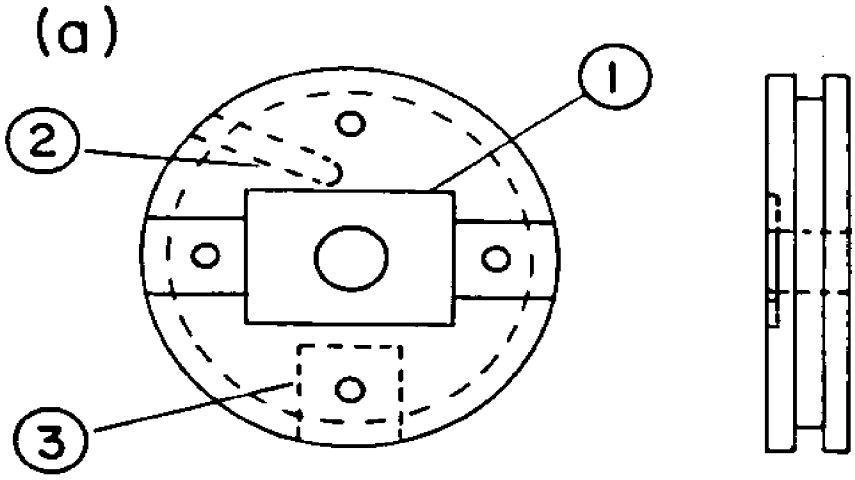

FIG. 2(a)

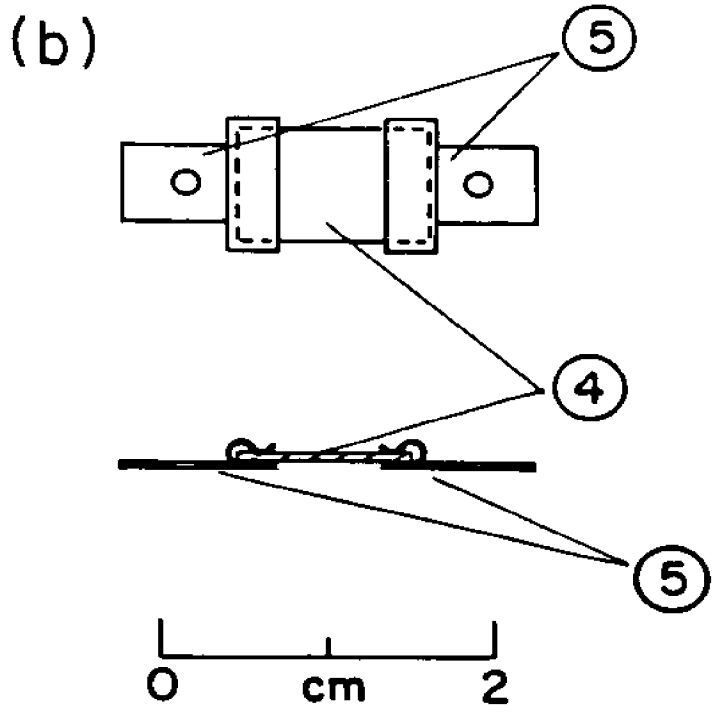

FIG. 2(b)

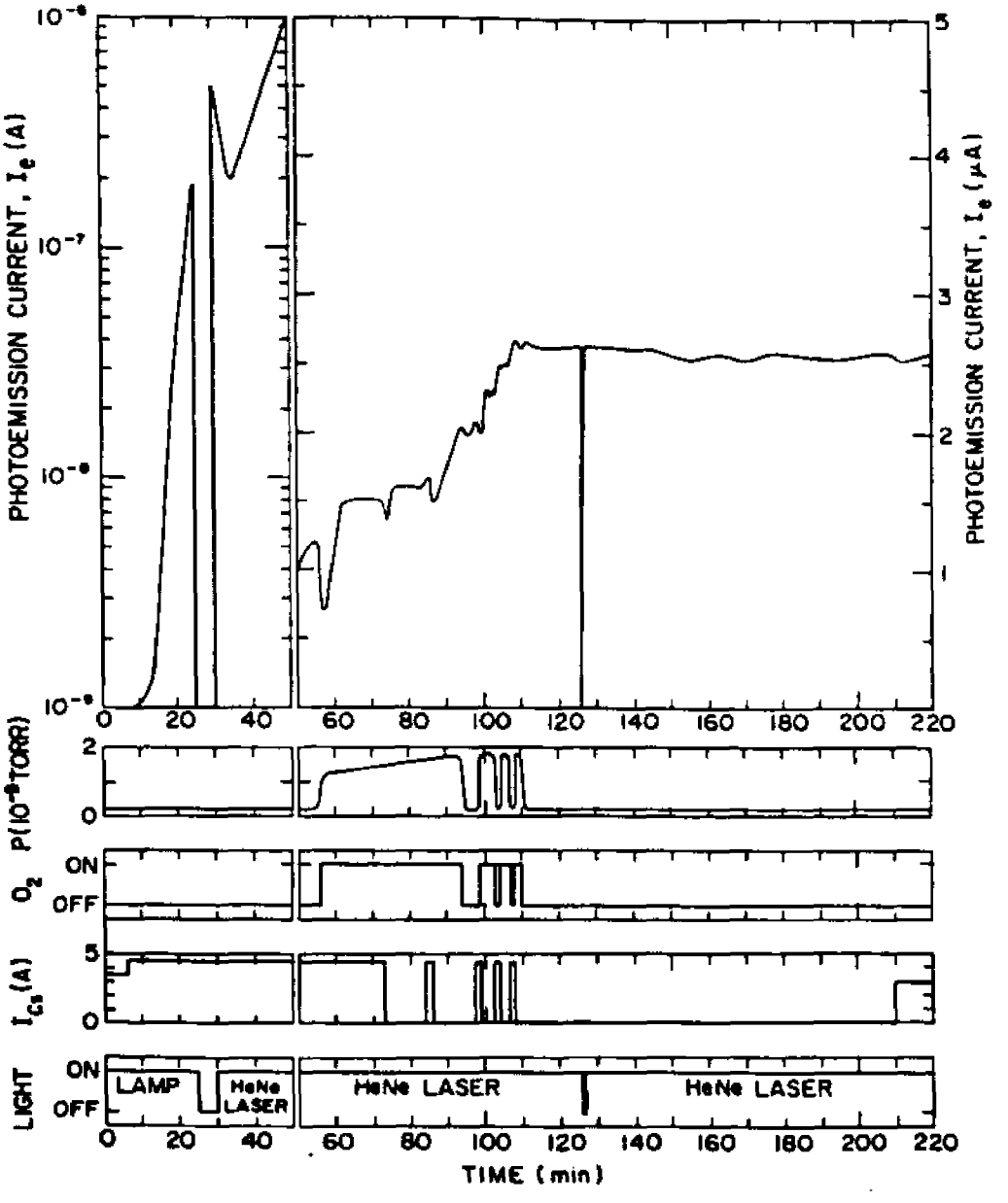
PHOTOEMISSION CURRENT, I_e (A)
PHOTOEMISSION CURRENT, I_e (μA)
P(10^{-6}TORR)
O_2
ON
OFF
I_{Cs} (A)
LIGHT
LAMP
HeNe LASER
HeNe LASER
HeNe LASER
TIME (min)

FIG. 3

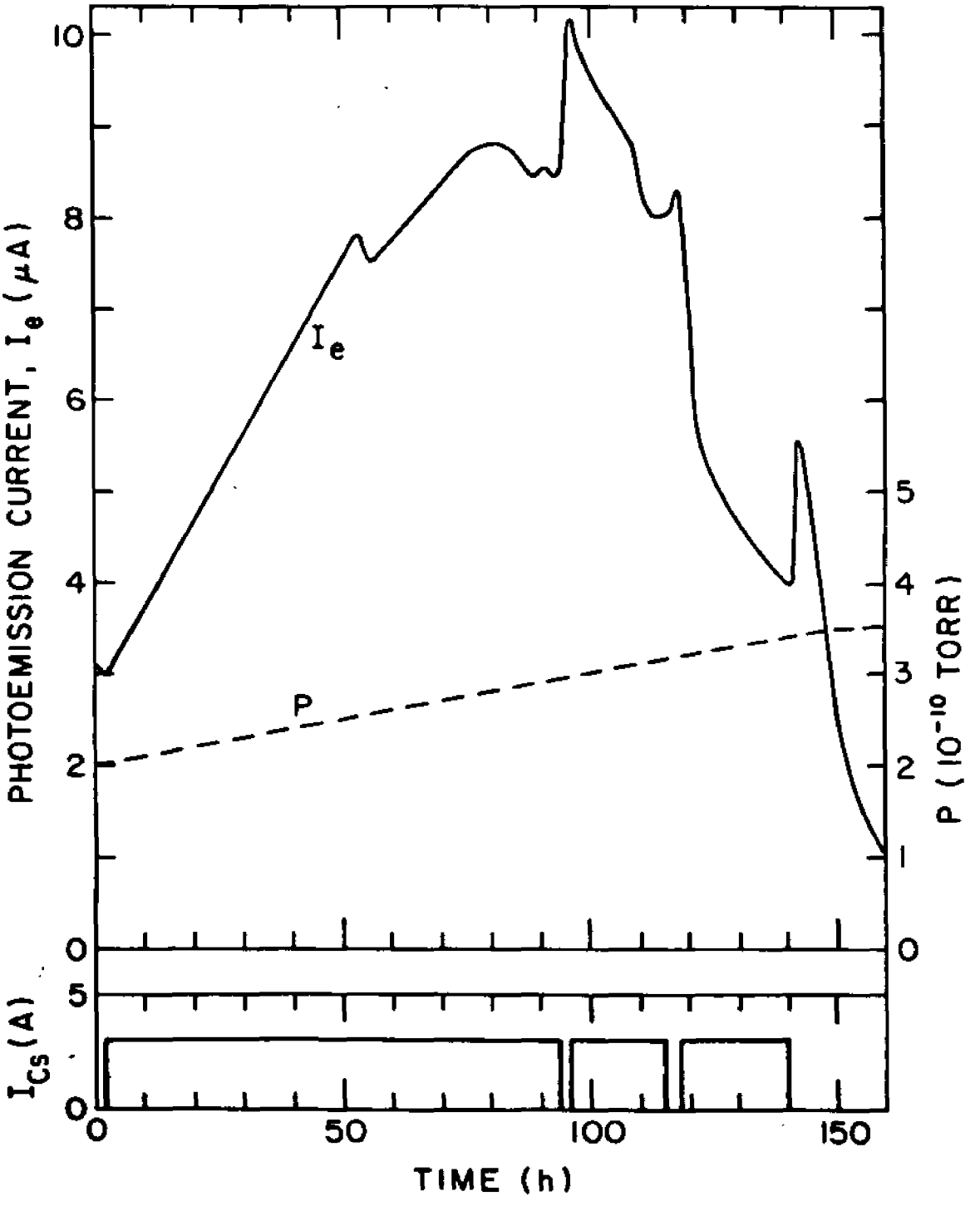
PHOTOEMISSION CURRENT, I_e (μA)
10
8
6
4
2
0
I_e
P
P (10^{-10} TORR)
5
4
3
2
1
0
I_{Cs} (A)
5
0
0
50
100
150
TIME (h)

FIG. 4

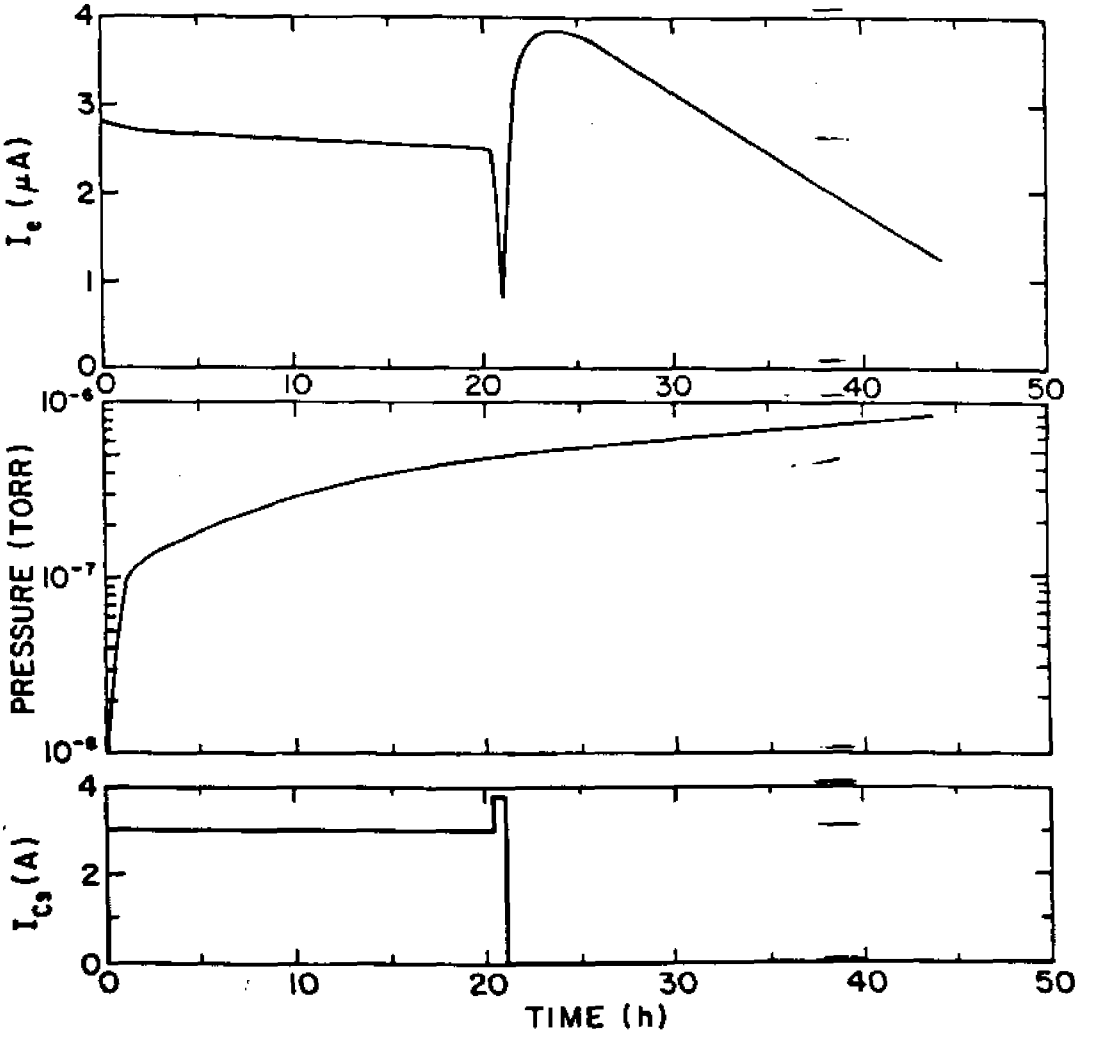
4
3
2
1
0
I_e (μA)
0
10
20
30
40
50
10^{-6}
10^{-7}
10^{-8}
PRESSURE (TORR)
4
2
0
I_{cs} (A)
0
10
20
30
40
50
TIME (h)

FIG. 5

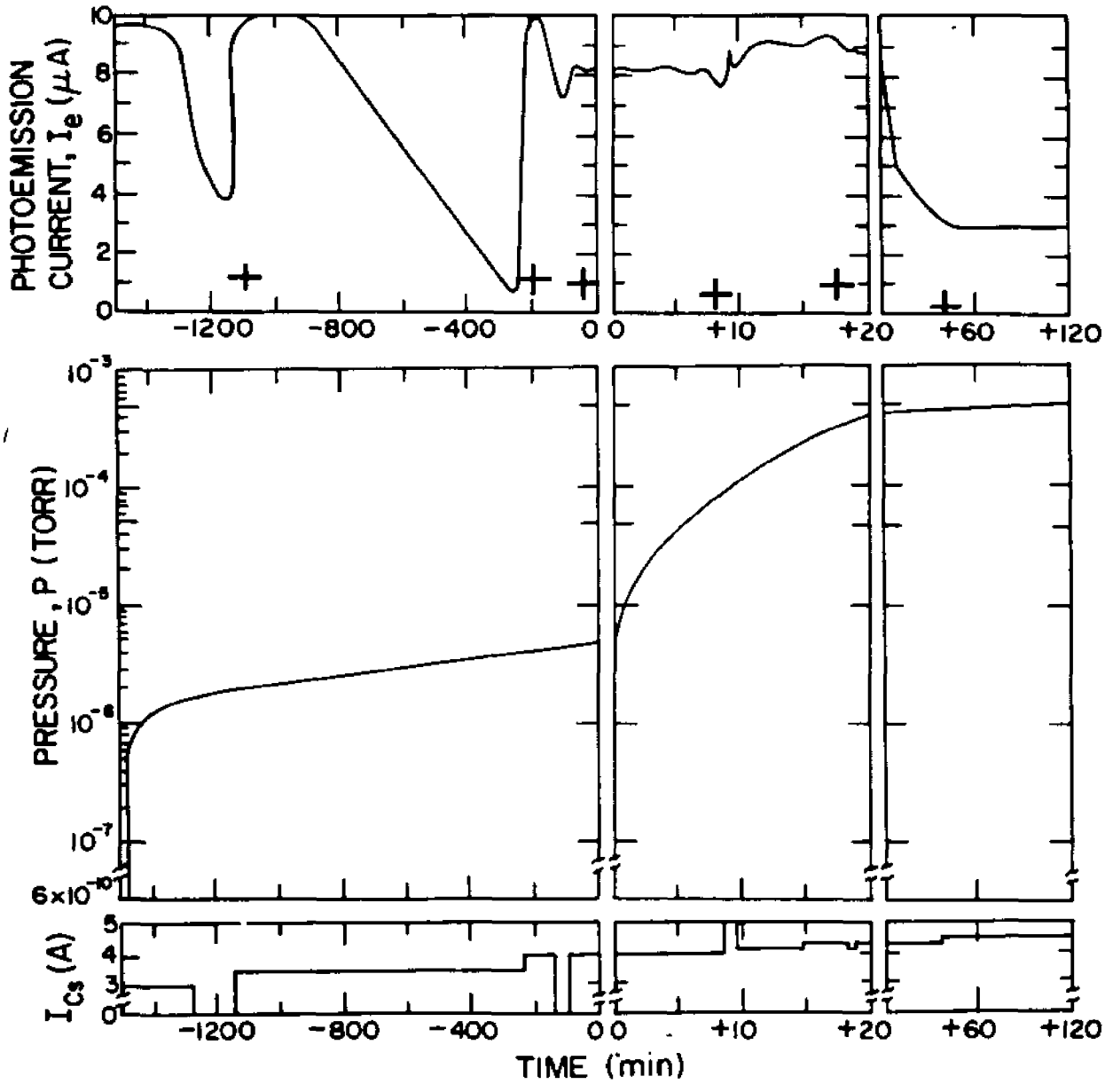
PHOTOEMISSION CURRENT, I_e (μA)
10
8
6
4
2
0
-1200
-800
-400
0
0
+10
+20
+60
+120
PRESSURE, P (TORR)
10^{-3}
10^{-4}
10^{-5}
10^{-6}
10^{-7}
6×10^{-10}
I_{Cs} (A)
5
4
3
0
TIME (min)

FGI. 6

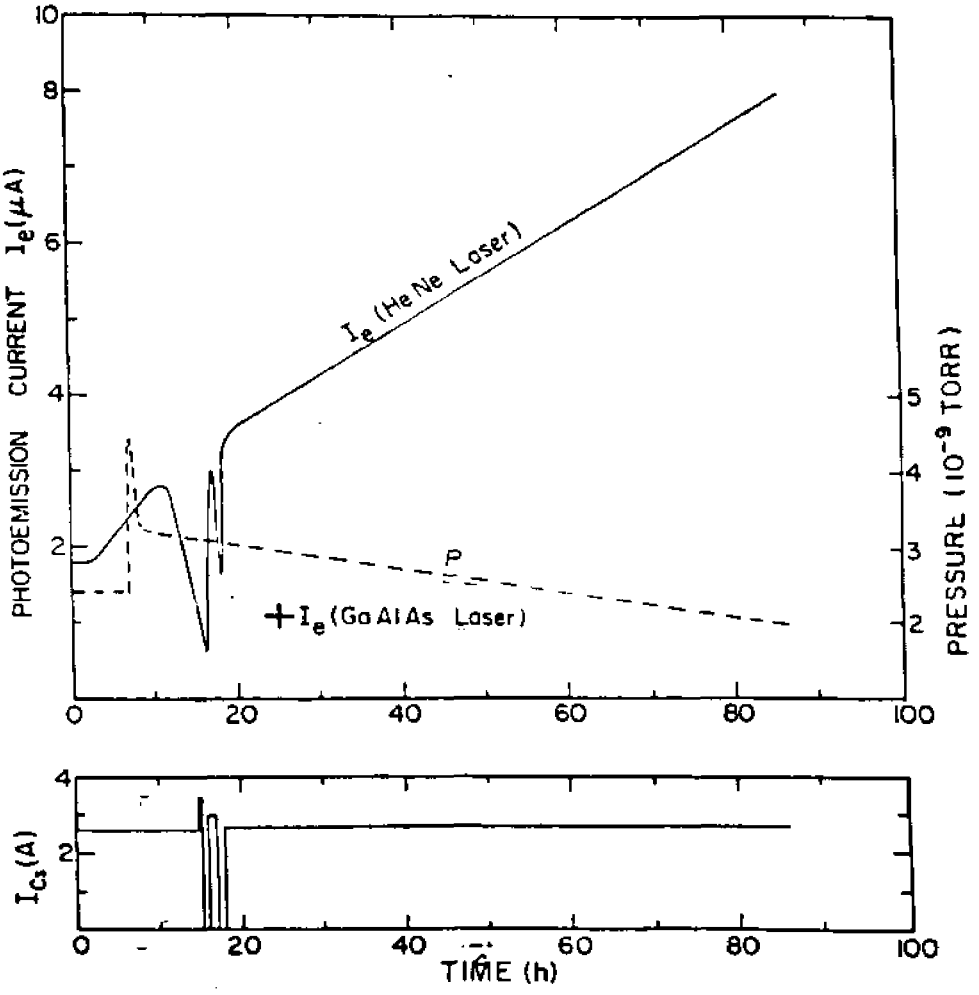
PHOTOEMISSION CURRENT $I_e(\mu A)$
PRESSURE (10^{-9} TORR)
I_e (He Ne Laser)
P
+I_e (Ga Al As Laser)
I_{Cs} (A)
TIME (h)

FIG. 7

APPENDIX B

A POLARIZED ATOMIC HYDROGEN BEAM

N. Chan, D. M. Crowe, M. S. Lubell, F. C. Tang, and A. Vasilakis
Department of Physics, City College of CUNY, New York, NY 10031

and

F. J. Mulligan and J. Slevin
Department of Experimental Physics, St. Patrick's College,
Maynooth, Co. Kildare, Ireland

ABSTRACT

We describe the design and operating characteristics of a simple polarized atomic hydrogen beam particularly suitable for applications to crossed beams experiments. In addition to experimental measurements, we present the results of detailed computer models, using Monte-Carlo ray tracing techniques, optical analogs, and phase-space methods, that not only provide us with a confirmation of our measurement, but also allow us to characterize the density, polarization, and atomic fraction of the beam at all points along its path. As a subsidiary result, we also present measurements of the relative and absolute efficiencies of the V/G Supavac mass analyzer for masses 1 and 2.

(To be submitted for publication)

I. INTRODUCTION

The uniquely simple structure of atomic hydrogen makes it an ideal system for the theoretical and experimental study of fundamental physics. Whether used as a probe of the weak interaction,[1] as a testing ground for quantum electrodynamics,[2] as a laboratory for metrology[3] and the determination of the values of fundamental constants,[4] or as a target for the study of basic atomic collisions,[5-8] the hydrogen atom has continued to play a central role in our attempt to understand physical phenomena at their most basic level. As a consequence, much effort has been devoted to the development of atomic hydrogen beams, both ground state and excited state, both polarized and unpolarized.[9-16] Since the late 1960's a large fraction of this effort has been directed toward the production of polarized proton, deuteron, and H^- beams for applications to nuclear and particle physics.[17] Recently, substantial attention has also been given to the development of extremely cold, intense neutral beams[14] for use as internal targets in high-energy storage rings, as polarized proton sources for accelerator injection, and as the central element in hydrogen masers for time and frequency standards. Many of the hydrogen beams described in the literature, whether polarized or unpolarized, are large, complex, and costly devices that are not particularly suitable for small scale laboratory physics. In this paper we describe the characteristics of a relatively compact and inexpensive polarized ground-state atomic hydrogen beam that we developed for crossed-beams studies of low-energy electron-hydrogen scattering. We present the results of detailed computer modeling of the beam, as well as measurements of operating parameters.

The principal properties of a polarized hydrogen beam comprise its dissociation fraction or purity, its useful density and flux, and its

polarization or state selection parameter. Such factors as its operational duty factor, its long and short-term stability, and its ease of operation are clearly important also. All of these characteristics depend upon the method used for producing the atoms, the technique employed for polarizing the atoms, and the specific details of the beam-line geometry.

Ground-state beams of atomic hydrogen are almost universally generated through the dissociation of hydrogen molecules by dc (Wood's),[18] rf, or microwave discharges,[9] or alternatively by thermal methods that employ high-temperature tungsten or tantalum ovens.[6,19] Regardless of the method chosen, each beam design must confront vacuum needs, choice of materials, heating or cooling requirements, and the geometry of skimmers and collimators, all of which have a direct bearing on the densities, fluxes, and dissociation fractions that will be achieved, in addition to the overall performance reliability of the beam. Often the choice of source technique will be dictated by the specific requirements of the experimental application.

In spite of their more specialized application, polarized hydrogen beams have been the subject of extensive development, although most of the attention they have received has been directed toward their use in polarized proton sources for high-energy and nuclear physics, as we have already noted. For these purposes, the spin of the proton is of paramount importance, and hence the neutral beams from which they derive must have a nuclear as well as an electronic polarization. The methods used to achieve the nuclear polarization vary depending upon whether metastable beams or ground state beams are the starting points. In virtually all cases, however, spin filters involving rf transitions are employed. By contrast, for our application, where the electron spin is of prime importance, we elected not to incorporate any rf spin-filtering, at the loss of some

polarization at low magnetic field, but with the consequent gain in simplicity and beam intensity.

In Section II of the paper we review the experimental details of the hydrogen beam line including the rf source, the hexapole state selector, the Stern-Gerlach polarimeter and the quadrupole beam analyzer. In Section III we discuss the operating principles of the beam and the techniques we employed to determine its salient characteristics of polarization, density, and dissociation function. In Section IV we explore three methods of computer modeling of the beam including Monte-Carlo ray tracing, an optical approach that treats the hexapole magnet as a thick lens, and a Cartesian phase space technique that yields approximate information for axially symmetric beams. Finally, in Section V we discuss the results of our measurements, summarize the properties of the beam, and briefly compare our beam with several other polarized hydrogen beams developed elsewhere.

II. EXPERIMENTAL DESIGN

A. Overview

The beam line comprises five stainless steel vacuum chambers separated from each other by collimating apertures or conductance limiting tubes, as shown in Fig. 1. The locations and critical dimensions of the components and apertures encountered by the hydrogen beam are shown schematically in Figs. 2a and 2b.

High-purity hydrogen, having entered the source through a heated palladium finger, is dissociated by an rf discharge in a water-cooled Pyrex tube.[9] The atoms and molecules effusing from the 1 mm diameter nozzle of the source are formed into a beam by a stainless steel skimmer, 1.4 mm in diameter, located 16.5 mm away and mounted on a stainless steel bulkhead. Slightly further downstream, 25.4 mm from the skimmer, the beam enters a pair of state-selecting hexapole magnets[20] each 152 mm long and each having a pole gap of 6.4 mm. The magnets, which transmit atoms in the $m_S = + {}^1/_2$ state and deflect those in the $m_S = - {}^1/_2$ state, as described in Section IIIC, are separated by a gap of 19 mm to facilitate pumping. A beam chopper, driven by a stepping motor that is capable of modulating the beam at a maximum frequency of 10 Hz with typical open and closed times of 50 ms each, is mounted in the gap between the two magnets. The position of the hexapole pair is chosen on the basis of a computer analysis that optimizes the density of the beam at the interaction region for a room-temperature v^2-Maxwellian velocity distribution, as described in Sections III and IV.

Upon leaving the downstream magnet, the beam first passes through a small gate valve that serves to isolate the source and magnet chambers from the rest of the beam line and then through a small conductance

limiting aperture and tube around which is wound a spin-guiding solenoid, as shown in Fig. 2b. The solenoid, together with two additional ones mounted inside the interaction chamber, serves to transport the atoms into the interaction region in such a manner that the spins are adiabatically rotated[6] and maintained either parallel or antiparallel to the direction of the beam by the 100 mG longitudinal magnetic field that is present at the center of the interaction region. A circular aperture 6.0 mm in diameter and located 38 mm upstream from the center of the interaction region serves to define the dimension of the beam.

At the exit of the interaction chamber, the beam again passes through a conductance limiting tube and aperture as shown in Fig. 2b. Magnetic guide fields (not shown in the figure) again serve to adiabatically rotate the atomic spins, this time into the transverse orientation, in preparation for polarization analysis by a Stern-Gerlach dipole magnet.[21] In front of the Stern-Gerlach polarimeter are a pair of slits each 0.7 mm wide by 9.5 mm high, that are externally movable while the system is under vacuum. For purposes of polarimetry, where scattering from the Stern-Gerlach pole tips poses a problem, the slits are inserted; for purposes of beam monitoring, where maximum signal strength is of paramount importance, however, the slits are removed. Since the dimension of the collimator associated with the Stern-Gerlach magnet is only of order 2.5 mm at a location where the beam diameter is approximately 10 mm, the vacuum chamber directly upstream of the entrance to the polarimeter effectively serves as a "dump" for at least half of the hydrogen beam.

The atoms and molecules that are accepted by the Stern-Gerlach unit enter the final beam line chamber which contains a Vacuum Generators Supavac quadrupole mass analyzer (QMA). Immediately in front of the QMA is a third movable slit 0.5 mm wide that is also externally accessible

while the system is under vacuum. As with those upstream, the QMA slit is inserted for polarizaton measurements and removed for normal beam monitoring. The QMA and its slit are both mounted in a vacuum pipe that is attached to a horizontal translator, thereby permitting the profile of the beam transmitted through the Stern-Gerlach magnet to be scanned as part of the polarimetry procedure, as described in Section III.

For each section of the beam line, vacuum pumps were chosen that met the specific experimental requirements of the particular section and also minimized the cost per unit pumping speed. The hydrogen source chamber is pumped by a high-speed oil diffusion pump[22] and the hexapole chamber, by a turbomolecular pump,[23] with each backed by a dedicated mechanical pump. Immediately beyond the hexapole chamber and mounted directly in the beam line is a low-conductance freon-cooled tube that protects sensitive downstream pumps and experimental components from any accidental upstream release of hydrocarbon contamination. (In this context, however, it should be noted that in more than four years of operation, there has not been a single instance of such a release.) For purposes of meeting ultra-high vacuum requirements and maintaining a hydrocarbon-free environment, the interaction chamber is pumped by an ion pump[24] designed for hydrogen use. An optically opaque "spiral staircase" baffle effectively eliminates charged particle backgrounds resulting from ion and electron backstreaming. The Stern-Gerlach is pumped by another ion pump,[25] also designed for hydrogen use, but in this case in an unbaffled configuration. At the QMA location, where greater precaution must be taken against ion backgrounds, a closed loop helium cryopump[26] is used.

B. RF Hydrogen Source

Fabricated in Scotland and essentially a duplicate of a source previously described[9] (a version of which is now available commercially),[27] the rf dissociator utilizes a water cooled Pyrex discharge tube operating in a coaxial cavity with 15 W of power at 35 MHz. With standard precautions taken to avoid ground loops in sensitive amplifiers throughout the experimental apparatus, the source, shown schematically in Fig. 3, produces minimal rf interference. The stability of the discharge and the degree of dissociation are critically dependent upon both the steady flow of bubble-free cooling water and the cleanliness of the Pyrex surface. The former condition is easily achieved if the cooling water is turned on several hours before the source is to be used. The latter condition is met through careful cleaning of the Pyrex tube (as described in Ref. 9) prior to installation of the source and through the use of a heated palladium leak to provide high-purity hydrogen during operation.

High purity hydrogen gas is provided by the gas handling system shown in Fig. 4. Pre-purified grade hydrogen at a supply pressure of 15-20 psig is allowed to enter a palladium finger. Under normal operating conditions, the finger is resistively heated to a temperature of about 150° C, an operating point that produces a pressure of 400 mTorr in the 0.3 ℓ ballast cross piece shown in the figure. In order to preclude contamination of the palladium finger, care is taken to maintain the hydrogen supply line at a positive pressure with respect to atmosphere whether or not the source is in use.

C. Hexapole Magnet

The permanent hexapole magnet, a cross section drawing of which is shown in Fig. 5, consists of two identical units, each 152 cm long and

separated from each other by a gap of 19 mm. The design of the magnet is based upon that used in the first polarized electron source installed at the Stanford Linear Accelerator Center[20] and produces a pole-tip field strength $H(R_M)$ of 0.79 T with a pole gap $2R_M$ of 6.4 mm. An alternate approach that achieves similar operating characteristics, still with permanent magnet construction, involves the use of samarium-cobalt elements that serve as integral drivers and pole tips.[28,29]

D. Interaction Region

The crossed beams interaction region contains many components that are specific to the spin-tagged electron-hydrogen collisions studies being carried out and are not germane to this paper. The only elements that are pertinent to the hydrogen beam are the apertures and spin-guiding field coils shown in Fig. 2b, the dimensions and operating conditions of which are given in the figure. At the interaction region center, the influence of the earth's magnetic field is maintained below 10 mG with the use of a single layer of μ-metal shielding 1.5 mm thick. The shielding, in the shape of a capped cylinder, located just inside the vacuum chamber walls, is equipped with coils that permit the μ-metal to be degaussed in situ, a procedure that obviates the need for any annealing of the material. When the guide fields are on, the magnetic field at the center of the interaction chamber is approximately 100 mG oriented either parallel or antiparallel to the direction of the hydrogen beam line.

E. Stern-Gerlach Magnet

The Stern-Gerlach magnet,[21] employed for polarimetry measurements, consists of an electromagnetic driver located outside the vacuum system and low-carbon magnet iron pole faces placed inside the vacuum system. Of

a standard "two wire" geometry, the pole faces, 101.6 mm long with a minimum horizontal gap of 3.18 mm, are shown in cross section in Fig. 6, producing a field to gradient ratio of - 6 mm. The entrance to the magnet is masked by a collimating aperture 2.5 mm in height in combination with a single knife edge that extends horizontally into the gap a distance of 0.7 mm from the leading edge of the convex pole tip. Such a configuration on one hand provides reasonable throughput during ordinary beam intensity monitoring and on the other hand, in conjunction with a pair of movable upstream slits, minimizes pole tip scattering during beam polarization measurements. In the latter application, the magnet is energized with a maximum current of 5.5 A, which produces a pole tip field strength H( ) of approximately 0.33 T. For beam intensity monitoring, the energizing dc current is turned off, the magnet is degaussed, and the pair of upstream slits, 0.5 mm wide by 9.5 mm high, are removed from the beam path.

F. Quadrupole Mass Analyzer

The quadrupole mass analyzer (QMA) is a Vacuum Generators Supavac model that uses a Faraday cup and a high-gain amplifier for ion detection. During polarization measurements, the analyzer entrance is masked by a slit 0.5 mm wide. With the slit removed, as is the case during beam intensity monitoring, the analyzer presents a circular entrance aperture 6.4 mm in diameter, a dimension that effectively characterizes the entrance height when the slit is in place.

The analyzer, having a maximum sensitivity (defined by a signal to noise ratio of 2:1) of 2×10^{-11} mbar, produces typical readings of 3.0×10^{-10} mbar and 1.3×10^{-10} mbar respectively for H_1 and H_2 detection when the rf source is operating under standard conditions and the beam line slits are removed for intensity monitoring. When the rf power is turned off, the H_1

signal drops to 3×10^{-11} mbar and the H_2 signal rises to 4.3×10^{-10} mbar. In the polarization measurement mode, with the slits inserted and the lateral position of the QMA adjusted for maximum signal, the typical H_1 and H_2 readings for rf power on are 4×10^{-11} mbar and 5×10^{-11} mbar respectively. With the rf power turned off the corresponding readings are 1×10^{-11} mbar and 1.3×10^{-10} mbar. The signals measured by the QMA during the horizontal translational scans that are integral to the polarimetry method are discussed in greater detail in Section IV.

III. OPERATING PRINCIPLES AND EXPERIMENTAL METHODS

A. Basic Concepts

The principles of state-selected neutral atom beams are well understood and have been discussed a number of times.[30] When restricted to the case of electronic state selection, these principles can be understood with ease and require only a brief account of the behavior of an atom in an inhomogeneous magnetic field. As the Breit-Rabi diagram of Fig. 7 demonstrates for ground state atomic hydrogen, the hyperfine substates, characterized at low magnetic field by the total angular momentum quantum numbers F and m, are split and regrouped at high magnetic field according to the electronic and nuclear spin quantum numbers m_J and m_I. At fields sufficiently high to decouple electron and nuclear spins (but not high enough to decouple spin and orbital angular momentum), the magnetic energy of an atom, ΔW, in an external magnetic field $\vec{H}$ is given by[31]

$$\Delta W = \mu_B H m_J g_J + A m_I m_J, \tag{1}$$

where μ_B is the Bohr magneton, g_J is the Lande g-factor, and A is the hyperfine contact energy, with the nuclear multipole interactions with the external field being neglected. The atom then has an effective magnetic moment μ_{eff} given by

$$\mu_{eff} = - \mu_B m_J g_J. \tag{2}$$

In a non-uniform magnetic field, a ground state hydrogen atom will thus experience a force $\vec{F}$ given by

$$\vec{F} = -\vec{\nabla}(\Delta W) = \mp \mu_B \vec{\nabla} H, \tag{3}$$

for $m_J = m_S = \pm 1/2$, where g_J is taken to be equal to 2. From Eq. (2) it is obvious that in principle any inhomogeneous magnetic field will create a spatial separation between atoms in the $m_S = + 1/2$ state and those in the $m_S = - 1/2$ state. In practice, two field geometries afford the greatest advantage. For polarized beam generation, hexapole magnets provide the geometry of choice, while for polarimetry applications, both hexapole and two-wire dipole fields can be used with success.

In the former instance, the hexapole field, which has a radial dependence given by[30]

$$H(r) = \frac{r^2}{R_M^2} H(R_M) \tag{4}$$

with r the radial coordinate, $2R_M$ the pole gap, and $H(R_M)$ the pole tip field strength, causes the $m_S = + 1/2$ atoms to oscillate with elliptical trajectories about the beam axis and the $m_S = - 1/2$ atoms to be deflected out of the beam entirely. Thus for $m_S = + 1/2$ atoms, a hexapole state-selecting magnet preserves the cylindrical qualities of the entering beam; moreover, it acts as a lens for these atoms, albeit with chromatic aberration, as has been discussed in detail elsewhere.[30,32] For a given field strength, the length of the magnet, and its position relative to both the atom source and the downstream interaction point therefore can be chosen to optimize the atom density at the interaction point. In the case of the atomic hydrogen beam described in this paper, the field strength of the hexapole was actually chosen to be the highest that could be achieved with permanent Alnico magnetic drivers, the objective being generation of

maximum m_S = + 1/2 state selection. The pole gap dimension was then chosen together with the remaining parameters to maximize the atom density for a 6.0 mm beam diameter at the interaction point, in accordance with the computer projections described in Section IV.

By constrast with the upstream polarizer, the downstream Stern-Gerlach polarimeter was designed around a dipole geometry, an approach that permits detailed scanning of the beam profile. In addition, while the hexapole uses a permanent magnet design, which minimizes cost and space, the Stern-Gerlach polarimeter employs an electromagnet approach, which allows the device to be demagnetized, an essential condition for both beam intensity monitoring and centroid determination. In the polarimetry process, the latter is an integral step, as explained in Section III C.

Throughout the preceding description, the high-field approximation has been assumed for magnetic substates. While this condition may be met in the Stern-Gerlach magnet, given its narrow acceptance slit and its operating pole tip field strength, the assumption certainly needs further justification for the hexapole magnet. Moreover, an approach is required that relates the state selection achieved and measured at high fields to the electronic polarization that is applicable at the low fields characteristics of the interaction region.

For any field strength, H, the energy, ΔW, associated with a magnetic substate is found from the diagonalization of the energy matrix. In particular, for $^2S_{1/2}$ terms, which comprise the ground state hyperfine $^2S_{1/2}$ multiplet of hydrogen, the secular determinant is of second order, and ΔW can be shown to be[31]

$$\Delta W = -\frac{\delta W}{2(2I+1)} \pm \frac{\delta W}{2}\sqrt{1 + \frac{4m}{2I+1}\,x + x^2} \qquad (5)$$

for $m = +(I+{}^1/_2), +(I-{}^1/_2), \ldots, -(I-{}^1/_2), -(I+{}^1/_2)$, where I is the nuclear spin, $\delta W = (2I+1)A/2$ is the zero field hyperfine structure splitting between the

$F = I-{}^1/_2$ and $F = I+{}^1/_2$

and χ is a dimensionless field variable defined by

$$\chi \equiv g_J \mu_B H/\delta W, \tag{6}$$

the nuclear multipole interactions with the external field being neglected throughout. Now the effective magnetic moment of the atom must be defined through the relation

$$\mu_{eff} = -\frac{\partial(\Delta W)}{\partial H}. \tag{7}$$

For the maximum and minimum values of m; namely, $m = \pm(I+{}^1/_2)$, μ_{eff} is independent of χ and is given by

$$\mu_{eff}\,[m = \pm(I+{}^1/_2)] = \mp \frac{1}{2} g_J \mu_B. \tag{8}$$

For hydrogen, where $I={}^1/_2$ and $g_J = 2$, Eq. (8) reduces to

$$\mu_{eff}\,(m = \pm 1) = \mp \mu_B. \tag{9}$$

For other values of m, μ_{eff} depends upon χ in a complex fashion, as suggested by Fig. 8 which illustrates the behavior of μ_{eff} as a function of H or χ for the ground state of atomic hydrogen. As can be seen from the

figure, the limiting values of μ_{eff} for m = 0 are given by $\mu_{eff} = 0$ for $\chi = 0$ and $\mu_{eff}\ (m_S = \pm 1/2) \rightarrow \pm\ \mu_B$ for $\chi \rightarrow \infty$.

Conventionally, the polarization $\vec{P}$ of a collection of electrons is defined[33] as the ensemble average of the expectation value of the Pauli spin operator $\vec{\sigma}$:

$$\vec{P} = \langle \vec{\sigma} \rangle. \tag{10}$$

By virtue of the relationships

$$\vec{\mu} = - g_e \mu_B \vec{S}/\hbar = - g_e \mu_B \vec{\sigma}/2, \tag{11}$$

where $\vec{S}$ is the spin operator and $g_e = 2$ is the electron g-factor, $\vec{P}$ can also be expressed as

$$\vec{P} = - \langle \vec{\mu}/\mu_B \rangle. \tag{12}$$

For an atomic beam which has undergone high-field state selection with $m_S = + 1/2$ substates <u>equally</u> sharing one population and all $m_S = - 1/2$ substates <u>equally</u> sharing another population, it is therefore reasonable to define a field-dependent quantity $f(\chi)$, conventionally called the hyperfine coupling function,[30] by applying the concepts embodied in Eq. (14) to the expression for μ_{eff} derived from Eqs. (5) and (7). Specifically, with $\vec{P}$ replaced by $f(\chi)$ and $\vec{\mu}$ replaced by μ_{eff}, we obtain the result

$$f(\chi) = \frac{1}{2I+1} \sum_{m=-I+\frac{1}{2}}^{I+\frac{1}{2}} (\mu_{eff}/\mu_B), \tag{13}$$

which has the limiting values of $f(0) = 1/(2I+1)$ and $f(\infty) = 1$. For hydrogen, Eq. (13) reduces to

$$f(\chi) = \frac{1}{2}\left[1 + \frac{\chi}{\sqrt{1+\chi^2}}\right], \tag{14}$$

a graphical display of which is shown in Fig. 9. If at high-field, a state selection parameter s is defined by

$$s \equiv \frac{N_+ - N_-}{N_+ + N_-}, \tag{15}$$

where N_+ and N_- are respectively the number of atoms in the $m_S = +1/2$ and $m_S = -1/2$ states, then the electronic polarization $P(\chi)$ is given by

$$P(\chi) = s\, f(\chi). \tag{16}$$

For the case in which the $m_S = \pm 1/2$ substates have <u>differing</u> populations <u>after</u> high-field state selection, $P(\chi)$ must be calculated from the weighted average of (μ_{eff}/μ_B) over all the substates, the statistical weight, of course determinent from the relative population of the respective substate in the usual fashion.

In carrying out the design of the beam and in determining its properties, we applied the principles developed in the foregoing paragraphs

in two significant ways. First, using Eq. (6) and the radial reductions of Eqs. (2) and (7), we developed the computer models described in Section IV to determine the behavior of the hydrogen beam as it traverses the hexapole and Stern-Gerlach dipole magnets, with particular attention paid to tests of the validity of the high-field approximation. Second, from the results of the computer modeling, we related the high-field Stern-Gerlach polarization measurements to the value of the low-field polarization applicable at the interaction region. These applications will become clearer in the descriptions of the succeding sections.

B. Polarization Determination

From the concepts set forth in the preceding section, it is obvious that a dipole magnet with a cross section and orientation shown in Fig. 6 will cause a beam of atoms that is traveling outward from the plane of the figure to be deflected to the right or to the left depending upon whether μ_{eff} is positive or negative respectively. In other words, atoms in the $m_S = + 1/2$ state will be deflected to the left while those in the $m_S = - 1/2$ state will be deflected to the right. With the magnet power turned off and the pole tips degaussed, atoms in either state will pass through the unit undeflected.

The high-field polarization of the beam at the Stern-Gerlach magnet is thus determined as follows. From appropriate readings of the QMA and with appropriate settings of the source rf power, the net mass-one signal, is measured as the QMA is scanned horizontally across the beam. Based upon the beam profile when the Stern-Gerlach field is set at zero, a centroid x_C is established, in terms of which a right-left asymmetry can be defined for all non-zero settings of the Stern-Gerlach field. The high-field polarization is then given by the high-field limit of this asymmetry as the

Stern-Gerlach field is steadily increased.

Fig. 10 provides a pictorial representation of the profile generated when a motorized translator under the control of an LSI 11/23 computer drives the QMA horizontally across the beam in steps of 0.125 mm. During acquisition of the polarization data, all three collimating slits are inserted into the horizontal position, as described in Section II.A. At each horizontal position, up to 9,000 samples are taken of the QMA output voltage, with the actual number entered as input information to the data acquisition program.

As illustrated in Fig. 10, the profile obtained with the rf source power on and the QMA tuned to mass one can be divided into four regions, two central ones on either side of the centroid containing signals related to both the beam and the molecular background, and two outer regions containing signals related to the molecular background alone. In all four regions, the background is found to vary linearly with position. Thus, in the central regions, the QMA signal can be characterized by three separate contributions -- first, a pedestal due to dissociative ionization of the molecular background by the QMA electron bombarder; second, a portion (not labeled in the figure) due to dissociative ionization of the molecular component of the beam; and third, the net mass-one signal, which is the quantity of interest. The analysis procedure begins with the determination of the first two contributions and concludes with the subtraction of these from the total signal to generate the net mass-one signal.

At the outset of the procedure, the boundaries x_L and x_R, between the central and outer regions on the left and right sides of the centroid respectively, are chosen by visual inspection. A standard regression analysis is then performed in the outer regions to determine the pedestal function $y^P(x)$, which enables the areal contributions of the pedestal, $A_L{}^P$

and A^P_R, to the left and right central regions to be calculated according to the prescriptions $A^P_L = (y_L{}^P + y_C{}^P)(x_C - x_L)/2$ and $A_R{}^P = (y_R{}^P + y_C{}^P)(x_R - x_C)/2$. It should be noted that the variance calculated by the linear regression from the reduced chi-square is used as the variance of each point of the profile in all subsequent treatment of the data.[34]

The determination of the areas $A_L{}^D$ and $A_R{}^D$, associated with contributions from molecules in the beam, requires the acquisition of three additional profiles corresponding to rf off with mass-one tuning $[(Q_1)^{off}]$, rf off with mass-two tuning $[(Q_2)^{off}]$, and rf on with mass-two tuning $[(Q_2)^{on}]$. In each case, the pedestal is subtracted from the total signal in accordance with the procedures described for the case of $[(Q_1)^{on}]$, thereby producing a net signal that is proportional to the molecular content of the beam for each case. As a consequence, it is easily seen that $A_L{}^D$ and $A_R{}^D$ are given by

$$A_{L,R}{}^D = \frac{A[(Q_2)^{on}]}{A[(Q_2)^{off}]} A_{L,R}[(Q_1)^{off}], \tag{17}$$

where $A[(Q_2)^{on,off}] = A_L[(Q_2)^{on,off}] + A_R[(Q_2)^{on,off}]$ and where all three profile areas are calculated from simple Riemann sums. Empirically it was found that $A_L{}^D$ and $A_R{}^D$ remained constant for at least a twelve-hour period while the source was operating. Thus the $(Q_1)^{off}$, $(Q_2)^{off}$, and $(Q_2)^{on}$ profiles were measured only once a day, and the values of $A_L{}^D$ and $A_R{}^D$ determined from them were applied to all $(Q_1)^{on}$ profiles measured that day.

Once $A_{L,R}{}^{P}$ and $A_{L,R}{}^{D}$ are determined, they are subtracted from the respective areas, A_L and A_R, corresponding to the total signals in the left and right central regions of the $(Q_1)^{on}$ profile. In this way the net areas, $A_{L,R}{}^{net}$, are obtained, in terms of which a right-left asymmetry, Δ_H, can be constructed according to the prescription

$$\Delta_H = \frac{A_R{}^{net} - A_L{}^{net}}{A_R{}^{net} + A_L{}^{net}} = \frac{(A_R - A_R{}^{P} - A_R{}^{D}) - (A_L - A_L{}^{P} - A_L{}^{D})}{(A_R - A_R{}^{P} - A_R{}^{D}) + (A_L - A_L{}^{P} - A_L{}^{D})}. \tag{18}$$

It should be noted that throughout this discussion it has been assumed that the Q_1 and Q_2 signals and hence all the areas used in Eq. (18) are related to QMA readings obtained with the hydrogen beam chopper fixed in the open position.

The validity of the foregoing analysis rests strongly on the proper identification of the profile centroids that correspond to the true beam center when the Stern-Gerlach field is set at zero. Unless the hexapole magnet is perfectly aligned, it is clear that the centroids of the $(Q_1)^{off}$ signal and the determination of the true centroid of the net $(Q_1)^{on}$ signal for zero field thus requires that x_C be varied until Δ_H is minimized. The value of x_C so obtained then serves as the centroid for all calculations of Δ_H corresponding to non-zero values of the Stern-Gerlach field.

With Δ_H determined for a number of field settings, a plot can then be made of Δ_H as a function of the Stern-Gerlach driving current. As the current increases and $M_S = \pm 1/2$ states are separated from each other further in space, Δ_H increases continuously until, under ideal conditions, the separation is complete, at which point Δ_H remains constant for all further increases in current. The saturation value $\Delta_H{}^{max}$ is then taken as the high-field polarization of the analyzed portion of the beam.

C. Density Determination

Information about the density of the hydrogen beam at the interaction region can be gleaned from several sources. Probably the least accurate determination, but by far the easiest one to make, results from the pressure increase, Δp, measured at the interaction chamber pump when the hydrogen beam chopper is opened and the beam is fully dumped in the interaction chamber. If the chamber is pumped with an effective speed S (ℓ/s), then the number of atoms of gas N entering the chamber per unit time is given by[35]

$$\frac{dN}{dt} = \frac{2S\ \Delta p}{kT}, \tag{19}$$

where T is the Kelvin temperature of the gas, k is Boltzmann's constant, and the factor of two reflects recombination of the atoms prior to entry into the pump. Now for a radius R_H characterizing the cylindrically symmetric, collimated beam at the interaction region, an average atom density $\bar{\rho}$ can be defined as

$$\bar{\rho} \equiv \frac{1}{\pi R_H^2} \int_0^{R_H} \rho(r)\ 2\pi r dr, \tag{20}$$

where $\rho(r)$ is the atom density of the beam in the interaction region at a radius r. It should be clear that $\bar{\rho}$ and dN/dt are related to each other by the expression

$$\bar{\rho} = \frac{f}{\pi R_H^2 \bar{v}}\ \frac{dN}{dt}, \tag{21}$$

where $\bar{v}$ is the average atom velocity in the interaction region, and f is the fraction of atoms in the beam falling within a radius R_H. From Eqs. (19) and (21) it then follows that $\bar{\rho}$ is given by

$$\bar{\rho} = \frac{2f\ S\ \Delta p}{\pi R_H^2 \bar{v} kT}. \tag{22}$$

It should be noted that $\bar{v}$ is not the customary velocity obtained from kinetic theory, since the hexapole magnet is a strongly chromatic lens. The only easy access to $\bar{v}$ is gained through computer modeling, as will be discussed in Section IV D. Of the other quantities in Eq. (22), all are known either by specification or measurement except for the fraction f which depends upon the shape of the beam profile at the interaction region. As with $\bar{v}$, the experimental determination of f cannot be made with ease, as a consequence of which the value must be calculated from the profiles generated by the computer models described in Section IV. With these caveats, the density $\bar{\rho}$ is thus determined experimentally from a measurement of Δp, in accordance with Eq. (22).

A second determination of $\bar{\rho}$ results from the computer models themselves. This approach, however, relies not only on the validity of the transport modeling, but also on the specification of the initial flux of the beam as it leaves the nozzle of the source. Unfortunately, this specificaiton contains substantial inherent uncertainties, as will become clear during the discussion of the Monte-Carlo ray tracing computations presented in Section IVB.

A third approach to the density determination involves the measurement of the angle integrated ion production rate, I, that results from electron impact ionization. In some sense this determination has the

greatest relevance, since the polarized hydrogen beam line was designed specifically for studies of crossed beams electron-atom scattering. However, the density so obtained is an effective density, ρ_{eff}, specific to the geometry of the crossed beams interaction, which can be related to $\bar{\rho}$ only through detailed knowledge of the interaction volume and the variation of $\rho(r)$ within the volume. This point can be illustrated for a choice of coordinates in which the hydrogen beam lies along the z axis and the electron beam lies along the y axis, with both beams assumed to have cylindrical symmetry. In this case, the total number of atoms, N', in the interaction volume, V, can be expressed as

$$N' = \rho_{eff} V \tag{23}$$

or more specifically as

$$N' = 8 \int_0^{R_e} dz \int_0^{Y} dy \int_0^{X} dx\, \rho(r), \tag{24}$$

where R_e is the effective radius of the electron beam, $r = \sqrt{x^2+y^2}$ is the radial coordinate applicable to the hydrogen beam, and the upper limits, X and Y, are given by $X = \sqrt{R_e^2-z^2}$ and $Y = \sqrt{R_H^2-R_e^2+z^2}$. In terms of the electron current density, j_e (expressed in electrons$\cdot$cm$^{-2}\cdot$s^{-1}), the ion production rate (expressed in ions$\cdot$s^{-1}) can now be written as

$$I = \varepsilon \sigma_I N' j_e, \tag{25}$$

where ϵ is the overall experimental efficiency and σ_I is the total ionization cross section.

From Eqs. (23) and (25) it is clear that even if σ_I is known, ρ_{eff} can be obtained from measurements of I and j_e, only if V and ϵ are known as well. The volume V, as illustrated by Eq. (24), depends not just upon R_H but also on R_e, a dimension that unfortunately cannot be determined with great accuracy. The efficiency ϵ also suffers from some uncertainty as will be seen in Section V. A comparison of Eqs. (20), (23) and (24) shows moreover that the dependence of ρ on r must indeed be specified, if $\bar{\rho}$ is to be obtained from a measurement of ρ_{eff}.

All three methods of density determination are thus frought with deficiencies. Consequently, confidence in a quoted value of $\bar{\rho}$ requires reasonable consistency among the various results, an issue that will be addressed further in Sections IV and V.

D. Dissociation Fraction Determination and QMA Calibration

The mass one and mass two signals produced by the QMA for an incident mixture of hydrogen atoms and hydrogen molecules can be written in terms of four response functions, α_{11}, α_{12}, α_{21}, and α_{22}. For incident densities ρ_1^q and ρ_2^q, corresponding to atoms and molecules respectively, the specific relations for the mass one and mass two signals are given by

$$Q_1 = \alpha_{11}\rho_1^q + \alpha_{12}\rho_2^q \tag{26}$$

and

$$Q_2 = \alpha_{21}\rho_1^q + \alpha_{22}\rho_2^q, \tag{27}$$

where Q_1 and Q_2 in this section are understood to be beam related signals derived from chopper-open minus chopper-closed readings.

From the form of these equations, it is clear that α_{11} characterizes the mass one response of the QMA to atoms, while α_{22} characterizes the mass two response to molecules. The function α_{12}, which produces a mass one response to incident molecules, results from dissociative ionization processes in the electron bombarder of the QMA. The function α_{21}, which produces a mass two response to incident atoms, by contrast, results from recombination processes in the QMA and, for the geometry and atom densities involved, in fact may be neglected.

If the rf power at the hydrogen source is turned off, dissociation ceases, and the QMA signals become

$$(Q_1)^{off} = \alpha_{12}(\rho_2 q)^{off} \tag{28}$$

and

$$(Q_2)^{off} = \alpha_{22}(\rho_2 q)^{off}, \tag{29}$$

with the consequence that the ratio α_{12}/α_{22} can be found from measurements of $(Q_1)^{off}$ and $(Q_2)^{off}$ according to the relation

$$(\alpha_{12}/\alpha_{22}) = (Q_1)^{off}/(Q_2)^{off} \tag{30}$$

Note that Eq. (30) is applicable to any portion of the beam profile sampled by the QMA. If, however, measurements are restricted to the center of the profile, the dissociation fraction, F^O, at the source can be determined, where F^O is defined as[36]

$$F^O \equiv \frac{(\rho_1{}^O)^{on}}{(\rho_1{}^O)^{on} + (\rho^O{}_2)^{on}} \tag{31}$$

for respective atom and molecule densities $(\rho_1^o)^{on}$ and $(\rho_2^o)^{on}$ at the exit of the source nozzle when the rf power is on. An expression for F^o in terms of measurable QMA signals follows from the observation that when the rf power is turned on, the decrease in the Q_2 signal is directly attributable to the dissociation of each molecule into two atoms. Since the temperature of the source remains practically constant when the rf power is turned on, the molecular transport efficiency from the source to the QMA remains essentially unchanged. As a consequence, the ratio of densities $(\rho_1^o)^{on}/(\rho_2^o)^{on}$ for rf power on is given by

$$\frac{(\rho_1^o)^{on}}{(\rho_2^o)^{on}} = 2\,\frac{(\rho_2^o)^{off} - (\rho_2^o)^{on}}{(\rho_2^o)^{on}} = 2\,\frac{(\rho_2 q)^{off} - (\rho_2 q)^{on}}{(\rho_2 q)^{on}} = 2\,\frac{(Q_2)^{off} - (Q_2)^{on}}{(Q_2)^{on}} \tag{32}$$

where $(Q_2)^{on}$ and $(Q_2)^{off}$ are understood to be QMA readings in the central region of the beam profile. From Eqs. (31) and (32) it is clear that F^o can be written as

$$F^o = \frac{2(R_{22}-1)}{2R_{22}-1}, \tag{33}$$

where the ratio R_{22} is given by

$$R_{22} = (Q_2)^{off}/(Q_2)^{on}. \tag{34}$$

Consider now a corresponding ratio

$$r_{22} = (q_2)^{off}/(q_2)^{on} \tag{35}$$

for QMA signals $(q_2)^{on}$ and $(q_2)^{off}$ obtained in the extreme wings, where, as in the case of signals taken from the central section, $(q_2)^{on}$ and $(q_2)^{off}$ are understood to be derived from chopper-open minus chopper-closed readings. Unlike those taken from the central section, however, the mass two signals obtained from the wings contain contributions from recombination of atoms that have struck the walls of the beam pipe in the vicinity of the QMA. Thus if β_1 and β_2 represent respectively the transport efficiencies from the source to the QMA for atoms and molecules, $(q_2)^{on}$ and $(q_2)^{off}$ can be written as

$$(q_2)^{on} = \alpha_{22}\left[\frac{1}{2}\,\beta_1\,(\rho_1{}^o)^{on} + \beta_2\,(\rho_2{}^o)^{on}\right] \tag{36}$$

and

$$(q_2)^{off} = \alpha_{22}\,\beta_2\,(\rho_2{}^o)^{off} = \alpha_{22}\,\beta_2\left[(\rho_2{}^o)^{on} + \frac{1}{2}\,(\rho_1{}^o)^{on}\right], \tag{37}$$

where the right side of Eq. (37) presumes no loss of atoms during the dissociation process. Through the combination of Eqs. (32) and (34)-(37), the ratio of transport efficiencies β_1/β_2 can be expressed as

$$\frac{\beta_1}{\beta_2} = \frac{R_{22} - r_{22}}{r_{22}\,(R_{22}-1)} = \frac{(q_2)^{on}(Q_2)^{off} - (q_2)^{off}\,(Q_2)^{on}}{(q_2)^{off}\,[(Q_2)^{off} - (Q_2)^{on}]}. \tag{38}$$

Finally with the ratio $(Q_1)^{on}/(Q_2)^{on}$ written as

$$\frac{(Q_1)^{on}}{(Q_2)^{on}}) = \frac{\alpha_{11}\beta_1(p_1{}^o)^{on} + \alpha_{12}\beta_2(p_2{}^o)^{on}}{\alpha_{22}\beta_2(p_2{}^o)^{on}}, \tag{39}$$

it can be shown with the assistance of Eqs. (30), (34), (35) and (38) that the QMA response functions α_{11} and α_{22} are related by

$$\frac{\alpha_{11}}{\alpha_{22}} = \frac{1}{2}\,\frac{(q_2)^{off}(Q_1)^{on} - (q_1)^{off}(Q_2)^{on}}{(q_2)^{on}(Q_2)^{off} - (q_2)^{off}(Q_2)^{on}}. \tag{40}$$

Thus, Eqs. (30) and (40) provide access to the relative calibration of the QMA for masses one and two, while Eq. (38) provides access to the relative transport efficiencies from the source to the QMA for atoms and molecules. Finally, Eqs. (33) and (35) provide the necessary relations for the dissociation fraction F^o at the source to be determined.

IV. COMPUTER MODELS

A. General Consideration

As suggested in Section III the determination of hydrogen beam density, polarization, and dissociation fraction cannot easily be made by experimental measurement alone. This is particularly true if the beam parameters need to be known at the interaction region, a location at which the requisite measurement devices cannot be placed without causing severe disruption of the beam line itself. Thus, detailed theoretical modeling of the beam becomes an integral part of the measurement process, placing great importance on the confidence with which the calculational results are held.

In order to increase the reliability of our results, we therefore used three different modeling methods: (1) a Monte-Carlo ray-tracing analysis, (2) an approach that treated the hexapole state selector as a thick lens, and (3) a Cartesian phase space calculation. All three techniques relied on the application of standard kinetic gas theory to establish the operating density of the source in terms of the ballast volume pressure. In the following sections we will review the principal elements of the calculations and present summaries of their predictions.

B. Source Density and Gas Kinetics

All three calculational methods require specification of the hydrogen density either inside the source or immediately outside the discharge nozzle. Since direct measurement of the discharge pressure is precluded by the design of the source, the kinetic theory of gases must be used to extract the information from pressure measurements carried out at the hydrogen ballast tank.[21,35,37] Unfortunately, the conditions under which the

source operates makes this extraction very difficult and leads to some uncertainty in the effective operating pressure.

The nature of the difficulty is best illustrated with the aid of the schematic diagram shown in Fig. 11, which depicts the ballast tank, the discharge volume, and the discharge nozzle, as well as the connections between the elements. The connection between the ballast tank and the discharge volume can be reasonably characterized by an effective diameter D_{ts} = 6 mm and an effective length L_{ts} = 800 mm. The nozzle, however, is more complex, having an entry section, with a diameter D_{ss} = 3 mm and a length L_{ss} = 25 mm, and an exit section, with a diameter D_{sr} = 1 mm and a length L_{sr} = 25 mm. Separating the two sections is a kink that reduces the Lyman-α emission of the source, and it is this kink combined with the operating pressure of the source that creates the major difficulty.

At the operating ballast tank pressure p_t = 400 mTorr, the mean free path of molecular hydrogen, λ_{H_2}, is approximately 0.2 mm, which places the molecular gas transport from the ballast tank to the discharge volume in the intermediate flow regime.[35] The conductance of the transport tube, C, must then be expressed in the form

$$C = (c_1 D^4 \bar{p} + c_2 D^3)/L, \tag{41}$$

where $\bar{p}$ is the average pressure in the tube; where the parameter c_1 depends simply upon the viscosity of the gas, η; where the parameter c_2 depends in a complex fashion upon the molecular weight, M, and the Kelvin temperature, T, of the gas in the combination $\sqrt{T\ M}$, as well as upon the ratio $D\bar{p}/\eta$; and where the subscripts on C, D, L, and $\bar{p}$ are implicit. The limiting condition of molecular flow occurs when the pressure and

temperature of the gas are such that the mean free path λ satisfies the inequality $\lambda/D > 1$. In this case, the term c_2D^3 dominates in Eq. (41). On the other hand, when the condition $\lambda/D < 0.01$ obtains, the limiting case of viscous flow is achieved, and it is the term $c_1D^4\bar{p}$ that dominates in Eq. (41).

Although the intermediate flow regime is somewhat complicated to handle, it is nonetheless amenable to analytic calculation. It applies along the entire length of the transport tube between the ballast tank and the discharge volume, since the pressure gradient along the tube is quite small, and λ_{H_2} consequently remains close to 0.2 mm throughout. The situation in the nozzle, by contrast, is far more complex, since not only must the intermediate flow regime be anticipated, but also some turbulence must be assumed because of the presence of the kink.

Regardless of the details, however, it is clear from the relative dimensions of the nozzle that the conductance of the nozzle, C_{sr}, is considerably smaller than that of the transport tube, C_{ts}. Moreover, the difference is only enhanced by the presence of turbulence in the nozzle. Under these circumstances, the pressure p_s in the discharge tube can be estimated from the throughput relations

$$\mathcal{Q}_{ts} = C_{ts}\,(p_t - p_s) \tag{42}$$

and

$$\mathcal{Q}_{sr} = C_{sr}\,(p_s - p_r), \tag{43}$$

where $\mathcal{Q}_{ts}$ and $\mathcal{Q}_{sr}$ are the throughputs in the transport tube and the nozzle respectively, and p_r is the vacuum chamber residual gas pressure. If the

the full length of the nozzle, and the usual expression for the number of atoms leaving the nozzle

$$\mathcal{I}^{o} = \frac{\rho_i^{s}\langle v\rangle \pi R_{sr}^{2}}{4\kappa} \tag{47}$$

does <u>not</u> apply,[37] where $\langle v\rangle$ is the mean velocity of atoms in the source,[21] R_{sr} is the effective radius of the nozzle and κ is given by

$$\kappa = \frac{3}{8}\,\frac{L_{sr}}{R_{sr}}, \tag{48}$$

with L_{sr} the effective length of the nozzle. A more reasonable characterization of the nozzle, perhaps, relies on an assumption of intermediate flow up to the kink, a turbulent condition at the kink with a consequent small (~ 10%) reduction of pressure, and finally an approach to effusive flow very close to the nozzle exit. Given the uncertainties in the model, we simply assume an approximate hydrogen gas pressure p_{ss} of 350 Torr near the nozzle exit, and with $\lambda_H \sim R_{sr}$ we accept the effusive flow relation for beam formation at an aperture; namely,[21,37]

$$\mathcal{I}^{o} = \frac{\rho_i^{ss}\langle v\rangle \pi R_{sr}^{2}}{4} \tag{49}$$

We further assume the normal $\cos\theta$ distribution associated with effusive flow. We note finally that in terms of ^{o}, the density of atoms just outside the nozzle, ρ_i^{o}, can be written as

dissociation fraction F^{o} is taken to be approximately 0.85, consistent with measurement, it follows that $_{sr} = 1.75\ _{ts}$, in which case Eqs. (42) and (43) lead to the expression

$$p_s = \left[\frac{4}{7}\ \frac{C_{sr}}{C_{ts}} + 1\right]^{-1} p_t, \tag{44}$$

where use has been made of the relation $p_s >> p_r$. Bounds on the ratio C_{sr}/C_{ts} can be found from the limiting cases of purely viscous flow and purely molecular flow, with turbulence neglected. For these two cases the conductance given by Eq. (41) can be written as[35]

$$C = 3.27 \times 10^{-2}\ [D^4/\eta L)]\bar{p} \qquad \text{Viscous} \tag{45}$$

and

$$C = 3.81\ (T/M)^{1/2}\ (D^3/L), \qquad \text{Molecular} \tag{46}$$

where dimensions are expressed in cm; η, in poise; $\bar{p}$, in Torr; and C, in ℓ/s. It is clear that Eq. (46) leads to the upper bound on the ratio C_{sr}/C_{ts}, and with appropriate values used for M, D, and L for the nozzle and the transport tube it follows that $C_{sr}/C_{ts} < 0.2$, assuming constant T throughout the system. Application of Eq. (44) immediately leads to the condition $p_t > p_s > 0.9\ p_t$. For purposes of further estimation, we therefore use the approximate value of 380 mTorr for p_s.

In order to model the flow out of the nozzle, we first observe that at a pressure of 380 mTorr, the mean free path of atomic hydrogen, λ_H, is of the order of 0.5 mm. Thus, effusive flow conditions do <u>not</u> apply along

$$\rho_1^{\,o} = \frac{\mathcal{J}_o}{\langle v \rangle \pi R_{sr}^{\,2}} \tag{50}$$

as a consequence of which $\rho_1^{\,o}$ is given by

$$\rho_1^{\,o} = \rho_1^{\,ss}/4. \tag{51}$$

For an assumed pressure p_{ss} ~ 350 mTorr, the ideal gas law leads to a density $\rho_1^{\,ss}$ ~ 10^{16} atoms/cm^3 just before the nozzle exit and consequently to a density $\rho_1^{\,o}$ ~ 2.5×10^{15} atoms/cm^3 just outside the nozzle.

C. Monte-Carlo Ray Tracing

Using the value of $\rho_1^{\,o}$ for normalization and assuming the $\cos\theta$ distribution characteristic of an effusive flow source, we carried out a Monte-Carlo analysis of the hydrogen beam. In terms of the coordinate system and angles shown in Fig. 12, we specified initial conditions for each trajectory as follows: α_o, β_o, θ_o, r_o, and v_o where the initial velocity $\vec{v}_o$ is given by

$$\vec{v}_o = v_o\{\sin\theta_o\,[\cos(\alpha_o+\beta_o)\hat{x} + \sin(\alpha_o+\beta_o)\hat{y}] + \cos\theta_o\,\hat{z}\}, \tag{52}$$

and the initial radial coordinate r_o is related to the initial cartesian coordinates by the usual expressions $x_o = r_o\cos\beta_o$ and $y_o = r_o\sin\beta_o$. Employing the subscript zero to denote the initial value of the relevant quantity at the start of a computer step, we can summarize the equations of motion as follows:

(1) In drift regions,

$$x = x_o + (z-z_o)\left.\frac{dx}{dz}\right|_o \tag{53}$$

$$y = y_o + (z-z_o)\left.\frac{dy}{dz}\right|_o. \tag{54}$$

(2) Inside the hexapole magnet,[30] with M_H the mass of the hydrogen atom, $v = v_z$ the velocity of the hydrogen atom, and K defined by

$$K = \frac{1}{v}\left[\frac{\mu_{eff}\, H(R_M)}{M_H\, R_M^2}\right]^{1/2}, \tag{55}$$

(a) for $\mu_{eff} < 0$

$$x = x_o \cos(Kz) + \frac{1}{K}\left.\frac{dx}{dz}\right|_o \sin(Kz) \tag{56}$$

$$y = y_o \cos(Kz) + \frac{1}{K}\left.\frac{dy}{dz}\right|_o \sin(Kz); \tag{57}$$

(b) for $\mu_{eff} > 0$

$$x = x_o \cosh(Kz) + \frac{1}{K}\left.\frac{dx}{dz}\right|_o \sinh(Kz) \tag{58}$$

$$y = y_o \cosh(Kz) + \frac{1}{K}\left.\frac{dy}{dz}\right|_o \sinh(Kz). \tag{59}$$

(3) Inside the Stern-Gerlach magnet[21] with a the radius of the convex pole piece and with the field and its gradient given respectively by

$$H = \frac{2\mathcal{R}^2}{\mathcal{R}^2+x^2}\, H(\mathcal{R}) \tag{60}$$

and

$$\frac{\partial H}{\partial x} = -\frac{4\ \ ^2x}{(\ ^2+x^2)^2}\, H(\mathcal{R}), \tag{61}$$

$$x = x_0 + (z-z_0)\ \frac{dx}{dz}\Big|_0 + \frac{1}{2}\ \frac{\mu_{eff}}{M_H}\ \frac{\partial H}{\partial x}\left[\frac{z-z_0}{v}\right]^2 \tag{62}$$

$$y = y_0 + (z-z_0)\ \frac{dy}{dz}\Big|_0. \tag{63}$$

For many trajectories, the magnitude of the field inside the hexapole and Stern-Gerlach magnets remains sufficiently high that within these regions μ_{eff} remains constant and equal to $\pm\mu_B$. As a consequence, for these trajectories the computer step size is irrelevant, and Eqs. (56) - (59), (62), and (63) may be regarded as analytic equations, with the subscript zero denoting the value of the relevant quantity at the entrance to the particular region. For other trajectories, however, the step size is critical and must be examined with great care. For all trajectories, the drift region behavior described by Eqs. (53) and (54), clearly satisfies the requirement for analytic treatment.

Regardless of circumstance, the characteristics of the beam at any location, z, along the beam line requires a tally of the trajectories arriving at that point. To that end, we set up bins of dimension Δx and Δy and calculated the density $\rho_1^z(x,y)$, the low-field polarization $P^z(0;x,y)$, and the high-field state-selection parameter $s^z(x,y)$ according to the respective prescriptions

$$\rho_i^z(x,y) = \frac{1}{n_{tot}} \frac{n^z(x,y)}{\Delta x\ \Delta y}\ \pi R_{sr}\ \rho_i^o, \tag{64}$$

$$P^z(0;x,y) = \frac{n_{++}^z(x,y) - n_{--}^z(x,y)}{n^z(x,y)}, \tag{65}$$

and

$$s^z(x,y) = \frac{(n_{++}^z(x,y) + n_{+-}^z(x,y)) - (n_{-+}^z(x,y) + n_{--}^z(x,y))}{n^z(x,y)}, \tag{66}$$

where n_{tot} is the total number of trajectories starting from the source, $n^z(x,y)$ is the total bin tally, and $n_{++}^z(x,y)$ is the bin tally corresponding to the high-field spin assignments $(m_S,\ m_I) = (+^1/_2,\ +^1/_2)$, with the remaining n's correspondingly defined.

The results of the Monte-Carlo computations, based upon a sample of 10^{10} atoms effusing from the source and reduced by the conservative solid angle acceptance of downstream beam elements to 4.6×10^6 interrogated trajectories, are summarized in Figs. 13-18 which illustrate the beam characteristics at the interaction region, at the entrance to the Stern-Gerlach magnet, and at the entrance to the QMA, the last two of which assume the insertion of all collimating slits. It should be noted that in obtaining these results we treated both magnets as ideal systems with all fringe fields completely neglected. As can be seen from Fig. 13, the low field polarization, P(0), and the high-field state selection parameter s, vary only slightly over the volume of the interaction region, the former remaining close to 0.5 and the latter, close to unity throughout. With the uncertainty reflecting counting statistics only, the average value $\bar{P}(0)$ of

the low-field polarization at the interaction region is 0.515(2), while the average value of the state selection parameter $\bar{s}$ is 0.99102(4). It should be noted that if μ is improperly treated as a constant $\pm\mu_B$, the radial dependence of s changes its character, as shown in Fig. 13(b), and the value of $\bar{s}$ becomes 0.99758(3). With the application of Eqs. (14) and (16), P(0) becomes 0.49879(2). The discrepancy, while small for $\bar{s}$ is larger for P(0) and should be of more than passing interest to other groups working with hexapole state selectors.

Fig. 14 illustrates the variation of P(0) and s with the horizontal position of the first entrance slit of the Stern-Gerlach polarimeter. Representing convolutions over the 0.7 mm-wide by 2.5 mm-high acceptance dimensions of the polarimeter, the data points in Fig. 14 continue to reflect (with some enhancement) the same small decrease on axis for both P(0) and s that is visible in Fig. 13. The presence of the axial dips plays a significant role in the interpretation of the polarization measurements described in Section V.

For the purpose of relating the actual measurements carried out with the Stern-Gerlach polarimeter to the low-field beam polarization present in the interaction region, we propagated the trajectories downstream through the polarimeter and into the QMA, convoluting the binned results with a horizontal window 0.5 mm wide which simulates the true acceptance slit of the mass analyzer. Fig. 15(a) illustrates the Monte-Carlo beam profile obtained when the Stern-Gerlach magnet is deenergized and when its collimating aperture is centered on the beam axis. For completeness we have shown separately the four hyperfine magnetic sublevels labeled in accordance with their (m_S, m_I) high-field designations. As the energizing current increases from zero, the ++ and +- profiles shift toward the right and the -- and -+ profiles shift toward the left, so that at a current of

5 A, the combined profile takes on the appearance shown in Fig. 15(b). The peaked structures appearing in the profile are real and are related to the velocity classes that are preferentially transmitted by the hexapole magnet.

For each of fifteen settings of the Stern Gerlach driving current between 0 and 6 A, we divided the profile area into regions to the right, A_R, and to the left, A_L, of the beam axis, and, by analogy with the procedures described in Section III.B for the reduction of the laboratory data, we formed the asymmetry Δ_H according to the prescription

$$\Delta_H = \frac{A_R - A_L}{A_R + A_L}. \tag{67}$$

The dots and the curve connecting them in Fig. 16 illustrate the results for the Monte Carlo asymmetry so generated. The high-field state selection parameter s, obtained from the Monte-Carlo analysis when the Stern-Gerlach polarimeter is centered on the beam axis, is given by the asymptotic limit of Δ_H, which has the value 0.9821(4).

As t last illustration of the output of the Monte-Carlo computation, we present in Fig. 17 plots of the radial dependence of the total atom density at the interaction region for two cases: a field-dependent μ_{eff} and a constant $\mu_{eff} = \pm \mu_B$. The plots are truncated at a radius of 3 mm in accordance with the cutoff imposed by the collimating aperture located 38 mm upstream from the crossed-beams interaction center. The Monte-Carlo computation for the field dependent μ_{eff} case predicts an average density $\bar{\rho}$ of 9 x 10^9 atoms/cm^3 over the approximately 7 mm diameter beam present at the interaction region.

D. Optical Model of Hexapole Magnet

With the use of Eqs. (55) - (59) it is possible to develop a model of the hexapole magnet in terms of an optical analog. This approach, which has been described in detail elsewhere,[30,38] assumes the high-field approximation for μ_{eff} and determines the density and state-selection parameter of the beam from the spectral transmittance $\Omega_{\pm}(K)$ of the magnet for atoms in the $m_S = \pm 1/2$ state and the v^2-Maxwellian distribution function $F_{V_2}(K)$ expressed in terms of inverse velocity parameter defined by Eq. (55). The number of atoms reaching the interaction region within a radius R_H located a distance L_2 from the exit of the magnet is then given by

$$N_{\pm} = (\text{const}) \int_0^{\infty} F_{V_2}(K)\ \Omega^{\pm}(K,L_1,L_2,L_M,R_H)dK, \tag{68}$$

where L_1 is the distance from the source to the entrance of the magnet, and L_M is the length of the magnet.

For atoms in the $m_S = -1/2$ state, Ω_- can be shown to be given by

$$\Omega_- = \pi R_H^2\ [(L_1L_2K+1/K)\sinh(KL_M) + (L_1+L_2)\cosh(KL)]^{-2}. \tag{69}$$

Similarly, for atoms in the $m_S = +1/2$ state, Ω_+ can be shown to be given by

$$\Omega_+ = \pi R_H^2\ [(L_1L_2K-1/K)\sin(KL) - (L_1+L_2)\cos(KL)]^{-2}, \tag{70}$$

provided the result does not exceed the acceptance angle Ω_+^{acc} of the

magnet itself. The latter is also a function of K and depends upon whether the trajectories are still diverging at the exit of the magnet, as is the case for high velocity, or whether they are bent toward the axis inside the magnet at radial distances less than or equal to R_M. The value of K, denoted by K^*, which separates these two regimes can be found from the solution of the equation

$$\cot (K^* L_M) = K^* L_1, \tag{71}$$

in which case Ω_+^{acc} can be obtained from one of two relations:

$$\Omega_+^{acc} = \pi R_M^2 K^2 [1+ (KL)^2]^{-1} \qquad \text{for } K > K^* \tag{72}$$

or

$$\Omega_+^{acc} = \pi R_M^2 K^2 [\sin(KL) + KA\cos(KL)]^{-2} \qquad \text{for } K < K^*. \tag{73}$$

The results summarized by Eqs. (68) - (73) apply to a point source of atoms. However, as has been explained elsewhere,[30,38] the model can be corrected to include vignetting, penumbra, and magnification losses that may occur for extended sources. In the case of the hydrogen beam under discussion, for which the source diameter is small compared to the magnet pole-gap, the corrections are small and amount to changes of no more than a few percent of the values calculated.

We employed the optical model of the hexapole magnet, including the effects of vignetting, peneumbra and magnification, to obtain values of $\Omega_\pm$ in accordance with Eqs. (69) - (73), and used these results together with Eqs. (15) and (68) to obtain the state selection parameter s, as a function

of radius at the interaction region, as shown in Fig. 13(b). The results are in reasonable agreement with those already presented in Fig. 13(b) for the Monte-Carlo computations carried out with constant $\pm \mu_B$. Moreover the value of 0.998 obtained for $\bar{s}$ from the optical model agrees well with the value of 0.99758(3) obtained from the constant $\pm \mu_B$ Monte-Carlo analysis.

The results of the optical model combined with the relations

$$\Omega = \int_0^\infty F_V^2(K) \frac{1}{2} [\Omega_+ (K) + \Omega_- (K)] dK \tag{74}$$

and

$$\bar{\rho} (L_1, L_2, L_M, R_H) = \frac{\rho_1^{SS} \Omega R_{Sr}^2}{4 R_H^2}. \tag{75}$$

lead us to a value of 1×10^{10} atoms/cm^3 for the average density of atoms in the interaction region, which is also in reasonable agreement with the value obatined from the Monte-Carlo analysis. However, the dependence of the density on the radial position at the interaction region shows some small disagreement between the two methods, as illustrated by a comparison of the curves in Fig. 17. For completeness, it should be noted that in obtaining the results from the optical model we treated the pair of hexapole magnets as a single unit 323 mm long without any gap between them. In addition we treated them as ideal hexapoles without any other moments being represented and with fringe fields neglected, as was the case for the Monte Carlo calculations described in the previous section.

As was suggested in the previous section, the chromatic properties of the hexapole magnet lead to the assignment of a common focal plane for a series of velocity classes of $m_S = +\,{}^1/_2$ atoms. This point is well illustrated by Fig. 18(a), in which the spectral transmittance function $\Omega_+(K)$ is plotted versus K for atoms reaching the interaction region. With the use of the v^2-Maxwelliam distribution function, $F_{v^2}(K)$, shown in Fig. 18(b), the corresponding spectral transmission function $\Omega_+(K)\, F_{v^2}(K)$can be obtained, as dipicted in Fig. 18(c). The three peaks visible in Fig. 18(c) correspond to the three peaks in the beam profile of Fig. 15(b). From a comparison of Figs. 18(b) and (c) it is apparent that the average value $\bar{K}$ associated with the spectral transmission is shifted upward from the average value $\langle K \rangle$ associated with $F_{v^2}(K)$ alone. Hence, as we stated in Section III C, the average value $\bar{v}$ that characterizes the beam at the interaction region is lower than that ordinarily associated with the v^2-Maxwelliam appropriate to density calculations; namely, $\langle v \rangle = \sqrt{\frac{8kT}{\pi M_H}}$.

For completeness, we have included a plot of the spectral transmittance $\Omega_-(K)\, F_{v^2}(K)$, shown in Fig. 18(d).

E. Cartesian Phase Space Calculation

The phase space method has been successfully employed[21,39] a number of times to calculate intensities and polarizations of state-selected and focused beams of atoms and molecules. In fact, the technique has been specifically applied to the case of magnetically state-selected hydrogen in a situation not too different from ours.[21] The parameterization of the problem derives from the harmonic equation of an atom in a hexapole magnet which leads to Eqs. (56) - (59). Specifically, in any direction, x, perpendicular to the beam direction z, the equation takes the form

$$\frac{d^2x}{dt^2} + \omega^2 x = 0, \tag{76}$$

where ω is given by

$$\omega = vK = \left[\frac{\mu_{eff} H_R}{M_H R_M^2}\right]^{1/2}. \tag{77}$$

With $p_x = M_H v_x$, Eq. (76) can be recast as

$$\frac{p_x^2}{2M_h} + \frac{M_H \omega^2 x^2}{2} = W, \tag{78}$$

where W is a constant. Using the paraxial approximation, we can express p_x as

$$p_x = M_H \frac{dx}{dt} = M_H \frac{dx}{dz} \frac{dz}{dt} = M_H v_z \tan\phi_x = M_H v \phi_x, \tag{79}$$

where ϕ_x is the angle that the tangent to the trajectory makes with the z axis. Then with ξ_x and η_x defined respectively by ξ_x x/R_M and η_x ϕ_x/KR_M, Eq. (78) can be rewritten in dimensionless form as

$$\xi_x^2 + \eta_x^2 = w, \tag{80}$$

where w is given by

$$w = \frac{2W}{M_H \omega^2 R_M^2}. \tag{81}$$

Thus in the phase space described by (ξ_x, η_x), the trajectories inside a hexapole magnet are circles of radius $\sqrt{w}$ centered at the origin. For a magnet of length L_M, the effect on an ensemble of atoms in (ξ_x, η_x) space is a rotation of all points counterclockwise about the origin through an angle KL_M.

In a field free region, the equations of motion for χ and ϕ_x have the obvious forms $\phi_x = (\phi_x)_0$ and $x = x_0 + \phi_x z$, where the subscript zero denotes the initial value of each parameter. Thus in terms of ξ_x and η_x, all trajectories satisfy the relations

$$\eta_x = (\eta_x)_0 \tag{82}$$

and

$$\xi_x = (\xi_x)_0 + K z \eta_x \tag{83}$$

where $(\eta_x)_0$ and $(\xi_x)_0$ are constants related to $(\phi_x)_0$ and x_0 respectively through the definitions of ξ_x and η_x. Therefore the effect on an ensemble of atoms undergoing field-free motion is a shearing action in (ξ_x, η_x) space, with points above the horizontal ξ_x axis displaced to the right and those below the ξ_x axis displaced to the left, all displacements being proportional to the distances of the points from the ξ_x axis.

Following the application of Liouville's theorem and the phase space arguments presented elsewhere, it can be shown that the total number of $m_S = \pm 1/2$ atoms per second passing through a region of interest of area Σ along the beam line downstream from the hexapole magnet as given by

$$\mathcal{J}_{\pm}^{\Sigma} = \frac{1}{4\pi} \frac{\rho_i^{ss}}{2} \langle v \rangle R_M^{*} \int_0^{\infty} [A^{\Sigma}(K)]^2 K^2 F_v^2(v)\, dv, \tag{84}$$

where $A^{\Sigma}(K)$, the evolved phase space area intercepted by Σ is simply

$$A^{\Sigma}(K) = \int_{\Sigma} d\xi_x d\eta_x. \tag{85}$$

Similarly, the density of $m_S = \pm 1/2$ atoms at the region of interest is given by

$$\rho_{i\pm}^{\Sigma} = \frac{1}{4\pi} \frac{\rho_i^{o}}{2} R_M^{*} \int_0^{\infty} [A^{\Sigma}(K)]^2 K^2 F_v^2(v) dv. \tag{86}$$

It should be noted that the phase space procedure we have just outlined is rigorously applicable only in Cartesian coordinates. For beam geometries containing circular cross sections, such as those in our hydrogen beam line, the circular apertures must be bounded from below by inscribed squares and from above by circumscribed squares, the former leading to a lower limit for $\rho_{i\pm}^{\Sigma}$ and the latter, to an upper limit.

We applied these Cartesian phase space procedures to our beam line and obtained the spectral transmittance values $\Omega_+(K)$ shown in Fig. 18(a) for atoms reaching the interaction region. As can be seen by comparing the phase space result with the function $\Omega_+(K)$ obtained from the optical model, also shown in Fig. 18(a), the agreement between the two methods is quite good. In view of the approximations made for the circular apertures,

however, the phase space methods suffers considerably in accuracy, as consequence of which the phase space values of $\bar{s}$ and $\bar{\rho}$ are of diminished significance.

V. RESULTS AND CONCLUSIONS

Following the experimental procedures described in Section III, we investigated the polarization, density and dissociation fraction of the hydrogen beam, and as a corrollary, several calibration parameters of the Vacuum Generators Supavac quadrupole mass analyzer (QMA) as well. The determination of both the low-field polarization, P(0), and the high-field state selection parameter, s, requires the measurement of hydrogen beam profiles by the QMA for various settings of the Stern-Gerlach magnet driving current with the QMA alternately tuned for mass-one and mass-two observation and with the rf power applied and removed from the discharge tube. In Figs. 19(a) and (b) we display two sample mass-one profiles for Stern-Gerlach driving currents of 0 and 3 A respectively, both taken with full rf power applied to the discharge tube.

Under conditions of no driving current, the beam profile should be perfectly symmetric about the centroid, but as Fig. 19(a) shows profile actually measured was asymmetric, suggesting some small degree of misalignment of either the hexapole or the Stern-Gerlach magnet. While not of great consequence for beam operation, such a misalignment has some significance for the polarization measurement, as will become clearly shortly. Examination of the profile measured for the 3 A driving current, illustrated in Fig. 19(b), reveals not only an exaggerated asymmetry in the shape, as would be expected for a beam characterized by an asymmetric Maxwellian velocity distribution, but also a development of a small bump on the right side of the profile. Although reduced in prominance by slit-scattering and pole-tip scattering of the beam periphery, this bump is suggestive of one of the peaks present in the Monte-Carlo profile shown in Fig. 15(b) and no doubt is related to the chromatic properties of the

hexapole magnet indicated by the characteristics of the spectral transmittance $\Omega_+(K)$ and the spectral transmission $\Omega_+(K)\ F_V^2(K)$ shown in Figs. 18(a) and (c) respectively.

As is evident from Figs. 19(a) and (b), the linear and quadratic terms present in the pedestal function $Y^P(X)$ are both small, as a consequence of which the pedestals (thus dominated by a constant offset term) can be determined with good accuracy. Therefore we were able to apply the data reduction procedures summarized in Section III.B to obtain Δ_H for Stern-Gerlach driving currents between 0 and 3.5 A. At currents above 3.5 A, scattering of the low velocity components of the beam from the pole tips of the Stern-Gerlach magnet introduces substantial uncertainties into the determination of Δ_H. Unfortunately, as is evident from the Monte-Carlo analysis shown in Fig. 16, Δ_H is far from saturation at a driving current of 3.5 A and indeed achieves saturation only when the current reaches approximately 20 A.

Faced with the inability to carry out measurements at saturation, we attempted to fit the measured values of Δ_H to those predicted by the Monte Carlo analysis. To this end, we used standard magnetic circuit techniques in order to relate the magnetic field, $|\vec{H}|$, and its gradient, $\vec{\nabla}H$, in the "two-wire" geometry[15] to the applied driving current, thereby providing a common horizontal scale for the laboratory measurements and the Monte-Carlo results. We then found that the laboratory values of Δ_H agreed remarkably well with the on-axis Monte-Carlo values, shown in Fig. 16, provided for the former were scaled uniformly by a factor of 0.98. Indeed this downward scaling is entirely consistent with the slight beam misalignment indicated by the asymmetric profile shown in Fig. 19(a) combined with the positional dependence of the high-field state-selection parameter, s.

As illustrated in Fig. 14(b), the value of s at the Stern-Gerlach entrance slit, achieves a minimum of 0.975 on the beam axis and increases to more than 0.990 within a 4 mm horizontal offset. In other words, a small beam misalignment could easily require the application of a scale factor, of 0.985 to the measured values of Δ_H for purposes of comparison with the on-axis Monte-Carlo predictions. The remaining 0.5% discrepancy between the two sets of values falls easily within the experimental uncertainties. Thus we feel confident in asserting that the Monte-Carlo values of s and hence P(0) are verified by the experimental measurements of Δ_H. Based upon the various uncertainties that arise in the measurements and the analyses, we conclude that at the interaction region, the hydrogen beam is characterized by the Monte-Carlo values of 0.99 ± 0.01 for the high-field state-selection parameter s and 0.515 ± 0.005 for the low-field polarization P(0), the precision having been slightly degraded from that of the actual Monte-Carlo results.

The validity of the Monte-Carlo modeling receives further ennancement through a comparison of the measured and predicted beam densities, $\bar{\rho}$, although experimental measurement of $\bar{\rho}$ is frought with substantial uncertainty. As explained in Section III C, $\bar{\rho}$ can be determined experimentally either by beam loading pressure measurements or alternatively by electron-impact ionization rate measurements. We carried out both sets of measurements and applied Eqs. (22) - (25) to obtain values of $\bar{\rho}$.

For the beam loading pressure determination of $\bar{\rho}$, we make the following assumptions: effective pumping speed S ≈ 530 ℓ/s for hydrogen molecules in the interaction chamber, as suggested by the pumping speeds and conductances given in Fig. 1; average velocity $\bar{v}$ ≈ 6.5 x 10^5 cm/s, based upon an analysis of the transmission functions shown in Fig. 19(c); fraction

of atoms f ≈ 0.4 falling within 3 mm radius, based upon Monte-Carlo modeling; gas temperature T = 300 K, based upon an assumption of thermalization of molecules; and ionization gauge conversion factor of 2.2 for hydrogen molecules, based upon manufacturer's specification.[40] With these assumptions and from the measured pressure rise of 7.4×10^{-9} Torr in the interaction chamber when the hydrogen beam is turned on we obtain a value of $6\ (\pm 3) \times 10^{9}$ atoms/cm^3 for $\bar{\rho}$, the large uncertainty resulting dominantly from an imprecise knowledge of the effective pumping speed for the complex pump baffling goemetry used. The result is in resonable agreement with the value of 9×10^{9} atoms/cm^3 calculated from the Monte-Carlo analysis.

For the electron impact ionization rate determination of $\bar{\rho}$ we carried out measurements at an incident electron energy of 15 eV, a value below the threshold for ionization of H_2 molecules. In applying Eqs. (23) - (27), we assume an electron beam radius R_e, of 1.5 ± 0.5 mm and an overall experimental efficiency ε of 0.10, the latter resulting from the combination of two 90% optically transparent meshes, as shown in Fig. 2(b), and a proton impact energy of 700 eV on the cone of a Mullard[41] channel electron multiplier for which researchers[42] have measured a detection efficiency of 0.12 with an unknown absolute precision. In light of the uncertainty in the equivalence between optical and charged particle transparency for the two meshes, and with some reasonable assumptions about the efficiency curve provided by Mullard, we assign a conservative value of ± 0.025 to the uncertainty in ε.

For the total ionization cross section, σ_I, we use the value of $(0.762 \pm 0.038) \times 10^{-17}$ cm^2 recently determined by Shah, Elliot, and Gilbody.[43] We note that this value is consistent with that obtained from the earlier absolute measurement of Fite and Brackman[44] at 20 eV and scaled downward

to 15 eV in accordance with the relative measurements of McGowan and Clark.[7] With an ionization rate of 450 protons/s for an incident electron intensity of 10 nA, we obtain a value of $(1.9 \pm 0.7) \times 10^{10}$ atoms/cm^3 for ρ_{eff}, where we quote an overall uncertainty that includes the effect of the ~ 100 meV resolution (full width at half maximum) of the electron beam and the uncertainty in its energy centroid, as well as the specific uncertainties in ε and σ_I and to a minor degree R_e. Using the radial dependence of ρ from the Monte-Carlo analysis, shown in Fig. 17, we finally obtain a value for $\bar{\rho}$ of $(1.7 \pm 0.7) \times 10^{10}$ atoms/cm^3, the slightly increased relative uncertainty arising from the uncertainty in R_e. The result again is in reasonable agreement with the Monte-Carlo value of 9×10^9 atoms/cm^3 and in slight disagreement with the value of $(6 \pm 3) \times 10^9$ atoms/cm^3 obtained from the beam loading pressure measurements.

We conclude the presentation of experimental results with a summary of the determination of the dissociation fraction at the source, F^o, defined by Eq. (31); the QMA calibration parameters α_{12}/α_{22} and α_{11}/α_{22} defined through Eqs. (26) and (27); and the relative beam transport efficiency β_1/β_2 for atoms and molecules reaching the QMA from the source with the Stern-Gerlach magnet turned off and all slits removed. Following the procedures described in Section III D, we carried out measurements that under typical operating conditions lead to the following results upon the application of Eqs. (26) - (40): $F^o = 0.831 \pm 0.004$, $\alpha_{12}/\alpha_{22} = 0.033 \pm 0.006$, $\alpha_{11}/\alpha_{22} = 0.64 \pm 0.07$, and $\beta_1/\beta_2 = 0.32 \pm 0.03$. Since the dissociation fraction is really quite sensitive to the actual operating conditions (pressure and rf power) of the source, we believe that the source should be characterized by a nominal dissociation fraction, F^o, between 0.8 and 0.85.

We conclude our paper with a brief comparison of our polarized beam to hydrogen beams developed at other laboratories. As we suggested at the

outset of the paper, many hydrogen beams, some polarized and some unpolarized, have indeed been constructed throughout the years, and some of these surpass our beam in one or more of their operating characteristics.[11] As a rule, however, the superior beams are far more massive and far more costly in construction and often make use of complex and expensive technologies.

In order to illustrate these points, we cite several typical examples. Employing a water-cooled rf (500 W, 20 MHz) dissociator and a pair of large bore hexapole electromagnets, Dunham et al.[14] developed a polarized jet atomic beam for use as a gas target. While the density of the beam was found to be quite high, (2-6) x 10^{11} particles/cm^3, the polarization at low field, measured by α-p scattering, was observed to be, only 0.25 - 0.33. The low value of the measured polarization is attributed to a large molecular fraction produced during the formation of the hydrogen jet.

The performance of the jet source is thus not much better than that of a more conventional one manufactured by ANAC,[15] the characteristics of which were reported by Haeberli et al.[16] in the context of a colliding beam source for polarized ion production. The ANAC source also employs an rf dissociator and contains two large bore high field gradient hexapole magnets, one with a tapered bore and one with a fixed bore. Although achieving a high field state selection that apparently is close to unity, the ANAC source, as reported by Haeberli et al., delivers a beam whose density by contrast with the jet source is only about 8 x 10^{10} atoms/cm^3 at a location approximately 25 cm away from the exit of the downsteam hexapole. The dissociation fraction of the ANAC source, however, can be expected to be quite high.

The design geometry of the ANAC source does not differ greatly from those of a similar source developed some years earlier by Risler et al.[12]

which also uses an rf discharge (4 kW, 27 MHz) and a large bore hexapole electromagnet containing both a tapered and a parallel section. Operating with a discharge tube pressure of ~ 7 Torr and employing three stages of high-speed pumping (500 ℓ/s, 50.00 ℓ/s and 5000 ℓ/s), the source described by Risler et al., produces a beam density of about 8 x 10^{10} atoms/cm^3 within a 10 mm beam diameter at a distance of 55 cm from the hexapole exit. No figures were quoted by Risler et al. for dissociation fraction or polarization, although both should be quite high.

Within the last few years, conventional jet beams, as well as effusive beams, have been eclipsed to some extent by the application of liquid helium technology to hydrogen atom beam production. Motivated by the well known enhancement in hexapole solid angle acceptance as the beam temperature decreases,[46] the cold hydrogen sources employ "accommodators" that cool the atoms in preparation for hexapole injection. Designed for ultimate use at the Brookhaven AGS accelerator, the source developed by Herschcovitch, Kponou, and Niinikoski,[15] for example, produces[47] a flux of 9.4 x 10^{18} atoms sr^{-1} s^{-1} with a most probable velocity of about 6.8 x 10^4 cm/s at an accommodator temperature of 5.8 K or alternatively a flux of 4 x 10^{19} atoms sr^{-1} s^{-1} with a velocity of 9.8 x 10^4 cm/s at a temperature of 26 K. While these parameters are quite impressive -- at a distance of 5 cm from the exit of the source, the latter operating condition corresponds to an atom density of 1.6 x 10^{13} atoms/cm^3 -- the cold hydrogen sources remain very much in the development stage. Use with high-field state selectors is still under investigation, and dissociation fractions are not well known.

By constrast with the complexities of helium cryogenics, the massiveness of high-gradient hexapole electromagnets, and the large investment in the use of high speed pumps, the source we have described in this paper is quite simple and inexpensive. By comparison with other

simple designs,[19,48] its operating parameters are very favorable and as we have shown, well understood. It is eminently suitable for small laboratory physics and with additional effort directed toward nozzle cooling can probably be improved further.

ACKNOWLEDGEMENTS

We gratefully acknowledge the financial support of the U.S. National Science Foundation (Grant PHY-8603166), the City University of New York (Grants PSC-CUNY 6-65279 and 6-67353), St. Patrick's College, and the U.K. Science and Engineering Research Council.

REFERENCES

1. See for example L. P. Levy and W. L. Williams, Phys. Rev. A 30, 220 (1984) and references therein; E. A. Hinds, in Spectrum of Atomic Hydrogen:Advances, edited by G. W. Series (World Scientific, Singapore, 1987), Ch. 4.

2. See for example S. R. Lundeen and F. M. Pipkin, Phys. Rev. Lett. 46, 232 (1981) and references therein; M. G. Boshier, P. E. G. Baird, C. J. Foot, E. A. Hinds, M. D. Plimmer, D. M. Stacey, J. B. Swan, D. A. Tate, D. M. Warrington, and G. K. Woodgate, Eighth International Conference on Laser Spectroscopy, Are, Sweden, 1987, to be published; R. G. Beausoleil, D. H. McIntyre, C. J. Foot, E. A. Hildum, B. Couillaud, and T. W. Hänsch, Phys. Rev. A 35, 4878 (1987).

3. D. Kleppner, H. M. Goldenberg, and N. F. Ramsey, Phys. Rev. 126, 603 (1962); H. F. Hess, G. P. Kochanski, J. M. Doyle, T. J. Greytak, and D. Kleppner, Phys. Rev. A 34, 1602 (1986); M. D. Hürlimann, W. N. Hardy, A. J. Berlinsky, and R. W. Cline, Phys. Rev. A 34, 1605 (1986).

4. F. Biraben and L. Julien, Opt. Commun. 53, 319 (1985); E. A. Hildum, U. Boesl, D. H. McIntyre, R. G. Beausoleil, and T. W. Hänsch, Phys. Rev. 56, 576 (1986); P. Zhao, W. Lichten, H. P. Layer, and J. C. Bergquist, Phys. Rev. A 34, 5138 (1986).

5. See for example J. F. Williams, in Electron and Photon Interactions with Atoms, edited by H. Kleinpoppen and M. R. C. McDowell (Plenum, New York, 1976), p. 309 and references therein; P. J. O. Teubner, C. R. Lloyd, and E. Weigold, Phys. Rev. A 9, 2552 (1974); C. R. Lloyd, P. J. O. Teubner, E. Weigold, and B. R. Lewis, Phys. Rev. A 10, 175 (1974); J. F. Callaway and J. F. Williams, Phys. Rev. A 12, 2312 (1975); J. Slevin, M. Eminyan, J. M. Woolsey, G. Vassilev, H. Q. Porter, C. G. Back, and S. Watkin, Phys. Rev. A 26, 1344 (1982); S. T. Hood, E. Weigold, and A. J. Dixon, J. Phys. B 12, 631 (1979); J. F. Williams, J. Phys. B 14, 1197 (1981).

6. G. D. Fletcher, M. J. Alguard, T. J. Gay, V. W. Hughes, P. F. Wainwright, M. S. Lubell, and W. Raith, Phys. Rev. A 31, 2854 (1985).

7. J. W. McGowan and E. M. Clarke, Phys. Rev. 167, 43 (1968).

8. J. B. Donahue, P. A. M. Gram, M. V. Hynes, R. W. Hamm, C. A. Frost, H. C. Bryant, K. B. Butterfield, D. A. Clark, and W. W. Smith, Phys. Rev. Lett. 48, 1538 (1982).

9. J. Slevin and W. Stirling, Rev. Sci. Instrum. 52, 1780 (1981) and references therein.

10. G. Clausnitzer, R. Fleischmann and H. Schopper, Z. Physik 144, 336 (1956).

11. Excellent summaries of the status of high-intensity polarized hydrogen beams as applied to polarized sources and targets for

accelerator applications may be found in the Proceedings of the International Workshop on Polarized Sources and Targets, edited by S. Jaccard and S. Mango, Helv. Phys. Acta 59, 513 (1986) and in Polarized Proton Ion Sources, edited by G. Roy and P. Schmor, AIP Conf. Proc. No. 117 (American Institute of Physics, New York, 1984). For a comparison of earlier work on ground state sources, see H. F. Glavish, Proceedings of the Symposium on Ion Sources and Formation of Ion Beams, October 19-21, 1971, Brookhaven National Laboratory, BNL Report No. 50310, p. 207.

12. R. Risler, W. Grüebler, V. Konig, and P. A. Schmelzbach, Nucl. Instrum. Meth. 121, 425 (1974).

13. E. F. Parker, in High-Energy Physics with Polarized Beams and Targets (Argonne, 1976), AIP Conf. Proc. No. 35, edited by M. L. Marshak (American, Institute of Physics, New York, 1977), p.382; D. G. Mavis, J. S. Dunham, J. W. Hugg, and H. F. Glavish, ibid., p.517.

14. W. Haeberli, M. D. Barker, C. A. Gossett, D. G. Mavis, P. A. Quin, J. Sowinsky, T. Wise, and H. F. Glavish, Nucl. Instrum. Meth. 196, 319 (1982); J. S. Dunham, C. S. Galovich, H. F. Glavish, S. S. Hanna, D. G. Mavis, and S. W. Wissink, Nucl. Instrum. Meth 219, 46 (1984).

15. J. T. M. Walraven and I. F. Silvera, Rev. Sci. Instrum. 53, 1167 (1982) and references therein; A. Hershcovitch, A. Kponou, and T. O. Niinikoski, Rev. Sci. Instrum. 58, 547 (1987).

16. J. L. McKibben, G. P. Lawrence and G. G. Ohlsen, in Polarization Phenomena in Nuclear Reactions, Proceedings of the Third International Symposium, Madison, 1970, edited by H. H. Barschall and W. Haeberli (University of Wisconsin Press, Madison, 1971), p. 828; E. Preiskchat, G. Michel, G. W. Roth, J. G. Cramer, Jr., and W. G. Weitkamp, ibid., p. 832; T. B. Clegg, G. A. Bissinger, W. Haeberli and P. A. Quin, ibid., p. 835; B. L. Donnally, ibid., p. 295 and references therein.

17. The literature is rich with descriptions of such work. For a survey of some recent applications, the reader is referred to the proceedings of a number of specialized conferences such as High Energy Physics with Polarized Beams and Polarized Targets, Proceedings of the 1980, edited by C. Joseph and J. Soffer (Birkhäuser Verlag, Basel, 1981); High-Energy Spin Physics, Brookhaven 1982, AIP Conf. Proc. No. 95, edited by G. M. Bunce (American Institute of Physics, New York, 1983); Intersections Between Particle and Nuclear Physics, AIP Conf. Proc. No. 123, edited by R. E. Mischke (American Institute of Physics, New York, 1984); Polarized Beams at SSC & Polarized Antiprotons, AIP Conf. Proc. No. 145, edited by A. D. Krisch, A. M. T. Lin, and O. Chamberlain (American Institute of Physics, New York, 1986); Proceedings of the Sixth International Symposium on Polarization Phenomena in Nuclear Physics, Osaka, 1985, Suppl. J. Phys. Soc. Jpn. 55, 1062 (1986).

18. R. W. Wood, Proc. Roy. Soc. 97, 455 (1920); 102, 1 (1922).

19. M. B. Shah and H. B. Gilbody, J. Phys. B 14, 2361 (1981).

20. M. J. Alguard, J. E. Clendenin, R. D. Ehrlich, V. W. Hughes, J. S. Ladish, M. S. Lubell, G. Baum, W. Raith, R. H. Miller, and W. Lysenko, Nucl. Instrum. Meth. 163, 29 (1979).

21. N. F. Ramsey, Molecular Beams (Oxford University Press, London, 1963)

22. Innotec Group, Inc. (formerly Torr Vacuum Products) Model S-1000.

23. Balzers Model TPU 200.

24. Perkin-Elmer Model 207-0284.

25. Perkin-Elmer Model 207-0164.

26. CTI Cryogenics Model Cryo Torr 7.

27. Leisk Engineering.

28. K. P. Ziock and W. A. Little, Rev. Sci. Instrum. 58, 557 (1987).

29. G. Baum, private communication; M. Weber, Aufbau and Erprobung eines Spinpolarisierten He(2^3S)-Atomstrahls mit Umpolbarer Polarisationsrichtung (Diplomarbeit, Fakultät für Physik, Universität Bielefeld), unpublished.

30. See for example V. W. Hughes, R. L. Long, Jr., M. S. Lubell, M. Posner, and W. Raith, Phys. Rev. A 5, 195 (1972) and references therein.

31. P. Kusch, and V. W. Hughes, in Handbuch der Physik, edited by S. Flügge (Springer Verlag, Berlin, 1959), Vol. 3711, p. 1.

32. C. Audoin, M. Desaintfuscien, and J. P. Schermann, Nucl. Instrum. Meth. 69, 1 (1969).

33. J. Kessler, Polarized Electrons, 2nd Edition (Springer Verlag, Berlin, 1985).

34. P. Bevington, Data Reduction and Error Analysis for the Physical Sciences (McGraw Hill, New York, 1969).

35. A. Roth, Vacuum Technology, 2nd Edition (North Holland, Amsterdam, 1982).

36. Although an alternate definition of dissociation fraction, $(\rho_1^0)/(\rho_1^0+2\rho_2^0)$, is often used, we prefer the definition given by Eq. 45 since it is more directly analogous to the fraction of events related to atoms as obtained in crossed beams experiments (See Ref. 6).

37. H. Lew, in Methods of Experimental Physics, Vol. 4/A, edited by V. W. Hughes, and H. L. Schultz (Academic Press, New York, 1967), p.

155.

38. J. S. Ladish, Production of Polarized Electrons, Ph.D. Thesis, Yale University, 1974.

39. T. C. English and T. F. Gallagher, Rev. Sci. Instrum. 40, 1484 (1969).

40. Granville-Phillips Model 274-023 ionization gauge.

41. Mullard Model X919 BL.

42. A. F. Timothy and J. G. Timothy, Acta Electronica 14, 159 (1971).

43. M. B. Shah, D. S. Elliott, and H. B. Gilbody, J. Phys. B 20, 3501 (1987).

44. W. L. Fite and R. T. Brackman, Phys. Rev. 112, 1141 (1958).

45. ANAC Model No. 2909.

46. W. Haeberli, Ann. Rev. Nucl. Sci. 17, 373 (1967).

47. A. Hershcovitch, private communication.

48. S. T. Hood, A. J. Dixon, and E. Weigold, J. Phys. E. 11, 948 (1978).

FIGURE CAPTIONS

Fig. 1. Vacuum chamber layout of beam line showing conductances between chambers for molecular hydrogen, typical pressures under operating conditions, and effective speeds of pumping modules for both hydrogen and air, the latter enclosed in parentheses. The numbered elements shown are (1) hydrogen source chamber, (2) diffusion pump port, (3) turbomolecular pump port, (4) hexapole chamber, (5) hexapole magnets, (6) beam chopper, (7) beam-line gate valve, (8) ion pump port, (9) interaction chamber, (10) ion pump port, (11) Stern-Gerlach magnet, (12) cryopump port, (13) quadrupole/dump chamber, and (14) quadrupole mass analyzer. Not shown are bypass pumping lines and valves between the hexapole and hydrogen source chambers and between the quadrupole and interaction chambers. Note that conductances for air may be obtained by multiplying the hydrogen conductances by a factor of 0.27.

Fig. 2(a) Schematic diagram of beam-line components in the source region showing locations and critical dimensions of (1) nozzle, (2) skimmer, and (3) hexapole magnet entrance. All dimensions shown are in mm.

(b) Schematic diagram of major components of beam line showing locations and critical dimensions of (1) nozzle, (2) skimmer, (3) hexapole magnets, (4) beam chopper, (5) spin guiding magnetic field coils (transverse rotator

prior to Stern-Gerlach magnet not shown), (6) refrigerated tube and aperture, (7) interaction region beam collimator, (8) crossed beams intersection point, (9) channel electron multiplier, (10) polarimeter slits, (11) Stern-Gerlach entrance aperture, (12) Stern-Gerlach magnet, and (13) QMA entrance slit. All dimensions shown are in mm.

Fig. 3. Artist's representation of the rf hydrogen source.

Fig. 4. Schematic diagram of the hydrogen gas handling system. The numbered elements shown are (1) hydrogen ballast tank, (2) palladium finger, (3) glass to metal break, (4) exit to rf discharge volume (5) thermocouple vacuum gauge, (6) electrical feedthrough for palladium heating (7) source chamber bypass valve, (8) dry nitrogen admittance valve, (9) hydrogen admittance valve, (10) hydrogen purge valve, (11) low-pressure hydrogen holding tank, (12) valves and pressure regulators, (13) high-pressure hydrogen gas cylinder.

Fig. 5. Scale drawing of the hexapole magnet in cross sectional view.

Fig. 6. Scale drawing of the Stern-Gerlach magnet in cross sectional view.

Fig. 7. Breit-Rabi diagram of ground state hydrogen.

Fig. 8. Effective magnetic moments of the ground state hydrogen hyperfine multiplet as functions of magnetic field H and field parameter χ.

Fig. 9. Hyperfine coupling function $f(\chi)$.

Fig. 10. Pictorial representation of the QMA profile used in the

polarization determination, with symbols as defined in the text.

Fig. 11. Schematic diagram of the hydrogen gas transport system showing ballast tank, connecting tubing, and rf discharge volume with nozzle.

Fig. 12. Coordinate system and angles used in Monte-Carlo ray tracing computation.

Fig. 13. Radial dependence of low-field polarization P(0) in (a) and high-field state selection parameter s in (b) at the interaction region. Points with error bars reflecting counting statistics were obtained from the field-dependent μ_{eff} Monte-Carlo computation, while the solid and dashed lines represent the results of the optical model and Monte-Carlo analysis respectively for constant $\mu_{eff} = \pm \mu_B$.

Fig. 14. Results of field dependent μ_{eff} Monte-Carlo analysis for the low-field polarization P(0) in (a) and high-field state selection parameter s in (b) as functions of the horizontal position of the first acceptance slit of the Stern-Gerlach polarimeter. The data represent convolutions over the acceptance dimensions of the polarimeter (0.7 mm wide by 2.5 mm high) with the error bars reflecting counting statistics only.

Fig. 15. Monte-Carlo generated beam profiles containing convolutions with the horizontal acceptance window of the QMA. The results in (a), obtained with the Stern-Gerlach magnet turned off, are shown separately for the four hyperfine magnetic substates and are labeled in

accordance with the high-field designations (m_S, m_I). The profile in (b) is the combined result for all substates obtained with a 5 A driving current in the Stern-Gerlach magnet.

Fig. 16. Stern-Gerlach right-left profile asymmetry Δ_H. The solid dots are the results obtained from the Monte-Carlo analysis, with the solid line connecting them drawn to aid the eye. The data points shown are scaled as explained in the text based upon actual QMA measurements carried out in accordance with the description in Section III B. For the display of the Monte-Carlo results, standard magnetic circuit theory was used to relate the Stern-Gerlach driving current to the field and field gradient of the two-wire geometry (Ref. 15).

Fig. 17. Atomic density ρ at the interaction region as a function of radial position. The solid and dashed lines are the results from the Monte-Carlo analysis for the field-dependent μ_{eff} and the constant $\mu_{eff} = \pm \mu_B$ cases, respectively, as indicated on the figure. Also shown is the result from the optical model (dashed line with dots) which assumes a constant $\mu_{eff} = \pm \mu_B$.

Fig. 18. (a) Spectral transmittance $\Omega_+(K)$ for $m_S = + {}^1/_2$ atoms reaching the interaction region. The results are from the optical model (solid line) and the phase space method (dashed line). (b) Maxwellian spectral density function $F_{V^2}(K)$. (c) Spectral transmission $\Omega_+(R)\ F_{V^2}(K)$ for $m_S = + {}^1/_2$ atoms reaching the interaction region, calculated from the optical model. (d) Spectral transmission $\Omega_-(K)$

$F_V^2(K)$ for $m_S = -\frac{1}{2}$ atoms reaching the interaction region, calculated from the optical model.

Fig. 19. QMA beam profile scans carried out as described in Section III.B. The raw data shown are for the Stern-Gerlach magnet current off in (a) and a 3 A driving current in (b).

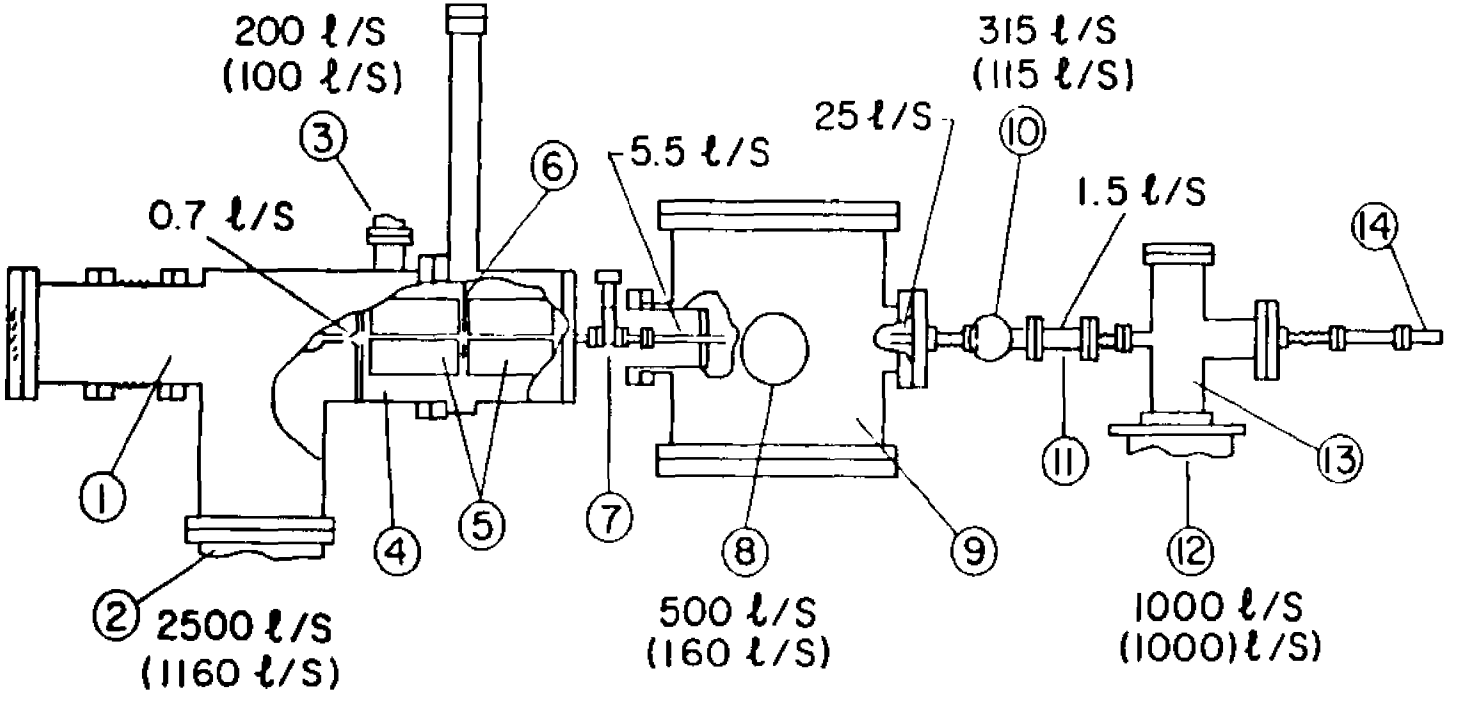
200 ℓ/S
(100 ℓ/S)
315 ℓ/S
(115 ℓ/S)
25 ℓ/S
5.5 ℓ/S
1.5 ℓ/S
0.7 ℓ/S
2500 ℓ/S
(1160 ℓ/S)
500 ℓ/S
(160 ℓ/S)
1000 ℓ/S
(1000) ℓ/S

FIG. 1

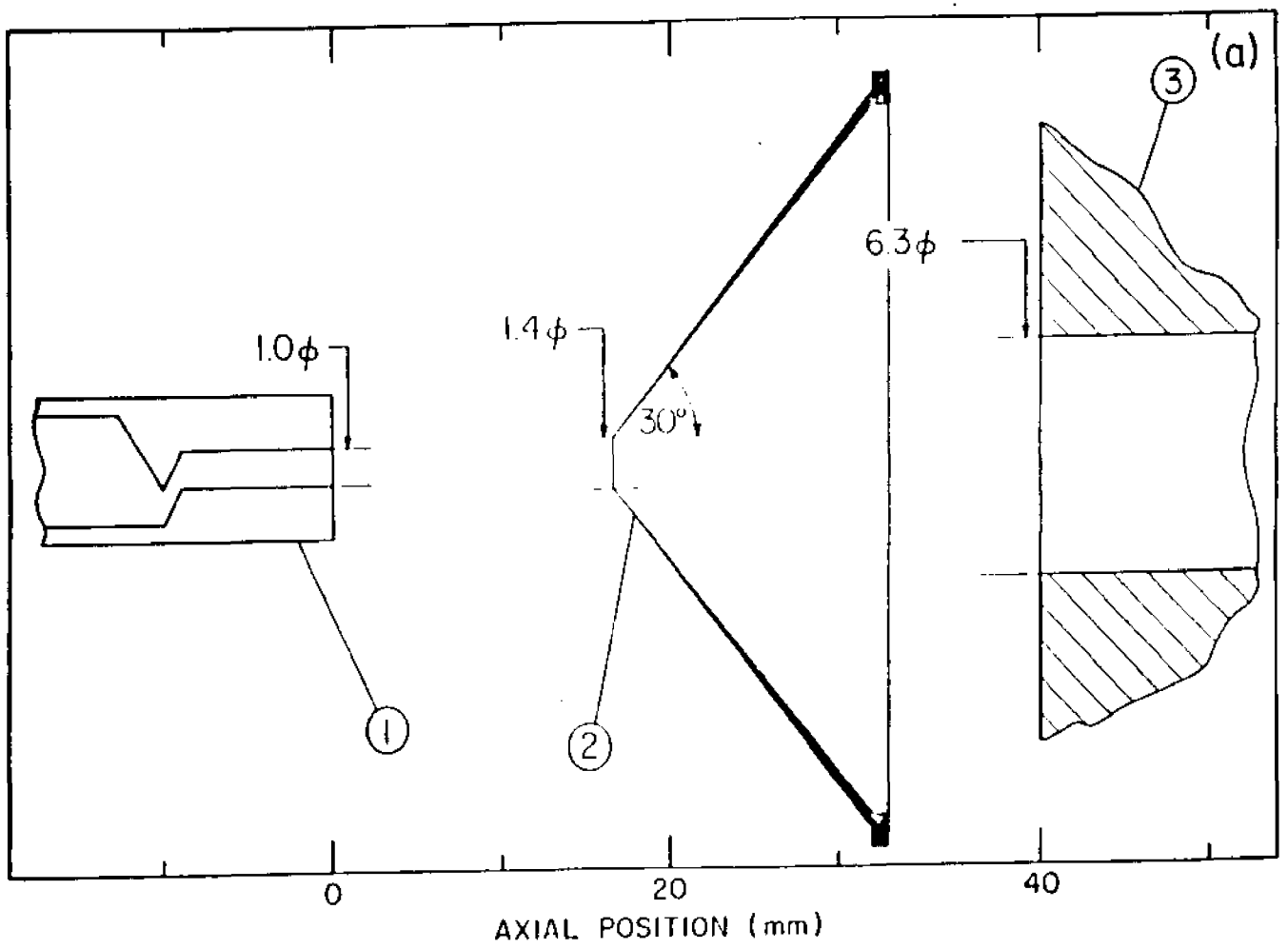

FIG. 2(a)

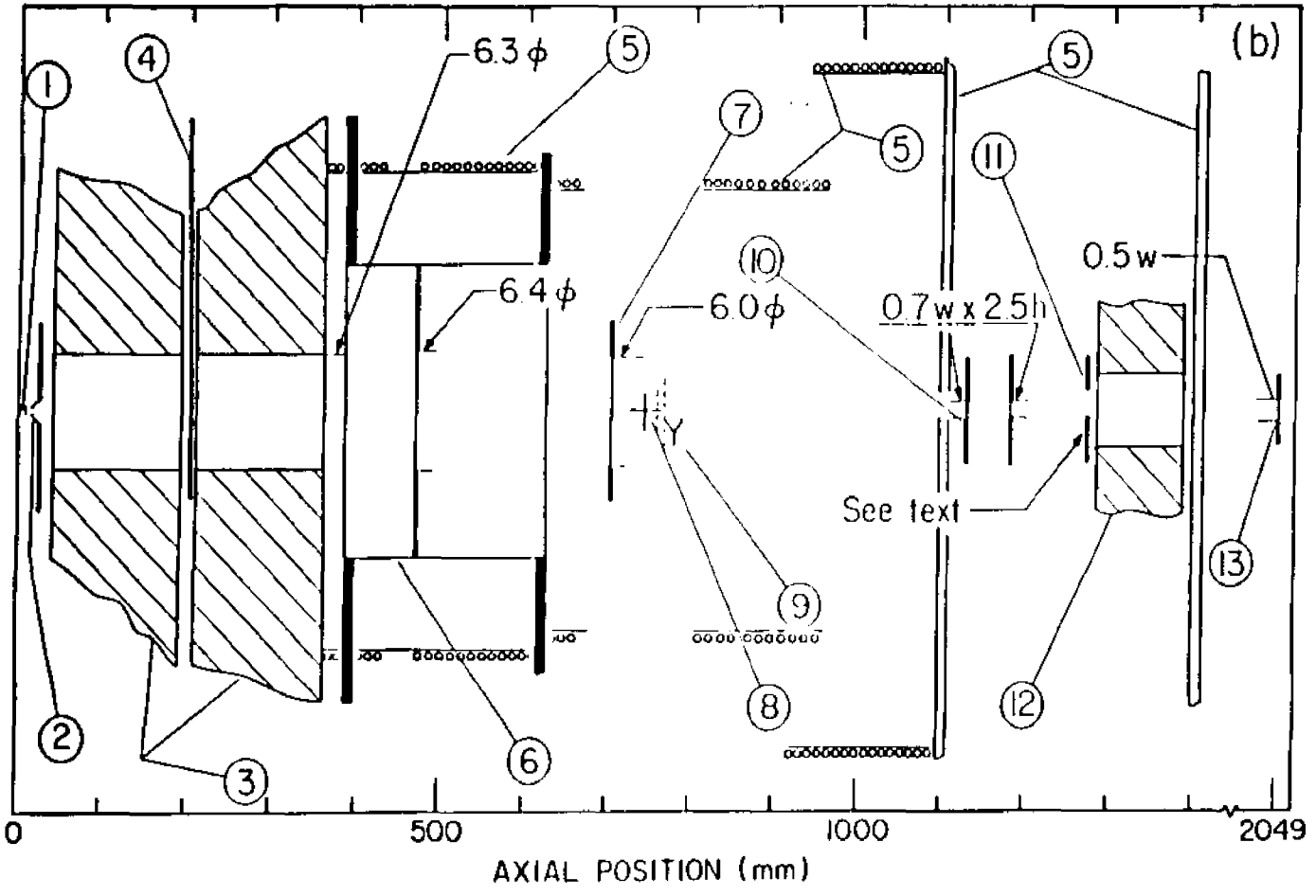
(b)
6.3 ϕ
6.4 ϕ
6.0 ϕ
0.7w x 2.5h
0.5w
See text
Y
0
500
1000
2049
AXIAL POSITION (mm)

FIG. 2(b)

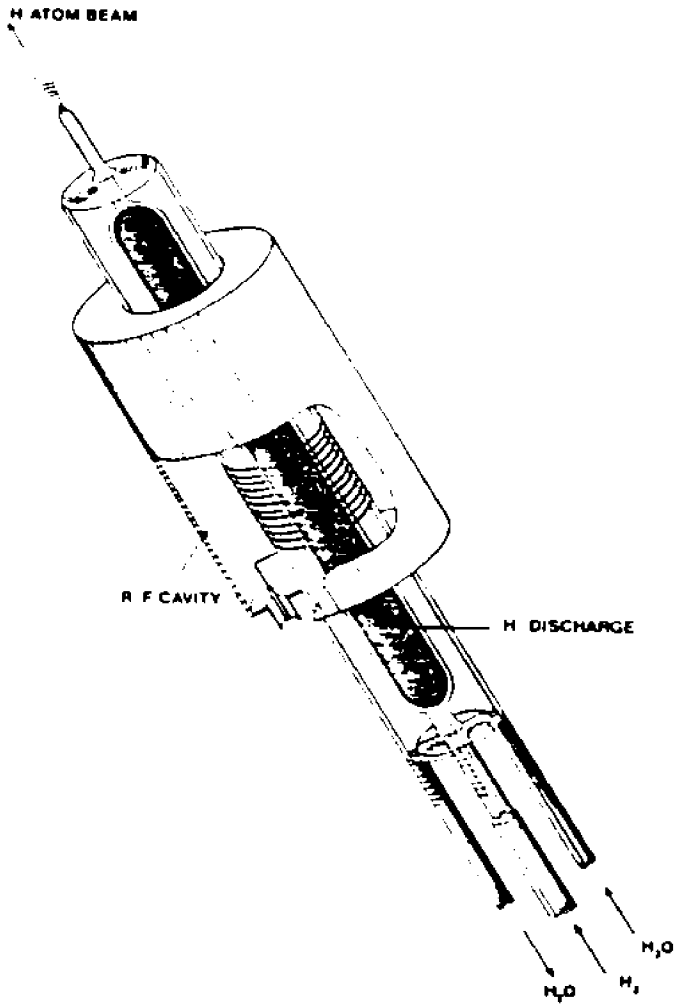

FIG. 3

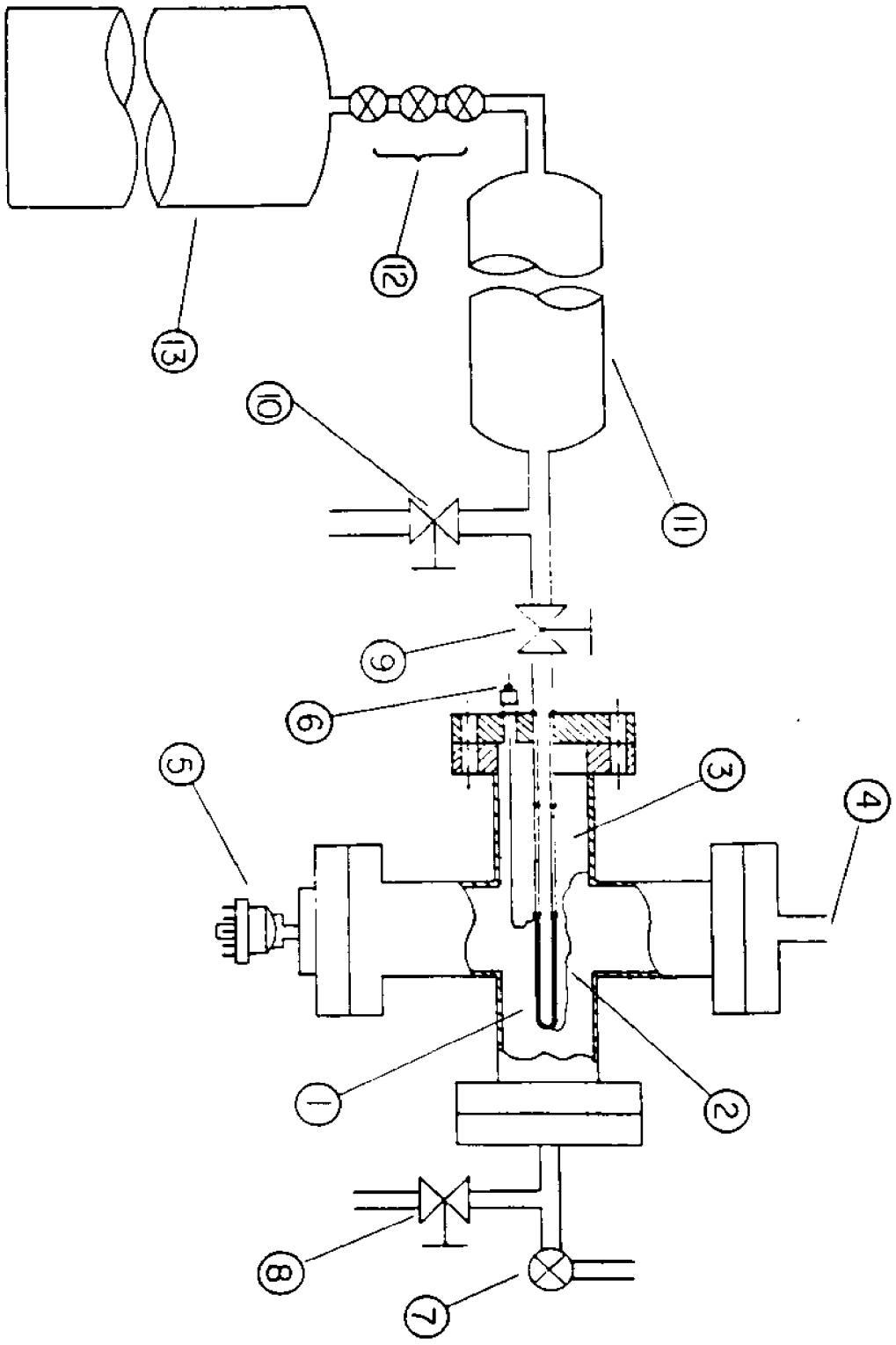

FIG. 4

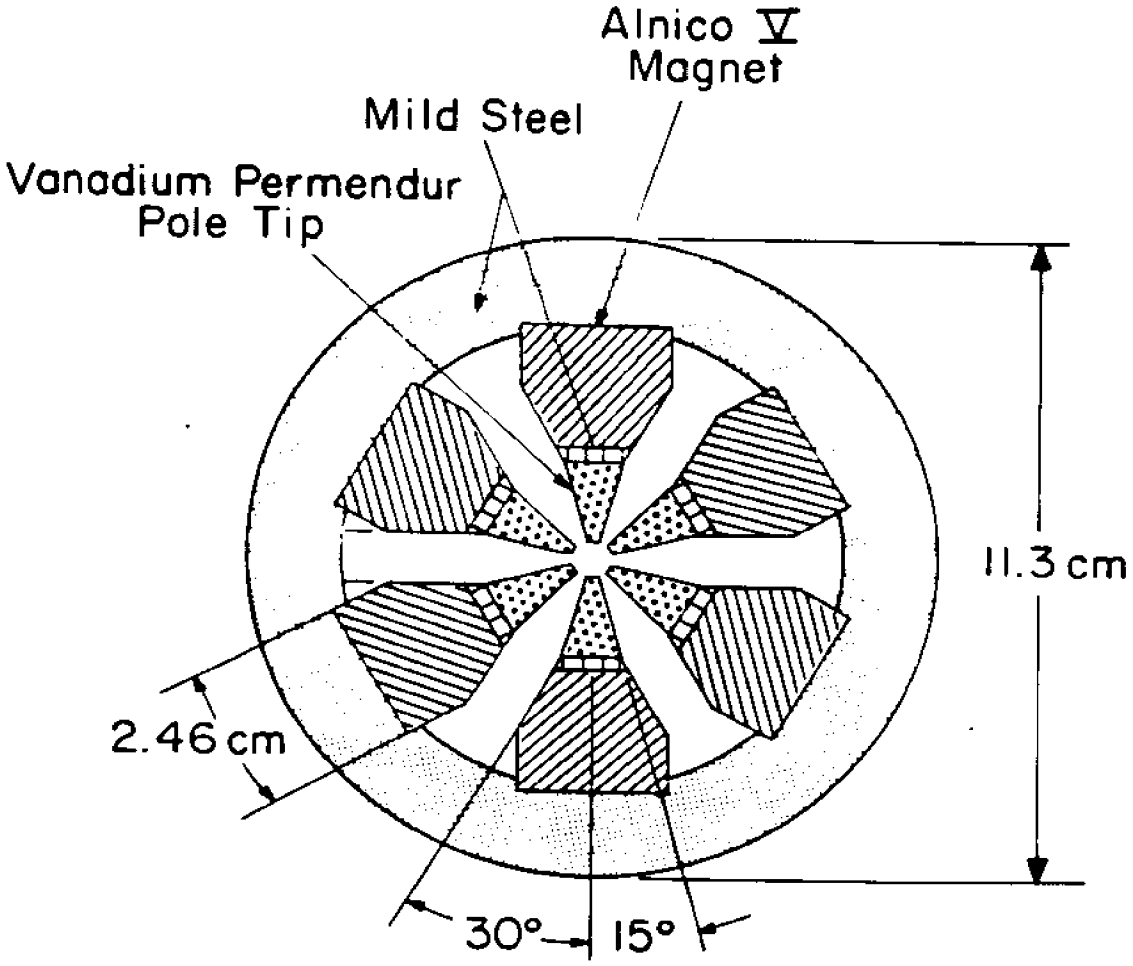
Alnico V
Magnet
Mild Steel
Vanadium Permendur
Pole Tip
11.3 cm
2.46 cm
30°
15°

FIG. 5

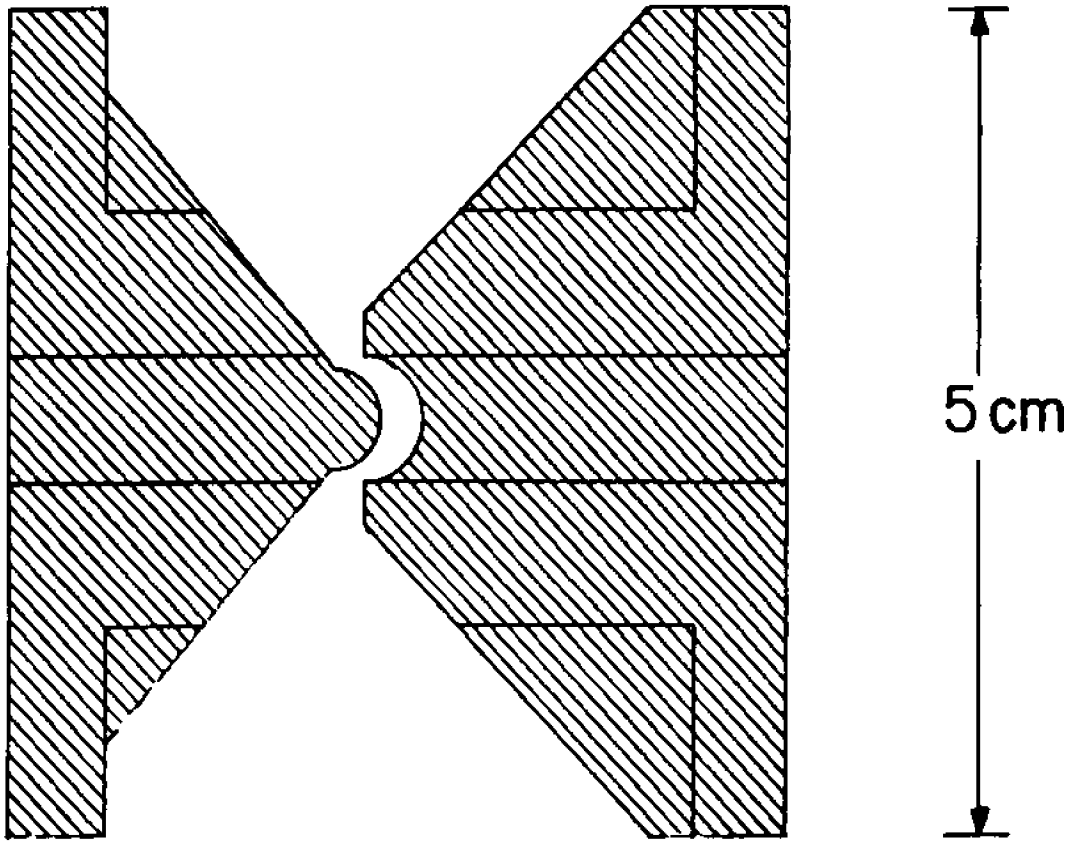

FIG. 6

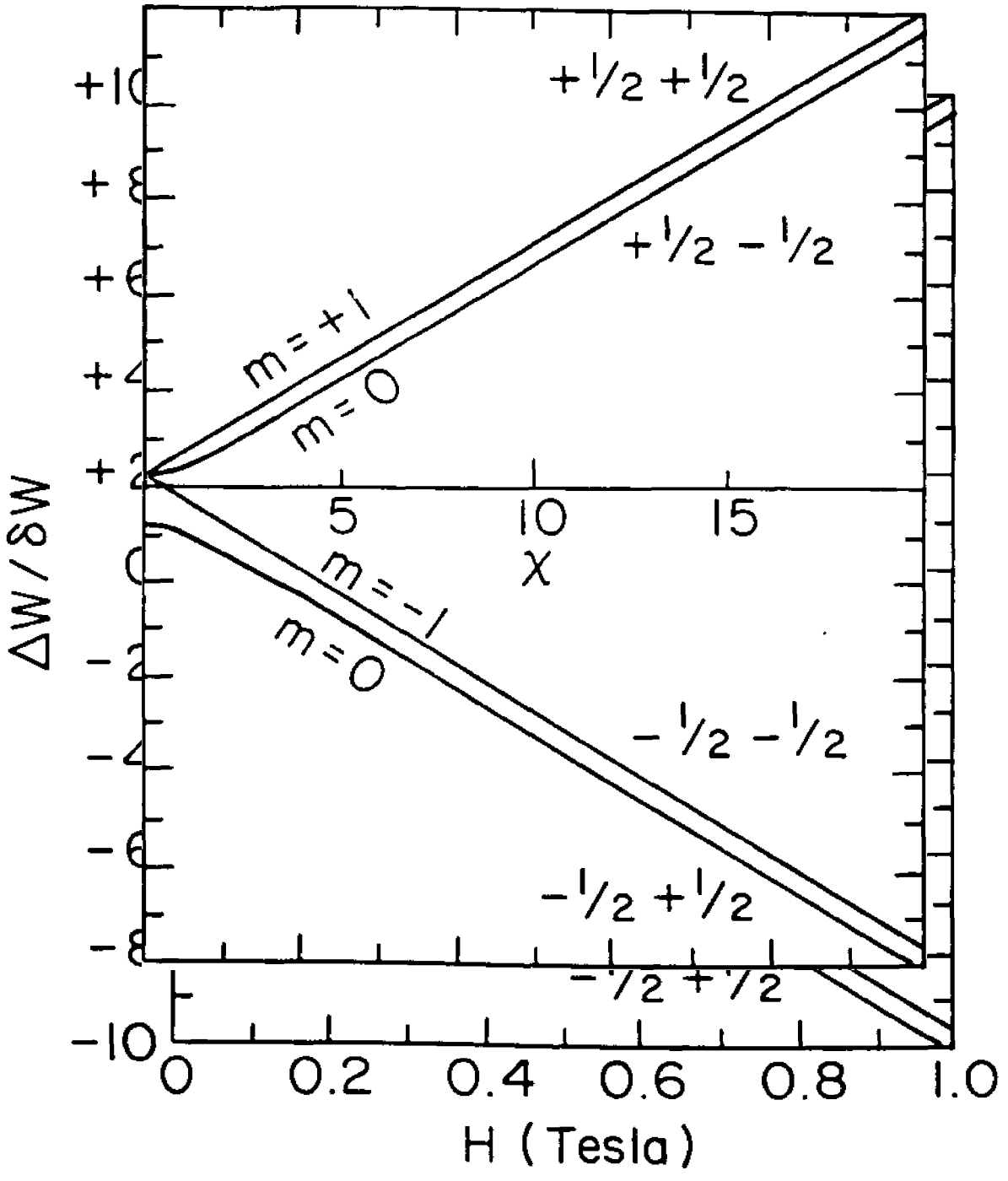
+1
+8
+6
+4
+2
0
-2
-4
-6
-8
-10
ΔW / δW
+½ +½
+½ -½
m=+1
m=0
5
10
15
χ
m=-1
m=0
-½ -½
-½ +½
-½ +½
0
0.2
0.4
0.6
0.8
1.0
H (Tesla)

FIG. 7

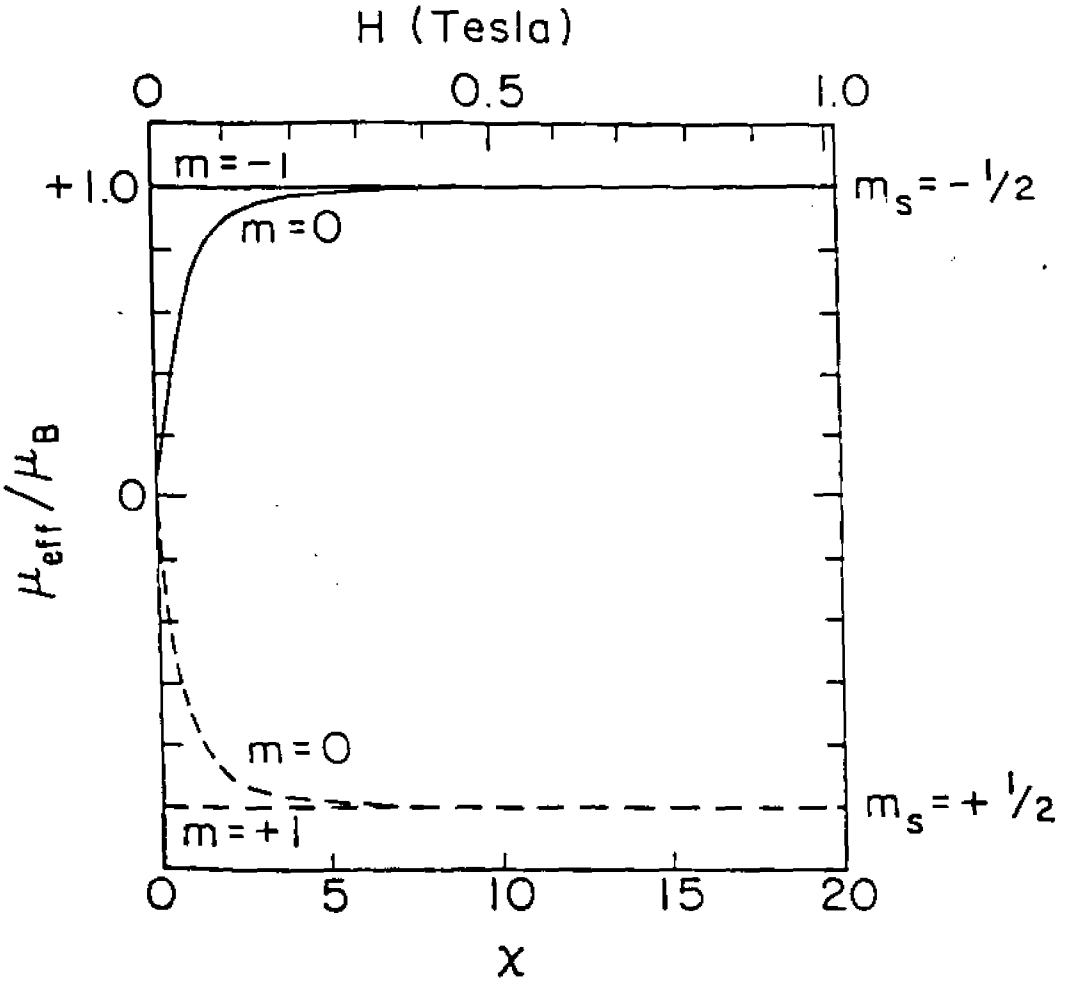

FIG. 8

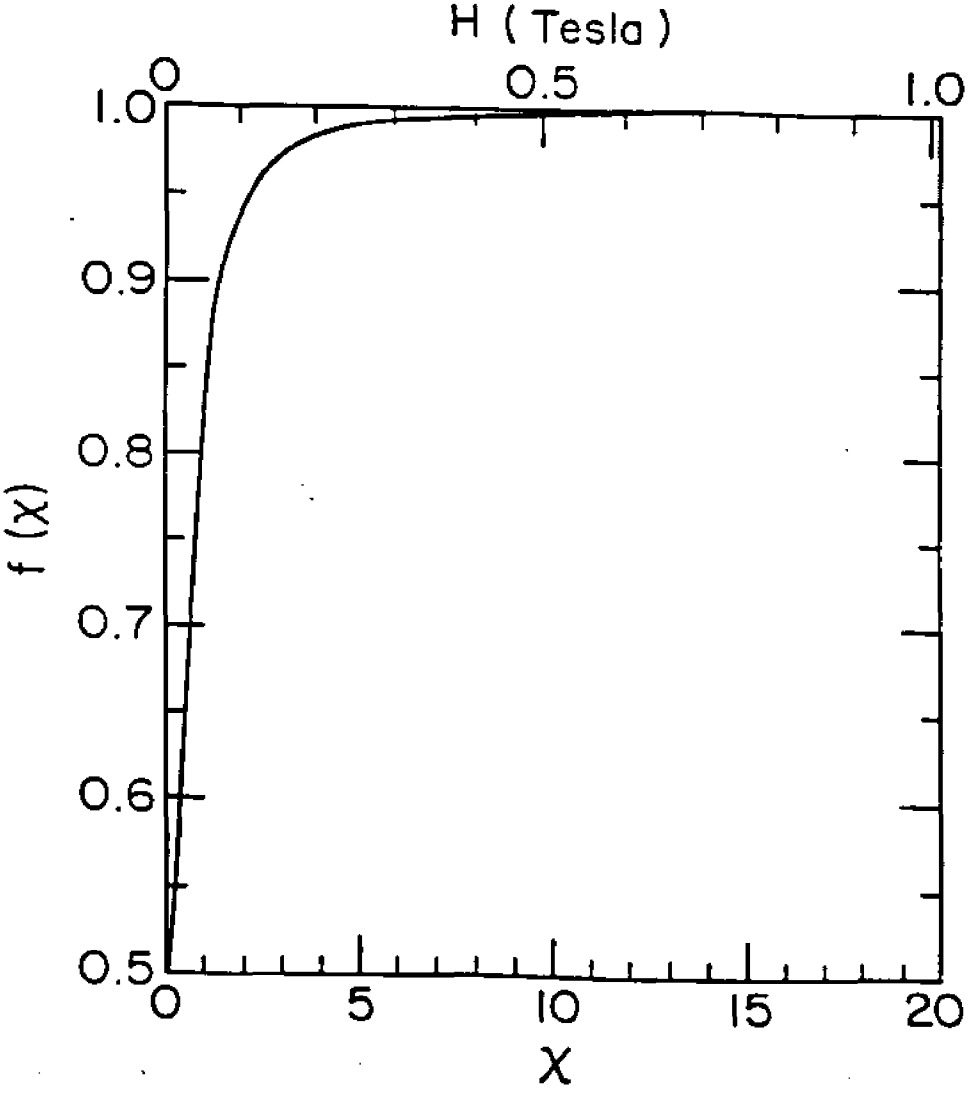

FIG. 9

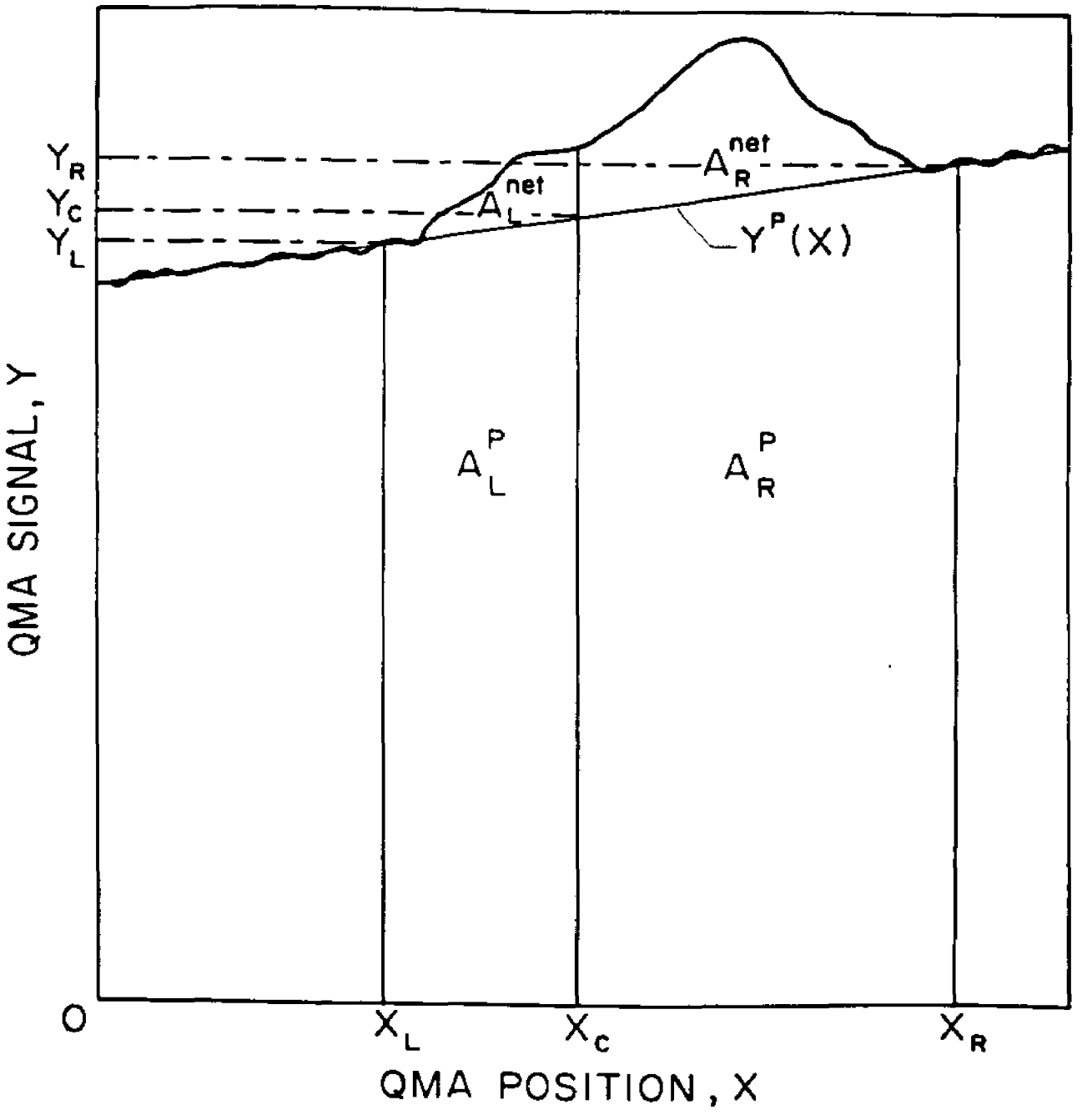
Y_R
Y_C
Y_L
A_L^{net}
A_R^{net}
$Y^P(X)$
A_L^P
A_R^P
QMA SIGNAL, Y
O
X_L
X_C
X_R
QMA POSITION, X

FIG. 10

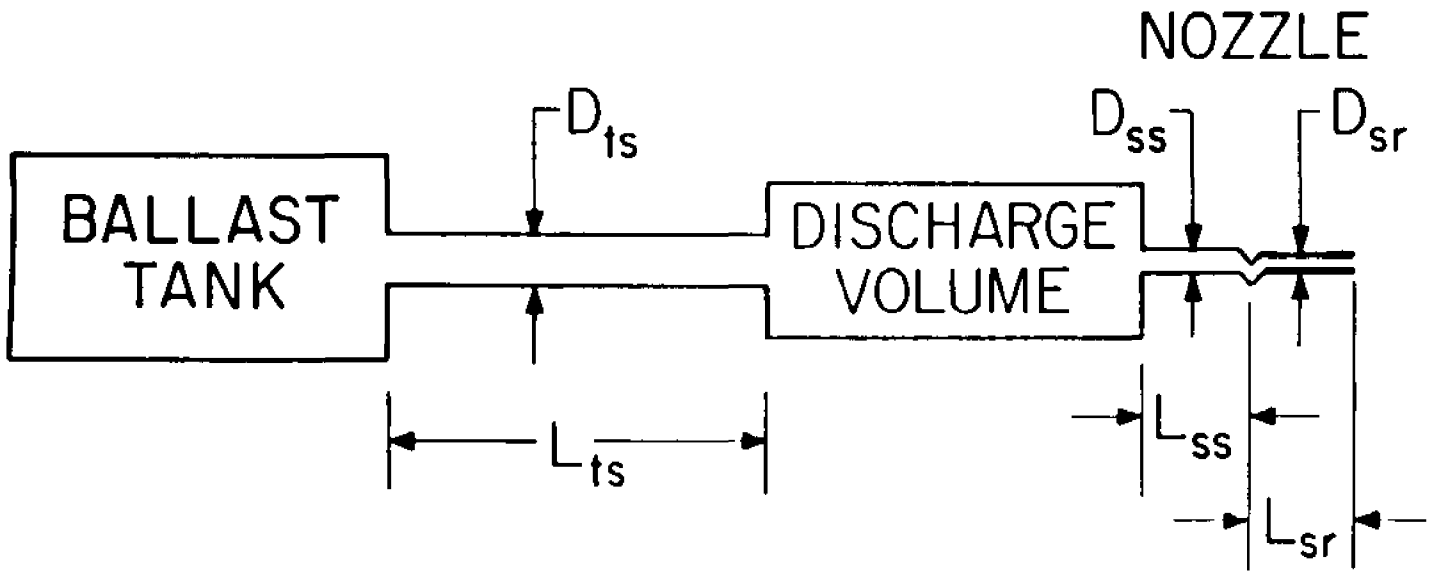
NOZZLE
D_{ts}
D_{ss}
D_{sr}
BALLAST TANK
DISCHARGE VOLUME
L_{ts}
L_{ss}
L_{sr}

FIG. 11

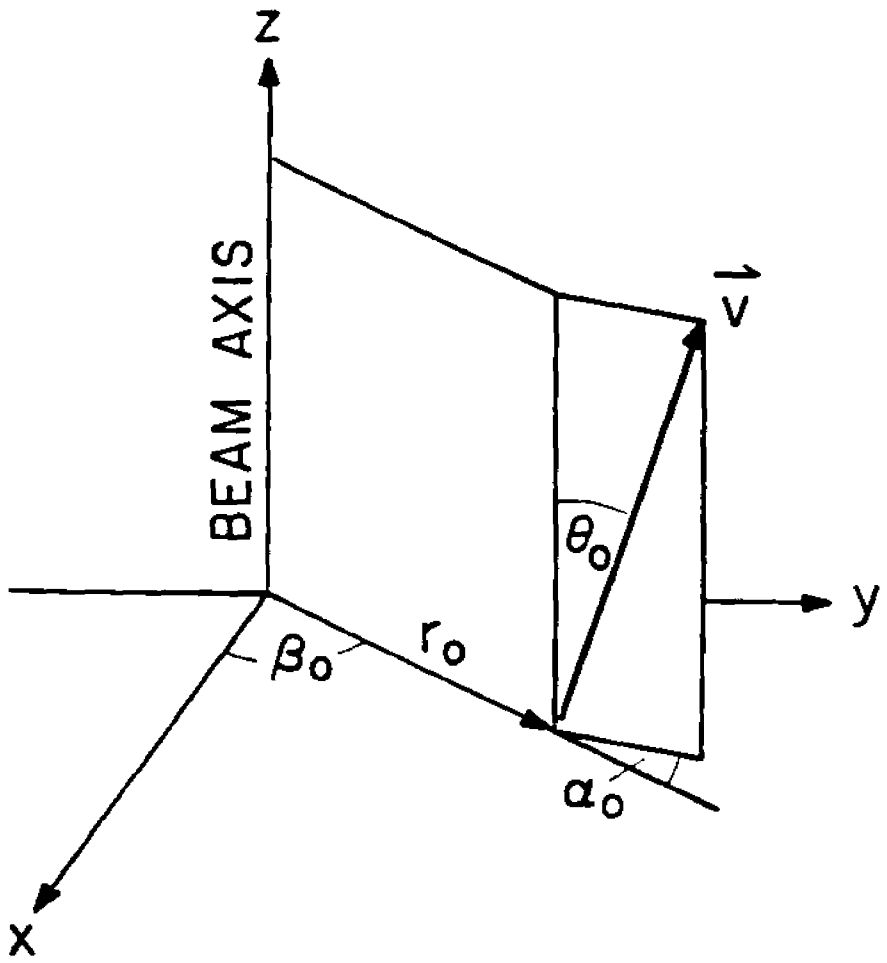

FIG. 12

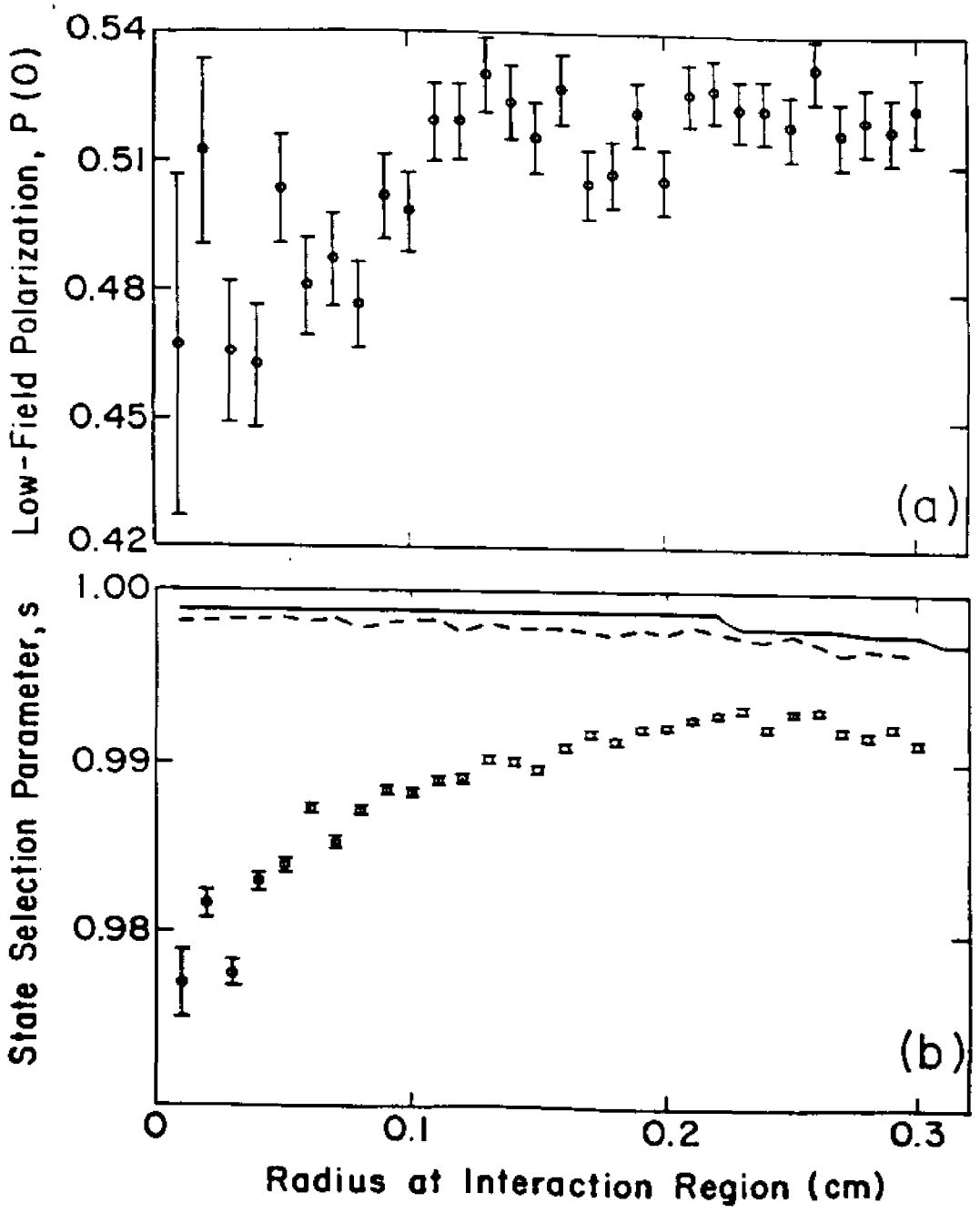
0.54
0.51
0.48
0.45
0.42
Low-Field Polarization, P(0)
(a)
1.00
0.99
0.98
State Selection Parameter, s
(b)
0
0.1
0.2
0.3
Radius at Interaction Region (cm)

FIG. 13

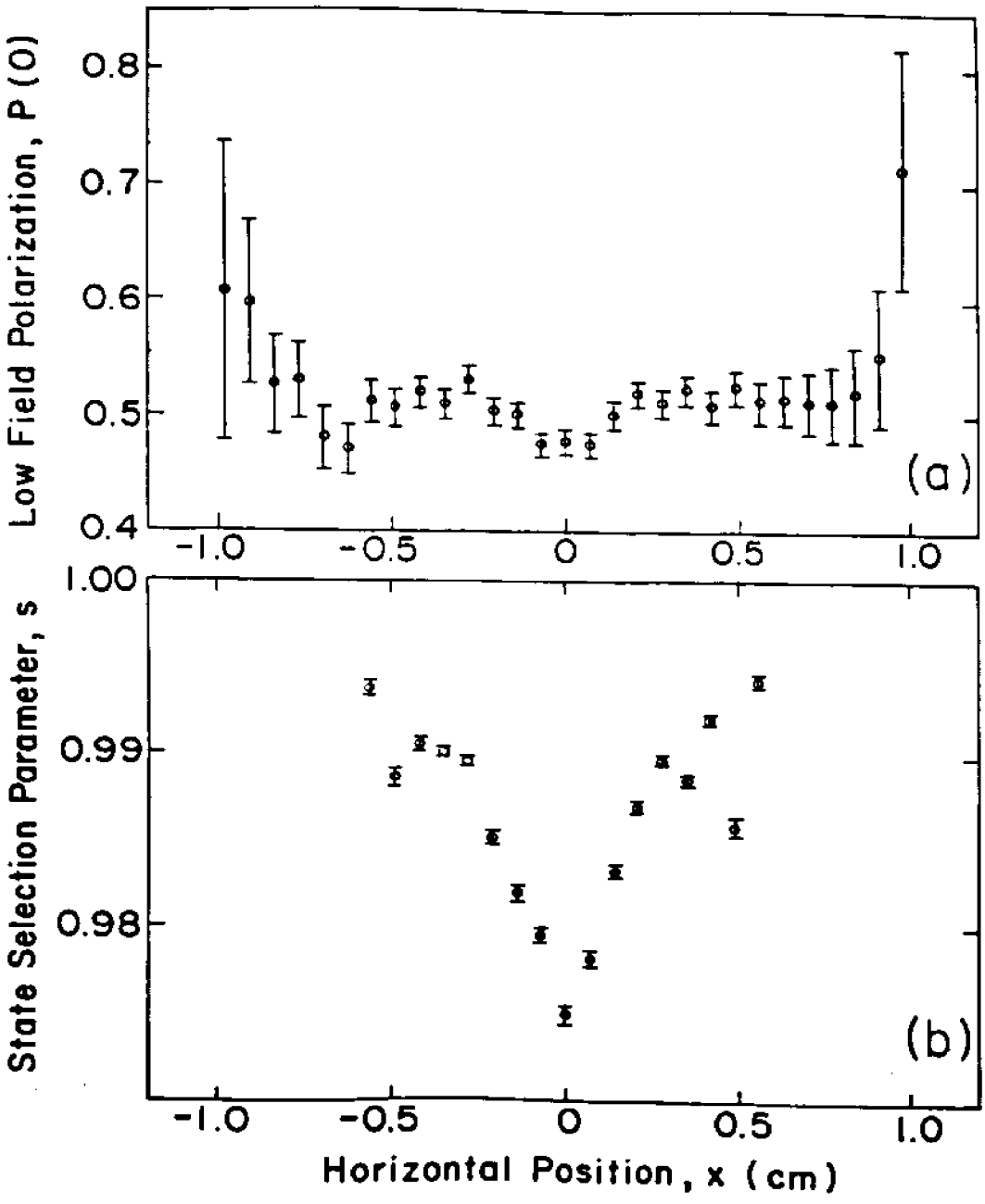
Low Field Polarization, P(0)
0.8
0.7
0.6
0.5
0.4
-1.0
-0.5
0
0.5
1.0
(a)
State Selection Parameter, s
1.00
0.99
0.98
-1.0
-0.5
0
0.5
1.0
(b)
Horizontal Position, x (cm)

FIG. 14

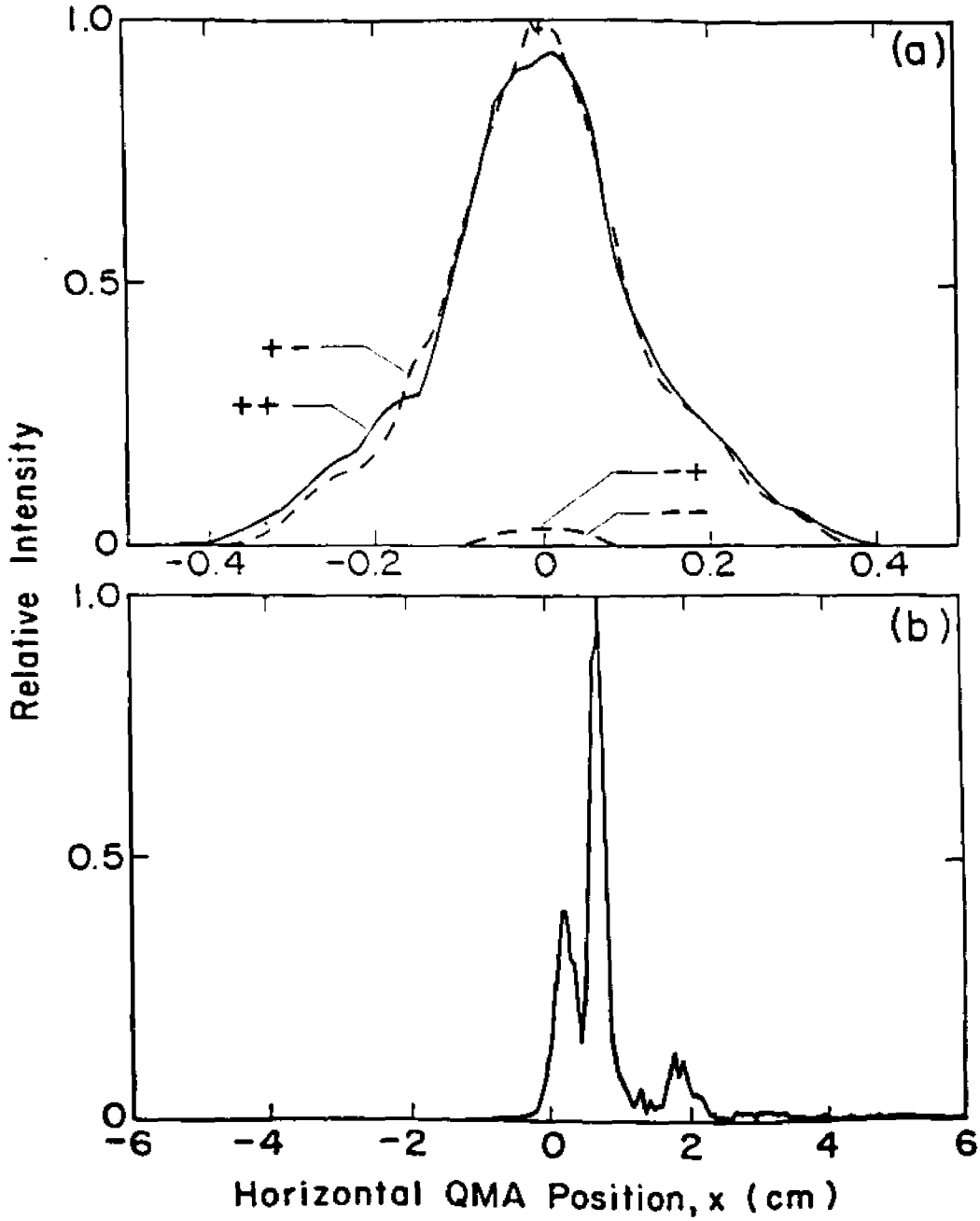
1.0
0.5
0
(a)
+ -
++
- +
- -
-0.4
-0.2
0
0.2
0.4
1.0
0.5
0
(b)
-6
-4
-2
0
2
4
6
Relative Intensity
Horizontal QMA Position, x (cm)

FIG. 15

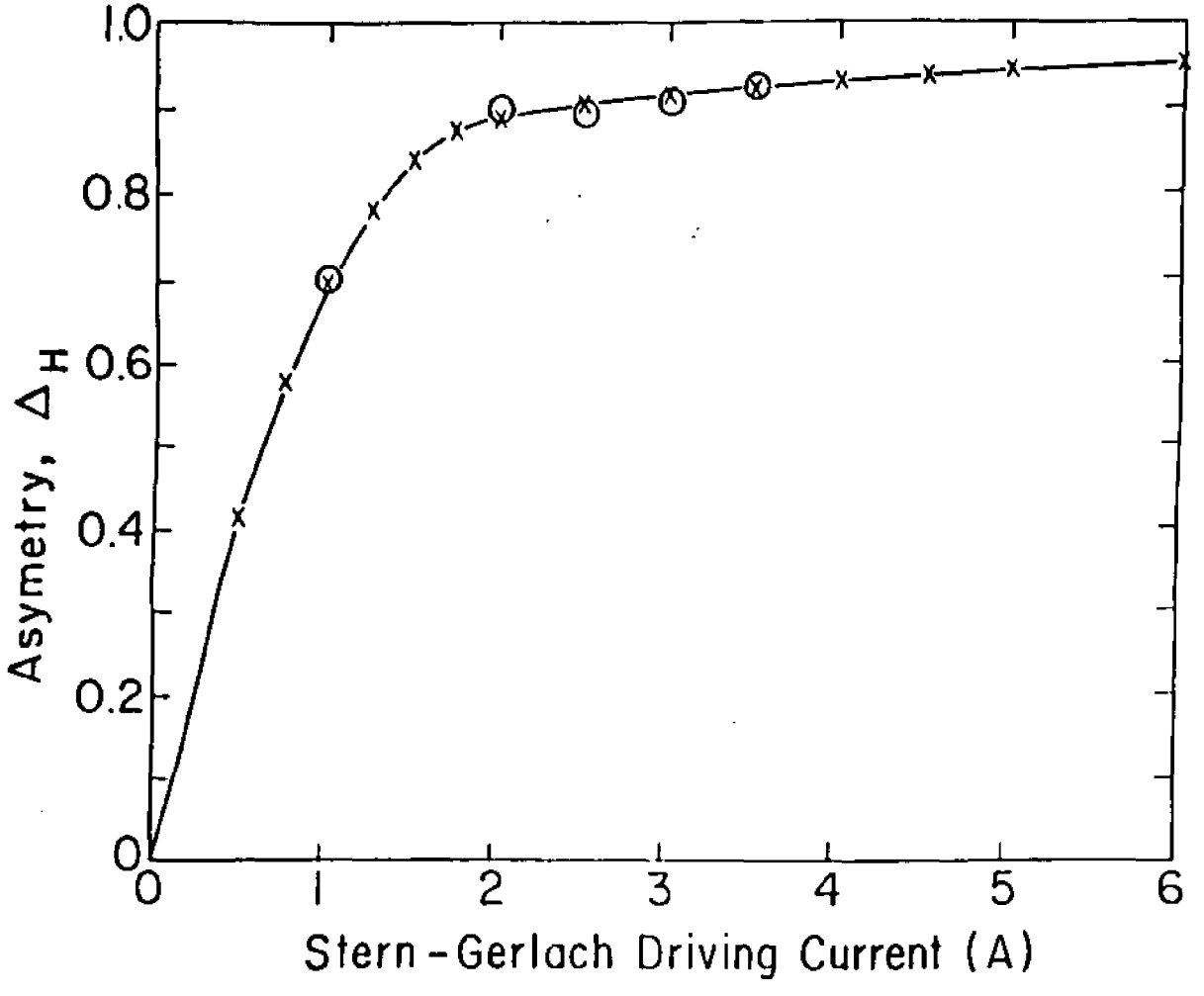
1.0
0.8
0.6
0.4
0.2
0
Asymetry, Δ_H
0
1
2
3
4
5
6
Stern-Gerlach Driving Current (A)

FIG. 16

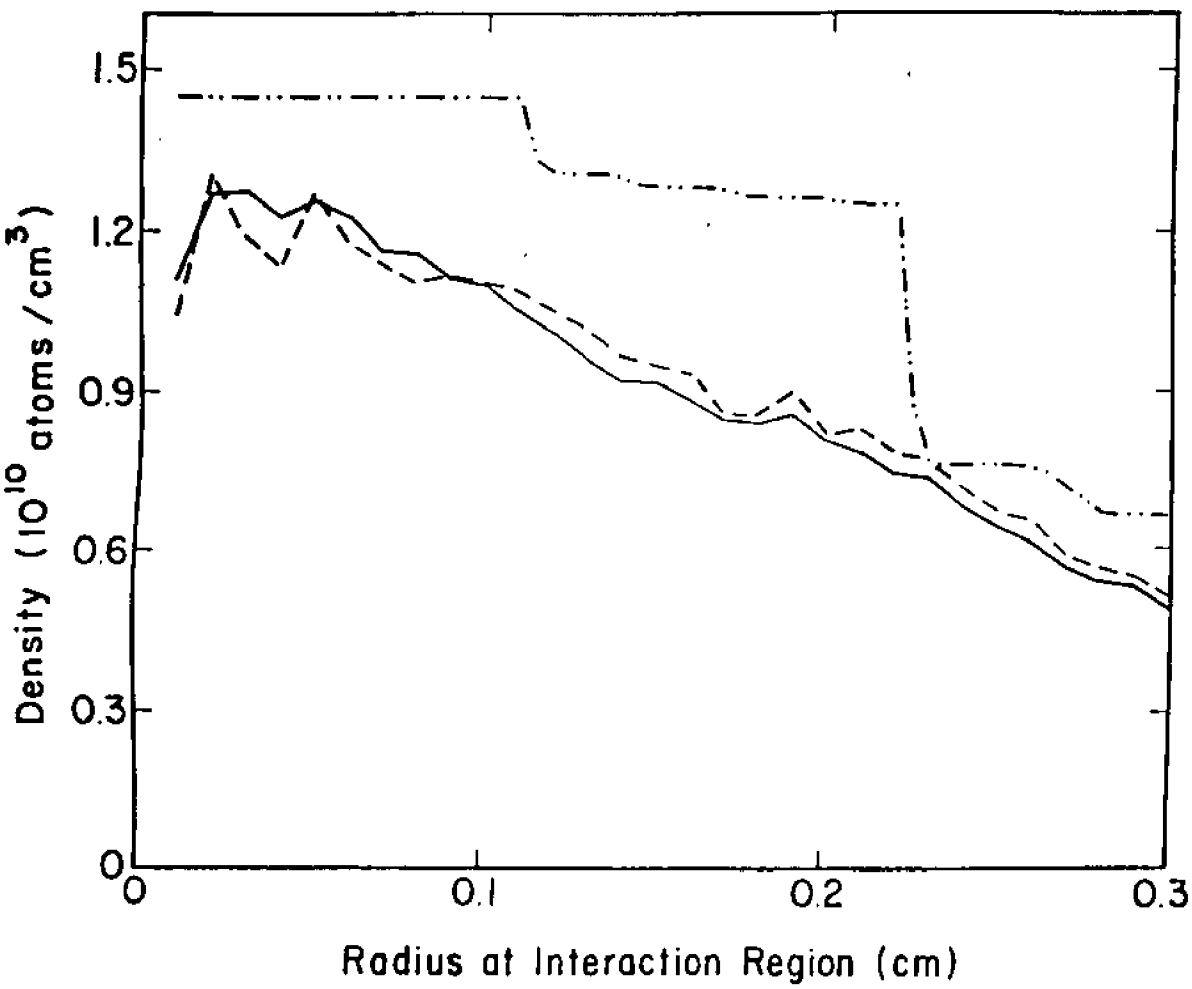
1.5
1.2
0.9
0.6
0.3
0
0
0.1
0.2
0.3
Density (10^{10} atoms/cm^3)
Radius at Interaction Region (cm)

FIG. 17

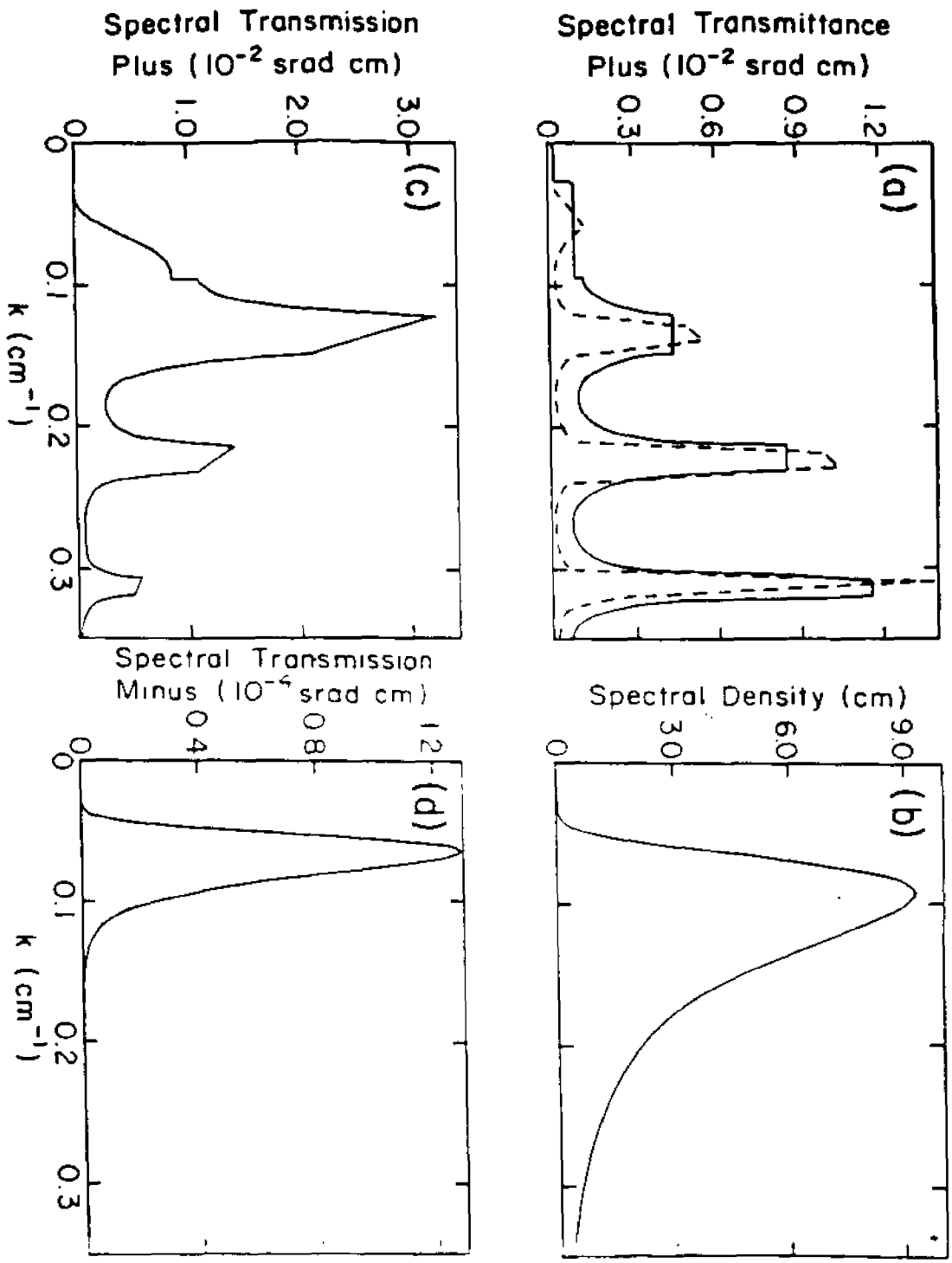
Spectral Transmittance
Plus (10^{-2} srad cm)
0
0.3
0.6
0.9
1.2
(a)
Spectral Transmission
Plus (10^{-2} srad cm)
0
1.0
2.0
3.0
(c)
k (cm^{-1})
0
0.1
0.2
0.3
Spectral Density (cm)
0
3.0
6.0
9.0
(b)
Spectral Transmission
Minus (10^{-6} srad cm)
0
0.4
0.8
1.2
(d)
k (cm^{-1})
0
0.1
0.2
0.3

FIG. 18

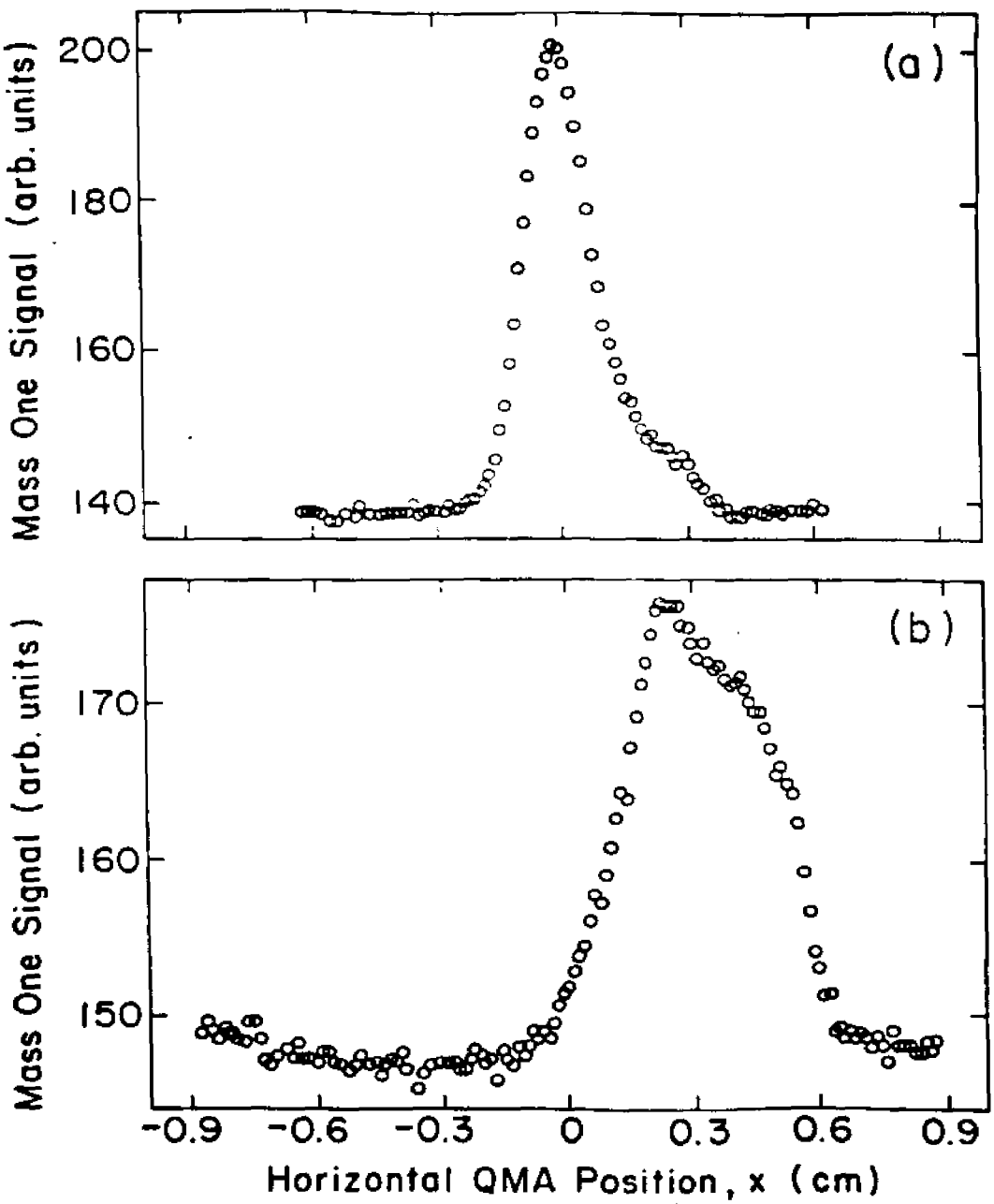
(a)
Mass One Signal (arb. units)
200
180
160
140
(b)
Mass One Signal (arb. units)
170
160
150
-0.9
-0.6
-0.3
0
0.3
0.6
0.9
Horizontal QMA Position, x (cm)

FIG. 19

APPENDIX C:COMPUTER SYSTEM AND ELECTRONICS

1. INTRODUCTION

This appendix describes the computer system used for the experimental control and data acquisition in the study of spin-dependent collisions of polarized electron and hydrogen atom beams. The description is divided into two sections. The first, dealing with the LSI 11/23 computer hardware and interfacing used for data acquisition and control, contains descriptions of the electronic modules, their addresses, and their bit assignments. The second, a brief writeup of user's applied programs, concentrates on the main control software. It should be noted that the communication between the LSI 11/23 computer, used for acquisition and control, and the VAX 11/780 computer, used for off-line data analysis, is accomplished by means of Kermit, a program provided by the Columbia University Computer Center.

2. COMPUTER HARDWARE AND INTERFACE

(a) Computer Hardware Specification

The experiment is controlled by a DEC LSI11 microcomputer supplied by the ADAC Corporation and specified as follows:

1000-M-60-110	Data acquisition system backplane 19" Subrack, 110 volt PSU; 18 std half quad slots; 11-full/22-half quad slots, 4 with interboard bus	
-	Master panel unit	-
1823AA	11/23 CPU board, incs MM unit	half quad
1823KDF	11/23 Floating point option	-
18MS/LK	MOS RAM, 256K	half quad
840-2-120-60-S	8" Dual floppy disc unit and interface	half quad
880-3-D-61-1	8" Winchester hard disc and interface	half quad
1799J	Asynch serial interface, 4 ports, RS232 only DC-DC conversion	half quad
1012EX-32SE	A/D converter multiplexor (to be added later)	half quad
1412DA-4-A-V-0-0	D/A converter, 4 channel 2 units	2 x half quad
1604 OPI	Pulse counter for use as scaler 2 units	2 x half quad
1664ATTL	4 x 16 Bit digital I/O	half quad
1632	2 x 16 Bit digital I/O	half quad
1604 POC	Pulse output controller	half quad

(b) Address and Bit Assignment Summary

The interfaces are arranged on the memory mapped principle. Interface register contents may thus be addressed and processed in the same way as memory data, using the full instruction set of the processor.

The memory map for devices and interfaces is as follows:

Disk drive interface	CH0	176500
	CH1	176510
	CH2	176520
	CH3	176560
A-D Conversion		176770
"	Vector	130
1604OPI Pulse Counter 1		164400
1604OPI Pulse Counter 2		164410
1604POC		64600
1601GPT Real time clock		164700
1601 Vector 310		
1412 Digital to Analog 1		176750
1412 Digital to Analog 2		176760
1664TTL 64 Bit digital I/O		164100
1632TTL 32 Bit digital I/O		167770

(c) Interfacing

The LSI-11 microcomputer has a 38 BIT asynchronous processor bus for address, data and control lines. The address and data lines are multiplexed and most lines are bidirectional. Asynchronous bus operation is not usually found on microcomputers, but it does ensure bus operation at the maximum speed

possible with each memory and interface device. Address decoding, async bus protocol, and all bus level interfacing functions are provided by the ADAC cards.

For interfaces of this type of system operation there are three general levels of hardware as shown in Fig. C.1. They may be summarized as follows:

System bus - Processor bus, asynchronous memory mapped operation

TTL - Parallel digital signals at standard levels

User - Laboratory signal input/outputs to suit the application.

For such a system, interfacing from the system bus to the TTL level is provided by DEC compatible ADAC modules, while interfacing from the standard level outputs of the ADAC modules to the laboratory requirements is performed by an interface built at Stirling University.

In general, any interface system must provide the functions of synchronization and signal level translation. In this system, these functions are provided by the combination of ADAC and Stirling hardware, with certain synchronization and timing functions implemented in software. The interfaces have been designed mainly with TTL 74 low power Shottky logic, and the modules are powered by a local 5 volt regulator on each module, operating from NIM 6 volt or 12 volt lines.

Interconnections for digital signals are provided on flat cables, terminated in insulation displacement crimped connectors. The assignment of signals on the flat cables had to be fixed to suit that of the ADAC interface connectors, and in some cases this led to difficulties in distributing the signals to the Stirling modules. All flat cables are reversible, end to end. The layout of system is as in Fig. C.2.

The interconnections between ADAC modules and Stirling interfaces are listed below:

	ADAC	STIRLING
1012	A-D conversion	Patch Panel
1412	D-A conversion	Patch Panel
1604/POC	Pulse generator	Not used
1664	64 bit digital Input/Output	
	Register 0	16 Bit output to Qvt
	Register 1	16 Bit input from Qvt
	Register 2	10 Bit cell select to Qvt, 3 bit memory quadrant select 3 bit digital output.
	Register 3	3 Bit Qvt control, 8 bit digital output.
1632	32 Bit digital Input/Output	
	Register 0	Scaler multiplexor channel selection
	Register 1	8 Bit control of motor position
2 x 16040PI Pulse Counters		Scaler multiplexor outputs

The layout of the experimental system is given in Fig. 3, and system control and monitor are given in Table C.1 and C.2.

3. USER'S APPLIED PROGRAMS

The computer chosen to perform the tasks of controlling the apparatus and data acquisition for the system is a DEC PDP 11/23, running the RT-11 operating system. The user applied programs are written as a series of small modules, in both FORTRAN and PDP 11 assembler, with each module designated to perform a particular task.

Some of those modules are grouped together and are called by higher level programs which execute the sequences associated with a particular event. The higher level programs eventually reach the penultimate level of all the major subroutines, any of which may be initiated by entering a command at the terminal.

No attempt has been made here to describe the details or to explain the subroutine programs. Most of them are contained in manual documents and lab files. The principal subroutine used for data acquisition (Subroutine DA) is based upon the following sequence chart and conforms to the timing illustrated in Fig. C.3.

Subroutine DA Sequencing

Data	Signal	Chopper	Gate
1	Ion	Open	0
2	Ion	Close	2
3	Electron	Open	6
4	Electron	Close	8
5	H_1	Open	10
6	H_1	Close	4
7	H_2	Open	10
8	H_2	Close	4

The open or closed position of the mechanical chopper generates a signal which is sent to the computer. After a time delay t, the computer starts the data taking. As indicated in Fig. C.3, T_O and T_C are the time intervals during which computer collects the data (ion events, incident electron current, and QMA H_1 and H_2 signals) and stores the information in blind scalers separately for chopper open and closed.

The signal response time from the QMA Faraday cup electronic circuit is about 150 ms on the 10^{-9} mbar pressure scale, a value which is much longer than the movement time of the mechanical chopper, the latter being ~ 2 ms. In order to avoid any confusion of the QMA signals, the chopper is left in a given state for 500 ms, and an intermediate mass state (mass 6), for which no input is present, is inserted in the mass sequencing between H_1 and H_2 as shown above and in Fig. C.3. While in the mass 6 state the QMA Faraday cup discharges, and the instrument is then ready for the next mass signal (H_1 or H_2). The oscilloscope displays of the H_1 and H_2 are shown in the bottom of Fig. C.3. (It should be clear that the gates 10 and 4 have to be long enough to cover the entire response time of the QMA signals.)

TABLE C.I - System Control

Physical Parameter	Description	Device and Module
E_e	Electron energy at scattering point with resolution ΔE - 100 meV.	DAC Programmable power supply
$\vec{P}_e$	Electron polarization direction, determined by the position of $\lambda/4$ and $\lambda/2$ plates, moved by stepping motor	TTL I/O Stepping motor controller power supply
$\vec{P}_H$	Hydrogen atom polarization direction determined by current direction of solenoid.	TTL I/O Switching box Regular current supply
Chopper	Open or closed, controlled by stepping motor.	TTL I/O Stepping motor controller power supply
Mass 1,2,6	Selection of mass detection of QMA, controlled by voltage sent to QMA corresponding to Mass 1(H_1) Mass 2 (H_2), and Mass 6.	DAC
H_1, H_2 Beam profiles	QMA scanning, controlled by stepping motor.	TTL I/O Stepping Motor controller power supply

TABLE C.II - System Monitor

Physical Parameter	Description	Device and Module
Chopper	Status open or closed	LED and circuit Schmit trigger TTL I/O
$\lambda/4$ and $\lambda/2$	Position of $\lambda/4$ and $\lambda/2$ plates	LED and circuit TTL I/O
Voltage	Bias voltage on cathode	ADC Voltage divider
Ion	Ion signal	Channeltron and pulse forming circuits Scaler Counter
Electron	Electron current	Faraday cup Electrometer UFC Counter
H_1 and H_2	H_1 and H_2 signals	QMA Controller ADC

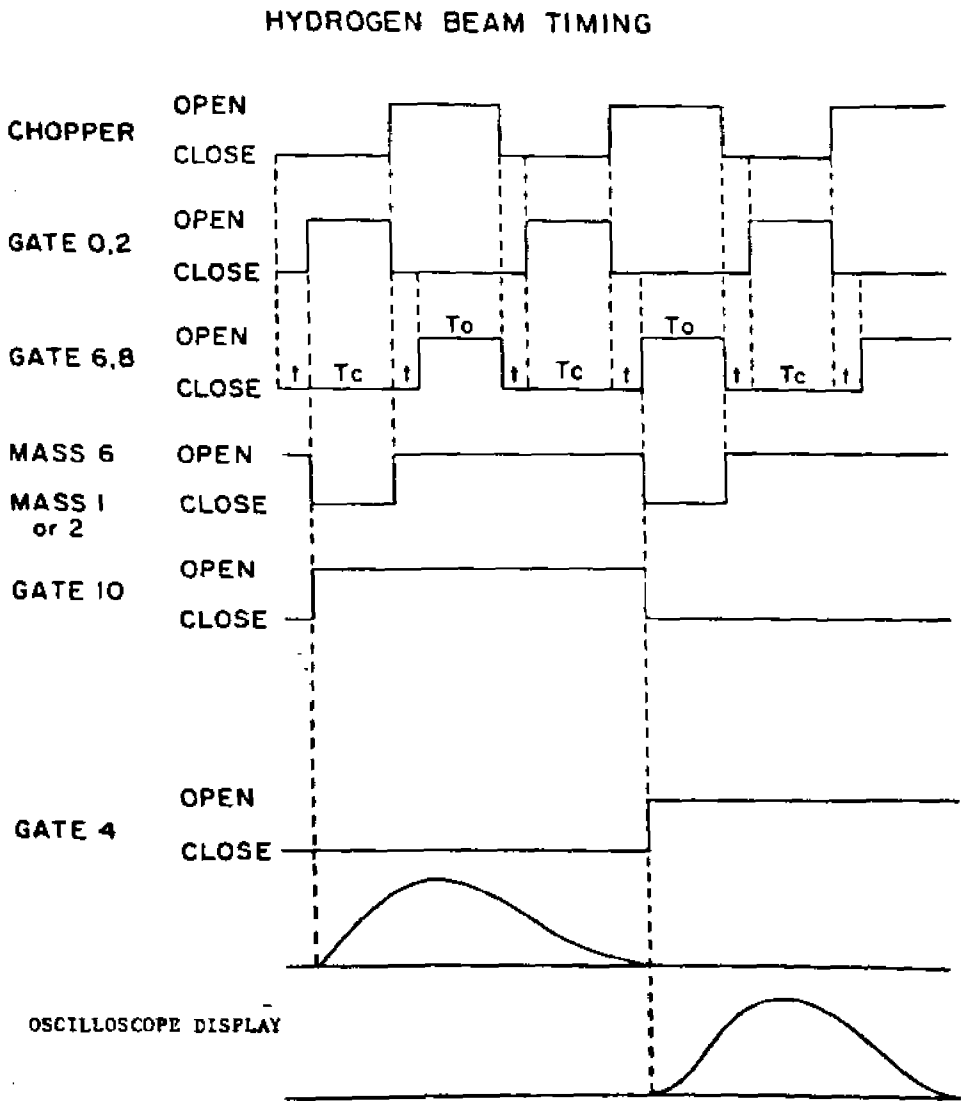

Fig. C.1. TIMING

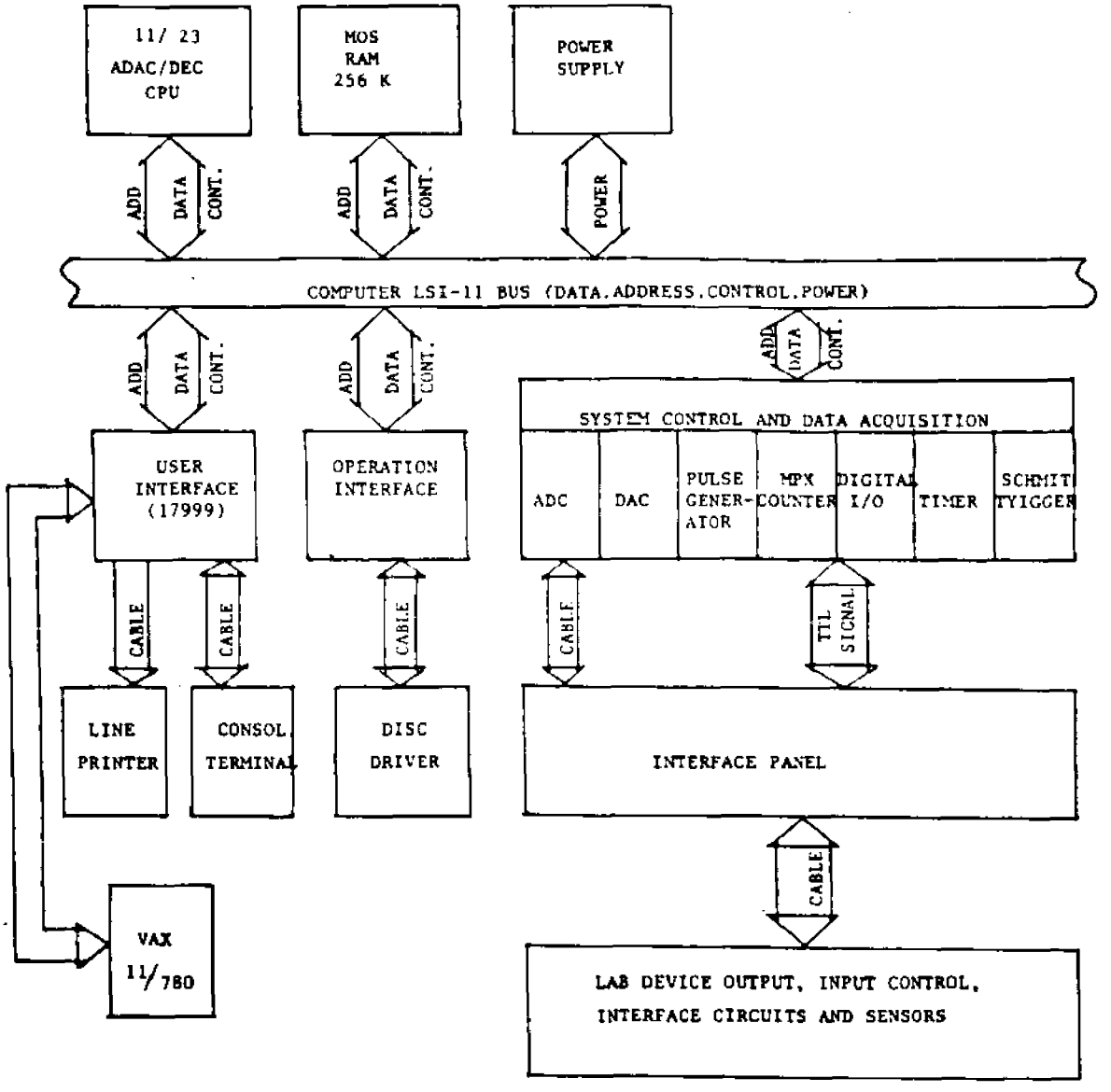

FIG. C.2. System Interface

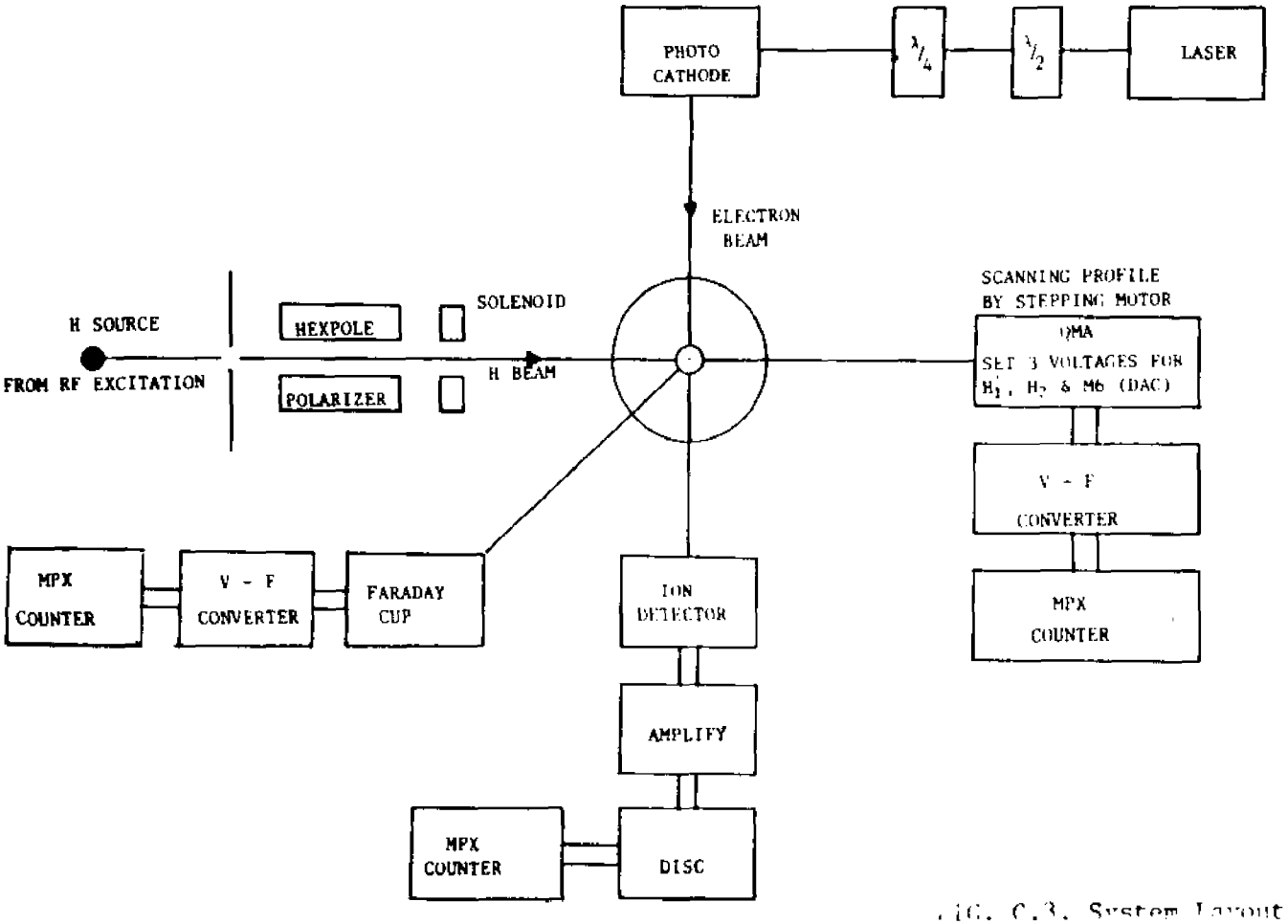

FIG. C.3. System Layout

APPENDIX D:ELECTRON OPTICS

The electrostatic electron-optics system consists of a diode extractor, a 90° bender, a straight transport section and a hemispherical monochromator. The voltages of all the elements "float" relative to the voltage of the crystal cathode which is biased negatively with respect to ground. The energy of the electron beam at the grounded interaction region is therefore determined by the potential of the cathode. In order to provide computer controlled fine adjustment (with resolution 10 meV) of the beam energy from 0 to 1 keV, two power supplies were used in series for the cathode bias. One, a Kepco power supply (model APH 1000M) was manually adjustable from 0 to 1 kV. The second, a Lambda power supply (model LDS-X-01) was computer controlled and provided a 10 meV resolution with the use of a 12-bit DAC.

Resistive potential dividers, connected to a Bertan (model 210-03R) power supply that "floats" relative to the cathode, provide the voltages to the various lenses and deflectors. The final lens in the system, a "zoom lens" is provided with its own computer-controlled power supply. The design values of the voltages and dimension are shown in Fig. D.1.

From the operation of the electron beam transport system, we found as expected, that work function differences between the cathode and the interaction region boundaries as well as the monochromator were easily discernable, although posing no impediment to proper performance. Several design errors, however, did create problems that made operation unnecessarily difficult.

First, the crystal to anode distance is fixed, and the transport system does not contain an input lens. This configuration requires precise

positioning of the cathode, since an error cannot be corrected electron optically. (Any movement of the focal plane at the input of the transport system naturally propagates throughout the entire length of the system. (Thus the commercial manipulator (V/G model LMD 950), used for moving the crystal from its activation to its operation location, had to be modified to improve its positional accuracy to ±0.1 mm.

Second, the calculation of lens system L_3 was not adequately carried out. As can be seen from Fig. D.1, the length of L_3 is only about $2^1/_2$ times its diameter, while the calculation upon which the design was based assumes tube lengths greater than 5 times their respective diameters. In order to overcome this design error, a set of practical operating voltages had to be found semi-empirically. (The up to 1.5 times the design values of Fig. D.1, are practical operating values, given in Table D.1).

Third, the loading and resistive heating of resistors in the divider circuitry can cause small drifts in the supply voltage. The 90° bender and monochromator regions are particularly sensitive to such drifts. Thus care had to be taken to minimize beam loading and to allow for thermal stabilization.

In the summary of the calculations that I will present shortly, the following references will be useful.

1. 90° Bender: H.J. Drouhin and M. Eminyan, Rev. Sci. Instrum. 57, 1052 (1986).

2. Herzog Correction: R.F. Herzog, Z. Physik 89, 447 (1934); Arch. Elektrotech. 29, 790 (1935); Z. Physik 97, 596 (1935).

3. Transport Optics: E. Harting and F.H. Read, Electrostatic Lenses (Elsevier Scientific Pub. Co., Amsterdam 1976).

4. Monochromator: C.E. Kuyatt and J.A. Simpson, Rev. Sci. Insrum. 38, 103 (1967).

5. Input and Output of Monochromator: E. Harting and F.H. Read, op. cit.

It should be noted additionally that the computer program for three or two cylinder lens systems, used to calculate focal lengths and electron trajectories, was taken from E. Kisker, Rev. Sci. Instrum. 53, 114 (1982).

In the following summaries, all the voltages are given with respect to the cathode potential. The various sections of the optics are - the diode extractor, the 90° bender, the straight transport, and the hemispherical monochromator with its own input and output optics -- are treated as discrete components, and the calculations are carried out accordingly. In view of their relative complexity, the 90° bender and monochromator designs were specified first with the diode extractor and straight transport dimensions and voltages chosen afterward.

1. 90° SPHERICAL BENDER

(a) Voltages of Inner Bender, V_{EBI}, and Outer Bender V_{EBO}

The voltages applied to inner bender EBI, and outer bender EBO are given by the equations

$$V_{EBI} = V_{EA} (2 R_O/DI - 1), \quad (D.1)$$

and

$$V_{EBO} = V_{EA} (2 R_O/DO - 1), \quad (D.2)$$

where V_{EA}, the energy centroid of the beam in the bender, is the voltage (100 V as shown in Fig. D.1) applied to the anode, DI and DO, are the inner and outer radii of the bender, and $R_O = (DI + DO)/2$, is the mean radius of the bender. For the design dimensions of 19.0 mm for DI and 31.75 mm for DO, Eqs. (D.1) and (D.2) yield the values $V_{EBI} = 1.671\ V_{EA}$ and $V_{EBO} = 0.984EA$, or with EA taken as its nominal value of 100 V, $V_{EBI} = 167.1$ V and $V_{EBO} = 98.4$ V.

(b) Herzog Correction for 90° Bender Input and Output Plates

If an electron near a fringe field region is curved rather than straight, the geometric corrections (called Herzog corrections) are generally applied which allow standard focusing formulas to be applied to the electron optical element in question. For example, the regions near the input plate EA and output plate EP (shown in Fig. D.2) require Herzog corrections, which are achieved with the proper choice of apertures in these plates and the proper spacing of these plates from the bender. For input and output apertures charecterized by radii b_1 and b_2 respectively, both chosen as 5.4 mm and with the 90° bender gap c = (DO-DI)/2 given by 6.4 mm, the input and output plate spacings, d_1 and d_2 respectively, must be chosen as $d_1 = d_2 = 0.1\ c = 0.64$ mm according to the Herzog analysis.

(c) Determination of Cathode (Crystal) Position

The image of the cathode produced by the cathode-extractor diode lens system (crystal and anode plate) is the object of 90° bender. The object and image locations are related by the standard lens equation,

$$\frac{1}{f} = \frac{1}{X} + \frac{1}{Q}, \tag{D.3}$$

where f is the focal length of the lens, X is the object (crystal) distance from the anode, and Q is the image distance from the anode. For the operational configuration employed, which assumes that the extractor produces a virtual image, the diode lens focal length f is chosen for convenience to be -4X. The from Eq. (D.3) Q is given by

$$Q = -\frac{4X}{5}. \qquad (D.4)$$

(d) Object and Image of 90° Bender

The lens characteristics of a 90° bender follow the relation

$$X_O\, Q_O = R_O^2$$

where X_O is the distance of object to the entrance of 90° bender, Q_O is the distance of image to the exit of 90° bender, and R_O is the mean radius of 90° bender. With R_O chosen as 25.4 mm, as already indicated, and with Q_O taken as 64.5 mm for mechanical reasons, X_O becomes 10.0 mm in accordance with Eq. (D.4). Since the anode is 3.0 mm thick and the input plate, EA, is 0.86 mm thick, and since the input plate is located a distance d_1 = 0.64 mm from the 90° bender entrance, $|Q|$ is given by $|Q| = X_O - (3.0 + 0.86 + 0.64)$ mm or $|Q| = (10.0 - 4.5)$ mm = 5.5 mm. Then by virtue of Eq. (D.4), X, the distance from the crystal cathode to the anode, is determined to be 6.9 mm.

2. STRAIGHT TRANSPORT

The straight transport provides a focused beam into the input of monochromator system. It consists of lens systems L_1, L_2 and L_3: L_1, a two-cylinder immersion lens with accelaration; L_2 a three-cylinder einzel lens; and L_3 a three-cylinder immersion lens with deceleration. The spacing between pairs cylinder elements is one tenth of a cylinder diameter

according to the prescriptions of Hartung and Read. In our design the cylinder diameter, DIA, is taken as 15 mm.

(a) Lens L_1

Lens element voltages: $V_{EL2} = 100$ V, $V_{EL3} = 500$ V
Acceleration ratio: $V_{EL3}/V_{EL2} = 5$.
Object distance chosen: $X_1 = 15$ mm.

From the above data, with the help of Harting and Read, we obtain the image distance Q_1 for lens L_1: $Q_1 = -1.45$ DIA $= -21.75$ mm, the minus sign signifying as usual a virtual image. Since the image of the 90° bender serves as the object of lens L_1, the geometric relations among Q_0, X_1, and Q_1 are as shown in Fig. D.1.

(b) Lens L_2 (Einzel Lens)

Lens element voltages: $V_{EL3} = V_{EL4} = V_{TL1} = 500$ V.
$V_{TL1} = 1200$ V,
$V_{TL3} = 500$.
Acceleration ratio: $V_{TL2}/V_{TL1} = 2.4$
Deceleration ratio: $V_{TL2}/V_{TL3} = 2.4$
Object distance chosen: $X_2 = 142.2$ mm

From the above data and with the help of Harting and Read, we obtain the image distance for lens L_2: $Q_2 = 9.48$ DIA $= 142.2$ mm $= X_2$.

(c) Lens L_3

Lens element voltages: $V_{TD} = V_{TL4} = 500$ V
$V_{TL5} = 100$
$V_{TL6} = 25$.
Deceleration ratios: $V_{TL4}/V_{TL5} = 5$
$V_{TL5}/V_{TL6} = 4$
Object distance chosen: $X_3 = 120$ mm

From the above data and with the help of Harting and Read, we obtain the image distance for lens L_3: $Q_3 = 39.15$ mm.

As already indicated at the outset of this appendix, the length of the elements of lens L3 did not meet the criteria of Herting and Read. For optimal operation we found that all voltages in the transport system had to be scaled up by a factor of 1.5 as shown in Table D.1.

3. HEMISPHERICAL MONOCHROMATOR

The hemispherical monochromator, shown in Fig. D.3 provides a reproducible narrow energy spread for the transmitted electron beam based upon the dispersive properties of spherical electrostatic elements. The monochromator consists of a set of input, a 180° hemispherical bender, and a set of output optics.

(a) 180° Hemispherical Bender

(i) Applied Voltages to Inner and Outer Hemispheres

The relationship between the applied voltages and the geometric dimensions of the hemispheres is illustrated by the following equation:

$$V_1 - V_2 = \Delta V = V_o \left[R_2/R_1 - R_1/R_2\right], \tag{D.6}$$

where R_1 and R_2 are the inner and outer radius respectively, V_1 and V_2 are the voltages of the inner and outer hemispheres respectively, and V_O is the voltage associated with the centroid trajectory. With R_O the mean radius definetely $R_O = (R_1 + R_2)/2$, the applied voltages V_1 and V_2 are given by

$$V_1 = V_o \left[3 - 2\,(R_1/R_o)\right] \tag{D.7}$$

and

$$V_2 = V_0 [3 - 2 (R_2/R_0)]. \qquad (D.8)$$

From the monochromator used, the radii R_1 = 19.0 mm and R_2 = 31.75 mm.

(ii) Energy Resolution $\Delta E_{1/2}$

As shown by Kuyatt and Simpson, the full width at half maximum (FWHM) energy resolution, $\Delta E_{1/2}$, of the monochromator follows from the equation

$$\frac{\Delta E_{1/2}}{E_0} = \frac{w}{2R_0} \qquad (D.9)$$

where w is the diameter of the anuglar stop denoted by AS1 in Fig. D.3, and $E_0 = eV_0$ is the centroid energy of the beam in the monochromator. For an angular stop with w = 1.8 mm and for a centroid energy of 2 eV, the resolution $\Delta E_{1/2}$ is 70 meV according to Eq. (D.9); for an angular stop with w = 0.8 mm and for a centroid energy of 2eV, $\Delta E_{1/2}$ is 30 meV. During actual operation, the 1.8 mm stop was employed but the beam energy was raised to 3.0 eV resulting in a resolution $\Delta E_{1/2}$ of ~ 100 meV.

(iii) Input and Output Current

Space charge effects ultimately limit the energy resolution $\Delta E_{1/2}$ of a monochromator. Therefore the maximum input current I_{in} is limited and as shown by Kuyatt and Simpson, is determined by the relation

$$I_{in} = 19.3 E_0^{1/2} \Delta E_{1/2}, \qquad (D.10)$$

where E_0 and $\Delta E_{1/2}$ are in eV and I_{in} is in μA. The output current, I_{out}, in

turn is given by

$$I_{out} = I_{in} (\Delta E_{1/2})/(\Delta E_S), \qquad (D.11)$$

where ΔE_S is the energy spread of the incident beam in eV. For a pass energy E_0 of 2eV and an energy spread ΔE_S = 130 meV (characteristic of a GaAs polarized electron source), the space charge limiting input and output currents are I_{in} = 1.91 μA and I_{out} = 1.03 μA for $\Delta E_{1/2}$ = 70 meV and I_{in} = 0.82 μA and I_{out} 0.19 μA for $\Delta E_{1/2}$ = 30 meV. At the pass energy of 3.0 eV and the corresponding FWHM resolution of 100 meV the conditions under which the asymmetry data were obtained, the limiting input and output currents from Eqs. (D.9) and (D.10) should be I_{in} = 3.34 μA and I_{out} = 2.57 μA. Kuyatt and Simpson point out however that experimentally, values a factor of five lower than those given by Eqs. (D.9) and (D.10) are usually observed. Under our running conditions, we used a maximum input current of approximately 0.7 μA for which we obtained an output current of approximately 100 nA.

(b) Input Optics

The image position of the transport optics section (denoted by CAS1 in Fig. D.3) is the object of the monochromator input optics section. An X-Y deflector pair (denoted by D_2 in Fig. D.3) is used for incident angular adjustment.

The image of transport optics (denoted CAS1 position in Fig. D.3) is the object of input optics and be focused into the entrance of hemispherical sphere. A pair of X and Y direction deflector (denoted D_2 in Fig. D.3) is used for angle adjudgment.

As shown in the figure, the electron beam is collimated by CAS1 and analyzer stop AS1, and focussed into the entrance of monochromator by the three aperture aperture lens system denoted by AL2(1), AL2(2) and AL2(3). (The objects labeled S1 and S2 a geometric spacers).

Lens element voltages:	VAL2(3) = 3 V = V_0
	VAL2(1) = 37.5 V
	VAL2(2) = 18 V
Deceleration ratio:	VAL2(1)/VAL2(3) = 12.5
Deceleration ratio:	VAL2(2)/VAL2(3) = 6
Inner diameter of lens aperture:	d_1 = 5 mm
Object distance chosen:	X_4 = 5 d_1 = 25 mm

Note that eV_0 = 3 eV is the predetermined incident electron energy for monochromator input. From the above data and with the help of Harting and Read, we obtain the image distance for input lens: Q_4 = 15 mm.

(c) Output Optics

The purpose of the output section is to focus the electron beam emerging from monochromator to a fixed point (the scattering point) for variable energy. First, the electron beam is focussed at the location of angular stop A1 (with inner diameter 0.18 cm). Then it is focussed at the scattering point by a three element zoom lens system (AL1). An x-y deflector pair (denoted by D1 in Fig. D.3) is used for output angular adjustment.

(1) Lens System (LIA, LIB(1), LIB(2), (LIC))

Depending on the applied biased voltage, the four-elements can be combined as three-element or a two-element lens system, the choice determined by the range of energies desired at the scattering point.

Case I: Three-Element Lens System

Lens elements voltages:	VLIB(1) = VLIB(2) = 16.5 V
	VLIC = VLIA = 3 V
Acceleration ratio:	VLIB(1)/VLIA = 5.5
Deceleration ratio:	VLIC/VLIB(2) = 5.5
Inner diameter of lens cylinder:	d_2 = 4.8 mm
Object distance chosen:	$X_s = 3\ d_2$ = 14.4 mm
Magnification:	M = 1

From the above data and with the help of Harting and Read, we obtain the image distance for output lens: Q_s = 14.4 mm.

Case IIA: Two-Element Lens System (VLIC = 30 V)

Lens element voltages:	VLIA = VLIB(1) = 3 V
	VLIB(2) = VLIC = 30 V
Acceleration ratio:	VLIC/VLIA = 10
Magnification:	M = 0.6

Under these conditions, Q_s is again 14.4 mm when X_s is chosen as 14.4 mm.

Case IIB: Two-Element Lens System (VLIC = 0.3 V)

Lens element voltages:	VLIA = VLIB(1) = 3 V
	VLIB(2) = VLIC = 0.3 V
Deceleration ratio:	VLIC/VLIA = 10
Magnification:	M = 1.66

Under these conditions, Q_s is again 14.4 mm when X_s is chosen as 5 mm.

Thus the element LIC can be operated at voltages of 0.3, 3.0, and 30 V, to provide low ($\leq$ 10 eV), intermediate (10 eV $\leq E_e \leq$ 100 eV) and high ($\geq$ 100 eV) electron collision energy capabilities. We operated with Case I in our study for intermediate energies.

(ii) Zoom Lens (ALI(1), ALI(2), ALI(3))

The function of a zoom lens is to keep the image at the same point even though the electron energy is varied. The object distance X_6 = 28.8 mm and image distance Q_6 = 28.8 mm chosen and the diamter of the lens aperture is taken as 4.8 mm. With the help of Harting and Read, the values of $(V_2/V_1 + 1)$ and V_3/V_1 can be deduced from a zoom lens operating plots, where V_1,V_2, and V_3 are the voltage of first (ALI(1)). Second (ALI(2)) and last elements (ALI(3)) respectively. Now V_1 is determined by VLIC, V_3 is determined by the desired output electron energy, and V_2 is adjusted to keep the focal point fixed when V_3 is varied. It should be emphasized once again that, elements AL1, C1-2 and C1 indicated in Fig. D.3 are grounded, and the voltage V_3 is the floating voltage respect to the crystal cathode, which itself is biased at a negative voltage. The three possible operational modes discussed under the Output Optics allow V_3 to cover a wide range of voltage, thereby permitting the apparatus to operate at beam energies between 1 eV and 1 keV.

TABLE D.1 Operating Voltage (1.5 x Design Value)

Element	Voltage (Volts)
EA	150
EBI	256
EBO	92
EP	150
EL1	150
ED1	149
ED2	149
ED3	152
ED4	146
EL2	149
EL3	767
EL4	767
TL1	767
TL2	1800
TL3	726
TD1	335
TD2	716
TD3	732
TD4	718
TL4	726
TL5	250
TL6	55

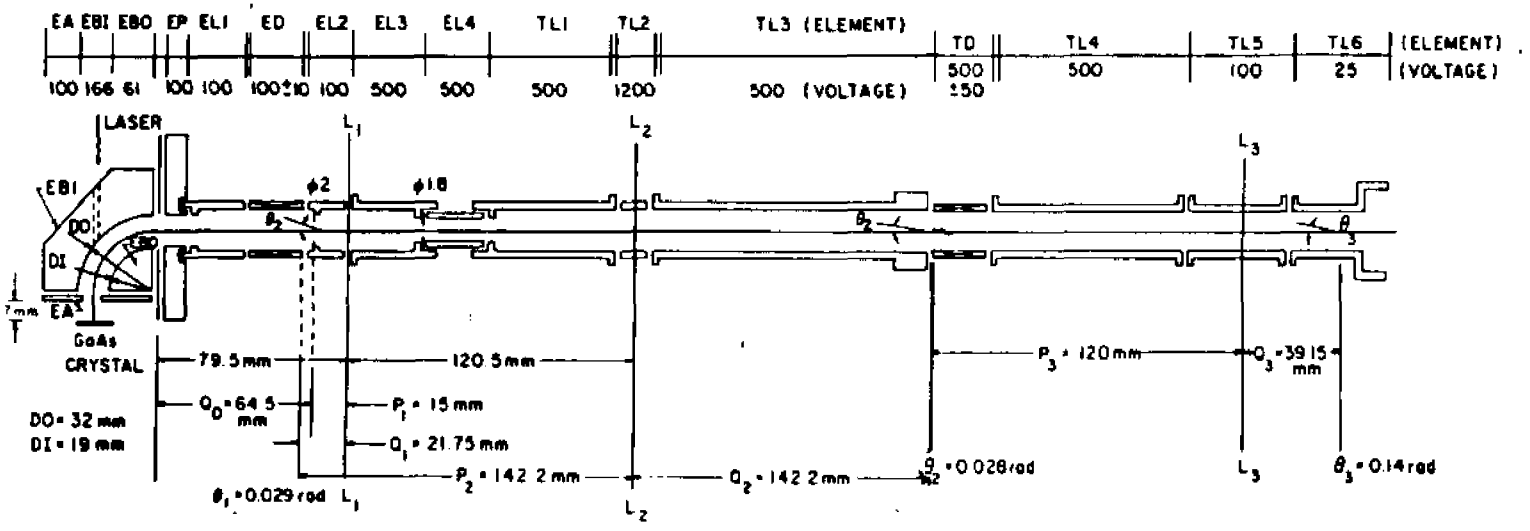

FIG. D.1. Electron Optics

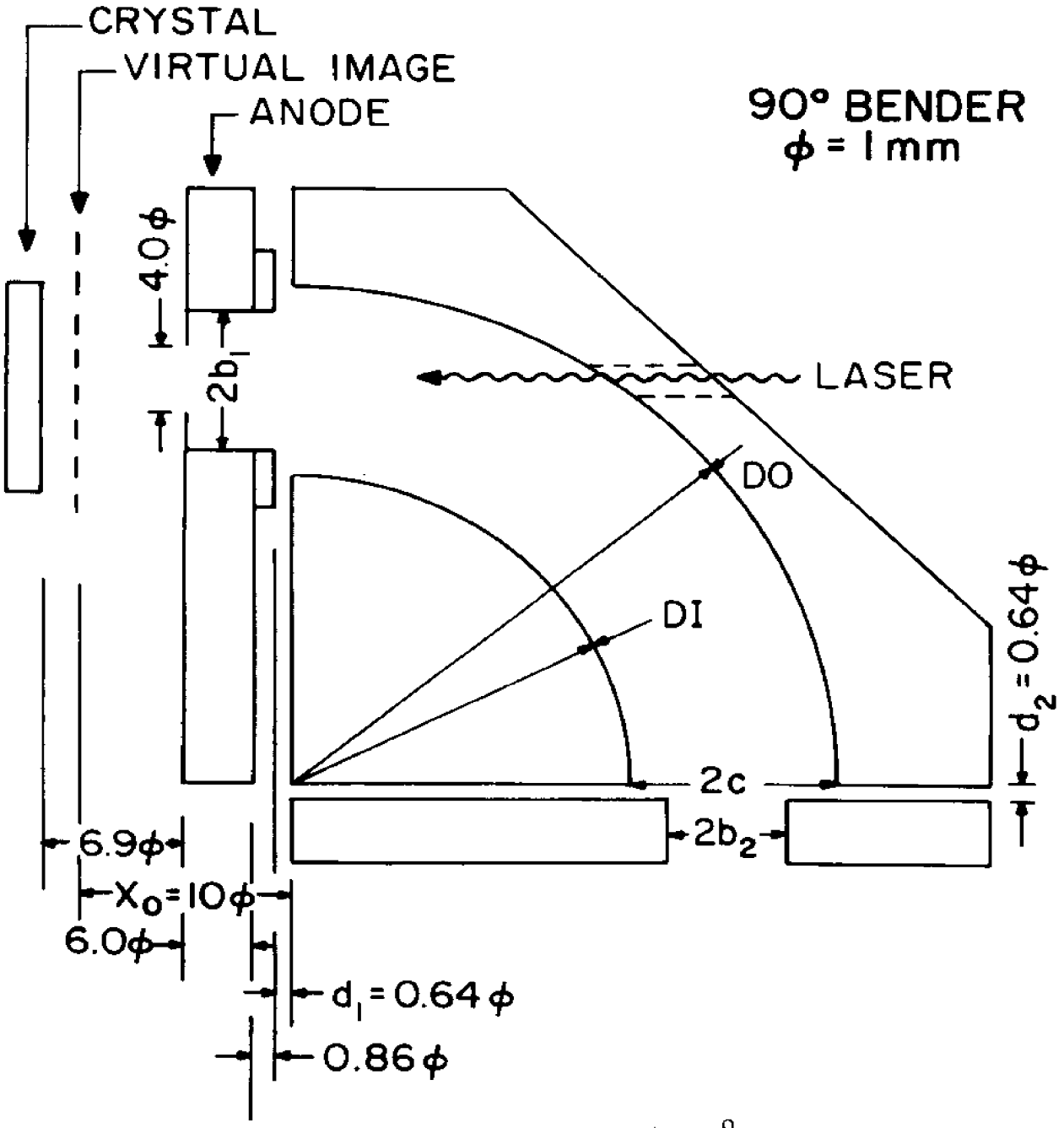

FIG. D.2. 90° Bender

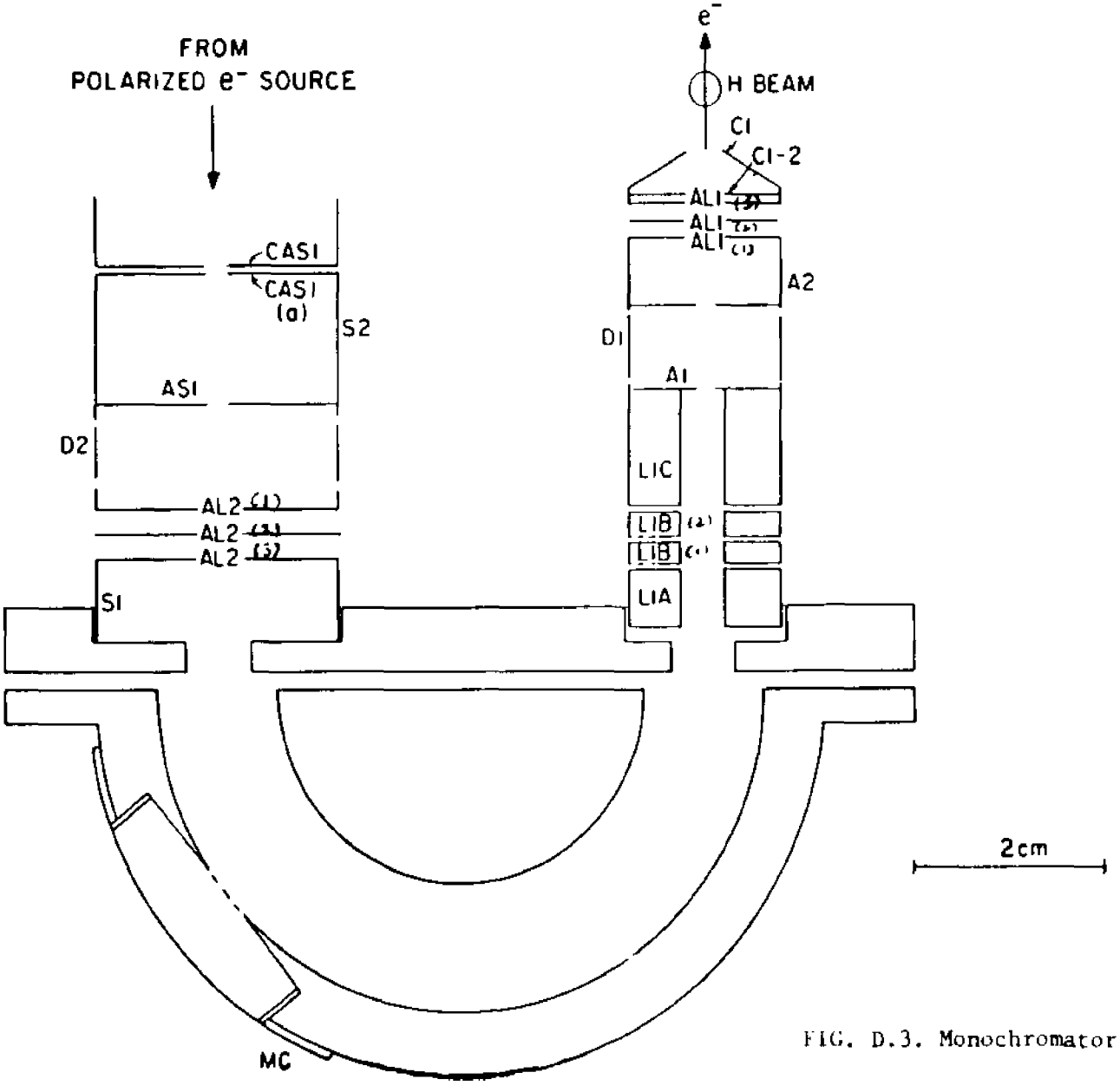

FIG. D.3. Monochromator

APPENDIX E

Spin-Tagged Electron-Hydrogen Scattering:Ionization in the Near Threshold Region

F. C. Tang,[a] D. M. Crowe, M. S. Lubell, K. Rubin, and A. Vasilakis
Department of Physics, City College CUNY, New York, NY 10031

J. Slevin
Department of Experimental Physics, St. Patrick's College, Maynooth, Co. Kildare, Ireland

M. Eminyan
Unites d'Eseignement et de Recherche de Physique, Universite Paris VII, F-75221 Paris,
France

ABSTRACT

Using a polarized electron beam, obtained from a GaAs photoemission source in conjunction with a hemispherical monochromator, and a high-field state-selected atomic hydrogen beam, obtained from an rf discharge source in conjunction with a permanent hexapole magnet, we performed crossed beams studies of the spin-dependence in angle-integrated ionization for the near-threshold region. Specifically, we measured a relative ionization rate asymmetry, $\Delta_I = [R(\uparrow\downarrow)-R(\uparrow\uparrow)]/[R(\uparrow\downarrow)+R(\uparrow\uparrow)]$, for incident and target electrons spins antiparallel ($\uparrow\downarrow$) and parallel ($\uparrow\uparrow$) over the energy range 13.6 to 15.0 eV.

(to be submitted for publication)

In the realm of electron-atom scattering, the electron-hydrogen collision system has long been accorded special status.[1] By virtue of its simplicity, it has served as the principal testing ground of the approximation methods that are used to make electron-atom scattering amenable to theoretical analysis. Yet in spite of its relative simplicity, this 3-body (or perhaps more appropriately $2^1/_2$ body) problem has continued to defy an elementary approach that has broad kinematic range.

The deficiencies and strengths of the various theoretical attacks are illuminated most clearly when comparisons are made with experiments that provide access to the collision system at the most rudimentary level, in which scattering amplitudes can be examined unencumbered by averages over momentum, energy, angular momentum, spin, or position. The measurement of differential cross sections,[2] the observation of narrow resonances,[3] the study of angular correlations,[4] and at least the partial separation of exchange effects[5] are examples of the experimental techniques that have enabled such comparisons to be made. In this Letter we report new measurements of spin-dependent asymmetries for impact ionization in the near threshold region.

We began these studies as a sequel to earlier investigations of impact ionization,[5-7] which today must be regarded as exploratory in nature as a consequence of the limitations placed on them by the technologies available at the time. The advent of the GaAs polarized electron source[8] in particular has now enabled us to make a substantial improvement in the quality of the measurements and has opened up the opportunity for observing effects previously obscured either by poor energy resolution or by poor statistical accuracy. In addition to addressing the need for generally more precise spin-dependent data, we were motivated in our

present studies by a desire to shed further light on the nature of ionization threshold laws which have been developed in two competing theoretical forms -- the classical Wannier[9] model with its quantum mechanical extensions due to Rau,[10,11] Peterkop,[12] Roth,[13], Klar,[14,15] Schlecht,[14] and Greene[11] and the Coulomb-dipole model due to principally to Temkin.[16] Unfortunately, analyses of the Coulomb-dipole model now suggest that its modulation signature may only be visible within 100 meV of threshold, a prediction that makes its experimental investigation extremely difficult, if not impossible, within the confines of technology.

The general methodology of the present experiment follows that of the earlier work[5-7] in that the quantity of interest is the ionization asymmetry A_I defined by

$$A_I \quad \frac{\sigma_I(\uparrow\downarrow) - \sigma_I(\uparrow\uparrow)}{\sigma_I(\uparrow\downarrow) + \sigma_I(\uparrow\uparrow)}, \tag{1}$$

where $\sigma_I(\uparrow\downarrow)$ and $\sigma_I(\uparrow\uparrow)$ are respectively the total ionization cross sections for the antiparallel and parallel spin configurations of the incident and atomic electrons. Alternatively, A_I can be expressed as

$$A_I = (1 - r_I)/(1 + 3r_I), \tag{2}$$

where r_I is the ratio of triplet to singlet total ionization cross sections. As in the previous work the quantity actually measured is the experimental counting rate asymmetry Δ_I defined by

$$\Delta_I \quad [R(\uparrow\downarrow) - R(\uparrow\uparrow)]/[R(\uparrow\downarrow) + R(\uparrow\uparrow)], \tag{3}$$

where $R(\uparrow\downarrow)$ and $R(\uparrow\uparrow)$ are the ion counting rates for the respective spin configurations. The quantities A_I and Δ_I are related by the expression

$$\Delta_I = P_e P_H (1 - F_2) |\cos\alpha| A,$$

where P_e, and P_H are the polarizations of the electron and hydrogen beams respectively, F_2 is the fraction of events attributable to hydrogen molecules, and α is the angle between the two polarization vectors.

Although completely redesigned for more precise measurements, the present experiment retains the crossed beams feature of the earlier work, as illustrated in Fig. 1. In brief, polarized electrons are produced by photoemission from a single crystal of <100> GaAs that has been prepared for negative electron affinity by application of Cs and O_2 to its surface. The operating principles and characteristics of the source have been described in detail elsewhere.[17] Suffice to say that the incident radiation is provided by a GaAlAs laser operating at 787 nm with a maximum specified cw power of 15 mW (a factor of 5 higher than the rating of the laser originally used[17]). The helicity of the electrons extracted from the crystal is dependent on the helicity of the incident radiation, which in turn is controlled by the rotation of either a quarter-wave or a half-wave retardation plate in the optics train, as shown in the figure. A beam flag allows the light to be blocked periodically for background measurements.

Before reaching the interaction region, the extracted beam passes through a set of electron optical elements containing a 90° spherical bender and a 180° hemispherical monochromator,[18] in addition to standard electrostatic lenses and steering elements. A movable Faraday cup located just beyond the interaction region serves as a beam monitor for purposes of

signal normalization. Although not used in the present studies, the apparatus also contains a hemispherical Mott-scattering polarimeter[19] to which the beam can be routed after it has passed through the interaction region. The entire electron beam line is surrounded by Mu-metal shielding except in the region of the GaAs photocathode where optical access is necessary. For the interaction chamber, where a magnetic field of 100 mG or less is required to be along the direction of the hydrogen beam, special care is taken with the shielding, which reduces the influence of the earth's magnetic field to 5-10 mG after in situ "degaussing."

The polarized atomic hydrogen beam originates in an rf dissociation[20] source and undergoes high-field state selection in a pair of permanent hexapole magnets. Following the magnets, the spins of the hydrogen atoms are rotated adiabatically into the longitudinal direction by a small solenoidal coil as illustrated in Fig. 1. Additional solenoids, not shown in the figure maintain the longitudinal direction of the field and trim it to the 100 mG required at the crossed-beams interaction site. Downstream from the interaction region additional coils are used, initially to maintain the axial field symmetry and somewhat further downstream to rotate the spins adiabatically into a transverse horizontal direction in preparation for high-field state analysis by a Stern-Gerlach polarimeter. At the end of the line, the beam is sampled by a quadrupole mass analyzer (QMA) that serves as an intensity monitor as well as an integral component of the hydrogen polarimeter, the latter application requiring the use of a horizontal mechanical translator for beam profile scanning. For purposes of real-time background subtraction, the hydrogen beam is equipped with a mechanical chopper located between the two hexapole magnets and operating at about 10 Hz with a duty factor of 50% and a dead time of 2%. The

properties and operating characteristics of the polarized hydrogen beam line are described in great detail in a separate publication.[21] The salient operating parameters of both the hydrogen and electron beams are summarized in Table I.

As in the earlier work, systematic effects were reduced by frequent reversal of the electron polarization, but in this case, a half-wave ($\lambda/2$) retarder was employed in the optical train in addition to a quarter-wave ($\lambda/4$) retarder, thereby providing two independent means of polarization reversal. The $\lambda/2$ plate was rotated back and forth through 45^{o}, while the $\lambda/4$ plate was rotated through 360^{o} in 90^{o} steps, as a consequence of which 8 unique combinations of $\lambda/4$ and $\lambda/2$ plate settings were obtained. For the determination of the "real" asymmetry, Δ_I, given by Eq. (3), data were binned according to the helicity of the light incident on the GaAs crystal. Data were also separately binned to generate a set of 18 false asymmetries, Δ_I^{Fi} ($i = 1,2...,18$), for combinations of $\lambda/4$ and $\lambda/2$ settings that should yield asymmetries equal to zero in the absence of systematic effects. In all instances, measured rates were corrected for background events, due to detector dark current, residual gas scattering, ion-pump charged particle contamination, and Lyman-α contributions produced by the rf source. Signal to background ratios varied from a maximum of 2.5 at an incident electron energy centroid $E = 15.0$ eV to a minimum of 0.2 at $E = 13.6$ eV. Maximum signal rates at these energies were 500 and 10 ions/s respectively. The rates decreased in time as the quantum yield of the GaAs crystal decayed with an e-folding time of 12-24 hours. Since the maximum energy examined, 15.0 eV, was 0.2 eV below the threshold for H_2 ionization, no correction for molecular background was necessary. Thus, with P_e, P_H, and $|\cos\alpha|$ constant Δ_I can be plotted directly against E, although for ease

of comparison, the results in Fig. 2 are shown normalized to earlier measurements[5] of A_I at E = 14.1 eV.

For purposes of ion detection, a Mullard channel multiplier (Model X91932) was used, with its cone biased at - 700 V relative to ground. The multiplier, located 3.3 cm from the interaction region and facing perpendicular to the hydrogen beam line, was enclosed in a stainless steel electrostatic shield that extended upstream along the hydrogen beam line and completely surrounded the interaction region, save appropriate apertures for the electron and hydrogen beams. The shield, containing two grids, served on one hand to maintain the interaction region at ground potential, independent of the voltages applied to the multiplier, and on the other hand to prevent stray fields from affecting the trajectories of the ions progressing downstream from the interaction region at the thermal velocities characterizing the neutral hydrogen beam.

All signals, including those from the ion detector, the Faraday cup, and the QMA, as well as indicator for the status and polarity of each beam, were routed through standard electronics modules and stored in digitized form on disk by an LSI 11/23 processor. The entire experiment was controlled by the computer with operator intervention minimized during data acquisition to avoid human bias. Data files were ultimately transferred to magnetic tape and analyzed off-line on a VAX 11/780 computer.

The results of the measurements of the "real" asymmetry are shown in Fig. 2, in which A_I is plotted against E over the range 13.6 - 15.0 eV in steps of 0.1 eV. Corrections, which increased A_I by 1% to 4%, were applied to the six lowest energy points to account for the effect of 1S-2S excitation on the detected ion signal. At each energy shown, the 18 false

asymmetries, Δ_I^{Fi}, were found to be consistent with zero within errors, and with the deviation of each such asymmetry considered with respect to zero for all 15 energies measured, the reduced chi-square with respect to zero, $\chi^2(0)$, ranged from 1.03 to 2.04 for 58 degrees of freedom. Prior to calculation of the asymmetries, the data set was examined for evidence of non-statistical behavior, as evidenced by ion event rates or electron and atom monitoring rates that deviated from the respective norms by more than 4 standard deviations. These occurrences, accounting for 0.5% of the data acquired and attributed to bursts of electronic noise, were rejected as spurious in accordance with Chauvenet's criterion.

In agreement with spin asymmetries in electron-alkali scattering,[22] the results of our experiment show no evidence of the modulation predicted by the Coulomb-dipole model. We therefore conclude that either the model is incorrect or its features appear so close to threshold that they are not visible under our present operating conditions.

The authors wish to thank the staff of the CCNY Machine Shop, in particular S. Forst and G. Cannella, for their assistance in the constructions of the apparatus, and the U.S. NSF, the Research Foundation of CUNY, NATO, the SERC of the U.K., and St. Patrick's College for financial support.

REFERENCES

(a) Present Address: Department of Physics, Rice University, P.O. Box 1892, Houston, TX 77251.

1. See for example N. F. Mott and H. S. W. Massey, The Theory of Atomic Collisions, 3rd ed. (Oxford University, London, 1965).

2. See for example J. F. Williams, in Electron and Photon Interactions with Atoms, edited by H. Kleinpoppen and M. R. C. McDowell (Plenum, New York 1976), p.309.

3. C. D. Warner, G. C. King, P. Hammond, and J. Slevin, J. Phys. B 19, 3297 (1986), and references therein.

4. J. Slevin, Rep. Prog. Phys. 47, 461 (1984); S. Chwirot and J. Slevin, J. Phys. B 18, L881 (1985); 20, 3885, 6144 (1987); J. Slevin, M. Eminyan, J. M. Woolsey, G. Vassiley, H. Q. Porter, C. G. Back, and S. Watkin, Phys. Rev. A 26, 1344 (1982); J. F. Williams, J. Phys. B 14, 1197 (1981); S. T. Hood, E. Weigold, and A. J. Dixon, J. Phys. B 12, 631 (1979).

5. G. D. Fletcher, M. J. Alguard, T. J. Gay, V. W. Hughes, P. F. Wainwright, M. S. Lubell and W. Raith, Phys. Rev. A 31, 2854 (1985), and references therein.

6. M. J. Alguard, V. W. Hughes, M. S. Lubell and P. F. Wainwright, Phys. Rev. Lett. 39, 334 (1977).

7. T. J. Gay, G. D. Fletcher, M. J. Alguard, V. W. Hughes, P. F. Wainwright, and M. S. Lubell, Phys. Rev. A 26, 3664 (1982).

8. See for example D. T. Pierce and F. Meier, Phys. Rev. B 13, 5484 (1976); D. T. Pierce, R. J. Celotta, G.-C. Wang, W. N. Unertl, A. Galejs, C. E. Kuyatt, and S. R. Mielczarek, Rev. Sci. Instrum. 51, 478 (1980); H. J. Drouhin, C. Hermann, and G. Lampel, Phys. Rev. B 31, 3859, 3872 (1985).

9. G. H. Wannier, Phys. Rev. 90, 817 (1953).

10. A. R. P. Rau, Phys. Rev. A 4, 207 (1971).

11. C. H. Greene and A. R. P. Rau, Phys. Rev. Lett. 48, 533 (1983); J. Phys. B 16, 99 (1983).

12. R. Peterkop, J. Phys. B 4, 513 (1971).

13. T. A. Roth, Phys. Rev. A 5, 476 (1971).

14. H. Klar and W. Schlecht, J. Phys. B 9, 1699 (1976).

15. H. Klar, J. Phys. B 14, 3255 (1981).

16. A. Temkin, Phys. Rev. Lett. 16, 835 (1966); 49, 365 (1982); J. Phys. B 7, L450 (1974); IEEE Trans. Nucl. Sci. NS-30, 1106 (1983); Phys. Rev. A 30, 2737 (1984); A. Temkin and Y. Hahn, Phys. Rev. A 10, 708 (1974).

17. F. C. Tang, M. S. Lubell, K. Rubin, A. Vasilakis, M. Eminyan, and J. Slevin, Rev. Sci. Instrum. 57, 3004 (1986).

18. See for example C. E. Kuyatt and J. A. Simpson, Rev. Sci. Instrum. 38, 103 (1967).

19. L. G. Gray, M. W. Hart, F. B. Dunning, and G. K. Walters, Rev. Sci. Instrum. 55, 88 (1984).

20. J. Slevin and W. Stirling, Rev. Sci. Instrum. 52, 1780 (1981).

21. N. Chan, D. C. Crowe, M. S. Lubell, F. C. Tang, A. Vasilakis, F. J. Mulligan, and J. Slevin, submitted to Rev. Sci. Instrum.

22. M. H. Kelley, W. T. Rogers, R. J. Celotta, and S. R.Mielczarek, Phys. Rev. Lett. 51, 2191 (1983); G. Baum, M. Moede, W. Raith, and W. Schroder, J. Phys. B. 18, 531 (1985).

TABLE I. Typical operating conditions at interaction region

Electron beam		
Intensity[a]	100	nA
Polarization, P_e	0.35	
Emittance	25	mrad cm $eV^{1/2}$
Energy resolution[b]	<100	meV (FWHM)
Hydrogen beam		
Density	2×10^{10}	atoms/cm^3
Electronic polarization, P_H	0.515	
Molecular fraction	0.02	
Residual gas pressure	7×10^{-9}	Torr

(a) The quantum yield of the GaAs crystal decays with an e-folding lifetime of 12-24 h.

(b) The electron monochromator was not operated at its ultimate design resolution of 30 meV full-width-at-half-maximum (FWHM), in order that high currents be maintained.

FIGURE CAPTIONS

FIG. 1 Schematic layout of the crossed-beams facility showing (1) rf hydrogen source; (2) hexapole magnetic high-field state selector; (3) hydrogen beam chopper; (4) post-hexapole solenoidal spin precessor; (5) direction of electronic polarization vector of hydrogen atoms; (6) molybdenum hemispherical electron monochromator; (7) channel multiplier ion detector; (8) molybdenum hemispherical electron spectrometer not used in these studies; (9) post-interaction spin-guide solenoid; (10) pre-Stern-Gerlach tranverse adiabatic spin rotator; (11) Stern-Gerlach polarimeter; (12) quadrupole mass analyzer; (13) circularly polarized 787-nm laser light for photoemission; (14) GaAs crystal mounted on sapphire block; (15) copper 90^{o}-spherical bender; (16) solenoidal electron spin precessor; (17) direction of polarization vector of electrons; (18) channel multiplier Lyman-α detector, not used in these studies; (19) movable Faraday cup; (20) electron beam exiting to Mott polarimeter, not used in these studies; (21) GaAlAs diode laser; (22) lenses; (23) quarter wave plate; (24) half-wave plate; (25) laser beam flag; (26) vacuum window.

FIG. 2 Ionization asymmetry, normalized to the 14.1 eV value of A_I in Ref. 5, as a function of incident electron energies. The vertical error bars are one standard deviaton uncertainties, while the horizontal error bars indicate the energy spread of the beam.

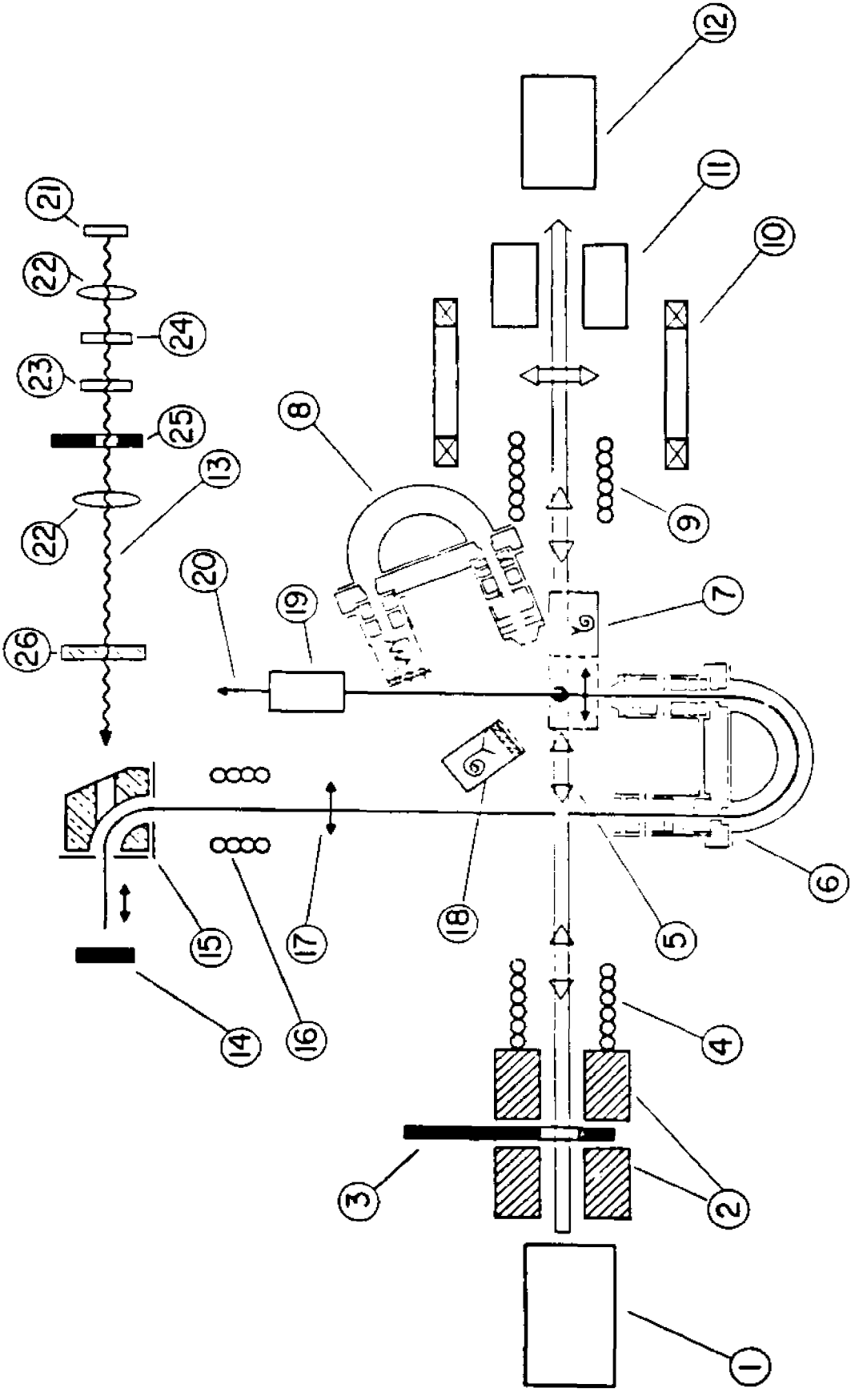

FIG. 1

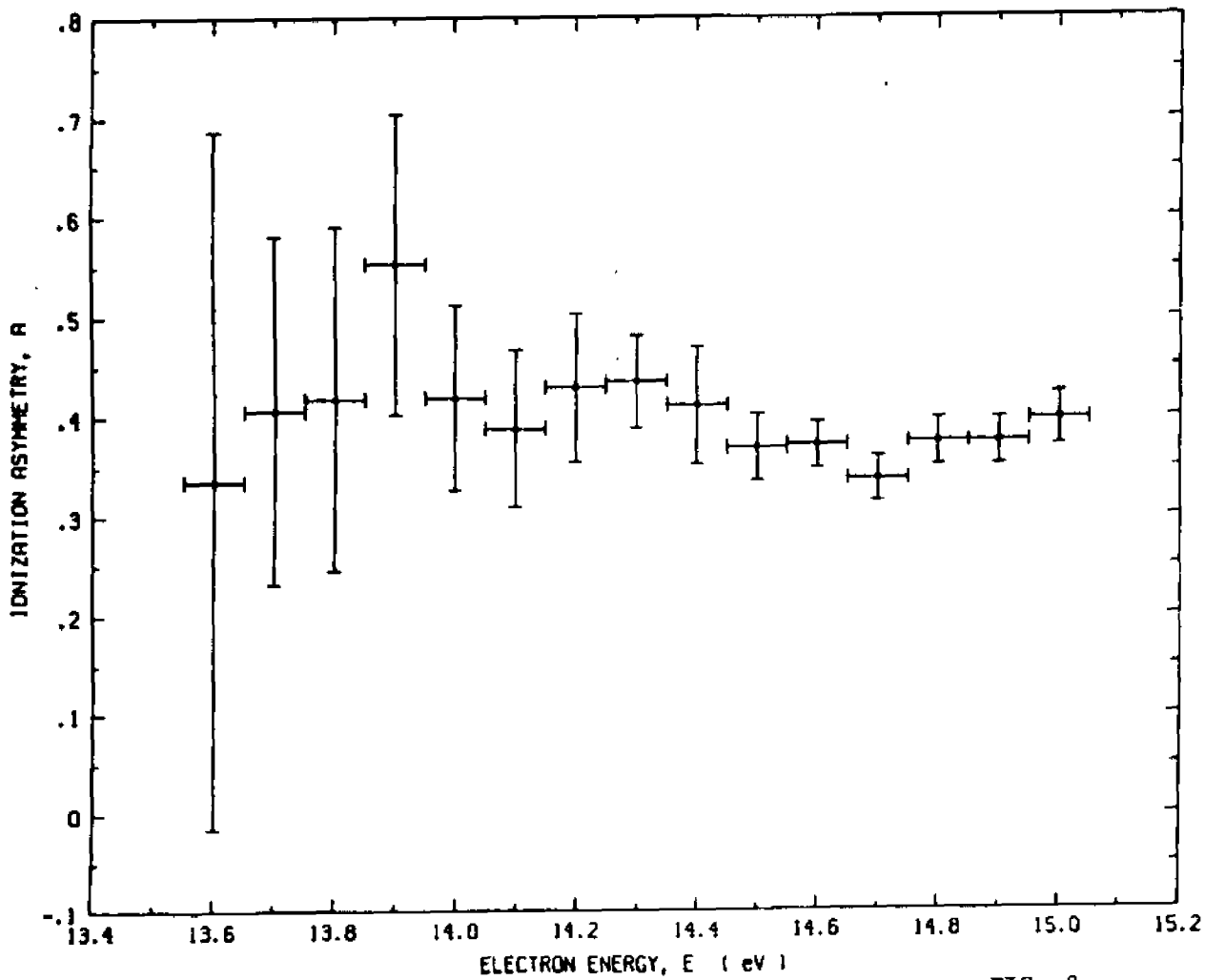
IONIZATION ASYMMETRY, A
.8
.7
.6
.5
.4
.3
.2
.1
0
-.1
13.4
13.6
13.8
14.0
14.2
14.4
14.6
14.8
15.0
15.2
ELECTRON ENERGY, E (eV)

FIG. 2

BIBLIOGRAPHY

CHAPTER I

1.1 W. L. Fite and R. T. Brackmann, Phys. Rev. **112**, 1141 (1958).

1.2 W. Lichten and S. Schultz, Phys. Rev. **116**, 1132 (1959); W. E. Kauppila, W. R. Ott, and W. L. Fite, Phys. Rev. A **1**, 1099 (1970); H. Koschmieder, V. Raible, and H. Kleinpoppen, Ibid. **8**, 1365 (1973); J. F. Williams, J. Phys. B **9**, 1519 (1976).

1.3 P. J. O. Teubner, C. R. Lloyd, and E. Weigold, Phys. Rev. A **9**, 2552 (1974); C. R. Lloyd, P. J. O. Teubner, E. Weigold, and B. R. Lewis, ibid. **10**, 175 (1974).

1.4 J. F. Williams, in Electron and Photon Interaction with Atoms, edited by H. Kleinpoppen and M. R. C. McDowell, (Plenum, New York, 1976), p. 309.

1.5 J. F. Williams, J. Phys. B **7**, L56 (1974); **8**, 1683 (1975); **8**, 2191 (1975).

1.6 J. Callaway and J. F. Williams, Phys. Rev. A **12**, 2312 (1975).

1.7 D. T. Pierce, R. J. Celotta, G. L. Wang, W. V. Unertl, A. Galejs, C. E. Kuyatt, and S. R. Mielczarek, Rev. Sci. Instrum. **51**, 478 (1980).

1.8 M. Eminyan, K. B. MacAdam, J. Slevin, and H. Kleinpoppen, J. Phys. B **12**, 1519 (1974) for citations of the early Electron-Photon Coincidence Experiments in Atomic Physics.

1.9 M. J. Alguard, V. W. Hughes, M. S. Lubell, and P. F. Wainwright, Phys. Rev. Lett. **39**, 334 (1977).

1.10 G. D. Fletcher, M. J. Alguard, T. J. Gay, V. W. Hughes, C. W. Tu, P. F. Wainwright, M. S. Lubell, W. Raith, and F. C. Tang, Phys. Rev. Lett. **48**, 1671 (1982).

1.11 G. Baum, E. Kisker, W. Raith, W. Schroder, V. Sillmen, and D. Zenses, J. Phys. B **14**, 4377 (1981).

1.12 D. Hils, W. Jitschin, and H. Kleinpoppen, J. Phys. B **15**, 3347 (1982).

1.13 M. T. Hollywood, A. Crowe and J. F. Williams, J. Phys. B (1979):Atom Molec. Phys. **12**, 819-34.

1.14 J. Slevin, M. Eminyan, J. M. Woolsley, G. Vassilev, and H. R. Porter, J. Phys. B (1980):Atom. Molec. Phys. **13**, 1341-3.

1.15 J. F. Williams, J. Phys. B (1981):Atom Molec. Phys. **14**, 1197-218.

1.16 E. Weigold, L. Frost and K. J. Nygaard, Phys. Rev. A **21**, 1950-4 (1980).

1.17 W. Gerlach and O. Stern, Z. Phys. **8**, 110 (1921).

1.18 J. C. Wesley and A. Rich, Phys. Rev. A **4**, 1341 (1971).

1.19 S. A. Goudsmit and G. E. Uhlenbeck, Naturwiss **13**, 953 (1925).

1.20 N. F. Mott, Proc. Roy. Soc. A **124**, 425 (1929); Proc. Roy Soc. A **135**, 429 (1932).

1.21 C. G. Shull, C. T. Chase and F. E. Meyers, Phys. Rev. **63**, 29 (1943).

1.22 M. S. Lubell in "Atomic Physics 5 (1977)," 325-373, edited by R. Marrus, M. Prior, and H. Shugart.

1.23 W. Raith, in "Atomic Physics 1," edited by V. W. Hughes, B. Bederson, U. W. Cohen and F. M. J. Pichanick, (Plenum Press, New York, 1969), pp. 389-415.

1.24 J. Kessler, Rev. Mod. Phys. **41**, 3 (1969).

1.25 H. Kleinpoppen, Phys. Rev. A **3**, 2015 (1971).

1.26 L. J. Weigert and M. E. Rose, Nucl. Phys. **51**, 529 (1964).

1.27 J. Kuti and V. W. Weisskopf, Phys. Rev. D **4**, 3418 (1971).

1.28 F. Close, Nucl. Phys. **1380**, 269 (1974).

1.29 S. M. Berman and J. R. Primack, Phys. Rev. D **9**, 2171 (1974).

1.30 W. Gerlach and O. Stern, Z. Phys. **9**, 349, 353 (1922).

1.31 W. Gerlach and O. Stern, Ann. Phys. **74**, 673 (1924).

1.32 S. A. Goudsmit and G. E. Uhlenbeck, Naturwiss **13**, 953 (1975).

1.33 P. A. M. Dirac, Proc. R. Soc. London A **117**, 610 (1928).

1.34 J. van Klinken, Nucl. Phys. **75**, 161 (1966).

1.35 P. Kusch and H. M. Foley, Phys. Rev. **74**, 250 (1948).

1.36 See, for example, R. S. van Dyck, Jr., P. B. Schwinberg, and H. G. Dehmelt, in New Frontiers in High Energy Physics, (Plenum Press, New York, 1979), p. 159; H. Dehmelt, in Atomic Physics 7, ed. by D. Kleppner and F. Pipkin, (Plenum Press, New York, 1981), p. 337.

1.37 M. J. Alguard, et al., Phys. Rev. Lett. **37** (1976), p. 1261; Phys. Rev. Lett. **41** (1978), p. 70.

1.38 R. N. Cahn and F. J. Gilman, Phys. Rev. D **17** (1978), p. 1313.

1.39 E. Fues, H. Hellmann, Phys. Z. B **1**, 465 (1980).

1.40 G. Baum, U. Koch, Nucl. Instrum. Meth. **71**, 189 (1969).

1.41 V. W. Hughes, R. L. Long, Jr., M. S. Lubell, M. Posner, W. Raith, Phys. Rev. A **5**, 195 (1972).

1.42 M. J. Alguard, etc., Nucl. Instrum. Meth. **163**, 29 (1979).

1.43 M. S. Lubell, in: "Atom Physics 5," R. Marrus, M. Prior, and H. Shugart, eds., pp. 325-373, Plenum Press, New York (1977).

1.44 K. Jost and J. Kessler, Phys. Rev. Lett. **15**, 575 (1965); M. Wilmers, R. Haug, and H. Deichsel, Z. Angew. Phys. **27**, 204 (1969).

1.45 J. Heinzmann, J. Kessler, J. Lorentz, Z. Phys. Rev. **240**,, 42 (1970); G. Baum, M. S. Lubell, W. Raith, Phys. Rev. A **5**, 1073 (1972).

1.46 R. L. Long, Jr., W. Raith and V. W. Hughes, Phys. Rev. Lett. **15**, 1 (1965); V. W. Hughes, R. L. Long, Jr., M. S. Lubell, M. Posner, and W. Raith, Phys. Rev. A **5**, 195 (1972).

1.47 P. J. Keliher, F. B. Dunning, M. R. O'Neill, R. D. Rundel, G. K. Walters, Phys. Rev. A **11**, 1271 (1975).

1.48 E. Kisker, G. Baum, A. M. Mahan, W. Raith, B. Reihl, Phys. Rev. B **18**, 2256 (1978).

1.49 H. C. Siegmann, F. Meier, M. Erbudak, M. Landolt: Adv. Electron. Electrons Phys. **62**, 1 (1984).

1.50 U. Heinzmann, K. Jost, J. Kessler, B. Ohnemus, Z. Phys. **251**, 354 (1972).

1.51 J. Kirschner, R. Feder, J. F. Wendelken, Phys. Rev. Lett. **47**, 614 (1981).

1.52 A. Eyers, F. Schäfers, G. Schonhense, U. Heinzmann, H. P. Oepen, K. Hünlich, J. Kirschner, G. Borstel: Phys. Rev. Lett. **52**, 1559 (1984).

1.53 R. T. Pierce, R. J. Celotta, G. C. Wang, W. N. Unertl, A. Galejs, C. E. Kuyatt, and S. R. Mielczarek, Rev. Sci. Instrum. **51**, 478 (1980).

1.54 M. R. O'Neill, M. Kalisvaart, F. B. Dunning, G. K. Walters, Phys. Rev. Lett. **34**, 1167 (1975).

1.55 V. W. Hughes, R. L. Long, Jr., M. S. Lubell, M. Posner, and W. Raith, Phys. Rev. A **5**, 195 (1972).

CHAPTER II

2.1 N. F. Mott and H. S. W. Massey, The Theory of Atomic Collisions, 3rd ed. (Oxford University, London, 1965).

2.2 S. Geltman, Topics in Atomic Collision Theory, (Academic Press, New York, 1969).

2.3 P. G. Burke, Potential Scattering in Atomic Physics, (Plenum Press, New York, 1977).

2.4 C. J. Joachain, Quantum Collisions Theory, (North-Holland, Amsterdam, 1979).

2.5 B. H. Bransden, Atomic Collision Theory, 2nd ed. (Benjamin/Cummings, Reading, MA 1983).

2.6 P. G. Burke and J. F. Williams, Phys. Rep. **4**, 525 (1977).

2.7 F. W. Byron, Jr., and C. J. Joachain, Phys. Rep. **34**, 233 (1977).

2.8 B. H. Bransden, and M. R. C. McDowell, Phys. Rep. **30**, 207 (1977); **46**, 249 (1978).

2.9 J. Callaway, Phys. Rev. **45**, 89 (1978); Adv. Phys. **29**, 771 (1980).

2.10 F. T. Chan, M. Lieber, G. Foster, and W. Williamson, Jr., Adv. Electron.Electron Phys. **49**, 133 (1979).

2.11 J. Kessler, Polarized Electrons (Springer, Berlin, 2nd ed., 1985).

2.12 M. S. Lubell, in Coherence and Correlation in Atomic Collisions, ed. by H. Kleinpoppen and J. F. Williams (Plenum Press, New York, p. 663 (1980).

2.13 M. Bron, Z. Physik **37**, 863 (1926).

2.14 R. H. Bassel and E. Gerjouy, Phys. Rev. **117**, 749 (1960).

2.15 J. E. Golden and J. H. McGuire, Phys. Rev. Lett. **32**, 1218 (1974).

2.16 M. R. H. Rudge and S. B. Schwartz, Proc. Phys. Soc. **88**, 563 (1966).

2.17 E. Gerjuoy, B. K. Thomas, and V. B. Sheorey, J. Phys. B **5**, 321 (1972).

2.18 G. Khayrallah, Phys. Rev. A **14**, 2064 (1976).

2.19 L. Hulthen, K. Fysiograf, Sällskap. Lund. Forh **14**, 21 (1944).

2.20 W. Kohn, Phys. Rev. **74**, 1763 (1948).

2.21 P. G. Burke and K. Smith, Mod. Phys. **34**, 458 (1962).

2.22 P. G. Burke and H. M. Schey, Phys. Rev. **126**, 147 (1962).

2.23 P. G. Burke, S. Ormonde and W. Whitaker, Proc. Phys. Soc. **92**, 319 (1967).

2.24 S. Geltman, Invited Papers, VII Int. Conf. on the Physics of Electronic and Atomic Collisions (North Holland, Amsterdam, 1972), p. 216.

2.25 A. Temkin, Phys. Rev. **107**, 1004 (1957).

2.26 A. Temkin, Phys. Rev. **116**, 358 (1959).

2.27 A. Temkin and J. C. Lamkin, Phys. Rev. **121**, 788 (1961).

2.28 A. J. Taylor and P. G. Burke, Proc. Phys. Soc. **92**, 336 (1967).

2.29 G. H. Wannier, Phys. Rev. **90**, 817 (1953).

2.30 A. Temkin, Phys. Rev. Lett. **49**, 365 (1982); comments At. Mol. Phys. **11**, 287 (1982).

2.31 A. R. P. Rau, Phys. Rev. A **4**, 207 (1971).

2.32 R. Peterkop, J. Phys. B **34**, 513 (1971).

2.33 J. W. McGowan and E. M. Clarke, Phys. Rev. **167**, 43 (1968).

2.34 S. Cvejanovic and F. H. Read, J. Phys. B **7**, 1841 (197).

2.35 T. A. Roth, Phys. Rev. A **5**, 476 (1971).

2.36 H. Klar and W. Schlecht, J. Phys. B **9**, 1699 (1976).

2.37 M. J. Alguard, V. W. Hughes, M. S. Lubell, and P. F. Wainwright, Phys. Rev. Lett. **39**, 334 (1977).

2.38 G. Baum, E. Kisker, W. Raith, W. Schroder, U. Sillmen, D. Zenses, J. Phys. B **14**, 4377 (1981).

2.39 C. H. Greene and A. R. P. Rau, Phys. Rev. Lett. **48**, 333 (1982).

CHAPTER V

5.1 P. Bevington, Data Reduction and Error Analysis for the Physical Science, (McGraw Hill, New York, 1969).

5.2 W.L. van Wyngaarden and H.R.J. Walters, J. Phys. B **19**, 1827-1842, (1986).

5.3 J. Callaway, McDowell and L.A. Morgan, J. Phys. B **9**, 2043-2051 (1976).

5.4 J. Callaway, Phys. Rev. A **32**, 775 (1985). Note that the theoretical calculations in this reference yield results that are consistent with measurements by J. Kauppila, W.R. Ott, and W.L. Fite, Phys. Rev. A **1**, 1099 (1970). The results of Callaway are deemed more accurate.

5.5 A.I. Timonthy and J.G. Timothy, Acta Electronica **14**, 159 (1971).

5.6 J.W. McGowan and E.M. Clarke, Phys. Rev. **167**, 43-51 (1968).

CHAPTER VI

6.1 A. Temkin, Phys. Rev. Lett. **49**, 365 (1982); Comments At. Mol. Phys. **11**, 2870 (1982).

6.2 M.S. Lubell, in Coherence and Correlation in Atomic Collisions, edited by H. Kleinpoppen and J.F. Williams (Plenum Publishing Corporation, 1980), p. 663.

6.3 W. Lichten and S. Schultz, Phys. Rev. **116**, 1132 (1959).

6.4 B. Bederson, Comments At. Mol. Phys. **1**, 65 (1969).

6.5 F.C. Tang, X. Zhang, F.B. Dunning and G.K. Walters, Rev. Sci. Instrum. **59**, (1988) p. 504.